PolyPublie
Polytechnique Montréal

POLYTECHNIQUE MONTRÉAL
UNIVERSITÉ D'INGÉNIERIE

Titre: Title:	Nonlinear Optics in Chalcogenide and Tellurite Microspheres for the Generation of Mid-Infrared Frequencies
Auteur: Author:	Francis Vanier
Date:	2015
Type:	Mémoire ou thèse / Dissertation or Thesis
Référence: Citation:	Vanier, F. (2015). Nonlinear Optics in Chalcogenide and Tellurite Microspheres for the Generation of Mid-Infrared Frequencies [Thèse de doctorat, École Polytechnique de Montréal]. PolyPublie. https://publications.polymtl.ca/2021/

Document en libre accès dans PolyPublie
Open Access document in PolyPublie

URL de PolyPublie: PolyPublie URL:	https://publications.polymtl.ca/2021/
Directeurs de recherche: Advisors:	Yves-Alain Peter, & Martin Rochette
Programme: Program:	Génie physique

Ce fichier a été téléchargé à partir de PolyPublie, le dépôt institutionnel de Polytechnique Montréal
This file has been downloaded from PolyPublie, the institutional repository of Polytechnique Montréal

https://publications.polymtl.ca

UNIVERSITÉ DE MONTRÉAL

NONLINEAR OPTICS IN CHALCOGENIDE AND TELLURITE MICROSPHERES FOR THE GENERATION OF MID-INFRARED FREQUENCIES

FRANCIS VANIER
DÉPARTEMENT DE GÉNIE PHYSIQUE
ÉCOLE POLYTECHNIQUE DE MONTRÉAL

THÈSE PRÉSENTÉE EN VUE DE L'OBTENTION
DU DIPLÔME DE PHILOSOPHIÆ DOCTOR
(GÉNIE PHYSIQUE)
DÉCEMBRE 2015

© Francis Vanier, 2015.

UNIVERSITÉ DE MONTRÉAL

ÉCOLE POLYTECHNIQUE DE MONTRÉAL

Cette thèse intitulée :

NONLINEAR OPTICS IN CHALCOGENIDE AND TELLURITE MICROSPHERES FOR THE GENERATION OF MID-INFRARED FREQUENCIES

présentée par : VANIER Francis
en vue de l'obtention du diplôme de : Philosophiæ Doctor
a été dûment acceptée par le jury d'examen constitué de :

M. FRANCOEUR Sébastien, Ph. D., président
M. PETER Yves-Alain, D. Sc., membre et directeur de recherche
M. ROCHETTE Martin, Ph. D., membre et codirecteur de recherche
M. SKOROBOGATIY Maksim A., Ph. D., membre
M. VALLÉE Réal, Ph. D., membre externe

To my family, Maripier, and Alice

À ma famille, à Maripier et à Alice

ACKNOWLEDGMENTS

I would like to manifest my greatest gratitude toward my research directors : Yves-Alain Peter and Martin Rochette. Your support throughout my doctoral studies allowed me to become a better researcher. You gave me the chance to conduct my researches according to my own ideas and wishes. Your follow-ups directed me toward simpler and more structured solutions. I will keep in mind your expertise, your diligence, your sense of priorities, and your attention to detail.

I leave a special note for Yves-Alain who accepted me into his laboratory more than eight years ago. Managing a research group is certainly not an easy task, but to ensure that the workplace is enjoyable every day calls for additional efforts. I tip my hat to him for this big family.

I thank all my colleagues and friends, older and new, interns and research associates, with whom I had enlightened discussions. I learned something from each one of you. I think of Sacha Bergeron, Annabelle Gascon, Pierre Pottier, Samir Saïdi, Jean-Philippe Coutu, Mathieu Auger, Frédéric Charbonneau, Max Klingmann Rönnqvist, Kazem Zandi, Alireza Hajhosseini Mesgar, Cecilia La Mela, Ahmad Hayat, Pablo Bianucci, Thomas Lazzara, Cédric Lemieux-Leduc, Philippe Jubinville, Léandro Acquaroli, Jérémy Maxin, Joseph André Bélanger, and Antoine Ramier. I keep a special thank for Alexandre Poulin, Raphaël St-Gelais, Tassadit Amrane, Hala Ghali, and Antoine Leblanc-Hotte for all those discussions about everything and nothing. My time with the research group would not have been as pleasant without you. I also thank Denis Gagnon for his relevant points of view throughout the years. Finally I cannot forget my colleagues and friends outside the research group : Patou, Julia, Polo, Gab, Rémi, André-Pierre, Philippe, and all the people from the *Lab des Fibres* and from the *Fabulas*.

I thank École Polytechnique de Montréal, the Department of Engineering Physics and their infrastructures for those ten years and unforgettable memories. I sincerely think that my learnings have nothing to envy to any university curriculum. They will always serve me. The link between students and the professors is different from other departments, it is more accessible and straightforward : it is more human. I never hesitated to ask them questions and I always felt the same reciprocal interest for Science. I also think about all the technicians, people from the *Laboratoire de Microfabrication*, and to Mikael Leduc for their help and precious advices.

I personally thank CoreActive High-Tech for supplying us high purity As_2S_3 glass optical

fibers that are the basis components of my researches. I also thank Pr. Messaddeq's laboratory at Laval University and especially Dr. Mohammed El Amaroui and François Côté for the high purity tellurite optical fibers and their relevant advices.

I thank the jury for their interest in my thesis project and for accepting to examine my work. Following your expertise and skills, your contribution is essential. I am very grateful.

I also thank the *Fondation de Polytechnique*, the *Fonds de recherche Québec Nature et technologies*, and the *Conseil de recherches en sciences naturelles et en génie du Canada* for their financial support throughout my studies. I know that the selection is highly competitive and I am grateful that they gave me this chance. I would not have started a doctoral project without this aid.

I greet my family who has always encouraged me with pride throughout the years, despite their understandable lack of understanding toward my research subject.

I keep my last and most important thanks for Maripier and her unmatched support throughout this adventure. Difficult moments were quickly forgotten in your presence. Your encouragement especially during tiresome redaction moments greatly contributed to my writings' quality. Thank you a thousand times !

RÉSUMÉ

Le développement de sources optiques émettant au-delà des bandes de télécommunication jusqu'à l'infrarouge moyen est grandissant. Des sources nouvelles et améliorées émettant à des longueurs d'onde allant de 2 μm à 12 μm sont régulièrement rapportées dans la communauté scientifique et quelques sources sont déjà disponibles sur le marché. Divers domaines profitent de ces développements dont l'imagerie, les télécommunications, le traitement des matériaux et l'analyse moléculaire pour n'en nommer que quelques-uns. Parmi ces sources, les lasers basés sur les microcavités à modes de galerie sont de plus en plus présents puisque beaucoup d'efforts sont déployés au transfert de leurs propriétés uniques du proche infrarouge à l'infrarouge moyen.

En plus de leurs dimensions micrométriques, les microcavités à modes de galerie sont naturellement adaptées à la génération non linéaire de signaux optiques : elles possèdent de grands facteurs de qualité et de petits volumes modaux. Les processus non linéaires de diffusion Raman stimulée et en cascade sont attrayants puisqu'ils ne requièrent aucune condition de dispersion particulière. De plus, ces processus sont observables sur toute la fenêtre de transmission du matériau. La silice qui est le matériel de choix typiquement utilisé pour la transmission de signal dans le proche infrarouge devient opaque aux longueurs d'onde excédant 2 μm. Pour cette raison, on tirera profit de matériaux moins conventionnels mais transparents dans l'infrarouge moyen, tels que les verres de chalcogénure et de tellure.

Parmi les microcavités à modes de galerie basées sur les verres de chalcogénure qui ont été rapportées, aucune démonstration de génération non linéaire n'a été faite. Cela s'explique par des pertes optiques trop élevées qui limitent les puissances de seuil aux dizaines de milliwatts, loin des puissances de seuil de quelques microwatts observées dans les microcavités en silice dans le proche infrarouge.

La première contribution de cette thèse répond à ce problème par la fabrication de microsphères de haute qualité en As_2S_3. Reconnus pour leur transparence entre les longueurs d'onde de 1 μm à 6 μm, les verres en As_2S_3 peuvent être produits avec une grande pureté et possèdent un gain Raman élevé comparé à la silice. Les microsphères en As_2S_3 sont produites à partir de fibres optiques de grande pureté et elles démontrent des pertes optiques similaires à celles des fibres. Grâce aux procédés d'usinage par laser, les facteurs de qualité optique sont deux ordres de grandeur supérieurs aux valeurs précédemment rapportées. Les microspheres peuvent être fabriquées avec des diamètres variant de 20 μm à 400 μm. Enfin, leur qualité est conservée par un procédé d'encapsulation. Les dispositifs inclus également une fibre optique

effilée permettant le couplage des signaux optiques avec la microcavité.

La seconde contribution de mes travaux de doctorat est la démonstration de l'émission Raman stimulée dans les microsphères en As_2S_3. Des puissances de seuil couplées de $\sim$ 13 μW jumelées à des efficacités de conversion interne de 10 % ont été observées pour des longueurs d'onde de pompe et de signal de 1550 nm et 1640 nm. Ces résultats sont les premières observations de processus non linéaire dans des microcavités en verres de chalcogénure. De plus, les performances de l'émission Raman dans les microsphères en As_2S_3 sont comparables aux meilleures sources à effet Raman basées sur des microcavités à modes de galerie. Afin d'obtenir des signaux à des longueurs d'onde supérieures à 2 μm, les microsphères en As_2S_3 sont également utilisées pour l'émission Raman en cascade. Jusqu'à cinq ordres Raman sont observés en utilisant une longueur d'onde de pompe de 1560 nm. Des raies d'émission sont générées à des longueurs d'onde de 1645 nm, 1750 nm, 1860 nm, 1990 nm et 2140 nm. De plus, plusieurs raies d'émission Raman à des longueurs d'onde supérieures à 2 μm sont observées en utilisant une longueur d'onde de 1880 nm. Des bandes d'émission situées à 2015 nm, 2710 nm et 2350 nm sont observées et mesurées. Ces résultats supportent l'utilisation potentielle des microsphères en As_2S_3 comme sources optiques compactes dans l'infrarouge moyen.

Les longueurs d'onde des raies d'émission Raman sont dictées par la longueur d'onde du signal de pompe. Les ions de terres rares tel que Tm^{3+} sont connus pour leurs bandes d'émission près et au-delà de 2 μm. Des microcavités à modes de galerie basées sur des verres de chalcogénure ou de tellure dopés pourraient servir de milieux de gain efficaces dans l'infrarouge moyen. De plus, l'émission Raman stimulée ou en cascade permettrait la génération de signaux à des longueurs d'onde plus longues si ces processus sont pompés à partir de l'émission laser.

La troisième contribution de cette thèse teste cette idée avec la génération d'émission laser dans des microsphères en verres de tellure dopés au thulium. Des raies d'émission laser sont observées à des longueurs d'onde centrées sur 1975 nm pour des puissances de seuil $\sim$ 30 μW. Ces résultats réduisent par dix les valeurs précédemment rapportées et démontrent le potentiel de sources optiques hybrides basées sur l'émission laser et Raman. Des calculs montrent qu'une amélioration de la pureté des verres de tellure dopés abaisse les puissances de seuil de l'émission Raman à quelques milliwatts.

ABSTRACT

In the recent years, the development of optical sources emitting outside the standard telecommunication bands and in the mid-infrared (mid-IR) region is thriving. New and improved sources with wavelengths spanning from 2 μm to 12 μm are regularly reported in the research community and various sources are already available on the market. Diverse domains including imagery, communication, material processing, and molecular analysis are taking advantage of these sources. Among these, micron-size lasers based on whispering gallery modes (WGM) microcavities are gradually entering the race as more effort is invested to transfer their unique properties from near-infrared to mid-IR regions. Along their compactness, WGM microcavities are naturally suitable for nonlinear signal generation: they possess relatively large Q-factors and small mode volumes. Stimulated and cascaded Raman scattering processes are especially attractive for signal generation as they require no particular dispersion condition. Furthermore, these processes can be observed across the entire transparency window of the host material. Typical near-IR materials such as silica have to be replaced by unconventional ones such as chalcogenide and tellurite glasses.

All previously reported WGM microcavities based on chalcogenide and tellurite glasses failed to demonstrate nonlinear interaction. They suffered from large optical losses that push threshold power levels to tens of milliwatts, far from the μW level usually observed in silica microcavities at near-IR wavelengths.

The first contribution of this thesis is therefore to solve this issue by fabricating low loss As_2S_3 WGM microcavities. Known for its $1-6$ μm transparency window, As_2S_3 glass can be produced with high purity and exhibits a large Raman gain compared to silica. Made from high purity optical fibers, As_2S_3 microspheres demonstrated loss levels similar to the optical fiber attenuation. Thanks to a fabrication technique based on laser shaping, the measured optical Q-factors exceed previously reported values by two orders of magnitude in As_2S_3. Microspheres can be produced with diameters varying between 20 μm and 400 μm. Their quality is maintained using an encapsulation method. The packaged device additionally includes a tapered optical fiber to couple light in and out of the microcavity.

The second thesis contribution is the demonstration of stimulated Raman scattering in As_2S_3 microspheres. Threshold coupled pump powers of ~ 13 μW with internal power conversion efficiency of 10 % were observed for pump and signal wavelengths of 1550 nm and 1640 nm. These results are the first observations of nonlinear processes in chalcogenide microcavities. Furthermore, Raman lasing performances in As_2S_3 microspheres are comparable to the best

WGM Raman sources. To push the emission wavelengths above 2 μm into the mid-infrared range, As_2S_3 microspheres were used to generate cascaded Raman emission. Up to five Raman orders were observed using a pump wavelength of 1560 nm. Raman emission lines at wavelengths of 1645 nm, 1750 nm, 1860 nm, 1990 nm and 2140 nm were generated. Additionally, multiple Raman emission lines with wavelengths above 2 μm were observed using a pump wavelength of 1880 nm. Emission bands at 2015 nm, 2170 nm and 2350 nm were detected. These results support the potential use of As_2S_3 microspheres as low power mid-IR micron-size Raman sources.

The emission wavelengths of Raman sources are dictated by the pump signal wavelength. Laser media doped with rare-earth ions such as Tm^{3+} are known for their emission bands near and beyond 2 μm. Ions-doped chalcogenide and tellurite WGM microcavities could potentially act as efficient gain media for the generation of mid-IR emission. Additionally, stimulated and cascaded Raman scattering could extend the emission wavelength further if these processes were pumped from the laser emission.

The third contribution tests this idea with the generation of laser emission in Tm-doped tellurite glass microspheres. The signal emission at wavelengths near 1975 nm was demonstrated with threshold pump powers ~ 30 μW. This tenfold improvement over the reported performances in Tm-doped tellurite microcavities puts the realization of hybrid ions doped/Raman sources at a reachable level. Calculations show that realistic improvements of tellurite glass purity will bring down threshold powers to the milliwatt level.

TABLE OF CONTENTS

DEDICATION iii

ACKNOWLEDGMENTS iv

RÉSUMÉ vi

ABSTRACT viii

TABLE OF CONTENTS x

LIST OF TABLES xiii

LIST OF FIGURES xiv

LIST OF ABBREVIATIONS xxii

LIST OF SYMBOLS xxiii

LIST OF ANNEXES xxvi

CHAPTER 1 INTRODUCTION 1
- 1.1 WGM microcavities as miniature Raman sources 3
- 1.2 Chalcogenide WGM microcavities 6
- 1.3 Extended emission in WGM microcavities 8
- 1.4 Achieved objectives & original contributions 11
- 1.5 Thesis structure 12

CHAPTER 2 BASIC CONCEPTS 13
- 2.1 The waveguide-cavity system 14
- 2.2 Linear coupled-modes equations 15
- 2.3 Linear characteristics of WGM microcavities 21
  - 2.3.1 Q-factor 21
  - 2.3.2 Transmission coefficient 22
  - 2.3.3 Q-factor measurement 22
  - 2.3.4 Coupled power 23
- 2.4 Eigenmodes of microspheres 24

2.5 Nonlinear coupled-modes equations 30
2.5.1 Stimulated Raman scattering 30
2.5.2 Cascaded Raman scattering 34
2.6 Quasi-two level laser modeling 38

CHAPTER 3 EXPERIMENTATION 43
3.1 Microspheres fabrication 43
3.1.1 Laser melting setup 44
3.1.2 Raman spectroscopy on As_2S_3 melted glass 46
3.1.3 Tapered silica fiber fabrication 48
3.1.4 Cavity encapsulation 49
3.2 Linear and nonlinear signals measurements 51
3.2.1 Transmission measurement setup 51
3.2.2 Thermal drifting 56
3.2.3 Raman and laser signal measurements through thermal drifting . . . 57
3.2.4 Self-frequency locking setup 60

CHAPTER 4 ARTICLE 1 - RAMAN LASING IN AS_2S_3 HIGH-Q WHISPERING GALLERY MODE RESONATORS 62
4.1 Authors and Affiliation 62
4.2 Abstract 62
4.3 Introduction 62
4.4 Sphere Fabrication 63
4.5 Stimulated Raman scattering measurements 64
4.6 Conclusion 69
4.7 Complementary results 70
4.7.1 Back on the Raman signal measurements 70
4.7.2 Theoretical analysis 72

CHAPTER 5 ARTICLE 2 - CASCADED RAMAN LASING IN PACKAGED HIGH QUALITY AS_2S_3 MICROSPHERES 74
5.1 Authors and Affiliation 74
5.2 Abstract 74
5.3 Introduction 74
5.4 Self-frequency locking laser setup 75
5.5 Sphere Encapsulation 76
5.6 Cascaded SRS emission from the 1550 nm wavelength region 78

5.7 Cascaded SRS emission from the 1880 nm wavelength region 80
5.8 Conclusion 82
5.9 Complementary results 83
5.9.1 Theoretical analysis : cascaded Raman with a pump wavelength of 1536 nm 83

CHAPTER 6 ARTICLE 3 - LOW-THRESHOLD LASING AT 1975 NM IN THULIUM-DOPED TELLURITE GLASS MICROSPHERES 86
6.1 Authors and Affiliation 86
6.2 Abstract 86
6.3 Introduction 86
6.4 Tellurite fiber and sphere fabrication 87
6.5 Tm-doped sphere laser emission 89
6.6 Conclusion 94

CHAPTER 7 GENERAL DISCUSSION 95
7.1 Are As_2S_3 microspheres good Raman WGM sources ? 96
7.2 Are As_2S_3 microspheres good cascaded Raman WGM sources ? 98
7.3 Stabilization issues of the self-frequency locking laser setup 100
7.4 Raman emission in Tm-doped tellurite glass WGM lasers 102
7.5 Achieving Raman lasing in ions doped WGM microcavities 103

CHAPTER 8 CONCLUSIONS & RECOMMENDATIONS 107

BIBLIOGRAPHY 110

ANNEXES 133

LIST OF TABLES

Table 1.1 : WGM microcavity applications and their references. 1

Table 1.2 : Estimated SRS threshold pump powers at 1550 nm based on WGM microcavity characteristics observed before this thesis work along their measured Q-factors (upper part) and their potential Q-factors (lower part). 5

Table 1.3 : Optical properties of As_2S_3 and As_2Se_3 glasses. 6

Table 1.4 : Chalcogenide WGM microcavities. 7

Table 2.1 : Linear rates, coupling constants, and lifetimes. 16

Table 3.1 : Extracted linear resonance characteristics of Fig. 3.13. 55

Table 4.1 : Measured pump Q-factors and extracted Raman signal Q-factors. . 72

Table 5.1 : Measured (top) and extracted (bottom) characteristic values of the Raman emission modes. 83

Table 7.1 : SRS performances of reported WGM microcavities. 96

Table 7.2 : Reported cascaded Raman performances in WGM microcavities. . . 100

Table B.1 : Linear coupled-modes approximations and outcomes. 160

Table B.2 : Linear rates, coupling constants, and lifetimes. 160

LIST OF FIGURES

Figure 1.1 : Upper part : material transparency window of demonstrated WGM microcavities [144–147]. Band colors are used to clearly separate the material windows. Lower part : molecular vibrations from HITRAN database. Darker areas represent stronger molecule's responses. . . . 4

Figure 1.2 : Frequency diagram of the cascaded Raman process. 8

Figure 1.3 : Guide to high-order Raman emission for As_2S_3 glass. For a given pump wavelength, Raman emission region are shown up to 4th order. Dotted lines denote the Raman gain bandwidth. Accessible Raman region are displayed in the cases where the pump signals are the emission bands from Er^{3+} and Tm^{3+}. 9

Figure 2.1 : Different coupling configurations - **(a)** Integrated waveguide and disk **(b)** Tapered optical fiber **(c)** Total internal reflection in a prism. . . . 13

Figure 2.2 : Schematic of the linear coupling processes between a waveguide and a WGM microcavity. 14

Figure 2.3 : T_j and R_j for $\Gamma_{jj} = 0$, $\Gamma_{j-j} = 0$, $\Gamma'_{jj} = \Gamma'_{j-j} = 0$ using Eq. B.77. Different coupling regimes are shown : critical (line), overcoupling (dashed line) and undercoupling (dash-dot line). 18

Figure 2.4 : T_j and R_j for $\Gamma_{jj} = 0$ and $\Gamma_{jj} = \frac{2}{\tau_j}$, $\Gamma_{j-j} = 0$, $\Gamma'_{jj} = \Gamma'_{j-j} = 0$ using Eq. B.77. 18

Figure 2.5 : T_j and R_j for $\Gamma_{jj} = 0$, $\Gamma_{j-j} = \frac{1}{\tau_j}$, $\Gamma'_{jj} = \Gamma'_{j-j} = 0$ using Eq. B.73 and B.74. 19

Figure 2.6 : T_j and R_j for $\Gamma_{jj} = 0$, $\Gamma_{j-j} = \frac{1}{\tau_j}$, $\Gamma'_{jj} = \frac{1}{10\tau_j}$ and $\Gamma'_{j-j} = \frac{1}{\tau_j}$ using Eq. B.68 and Eq. B.69. 20

Figure 2.7 : Spherical coordinates for a microsphere. 25

Figure 2.8 : Spatial distribution of TE solutions $|\mathbf{e}_j|^2$ for an As_2S_3 sphere with a radius of 15 μm. The wavelength is 1550 nm, $l_j = 139$ and $m_j = l_j$. The dashed line is the cavity's boundary. 26

Figure 2.9 : Spatial distribution of TE solutions $|\mathbf{e}_j|^2$ for an As_2S_3 sphere with a radius of 15 μm. The wavelength is 1547 nm, $l_j = 132$ and $m_j = l_j - 2$. The dashed line is the cavity's boundary. 26

Figure 2.10 : TE mode wavelengths and their associated l_j numbers for an As_2S_3 sphere with a radius of 15 μm. Red dots denote the 1st, 5th and 10th radial order. 27

Figure 2.11 : TE mode wavelengths and their associated l_j numbers for an As_2S_3 sphere with a radius of 150 μm. Red dots denote the 1st, 5th and 10th radial order. Mode wavelengths of radial order $> 10^{th}$ are located in the shaded area. Inset : Zoom on the C-band section to show the high density of modes. 28

Figure 2.12 : Linear sphere dispersion $\Delta\omega_{lin}$ for an As_2S_3 sphere with a radius of 150 μm. Two black lines indicate the resonance linewidth for a Q-factor of 1×10^7. 29

Figure 2.13 : Stokes photon $\hbar\omega_s$ and anti-Stokes photon $\hbar\omega_a$ creation through Raman scattering of a pump signal photon $\hbar\omega_p$. 31

Figure 2.14 : Schematic of the first three Raman order evolution. 37

Figure 2.15 : Typical energy level path for Er^{3+} and Tm^{3+} ions. Lines and dashed lines express radiative and non radiative decays. 38

Figure 3.1 : Microsphere fabrication steps : (a) A high purity optical fiber is placed under the CO_2 laser illumination. (b) The fiber is heated by the laser beam and is pulled into a tapered fiber until it breaks. A narrow tip is left. (c) A microsphere is obtained by heating the fiber tip. The surface tension of the molten glass naturally forms a spherical shape. 44

Figure 3.2 : Typical microspheres produced using the laser reflow technique - (a) and (b) Images of As_2S_3 spheres. (c) Scanning electron microscope image of an As_2S_3 sphere. (d) Visible image of a tellurite sphere. . . . 45

Figure 3.3 : (a) Laser setup - The CO_2 laser beam, depicted in a false red color, is focused on a fiber pulling system positioned by a 3-axis stage. A beamsplitter allows the simultaneous monitoring of the focusing spot and the target using visible optics and a camera. (b) Photograph of the setup. Additional components are present : red LED ring light for visible imaging, a nitrogen flow (white tube) pointing toward the focused region, and a vacuum vent (black tube) to extract vapors from the melting. 46

Figure 3.4 : Fiber pulling and tapering system used in the laser setup. (a) An optical fiber is clamped at two locations : a fixed block on the left side and a moving block in the middle. The moving block is linked to weights with a pulling rope. (b) While the laser beam heats the fiber, it is pulled and a tapered shape forms. (c) The tapered shape can be reduced to the required diameter. (d) A narrow glass filament eventually forms. (e) The tapered fiber finally breaks into a glass tip. (f) The glass tip is heated again to form a sphere. 47

Figure 3.5 : Raman spectra of As_2S_3 glass for three locations : the optical fiber, the tapered fiber part and the microsphere. The spectra are normalized and are offset vertically for clarity. 48

Figure 3.6 : Raman spectroscopy spectra of an As_2S_3 microsphere taken along a line perpendicular to the optical mode area. The spectra locations are separated by 0.5 μm. The optical mode area is denoted by red lines. The spectra are normalized and are offset vertically for clarity. 49

Figure 3.7 : Pulling setup used to fabricate silica tapered optical fiber. A flame is swept along the optical fiber while two motorized stages are pulling it apart. 50

Figure 3.8 : An As_2S_3 microsphere contaminated by dust. 50

Figure 3.9 : Packaged tapered fiber and microsphere. (a) 3D model of the silica glass tube. The silica tapered fiber is fixed to two glass half-rod blocks. The fiber tip holding the sphere is glued on the half-tube side. (b) Photograph of an encapsulated system. 51

Figure 3.10 : Basic setup for transmission spectra measurements - TLS : Tunable laser source, PC : Polarization controller, DET : Photodiode detector, OSC : Oscilloscope, TRIG : Trigger signal, and SM : Single mode. . . 52

Figure 3.11 : Evolution of transmission spectra taken with an increasing waveguide coupling. The input power is kept constant. Top spectrum has the lowest waveguide coupling. The bottom spectrum has the largest waveguide coupling when the tapered fiber touches the sphere. 53

Figure 3.12 : Transmission measurement spectra for two As_2S_3 sphere resonances. Lorentzian curve fits are used in red to extract the resonance FWHM. The resonance total Q-factors are 3.1×10^6 (left) and 7.0×10^6 (right). 54

Figure 3.13 : Transmission measurement spectra for two As_2S_3 sphere resonances with notable modal coupling. The fitted double peak curves in red are based on Relation B.68. 55

Figure 3.14 : Heat propagation in a microsphere. The optical mode is located on the equatorial line. 56
Figure 3.15 : Thermal drifting of a resonance as the tunable laser line is swept toward longer wavelengths for an increasing optical power. The black and green lines represent the lowest and largest power respectively. . 57
Figure 3.16 : Thermal drifting of a resonance for a fixed laser line with an increasing pump power and transmission shift dT. This effect is particularly important for As_2S_3 WGM microcavities. 58
Figure 3.17 : Left plot - Increasing coupled power during thermal drifting. If the coupled power threshold is achieved, the nonlinear or laser signal starts increasing. The constant input power and the threshold are shown as dotted black and blue lines respectively. Right plot - Signal power as a function of the coupled power. 58
Figure 3.18 : Basic setup for nonlinear and laser measurements - TLS : Tunable laser source, PC : Polarization controller, DET : Photodiode detector, OSC : Oscilloscope, OSA : Optical spectrum analyzer, TRIG : Trigger signal and WDM : Wavelength division multiplexer. 59
Figure 3.19 : Basic self-frequency locking setup - AMP : Optical amplifier, TF : Tunable bandpass filter, CIRC : Circulator, PC : Polarization controller, POL : Linear polarizer, and OSA : Optical spectrum analyzer. 60
Figure 4.1 : Transmission spectrum of a resonance with a $Q_L = 7 \times 10^7$. Inset : Micrograph of a typical microsphere produced with the laser melting process. 64
Figure 4.2 : Experimental setup for Raman laser emission measurements - TLS : Tunable Laser Source, PC : Polarization Controler, WDM : Wavelength Division Multiplexer, OSA : Optical Spectrum Analyzer, Det : Detector, Osc : Oscilloscope. 65
Figure 4.3 : **(a)** Raman laser emission with an input pump power of 123 μW(black curve). Superimposed (red curve) is the bandwidth-limited spectrum of a narrow cw laser, indicating that the Raman laser emission spectrum is also bandwidth-limited by the OSA. **(b)** Maxima of Raman emission spectra as a function of the input pump power. The Raman lasing threshold power is 61.3 μW. 66

Figure 4.4 : Scheme of the measurements. **(a)** Oscilloscope view of transmitted pump and Raman emission power P_R. **(b)** Raman emission power against coupled pump power P_{coup} gives the coupled pump threshold power P_{coup}^{th} and the internal conversion efficiency η_{in} of the Raman process. P_{in} and T are the input pump power and the transmission value respectively. 67

Figure 4.5 : Temporal domain measurements of SRS emission for an input pump power of 49 μW with transmitted pump power in black, forward Raman emission in red and backward Raman emission in blue. Raman lasing starts at a detuning of 2 pm. 67

Figure 4.6 : Raman emission power versus coupled pump power for an input pump power of 49 μW. Raman lasing starts at 12.9 μW of coupled power with an internal conversion efficiency of 10.7 %. 68

Figure 4.7 : Raman emission power curves taken with four input pump powers : (a) 33 μW, (b) 49 μW, (c) 82 μW and (d) 100 μW. 70

Figure 4.8 : Ratio of the forward Raman emission power over the total Raman power. The input pump power is 49 μW. 71

Figure 4.9 : Transverse view of the pump (left) and signal (right) TE modes corresponding to a wavelength of 1552.5 nm and 1640.7 nm respectively. The first radial pump mode is linked to $m_p = l_p = 338$. The signal mode is associated to $m_p = l_p = 319$. 72

Figure 5.1 : Self-frequency locking laser setup - The gain signal from a Er-doped fiber amplifer is filtered using a 0.2 nm bandwidth tunable band-pass filter. An As_2S_3 microsphere acts as a narrow-band mirror and sends back a single line emission in the fiber loop. The transmitted pump signal and the forward Raman signal is measured by the OSA. A powermeter measures the injected pump power in the tapered fiber. . . 76

Figure 5.2 : Glass tube packaging - (a) Glass half-rods are installed in the lower half of a glass tube. (b) The tapered fiber is attached to the glass half-rods. While the microsphere is in a optimal coupling condition, its fiber tip is glued to the side of the half-tube. (c) The upper half of the glass tube is placed on top. 77

Figure 5.3 : (a) Image of a typical packaged As_2S_3 microsphere. (b) Transmission spectrum of a high-Q resonance from a packaged As_2S_3 microsphere. The loaded Q-factor $Q_L = 1 \times 10^7$. 77

Figure 5.4 : Spectrum of a cascaded SRS emission of an As_2S_3 microsphere including 5 Raman orders generated from a pump wavelength of 1557 nm. The injected pump power in the tapered fiber is 6.3 mW. Each Raman order bands are centered on wavelengths of 1646 nm, 1747 nm, 1861 nm, 1991 nm and 2140 nm respectively. The inset shows a typical Raman spectroscopy measurement made on an As_2S_3 sphere surface. 78

Figure 5.5 : Forward Raman signal power measurements for the (a) 1st (b) 2nd and (c) 3rd Raman order. In the inset of (a), SRS threshold pump power is 370 μW. In (b), the threshold pump power of the second order Raman emission is 430 μW. The first order Raman signal saturates when the second order SRS emission power increases between 450 μW and 600 μW of pump power. In (c), the threshold power of the third Raman order is 607 μW. The first order Raman signal increases again when the third order Raman signal is getting stronger. 79

Figure 5.6 : Self-frequency locking laser setup at 1880 nm - The gain of a Tm-doped fiber is sent to the microsphere which acts as a narrow band mirror. The reflected signal is amplified in the fiber loop. The spectra are measured using an OSA. 81

Figure 5.7 : Spectrum of a cascaded SRS emission with 3 Raman orders with a pump wavelength band centered on 1880 nm. Multimode Raman emission band positions are 2015 nm, 2170 nm and 2350 nm respectively. 82

Figure 5.8 : Forward Raman signal power measurements for the (a) 1st (b) 2nd and (c) 3rd Raman order. In the inset of (a), SRS threshold pump power is $\sim$ 70 μW. The inset shows a close-up view near the threshold. In (b), the threshold pump power of the second order Raman emission is also $\sim$ 70 μW. In (c), the threshold power of the third Raman order is 220 μW. 85

Figure 6.1 : (a) Experimental setup for Tm-doped tellurite glass microsphere laser emission - TLS : Tunable laser source, PC : Polarization controller, DET : Optical detector and OSA : Optical spectrum analyzer. (b) Microscope image of a typical tellurite microsphere. 88

Figure 6.2 : Intrinsic Q-factor Q_0 for undoped tellurite spheres (black diamonds) and Tm-doped tellurite spheres (red circles) for an undercoupled regime. Theoretical intrinsic Q_0^{Tm} following absorption cross section values of [248, 273] are also shown. 89

Figure 6.3 : Forward emission spectrum of a Tm-doped tellurite glass microsphere. The photoluminescence of the Tm ions is filtered by the cavity resonances. Multimode laser emission lines are also visible and are centered at a wavelength of 1975 nm. 90

Figure 6.4 : Forward signal power at a wavelength of 1975 nm versus the coupled pump power. The input pump power is 86 μW. Curve A, B and C represent different pump resonances near a wavelength of 1554 nm. . 91

Figure 6.5 : Forward signal power at a wavelength of 1975 nm versus the coupled pump power near wavelengths of 1504 nm (black squares), 1554 nm (red circles), 1585 nm (green triangles), and 1629 nm (blue diamond). For each pump wavelength regions, three curves represent different pump resonances. 92

Figure 6.6 : Signal resonance Q_0 (black circles) and Q_c (black squares) at 1975 nm obtained by fitting their threshold curves at different pump wavelengths for 1st order radial modes. The fitted absorption cross sections (red triangles) are also shown. 93

Figure 7.1 : Consequence of a smaller coupling Q-factor $Q_{p,c}$ for the pump mode. The Raman mode Q-factors remain constant and are based on the results of Chapter 4. 97

Figure 7.2 : Consequence of a larger intrinsic Q-factor $Q_{p,0}$ for the pump mode. The Raman mode Q-factors remain constant and are based on the results of Chapter 4. 98

Figure 7.3 : Consequence of a larger intrinsic Q-factor $Q_{j,0}$ for the pump and the signal modes. The couping Q-factors $Q_{p,c} = Q_{s,c}$ remain constant. . . 99

Figure 7.4 : Modified self-frequency locking laser setup including additional filtering steps. EDFA : Erbium Doped Fiber Amplifier, Iso : Isolator, TBF : Tunable Bandpass Filter, PC : Polarization Controler, Pol : Polarizer, OSA : Optical Spectrum Analyzer, Det : Photodiode detector. 101

Figure 7.5 : Transverse view of the pump (top), laser signal (center) and Raman signal (bottom) TE modes corresponding to a wavelength of 1554 nm ($m_p = l_p = 106$), 1975 nm ($m_p = l_p = 82$), and 2270 nm ($m_p = l_p = 71$) respectively. 104

Figure 7.6 : Input pump threshold power to achieve lasing (black lines) and simultaneous first order Raman emission (blue lines). For each case, two curves are shown and represent two coupling conditions : $Q_{s,c} = Q_{R,c} = Q_{p,c}$ and $Q_{s,c} = Q_{R,c} = 10Q_{p,c}$. The laser signal external power conversion efficiency, $\eta_{ex}^{(s)}$, is shown in red. 105
Figure B.1 : Schematic of the linear coupling processes between a waveguide and a WGM microcavity. 136
Figure B.2 : **(a)** The cavity refractive index profile $n_0|_c$. **(b)** The waveguide refractive index profile $n_0|_g$. 150
Figure B.3 : Spherical coordinates. 170
Figure B.4 : Stokes photon $\hbar\omega_s$ and anti-Stokes photon $\hbar\omega_a$ creation through Raman scattering of a pump signal photon $\hbar\omega_p$. 174

LIST OF ABBREVIATIONS

CW	Continuous-wave
EM	Electromagnetic
FSR	Free spectral range
FWHM	Full width at half maximum
FWM	Four-wave mixing
IR	Infrared
LIDAR	Light detection and ranging
QCL	Quantum cascade laser
RI	Refractive index
SRS	Stimulated Raman scattering
TE	Transverse electric
TM	Transverse magnetic
WGM	Whispering gallery mode

LIST OF SYMBOLS

Physical constants

c	Velocity of light in vacuum
ϵ_0	Vacuum permittivity
μ_0	Vacuum permeability
$\hbar$	Reduced Planck constant

Material properties

$\sigma_{a,e}$	Effective absorption and emission cross sections
α	Polarizability
α_{el}	Polarizability electronic contribution
α_{lin}	Linear attenuation
$\delta\epsilon$	Permittivity perturbation
ϵ_r	Relative permittivity
$g_R^{(b)}$	Bulk Raman gain
N_T	Total ions concentrations
N_1	Ions concentrations in the ground levels
N_2	Ions concentrations in the upper levels
n	Refractive index
n_2	Nonlinear Kerr index
Q_v	Nucleus displacement
R_c	Cavity radius
T_g	Glass transition temperature
τ_{Tm}	Ions lifetime
Ω_v	Raman frequency shift (angular)
$\chi^{(n)}$	n^{th} order electric susceptibility

Coordinates

ϕ	Azimuthal component in spherical coordinates
$\boldsymbol{r}$	Spatial position vector
ρ	Radial component in spherical coordinates
t	Time coordinate
θ	Polar component in spherical coordinates
z	Spatial coordinate along the waveguide
z_0	Coupling region entrance position along the waveguide

z_1	Coupling region exit position along the waveguide

Associated to optical modes j or L

a_j	Cavity mode amplitude
$\delta\omega_j(T_j)$	Mode splitting spectral separation
$\boldsymbol{E_j}$	Electric field vector
$\boldsymbol{e_j}$	Spatial component vector of the electric field
η_{ex}	External power conversion efficiency
η_{in}	Internal power conversion efficiency
$\Delta\omega_j$	Resonance's full width at half maximum
Γ_{jj}	Transfer rates between two cavity modes
Γ'_{jj}	Loss rates due to perturbations
g_R	Cavity Raman gain
$g_{Tm}^{(j)}$	Cavity gain from thulium ions
$\boldsymbol{H_j}$	Magnetic field vector
$\boldsymbol{h_j}$	Spatial component vector of the magnetic field
I_j	Mode intensity
k_j	Wavenumber of light
l_j	Polar integer number
κ_{jL}	Coupling coefficient between a cavity mode and a waveguide mode
λ_j	Wavelength of light
m_j	Azimuthal integer number
M_L	Waveguide mode normalization factor
N_j	Cavity mode normalization factor
$\boldsymbol{P}$	Electric polarization vector
P_{coup}	Coupled power
P_{in}	Input power
P_{out}	Output power
P_S	Output signal power
P_j	Circulating mode power
$Q_{j,0}$	Intrinsic Q-factor
$Q_{j,c}$	Coupling Q-factor
$Q_{T,0}$	Total Q-factor
R_j	Reflection coefficient
s_L	Waveguide mode amplitude
T_j	Transmission coefficient
$T_{j,0}$	Transmission coefficient at the resonance's center

T_{ω_j}	One optical cycle duration
$\tau_{j,0}$	Intrinsic photon's lifetime
$\tau_{j,0}$	Extrinsic photon's lifetime
τ_j	Total photon's lifetime
Υ_j	Power accumulation factor
V_j	Mode volume
V_{iijj}	Effective modes volume of fields overlap
ω_j	Angular frequency of light

LIST OF ANNEXES

ANNEX A LIST OF SCIENTIFIC CONTRIBUTIONS 133
ANNEX B EXPLICIT COUPLED-MODES EQUATIONS 135

CHAPTER 1 INTRODUCTION

The optical whispering gallery mode (WGM) microcavity has been one of the pillars of the micro and nano photonics research over the past two decades [1–4]. The concept of WGM came long before that and Lord Rayleigh's work on sound waves published in 1910 [5] is believed, among the scientific community, to be the first attempt to describe it. A whispering gallery mode represents the path followed by a wave along a circular boundary. Since then, many publications applied the WGM concept to electromagnetic waves [6–16]. The WGM microcavity owes its popularity to its light confinement capability, and its versatility towards many application domains, from fundamental quantum light-matter experiments to on-field pathogen biodetection. A brief list of references is presented in Table 1.1

Table 1.1 : WGM microcavity applications and their references.

Theoretical analysis	Eigenmodes	[6–8, 10–22]
	Basic properties	[15, 21, 23–27]
	Coupled-mode analysis	[20, 21, 26, 28–37]
	Lasing	[38–40]
	Nonlinear processes	[41–56]
Passive components	Optical filters & delay lines	[57–65]
	Biodetection	[66–75]
	Signal stabilization	[76–78]
Laser sources	Ions doped material	[9, 40, 79–82]
	Doped coating	[83–87]
Nonlinear processes	All-optical signal processing & Switching	[88–93]
	Three-wave & four-wave mixing	[89, 94–108]
	Frequency combs	[109–121]
	Stimulated Raman and Brillouin scattering	[105, 106, 122–127]
	Thermally induced	[1, 128–139]
Review articles		[2–4, 21, 73, 75, 82, 102, 140, 141]

An optical microcavity confines light in a given volume and over a given duration. This is characterized by the cavity's mode Q/V_{mode} value. The optical mode's quality factor Q is linked to the loss processes : material absorption, surface scattering, external coupling, etc. They dictate the photon's lifetime inside the optical mode and consequently the mode resonance bandwidth. The mode volume V_{mode} represents the space occupied by the electromagnetic energy. A smaller volume leads to larger optical intensities. Compared to other optical resonators such as Fabry-Perot, WGM microcavities typically have large Q/V_{mode} values with Q-factors between $10^4 - 10^8$ and mode volumes between $100 - 20000$ μm^3. Furthermore, WGM microcavities are made from many structures and materials, offer compactness and are often integrable on chip using microfabrication and nanofabrication techniques.

Considering these properties, it is not surprising that WGM microcavities are used in this thesis and in many other works as laser media and for nonlinear optical interactions such as stimulated Raman scattering or parametric processes. As threshold values and conversion efficiencies for these interactions follow $V_{mode}/Q^{n>1}$ and $Q^{n>1}/V_{mode}$ respectively, WGM microcavities offer a great advantage in view of nonlinear optical signal processing and generation. As seen in Table 1.1, WGM microcavities are used for parametric four-wave mixing (FWM) processes, especially for engineering optical frequency combs sources. The main challenge for FWM generation in WGM microcavities is to achieve efficient phase-matching and energy conservation conditions. This often limits the frequency region where FWM is possible. Stimulated Raman or Brillouin scattering, on the other hand, is achievable virtually over the whole transparency window of the guiding material. In that sense, the use of stimulated Raman scattering (SRS) in WGM microcavities is an advantageous method to generate new optical frequencies that are not achievable using typical rare-earth doped glasses or semiconductors technologies. Mid-infrared (mid-IR) optical frequencies is a typical example.

Over the past decade, increasing efforts were taken towards the development of new mid-IR sources with wavelengths spanning from 2 μm to 12 μm. These efforts are motivated by many possible utilizations such as military detection, free space communication and Light Detection And Ranging (LIDAR) applications, material processing and analysis, medical interventions and imaging, and molecular sensing.

Many mid-IR sources were reported. The best known are fiber lasers based on Er^{3+}, Tm^{3+} or Ho^{3+} doped glasses [142], semiconductors quantum cascade lasers (QCL) [143] and sources based on nonlinear interactions through parametric gain : fiber-based, free space lasers and microcavities. Each application has its best-fitted source that fulfills its requirements : pumping method, emission wavelength(s), achievable output power, price and compactness.

Mid-IR micron-size sources such as WGM microcavities, with output powers typically < 1 mW,

are well-suited for material analysis and molecular spectroscopy. They generally offer low threshold conditions, good power conversion efficiency, compactness and can possibly be used in portable devices. All these sources rely on materials that are transparent across the mid-IR. Figure 1.1 shows the transparency window of different materials for which WGM microcavities have been reported. For a high purity material, the transparency window is usually limited by the bandgap absorption at larger energies and by the lattice vibrations at longer wavelengths. For example, in silica, the Si-O bond limits the transmission for wavelengths longer than 2 μm. Bonds formed by heavier atoms such as As-S and As-Se tend to vibrate at longer wavelengths. Consequently, As_2Se_3 allows optical transmission further in the IR than As_2S_3.

Figure 1.1 also presents the vibration wavelengths of molecules based on the HITRAN database [1]. Darker areas depict stronger molecule's responses. As it can be seen, many material transparency windows agree with these molecular vibrations, even in the shorter wavelengths range between 2 μm and 5 μm. Few WGM microcavity sources above 2 μm were reported. The frequencies generation are based on parametric conversion in specific wavelength ranges [119, 148, 149] or Er^{3+} ions lasing at a wavelength $\sim$ 2.8 μm [150]. Given the large transparency window of WGM material shown in Fig. 1.1, stimulated Raman scattering could be used on a broader wavelength range where a pump signal is available.

1.1 WGM microcavities as miniature Raman sources

For WGM microcavities, the SRS threshold pump power goes as (Eq. 2.30)

$$P_{th} \propto \frac{n^2 V_m}{\lambda^2 g_R^{(b)} Q^2}$$

where n is the material's refractive index (RI). Q, V_m and λ are the Q-factor, the volume and the wavelength of the optical mode and $g_R^{(b)}$ is the material's bulk Raman gain. The upper part of Table 1.2 presents the estimated SRS threshold pump power for different WGM microcavity materials from Fig. 1.1. The Q-factor Q_p and the mode volume V_m are retrieved from WGM microcavities reported before the present work at a wavelength of 1550 nm. The resulting threshold powers far below the milliwatt express the suitability of WGM microcavities for SRS generation for applications where compactness and low pump powers are needed such as portable gas sensing devices.

Typical SiO_2 microcavities already achieve threshold powers of few microwatts despite their

1. `https://www.cfa.harvard.edu/hitran/`

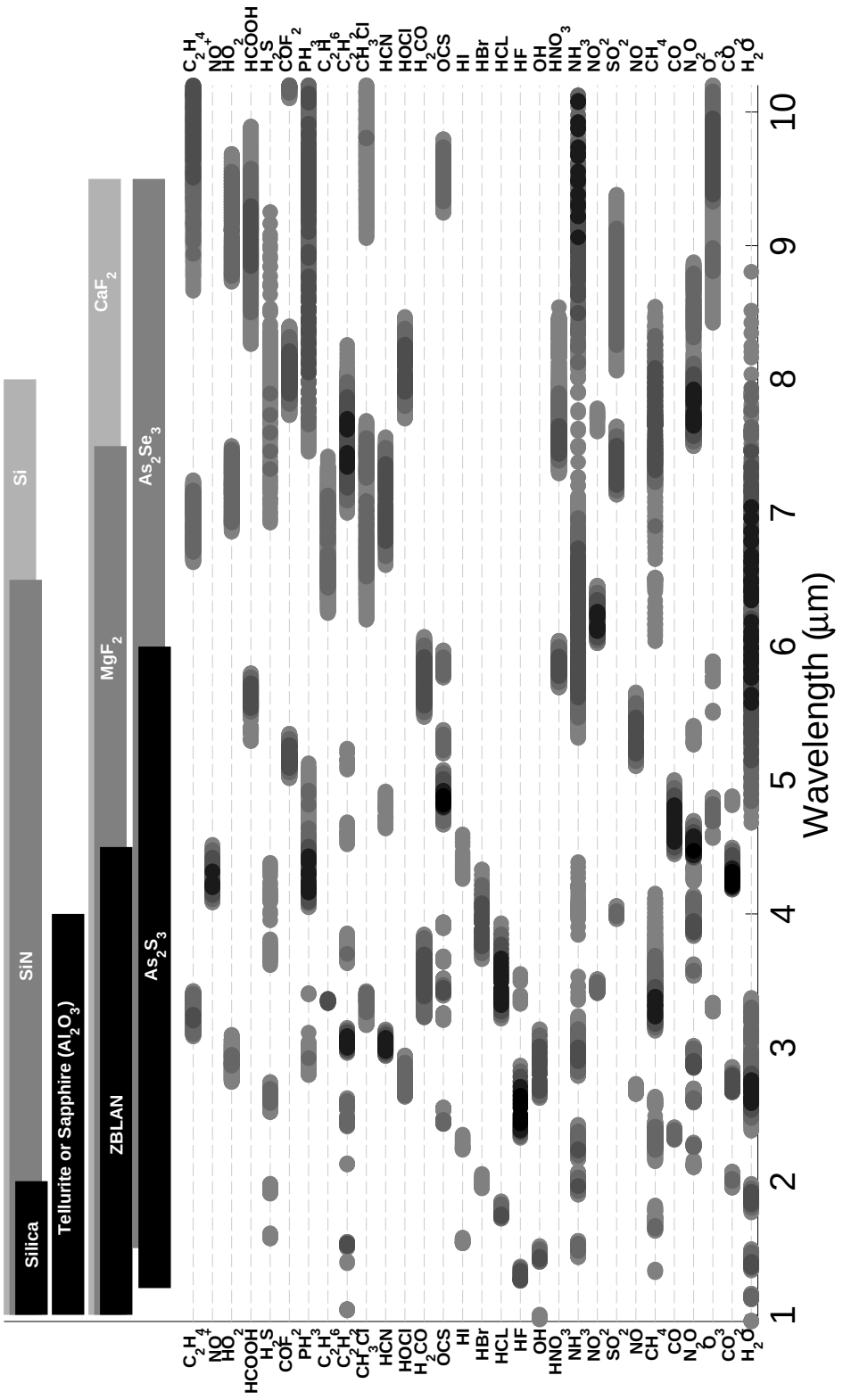

Figure 1.1 : Upper part : material transparency window of demonstrated WGM microcavities [144–147]. Band colors are used to clearly separate the material windows. Lower part : molecular vibrations from HITRAN database. Darker areas represent stronger molecule's responses.

small Raman gain, thanks to their large Q-factor. Most surprisingly, silicon do not perform well considering its Raman gain a 1000 times larger than silica. Silicon is mainly used as integrated ring cavities and suffers inherent surface scattering losses. Q-factors of $\sim 10^6$ in silicon are achieved in waveguides embedded in silica and combined with a small cavity radius, leading to small mode volume. Crystalline CaF_2 cavities reach the lowest estimated threshold power, mainly due to their very large Q. Those WGM microcavities are made using polishing techniques and the best performances are limited to millimeter-size cavities. Similar Q-factors were not achieved by micron-size CaF_2 cavities. Finally, As_2Se_3 chalcogenide glass can also achieve threshold powers of few microwatts. Worst performances are obtained with tellurite glass and As_2S_3 because of a lower demonstrated Q-factor. However, Q-factors of 1×10^5 for these glasses are misleading, as the attenuation of < 0.5 dB/m of a high purity optical fiber indicates an upper limit $> 5 \times 10^7$. For As_2S_3, this leads to a threshold power below the microwatt, as shown in the lower part of Table 1.2. Similar improvement is expected from As_2Se_3 optical fiber since it has the same attenuation, but thermal instabilities and degradation are anticipated for input powers of ~ 50 μW for Q-factors $\sim 5 \times 10^7$ [154].

The major challenge in achieving low threshold power SRS emission in As_2S_3 WGM microcavities – or any chalcogenide WGM microcavities for that matter – is first to fabricate resonators with large Q-factors. Fabricating As_2S_3 WGM microcavities with Q-factors above 10^7 would be significant. Compared to CaF_2 resonators, SRS performances in As_2S_3 would benefit from a larger Raman gain and a smaller cavity size, hence a smaller mode volume.

Table 1.2 : Estimated SRS threshold pump powers at 1550 nm based on WGM microcavity characteristics observed before this thesis work along their measured Q-factors (upper part) and their potential Q-factors (lower part).

Material	**Raman shift** $\Omega_v/2\pi$ **(THz)**	**Raman gain** $g_R^{(b)}$ **(m/W)**	Q **[Reference]**	**Mode volume** V_m **(μm^3)**	**Threshold power(μW)**
SiO_2	12.5	9.3×10^{-14}	1×10^8 [122]	480†	4.1
Si	15.6	2×10^{-10}	7.6×10^5 [151]	~ 25 [(e)]	10
CaF_2	9.65	2.4×10^{-13}	2.6×10^{10} [126]	2.7×10^6 [(e)]	0.13
Tellurite	19.9	1.8×10^{-12}	$< 1 \times 10^5$ [152]	320†	> 270000
As_2S_3	10.34	4.4×10^{-12}	1.8×10^5 [153]	260†	42 000
As_2Se_3	6.9	5.1×10^{-11}	2.3×10^6 [154]	220†	24
Tellurite	19.9	1.8×10^{-12}	$5 \times 10^{7\ddagger}$	320†	1.1
As_2S_3	10.34	4.4×10^{-12}	$1 \times 10^{8\ddagger}$	260†	0.14
As_2Se_3	6.9	5.1×10^{-11}	$5 \times 10^{7\ddagger}$	220†	0.05

† Calculated for a microsphere with a typical radius of 20 μm (Eq. B.28).
‡ Based on the attenuation of latest commercial tellurite, As_2S_3 and As_2Se_3 optical fibers.
[(e)] Estimated from the microcavity dimensions of the given reference.

1.2 Chalcogenide WGM microcavities

Chalcogenide glasses were first developed in the 50's for their transparency in the mid-IR, beyond the 5 μm oxides' limit [155] [2]. As its name indicates, a chalcogenide glass contains chalcogen atoms such as sulfur (S), selenium (Se) or tellurium (Te). Among the multiple glass compositions, As_2S_3 and As_2Se_3 were mostly used in photonics for their interesting optical properties, some of which are shown in Table 1.3. Many literature reviews, books and thesis on chalcogenide glasses are available [156–161].

Chalcogenide photonics first started with optical fibers [192, 193] that were later used to produce tapered fibers [194–198] and Bragg gratings [199]. First optical fibers were fabricated in the 60's but suffered of major losses [200]. In the 80's, multimode fibers with attenuation $\sim$ 100 dB/km at a wavelength of 1.5 μm and $<$ 100 dB/km at 2.4 μm were obtained [200]. With modern purification techniques, laboratories pushed the glass attenuation to $\sim$ 30 dB/km at 1.5 μm and $\sim$ 12 dB/km at 3 μm [174, 193]. Companies such as CorActive High-Tech sell As_2S_3 (As_2Se_3) multimode and single mode optical fibers with attenuation below 200 (500) dB/km over the wavelength range of $2-5$ μm ($1.5-8.5$ μm) [3].

In addition to their mid-IR transparency, chalcogenide glasses possess a large refractive index, useful for optical confinement or on-chip waveguide integration. Microfabrication steps are CMOS-compatible. Deposition can be done using evaporation techniques [201], spin-coating [202], laser deposition [172, 173] or sputtering. Etching is done using typical gas such as CF_4 [201, 202] or in solution (wet-etching) [203]. Lift-off and molding techniques are also used [204–206]. This lead to the fabrication of WGM microcavities with respectable Q-factors [207–211]. However, integrated designs are usually used for nonlinear optics purposes

2. This reference mentions a publication from C. Schultz-Sellack (1870) showing the good IR transmission of As_2S_3.

3. http ://coractive.com/products/mid-ir-fibers-lasers/ir-fibers/index.html

Table 1.3 : Optical properties of As_2S_3 and As_2Se_3 glasses.

Optical properties	**References**
Large refractive index $n \sim 2.43$ and 2.75	[162–167]
Transparency from 1.3 μm to $6-10$ μm	[155, 163–165, 168–174]
Large nonlinear RI $n_2^{\text{Chalco}} \sim 500\ n_2^{\text{Si0}_2}$	[173, 175–183]
NL figure of merit† $F = n_2/\lambda\beta_{\text{TPA}} > 1$	[177–181, 183]
Large Raman gain $g_R^{\text{Chalco}} \sim 50-500\ g_R^{\text{Si0}_2}$	[156, 184–187]
Photosensitivity	[160, 167, 182, 188–190]
Glass transition temperature $T_g \sim 180-215°\text{C}$	[147, 178, 191]

†β_{TPA} : Two-photon nonlinear absorption coefficient

based on high power pulsed pump signals [157, 212–215]. As seen in Table 1.3, chalcogenide glasses benefit from a large nonlinear refractive index at least two orders of magnitude larger than silica's nonlinear index. At telecommunication wavelengths, integrated chalcogenide glasses have a competitive advantage compared to silicon, their two-photon nonlinear absorption coefficients β_{TPA} being much lower. This means nonlinear phase changes saturate at much larger pump power.

Chalcogenide glasses WGM microcavities were reported over a limited extent. Table 1.4 provides an updated publication list of WGM microcavities made out of chalcogenide glass. The first reported cavities were microspheres made of Ga_2S_3-La_2S_3-La_2O_3 (Ga :La :S) by letting crushed glass pieces drop into a furnace. A large range of diameters from 1 μm to 450 μm and Q-factors up to 8×10^4 were obtained. Since then, other fabrication techniques were used. Microspheres are usually fabricated by first pulling and tapering an optical fiber using a heat source. The spheres themselves are also fabricated through a direct heating process [154, 220] or through light absorption [217]. By heating the fine tip of a broken tapered optical fiber, the melted glass naturally forms a sphere through surface tension. This results in a smooth surface with relatively low scattering losses and a relatively large Q-factor. Integrated resonators such as disks, racetracks or rings were also fabricated using standard microfabrication methods.

None of the published work before this thesis demonstrated nonlinear effects in chalcogenide WGM microcavities, which is due to the relatively low Q-factors reported in previous works.

Table 1.4 : Chalcogenide WGM microcavities.

Year	**Type**	**Material**	**Diameter (μm)**	***Q***	**References**
2007	Microsphere	Ga :La :S	1-450	8×10^4	[216]
2008	Microsphere	As_2Se_3	3-15	2×10^4	[217]
2008	Disk	As_2S_3 on SiO_2	40	2.1×10^5	[207]
2008	Disk	$Ge_{17}Sb_{12}S_{71}$ on SiO_2	40	1.1×10^5	[207]
2008	Racetrack	As_2S_3 on SiO_2	L $\sim$ 409	1×10^4	[208]
2009	Racetrack	As_2S_3 on Ti :$LiNbO_3$	L $\sim$ 4827	1×10^5	[209]
2009	Microsphere	As_2Se_3	55-400	2.3×10^6	[154]
2010	Microsphere	Nd^{3+} doped Ga :La :S	1-300	1×10^4	[218]
2011	Transverse fiber	As_2S_3	15.5	2.34×10^5	[219]
2012-13	Microsphere	As_2S_3	74-110	1.1×10^5	[153, 220]
2013-14	Microsphere	As_2S_3	40-350	7×10^7	This work
2014	Ring	$Ge_{23}Sb_7S_{70}$	60	4.6×10^5	[210]
2015	Microsphere	75GeS_2-15Ga_2S_3-10CsI	75	6×10^4	[221]
2015	Racetrack	$Ge_{11.5}As_{24}S_{64.5}$	L $\sim$ 13000	6×10^4	[211]

L : Cavity length

Chalcogenide microspheres possess Q-factors three orders of magnitude smaller than silica microspheres even if high purity chalcogenide optical fibers are available. The integrated resonator Q-factors are similar to what has been reported in silicon rings and racetracks. They suffer from the same attenuation processes, especially surface scattering. Better results are obtained when the cavity is embedded in a lower index material.

1.3 Extended emission in WGM microcavities

Cascaded Raman emission

The SRS emission has two main advantages : it allows wavelength generation that is not accessible with semiconductor or ions doped lasers and it can be generated as long as the material's transparency allows it. However, the generated frequency is shifted from the pump frequency by a fixed amount, the Raman shift frequency. The Raman gain bandwidth can be relatively large for glasses. For example, As_2S_3 glass has a Raman shift centered at 10.34 THz with a bandwidth of > 3 THz. For a pump wavelength of 1550 nm, the Raman emission wavelength will be located between 1625 nm and 1650 nm. With their axial symmetry, WGM microcavities are inherently suitable for exciting multiple Raman orders. The frequency diagram of Fig. 1.2 shows the cascading Raman generation. An incoming photon with an energy $\hbar\omega_p$ interacts with a phonon, loses an energy $\hbar\Omega_v$ and comes out with an energy $\hbar\omega_{R1}$. If the resulting photon stays in the material long enough to interact with another phonon, the process can repeat itself and possibly leads to a cascading Raman generation : $\hbar\omega_{R2}$, $\hbar\omega_{R3}$, etc.

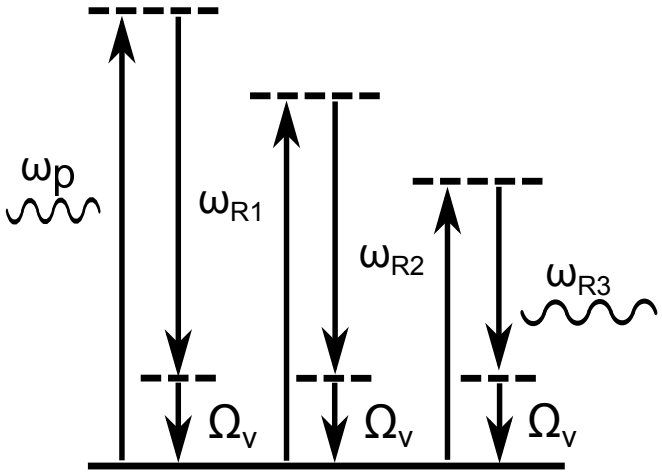

Figure 1.2 : Frequency diagram of the cascaded Raman process.

WGM microcavities have successive mode resonances that usually reach large Q-factors across the whole transparency window of its constituent material. Due to good field overlap, a pump mode can easily excite a first Raman emission. If the threshold power is of few microwatts, the generation of 2nd Raman order emission is usually obtained with few tens of microwatts only.

The successive generation of Raman order can push the emission further in the infrared. Figure 1.3 presents the Raman emission region in As_2S_3, up to the 4th order for a given pump wavelength, along with the Raman gain bandwidth for each order. The Raman emission wavelengths are increasing nonlinearly with the pump wavelength meaning that a pump wavelength located further in the IR can generate Raman lines with even larger wavelengths. For example, pump wavelengths of 1550 nm and 1850 nm can generate 3rd Raman order emissions 295 nm and 435 nm away at 1845 nm and 2285 nm respectively. To reach wavelengths longer than 2 μm using As_2S_3 cavities, pump wavelengths need to be $>$ 1870 nm and $>$ 1570 nm based on the 1st and 4th Raman order. This means that relatively cheap semiconductor diodes emitting telecommunication wavelengths could pump cascading Raman

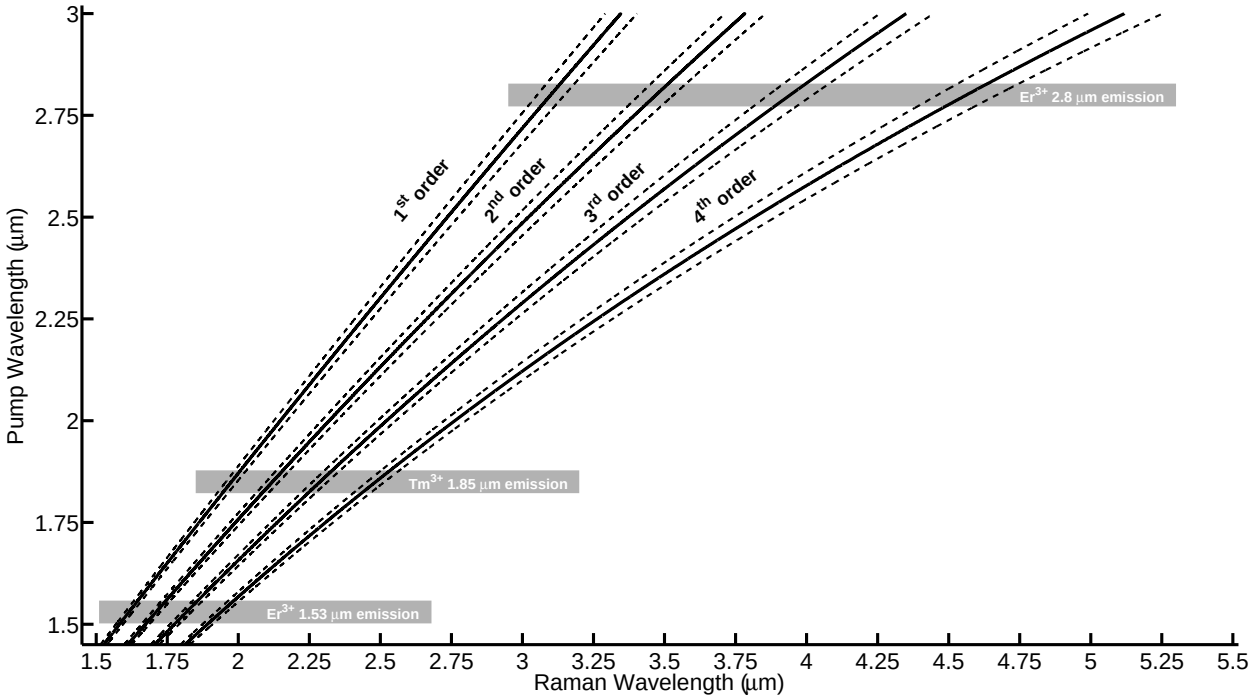

Figure 1.3 : Guide to high-order Raman emission for As_2S_3 glass. For a given pump wavelength, Raman emission region are shown up to 4th order. Dotted lines denote the Raman gain bandwidth. Accessible Raman region are displayed in the cases where the pump signals are the emission bands from Er^{3+} and Tm^{3+}.

emissions at wavelengths larger than 2 μm.

Observing Raman and cascaded lasing in As_2S_3 resonators, even at telecommunication wavelengths, would show that they are suitable for cascading Raman lasing at larger pump wavelengths. As they would need sub-mW of input pump power, those resonators could extend the emission of mid-IR compact sources such as cheaper low power QCL.

Raman lasing in ions doped glasses

As shown in Table 1.1, WGM microcavities are also used as laser media when they are doped with rare-earth atoms such as erbium, ytterbium or thulium. These atoms often have emission bands not only at telecommunication wavelengths, but also near 2 μm and further in the mid-IR. For example, thulium and erbium have emission bands near 1.85 μm and 2.8 μm and are regularly used in fiber lasers [142, 222–225]. Doped WGM microcavities are usually made of silica doped with erbium or ytterbium for emission in the C-band [40, 79, 81, 82]. Tm-doped silica and tellurite glass microspheres emitting near wavelengths of $1.9 - 2$ μm were also reported [226–229]. Finally, Er-doped ZBLAN microspheres emitting at 2720 nm were recently demonstrated [150]. Other works are limited to theoretical models [230–232].

The 1.85 μm and 2.8 μm emission bands of thulium and erbium can advantageously be pumped with accessible 980 nm or 1550 nm diodes. The use of ions emission band as a pump source for cascaded Raman emission could generate wavelengths above 3 μm using only tens of microwatts of pump power. Figure 1.3 displays the pump wavelength of the 1.53 μm and 2.8 μm emission band of erbium along with the 1.85 μm emission band of thulium. Tm-doped and Er-doped As_2S_3 could generate wavelengths up to 2.5 μm and 4.56 μm respectively if a 4th Raman order is obtained.

Nevertheless, doping of chalcogenide glasses remains a challenge as dopant induced crystallization during optical fibers fabrication [233, 234]. This issue needs to be solved to obtain high purity optical fibers and high Q-factors WGM microcavities. On the other hand, tellurite glasses offers a good alternative. As seen in Fig. 1.1, it provides transparency up to a wavelength of 4 μm and rare-earth ions doping is easier. Furthermore, it possesses relatively good Raman gain and WGM microcavities could achieve high Q-factor. Comparison in Table 1.2 shows that SRS threshold power could be in the μW range. However, similarly to As_2S_3, reported Q-factors of tellurite glass WGM microcavities are not large enough. This could explain the large lasing threshold power of few milliwatts in Tm-doped tellurite microspheres [227–229], far from the microwatts threshold found in Er-doped or Tm-doped silica WGM microcavities [40, 79, 226].

1.4 Achieved objectives & original contributions

Based on the exposed issues, this thesis objectives are threefold.

1. **Fabrication of high Q-factors WGM microcavities made of As_2S_3.**
   As_2S_3 microspheres are fabricated from high purity optical fiber using a laser reflow technique. The measured Q-factors $> 5 \times 10^7$ of these spheres are at least two order of magnitude larger than previously reported. To this day, these As_2S_3 microspheres achieve the highest Q-factors of all chalcogenide microcavities.
2. **Generating stimulated Raman scattering and cascaded Raman emission in As_2S_3 WGM microcavities.**
   High Q-factors As_2S_3 are ideal candidates for micron-size Raman sources. First order Raman emission lines were measured with a threshold power of 35 μW at a pump wavelength of 1550 nm. This is the first demonstration of nonlinear generation in chalcogenide WGM microcavities.
   Cascaded Raman emissions further in the IR were also obtained. Raman emission lines up the fifth order at 2140 nm and third order at 2350 nm were measured with pump wavelengths of 1550 nm and 1880 nm respectively.
3. **Generating low threshold power laser emission in Tm-doped tellurite WGM microcavities for SRS emission.**
   High Q-factors microspheres are made from Tm-doped tellurite optical fiber. Lasing lines near 1975 nm were measured with threshold powers of 30 μW, the lowest for a Tm-doped microcavity and a tenfold improvement over previously published tellurite cavities. These results pave the way for ions doped/Raman hybrid microsources.

1.5 Thesis structure

Chapter 2 presents the basic concepts to understand the WGM microcavities, from their coupled-modes equations to nonlinear interactions. To lighten the chapter reading, only the main relations are described. An explicit derivation of the coupled-modes equations, starting from Maxwell's equations, is presented in the appendix B. Relations such as Raman threshold power will be used in later chapters to support experimental results and to provide new insights for future improvements

Chapter 3 exposes the experimental techniques and setups used during this thesis. The microspheres fabrication steps using a high power CO_2 laser are reviewed. An encapsulation method for a microsphere and a coupled tapered optical fiber is also described. Finally, Q-factors measurements and Raman generation setups are detailed.

Chapter 4 fulfills the first thesis objective and part of the second one. It exposes the measurement of high Q-factors As_2S_3 microspheres followed by stimulated Raman scattering measurements. Chapter 5 addresses the last part of the second objective by describing and characterizing the cascaded Raman emission results. Chapter 6 achieves the last thesis objective. It describes the Tm-doped monoindex fiber fabrication and the Q-factors measurements of Tm-doped tellurite microspheres. Laser emission near a wavelength of 1975 nm is studied for different pump wavelengths, hence for different Tm ions absorption cross sections. Chapters 4 to 6 were published in peer-reviewed journals. Chapters 4 and 5 also contain complementary results that were not included in the articles.

Chapter 7 presents a general discussion and puts back this thesis results in context. Limitations and improvements are proposed. Finally, Chapter 8 concludes this thesis and expresses recommendations toward future work directions.

CHAPTER 2 BASIC CONCEPTS

Whispering gallery modes (WGM) are bound modes that propagate near the circumference of a circular cavity, usually with dimensions in the micron range. They are found in many geometries such as spheres, disks, toroids, oblate spheroids, integrated rings and racetracks. Each geometry has its unique optical mode characteristics. Among them, the most important attributes are the number of modes, the photon lifetime and the mode volume. The cavity material has to be chosen carefully as it dictates the wavelength transparency range, the light confinement, the material dispersion, the thermal properties and the nonlinear responses such as Kerr effect and Raman scattering. Furthermore, each cavity geometry can be coupled to an external structure to bring the light signal in and out. Integrated waveguides are the most popular structures to couple light in and out of rings and racetracks. Tapered optical fibers and prisms are preferred in combination with spheroids, disks and toroids. Figure 2.1 shows typical coupler-cavity configurations. In Figure. 2.1(a), an integrated disk is coupled to a waveguide and sits on a substrate with a lower refractive index. Figure 2.1(b) represents a tapered optical fiber coupled to a circular cavity. Finally, light can be coupled to a cavity using the evanescent wave of the internal reflection in a prism as seen in Figure 2.1(c).

To correctly describe the cavity's response, the theoretical framework must be able to include the cavity and waveguide optical modes. It needs also to describe all the possible linear and nonlinear coupling processes between these optical modes. The coupled-modes (CM) theory based on the eigenmodes expansion is ideal as the fast temporal components and the normalized spatial components of the fields are grouped in propagation constants. Intracavity, external and nonlinear coupling processes are added as perturbations. Additionally, knowing the exact distribution of the mode fields is often not mandatory to study the modes evolution in time. Application of the coupled-modes theory to WGM microcavities can be found in the

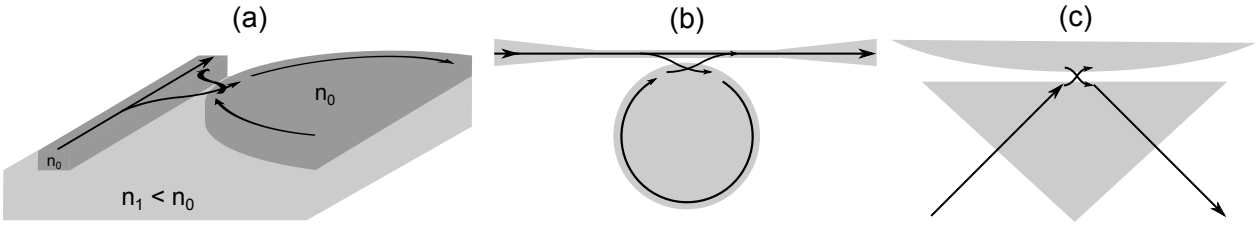

Figure 2.1 : Different coupling configurations - **(a)** Integrated waveguide and disk **(b)** Tapered optical fiber **(c)** Total internal reflection in a prism.

literature [20,30,32,34,36,49] among others. Notions on nonlinear CM theory in microcavities can be found in [49, 53, 235, 236]. Each work has its own notation and its own analysis for different kinds of cavities.

The following sections describe the important coupled-modes equations and cavity's characteristics for both linear and nonlinear responses. A step-by-step description of the theoretical background, starting from the Maxwell equations to the explicit definitions of Q-factors, is presented in the appendix Sections B.1 and B.2.

2.1 The waveguide-cavity system

Following Sections B.1.1 and B.1.2

Most of the literature works on WGM microcavities can be described by the waveguide-cavity system shown in Fig. 2.2. An incoming light wave $s_L(z_0)$ is guided through a waveguide. As it travels by the cavity, part of its power is transfered to a cavity mode wave a_j via evanescent coupling. During its propagation in the cavity, the wave energy can be coupled to other cavity modes such as a counterclockwise mode a_{-j} or radiative modes for example via surface scattering, or it can be attenuated by the material itself. It can also be coupled back into the waveguide. The outgoing light wave $s_L(z_1)$ is the resulting combination of the incoming waveguide wave and the cavity-coupled wave. All the coupling processes are characterized by coupling constants such as κ_{jL}. These constants depend on the spatial overlap of the optical modes and their optical frequencies.

To describe the waveguide-cavity system, we express the cavity and waveguide electric fields

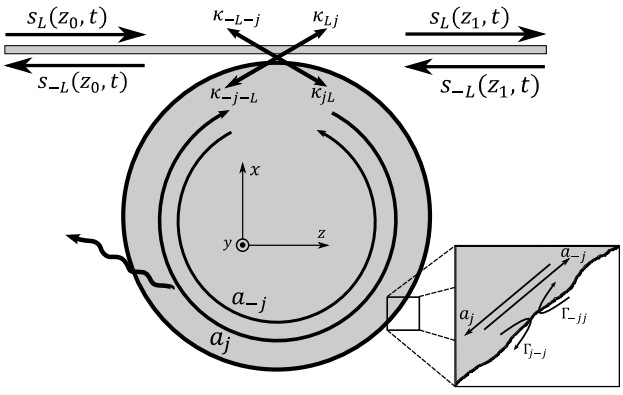

Figure 2.2 : Schematic of the linear coupling processes between a waveguide and a WGM microcavity.

as eigenmodes $\mathbf{e}_j(\mathbf{r})$ and $\mathbf{e}_L(\mathbf{r})$

$$\mathbf{E}_{\text{cavity}}(\mathbf{r},t) = \sum_j \mathbf{E}_j(\mathbf{r},t) = \sum_j \frac{a_j(t)e^{-i\omega_j t}\mathbf{e}_j(\mathbf{r})}{2\sqrt{N_j}} + \text{c.c.} \tag{2.1}$$

$$\mathbf{E}_{\text{guide}}(\mathbf{r},t) = \sum_L \mathbf{E}_L(\mathbf{r},t) = \sum_L \frac{s_L(z,t)e^{-i\omega_L t}\mathbf{e}_L(\mathbf{r})}{2\sqrt{M_L}} + \text{c.c.} \tag{2.2}$$

where vectors are written in bold. The cavity mode and waveguide mode frequencies are ω_j and ω_L respectively. $a_j(t)$ and $s_L(z,t)$ are the slowly varying amplitude of the cavity and waveguide modes respectively. The normalization factors N_j and M_L are written as

$$N_j = \frac{1}{2}\int_V \epsilon_0(n_0^2|_c)|\mathbf{e}_j(\mathbf{r})|^2 dV \tag{2.3}$$

$$M_L = \frac{1}{4}\oint_A (\mathbf{e}_L(\mathbf{r}) \wedge \mathbf{h}_L^*(\mathbf{r}) + \mathbf{e}_L^*(\mathbf{r}) \wedge \mathbf{h}_L(\mathbf{r})) \cdot \hat{\mathbf{z}} dA \tag{2.4}$$

where $n_0|_c$ is the refractive index (RI) profile of the cavity alone in the surrounding medium : the cavity RI, n_c, inside and the surrounding medium RI, n_a, outside the cavity. The cavity mode amplitudes are normalized in respect to their electromagnetic (EM) energy : $|a_j(t)|^2$ is the total EM energy stored in the j mode at given time t. Similarly, the waveguide mode amplitudes are normalized in respect to their propagating power : $|s_L(z,t)|^2$ is the total power circulating through the $x-y$ plane at a given time t. This normalization allows a direct association between the theoretical framework and the experimental power measurements.

2.2 Linear coupled-modes equations

Following Sections B.1.3 through B.2.1

The coupled-modes equations of the waveguide-cavity system are generally deduced from Maxwell's equations, as shown in Sections B.1.3 and B.1.4. The eigenmode equations naturally come out of the perturbative approach as

$$\boldsymbol{\nabla}^2\mathbf{e}_j(\mathbf{r}) + \frac{n_0^2(\mathbf{r})|_c}{c^2}\omega_j^2\mathbf{e}_j(\mathbf{r}) = 0 \tag{2.5}$$

$$\boldsymbol{\nabla}^2\mathbf{e}_L(\mathbf{r}) + \frac{n_0^2(\mathbf{r})|_g}{c^2}\omega_L^2\mathbf{e}_L(\mathbf{r}) = 0 \tag{2.6}$$

where $n_0(\mathbf{r})|_c$ and $n_0(\mathbf{r})|_g$ are the refractive index profile of the cavity and waveguide alone respectively. In this thesis, results were obtained using adiabatic tapered optical fibers and microsphere cavities. Fortunately, solutions can be found analytically [7, 21, 237, 238]. The microsphere solutions $\mathbf{e}_j(\mathbf{r})$ and their resonance frequency ω_j are detailed in Sections 2.4 and

B.3. They are used in the next sections to support the experimental results.

Section B.1.5 presents the final form of the linear coupled-modes equations. For modes propagating in clockwise direction, $a_j(t)$ and $s_L(z_1,t)$, CM equations are written as

$$\frac{\partial a_j(t)}{\partial t} = \left(i[\omega_L - (\omega_j - \Gamma_{jj})] - \Gamma'_{jj} - \frac{1}{2\tau_j}\right) a_j(t) + (i\Gamma_{j-j} - \Gamma'_{j-j})a_{-j}(t) + \sum_L i\kappa_{jL}s_L(z_0,t) \tag{2.7}$$

$$s_L(z_1,t) = s_L(z_0,t) + i\kappa_{Lj}(z_1)a_j(t) \tag{2.8}$$

For counterclockwise modes, $a_{-j}(t)$ and $s_{-L}(z_1,t)$, we have

$$\frac{\partial a_{-j}(t)}{\partial t} = \left(i[\omega_L - (\omega_j - \Gamma_{-j-j})] - \Gamma'_{-j-j} - \frac{1}{2\tau_{-j}}\right) a_{-j}(t) + (i\Gamma_{-jj} - \Gamma'_{-jj})a_j(t) + \sum_L i\kappa_{-j-L}s_{-L}(z_1,t) \tag{2.9}$$

$$s_{-L}(z_0,t) = s_{-L}(z_1,t) + i\kappa_{-L-j}(z_0)a_{-j}(t) \tag{2.10}$$

where

$$\frac{1}{2\tau_j} = \frac{1}{2\tau_{j,0}} + \frac{1}{2\tau_{j,c}} \quad \text{and} \quad \frac{1}{2\tau_{-j}} = \frac{1}{2\tau_{-j,0}} + \frac{1}{2\tau_{-j,c}}. \tag{2.11}$$

Each coupling constant are listed in Table 2.1 along with their roles and the explicit equation reference. All the Γ constants are rates expressed in s^{-1}, the κ constants are expressed in $s^{-1/2}$ and the lifetimes are expressed in seconds. Typical WGM microcavity photons lifetimes $\sim 0.1 - 10$ ns.

Table 2.1 : Linear rates, coupling constants, and lifetimes.

Description	**Symbols**	**Definitions**
Cavity phase shift due to the waveguide and a perturbation	Γ_{jj} and Γ_{-j-j}	B.43
Cavity losses due to a perturbation	Γ'_{jj} and Γ'_{-j-j}	B.47
Coupling between modes j and $-j$	Γ_{j-j} and Γ_{-jj}	B.44
Losses during modes j and $-j$ coupling	Γ'_{j-j} and Γ'_{-jj}	B.48
Cavity mode to waveguide mode	κ_{jL} and κ_{-j-L}	B.49 and B.54
Waveguide mode to cavity mode	$\kappa_{Lj}(z)$ and $\kappa_{-L-j}(z)$	B.50 and B.54
Intrinsic photon's lifetime	$\tau_{j,0}$	B.45
Extrinsic photon's lifetime	$\tau_{j,c}$	B.51 and B.54
Total photon's lifetime	τ_j	B.63

The advantage of this approach resides in its simplicity : the coupling constants can often be measured or deduced from measurements even if their explicit formulations are not known. For example, for sensing applications, when the refractive index changes locally in the surrounding medium or due to a particle, the values of Γ_{jj}, Γ'_{jj}, Γ_{j-j} and Γ'_{j-j} can change.

To understand how these constants modify the cavity's spectral response, we need to solve equations 2.7-2.10 for typical measurement conditions. Transmission spectrum measurements are usually done using a monochromatic input signal with a power $s_L(z_0, t) \neq 0$ and a frequency ω_L. While the input signal frequency is tuned across the resonance, the output signal $s_L(z_1, t)$ is monitored. To measure the reflection spectrum, $s_{-L}(z_0, t)$ is monitored while $s_{-L}(z_1, t)$ is set to zero. The equations can be solved for steady-state conditions for a slowly varying input power because the cavity response is in the nanosecond range.

The steady-state or continuous-wave (CW) solutions are described in Section B.2.1. To lighten the discussion, only the graphical results are shown here for three different cases. The transmission spectrum $T_j = |s_L(z_1, t)|^2/|s_L(z_0, t)|^2$ is depicted in black and the reflection spectrum $R_j = |s_{-L}(z_1, t)|^2/|s_L(z_0, t)|^2$ in red.

Unidirectional source, single mode waveguide and no modal coupling

The simplest case is obtained when there is no perturbation with $\Gamma_{jj} = 0$, $\Gamma_{j-j} = 0$ and $\Gamma'_{jj} = \Gamma'_{j-j} = 0$. It is represented in Fig. 2.3 for three $(\tau_{j,c}, \tau_{j,0})$ combinations : $\tau_{j,c} = 5\tau_{j,0}$, $\tau_{j,c} = \tau_{j,0}$ and $\tau_{j,c} = \frac{1}{3}\tau_{j,0}$. The resonance's shape is a simple Lorentzian centered at $\omega_L = \omega_j$. Its width and its depth depend on the values and ratio of $\tau_{j,c}$ and $\tau_{j,0}$, as we shall see in Section 2.3. There is complete extinction for $\tau_{j,c} = \tau_{j,0}$ or in *critical coupling* regime. *Undercoupling* and *overcoupling* regime happen when $\tau_{j,c} > \tau_{j,0}$ and $\tau_{j,c} < \tau_{j,0}$ respectively. As there is no perturbation, no signal is scattered in the counterclockwise mode a_{-j} and thus no signal is reflected back in the waveguide input.

Experimentally, there is always a perturbation such as dust particles, changing surrounding medium or temperature changes. Any perturbation will cause Γ_{jj} to change at least. This effect is shown in Fig. 2.4 for $\Gamma_{jj} = \frac{2}{\tau_j}$ representing a refractive index increase. The x-axis is now normalized to $1/\tau_j$ and $\tau_{j,c} = 2\tau_{j,0}$. The cavity resonance is red-shifted by a frequency $\Delta\omega = \Gamma_{jj}$ but its shape is untouched. As the resonance width of WGM microcavities are typically < 10 pm at a wavelength of 1550 nm, any dust particle attachment or comparable perturbations will result in a detectable frequency shift.

If the cavity is enclosed in a clean and stable environment, Γ_{jj} is relatively constant over time. For this reason, the measured resonance frequency is usually the combination of ω_j and

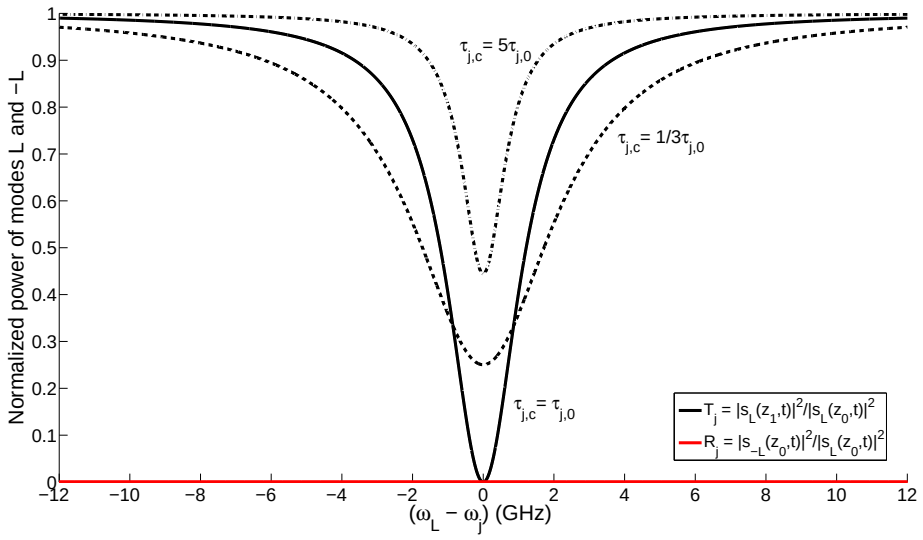

Figure 2.3 : T_j and R_j for $\Gamma_{jj} = 0$, $\Gamma_{j-j} = 0$, $\Gamma'_{jj} = \Gamma'_{j-j} = 0$ using Eq. B.77. Different coupling regimes are shown : critical (line), overcoupling (dashed line) and undercoupling (dash-dot line).

Γ_{jj}, so that we can replace $(\omega_j - \Gamma_{jj}) \to \omega_j$ or use $\Gamma_{jj} \to 0$ in the coupled-modes equations.

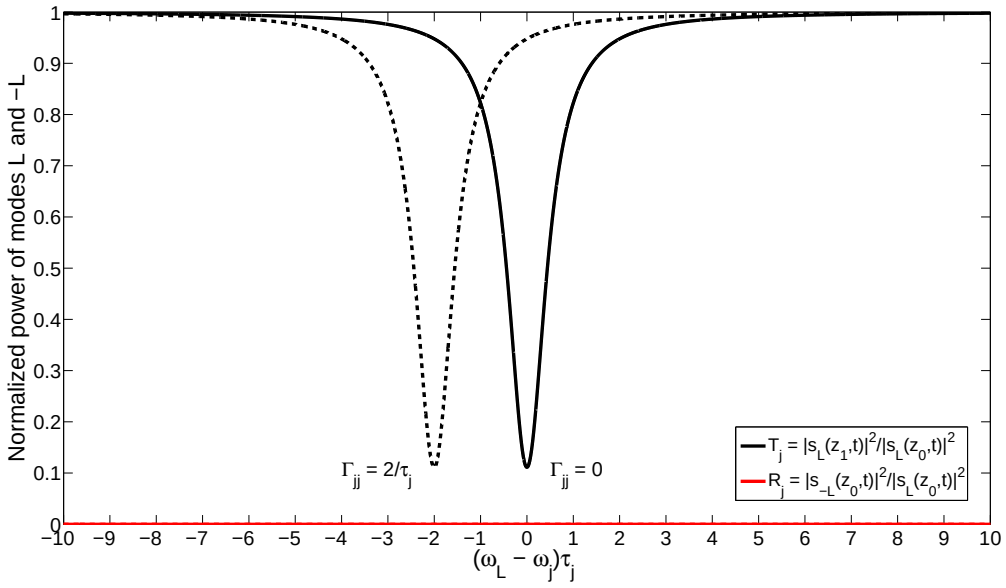

Figure 2.4 : T_j and R_j for $\Gamma_{jj} = 0$ and $\Gamma_{jj} = \frac{2}{\tau_j}$, $\Gamma_{j-j} = 0$, $\Gamma'_{jj} = \Gamma'_{j-j} = 0$ using Eq. B.77.

Unidirectional source, single mode waveguide, modal coupling and $\delta\epsilon'(\mathbf{r}) = 0$

When the perturbation is strong enough to cause a notable change to Γ_{j-j}, modal coupling is observable spectrally. Figure 2.5 shows its effect for $\Gamma_{j-j} = \frac{1}{\tau_j}$ and fixing $\Gamma_{jj} = 0$. Two things happen. Firstly, the resonance is split in two identical peaks. Based on Eq. B.90, the separation distance of the transmission peaks is

$$\delta\omega_j(T_j) = 2\left(\Gamma_{j-j}\sqrt{\frac{1}{\tau_j^2} + \Gamma_{j-j}^2\left(2 + \frac{\tau_{j,0}}{\tau_{j,c}}\right)^2} - \frac{1}{4\tau_j^2} - \Gamma_{j-j}^2\left(1 + \frac{\tau_{j,0}}{\tau_{j,c}}\right)\right)^{1/2} \quad \rightarrow \quad \delta\omega_j(T_j) \sim 2\Gamma_{j-j}$$

for $\Gamma_{j-j} > 1/\tau_j$. By sending part of the clockwise mode into the counterclockwise mode and vice versa, a perturbation causes both modes to interfere. This leads to symmetric and antisymmetric standing wave superpositions often denoted $a_+(t)$ and $a_-(t)$ [71, 239, 240] compared to the perturbation position. Secondly, the depth also changes because the modal coupling adds up to other loss terms $\tau_{j,c}$ and $\tau_{j,0}$, thus changing their ratio. Modal coupling also implies signal reflection and its spectrum also has two identical peaks.

The resonance splitting is observable when the energy transfer rate Γ_{j-j} between the clockwise and counterclockwise modes is larger than the modes loss rates $\frac{1}{\tau_j}$. In other words, two peaks are resolvable when they are narrow enough.

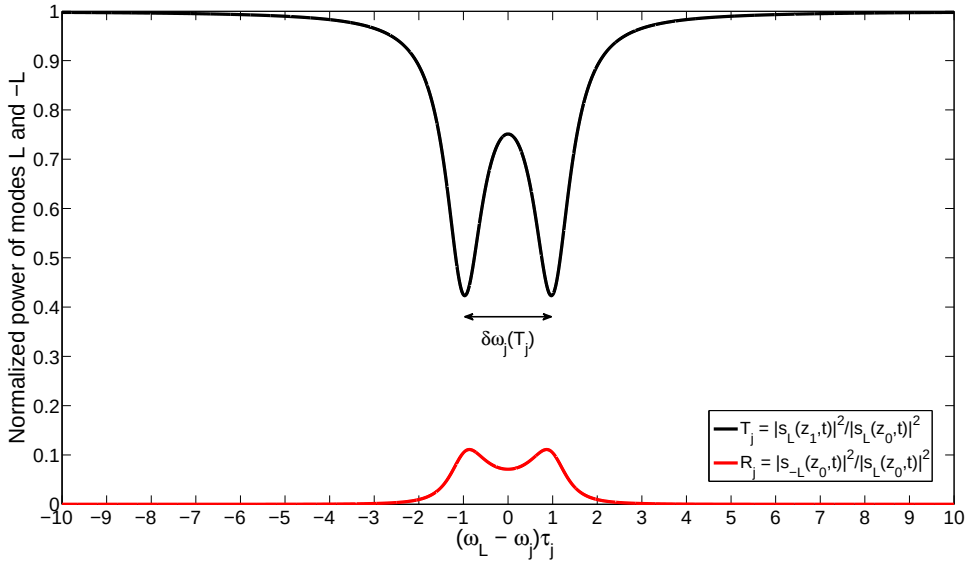

Figure 2.5 : T_j and R_j for $\Gamma_{jj} = 0$, $\Gamma_{j-j} = \frac{1}{\tau_j}$, $\Gamma'_{jj} = \Gamma'_{j-j} = 0$ using Eq. B.73 and B.74.

Unidirectional source, single mode waveguide, modal coupling and $\delta\epsilon'(\mathbf{r}) \neq 0$

Finally, transmission and reflection signals can have the shape presented in Fig. 2.6 when the cavity mode suffers modal coupling and radiative losses : $\Gamma_{j-j} = \frac{1}{\tau_j}$, $\Gamma'_{jj} = \frac{1}{10\tau_j}$ and $\Gamma'_{j-j} = \frac{1}{\tau_j}$. The spectra are now asymmetric splittings of Lorentzian curves. This asymmetry can be understood from the symmetric/antisymmetric modes perspective. The perturbation is located at the field maximum of the symmetric mode and at the field node of the antisymmetric mode, hence their name. The symmetric mode suffers larger radiative losses caused by the perturbation, leading to a broader peak.

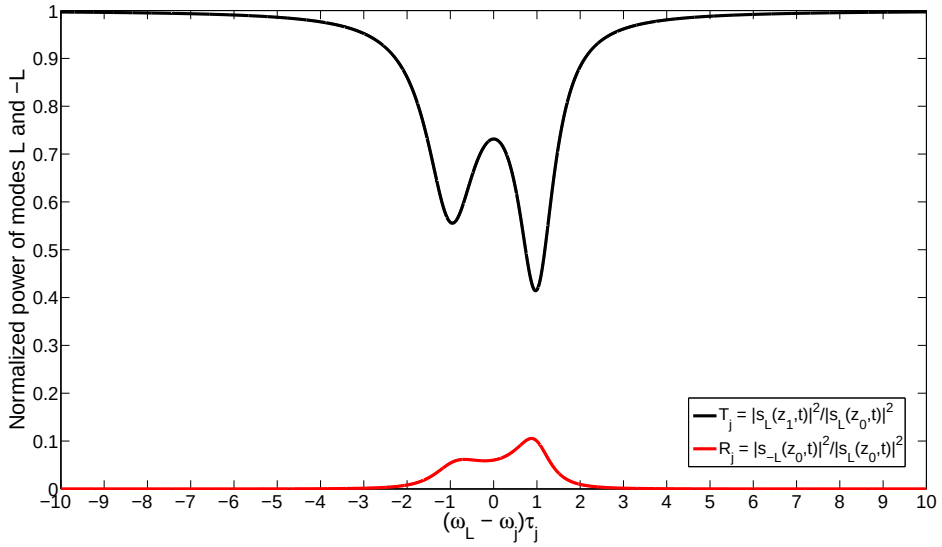

Figure 2.6 : T_j and R_j for $\Gamma_{jj} = 0$, $\Gamma_{j-j} = \frac{1}{\tau_j}$, $\Gamma'_{jj} = \frac{1}{10\tau_j}$ and $\Gamma'_{j-j} = \frac{1}{\tau_j}$ using Eq. B.68 and Eq. B.69.

2.3 Linear characteristics of WGM microcavities

Linear cavity characteristics are values associated to a specific mode resonance in the linear regime at low signal power. The explicit definitions are given in Section B.2.2 and the important results are given here.

2.3.1 Q-factor

The Q-factor is a metric used to compare different types of optical resonators. The Q-factor of an optical mode is proportional to the stored energy over the lost energy during one optical cycle $T_{\omega_j} = 2\pi/\omega_j$. It represents the number of optical cycles until the energy of its initial value falls off to e^{-1}. It is defined as

$$Q_{j,T} = \frac{2\pi}{T_{\omega_j}} \frac{|a_j(t)|^2}{-\frac{\partial |a_j(t)|^2}{\partial t}} = \omega_j \frac{|a_j(t)|^2}{-\frac{\partial |a_j(t)|^2}{\partial t}} \tag{2.12}$$

In the literature, we often see the simplest case where $\Gamma_{jj} = \Gamma'_{jj} = \Gamma_{j-j} = \Gamma'_{j-j} = 0$ (i.e. no perturbation). Using steady-state solutions of Eq. 2.7 and 2.9, we have

$$Q_{j,T} = \omega_j \frac{|a_j(t)|^2}{\left(\frac{1}{\tau_{j,0}} + \frac{1}{\tau_{j,c}}\right)|a_j(t)|^2} \;\Rightarrow\; \frac{1}{Q_{j,T}} = \frac{1}{\omega_j \tau_{j,0}} + \frac{1}{\omega_j \tau_{j,c}} = \frac{1}{\omega_j \tau_j} \tag{2.13}$$

More specifically, if the input signal is blocked suddenly ($|s_L(z_0,t)|^2 \to 0$), the mode energy decreases as $|a_j(t)|^2 e^{-t/\tau_j}$. This principle is exploited in cavity ring-down measurements to find τ_j [24]. Thus, a cavity with larger Q-factor modes implies that it retains light more efficiently and for a longer time.

The previous relation suggests that we can rewrite the intrinsic photon's lifetime $\tau_{j,0}$ as different loss processes such as absorption, scattering or radiative tunneling, together with their associated Q-factors [24] :

$$\frac{1}{\tau_j} = \frac{1}{\tau_{\mathrm{j,c}}} + \frac{1}{\tau_{\mathrm{j,0}}} \tag{2.14}$$

$$= \frac{1}{\tau_{\mathrm{j,c}}} + \frac{1}{\tau_{\mathrm{j,abs}}} + \frac{1}{\tau_{\mathrm{j,scat}}} + \frac{1}{\tau_{\mathrm{j,rad}}} + \dots \tag{2.15}$$

$$\frac{1}{Q_{j,T}} = \frac{1}{Q_{\mathrm{j,c}}} + \frac{1}{Q_{\mathrm{j,0}}} \tag{2.16}$$

$$= \frac{1}{Q_{\mathrm{j,c}}} + \frac{1}{Q_{\mathrm{j,abs}}} + \frac{1}{Q_{\mathrm{j,diff}}} + \frac{1}{Q_{\mathrm{j,rad}}} + \dots \tag{2.17}$$

where $Q_{j,c}$ is the *coupling* (or *extrinsic*) *Q-factor* of mode j and $Q_{j,0}$ is the *intrinsic Q-factor*.

$Q_{j,T}$ is the *total Q-factor*. It can also be written as the *loaded Q-factor*, Q_L, that implies a *loading* from an external coupled source like waveguides. When the mode j denomination is implicit, these Q-factors are usually rewritten as Q_T, Q_c, Q_0, etc.

As radiative tunneling is usually negligible, the intrinsic Q-factor upper limit is set by the material absorption and Rayleigh scattering. Considering that $\mathbf{e}_j(\mathbf{r})$ is much larger inside the cavity, it leads to

$$Q_{j,0} = \frac{k_j n_c}{\alpha_{lin}} = \frac{2\pi n_c}{\lambda_j \alpha_{lin}} \tag{2.18}$$

where $k_j = \omega_j/c$, n_c is the cavity's material refractive index, α_{lin} is the linear material attenuation in m^{-1}. This last definition of $Q_{j,0}$ is often seen in the literature [1, 24].

2.3.2 Transmission coefficient

It was previously mentioned that the depth of the transmission peak depends on the ratio of $\tau_{j,c}$ and $\tau_{j,0}$. In the simplest case where modal coupling is null (Fig. 2.3), the transmission is given by Eq. B.77

$$T_j = \frac{|s_L(z_1,t)|^2}{|s_L(z_0,t)|^2} = \frac{(\frac{1}{2\tau_j} - \frac{1}{\tau_{j,c}})^2 + (\omega_L - [\omega_j - \Gamma_{jj}])^2}{\frac{1}{4\tau_j^2} + (\omega_L - [\omega_j - \Gamma_{jj}])^2} \tag{2.19}$$

The transmission value, $T_{j,0}$, at the peak center $\omega_L = \omega_j - \Gamma_{jj}$, is

$$T_j|_{\omega_L=\omega_j-\Gamma_{jj}} = T_{j,0} = \left(\frac{\tau_{j,c} - \tau_{j,0}}{\tau_{j,c} + \tau_{j,0}}\right)^2 = \left(\frac{Q_{j,c} - Q_{j,0}}{Q_{j,c} + Q_{j,0}}\right)^2 \tag{2.20}$$

The normalized transmission coefficient, T_j, is bounded between 0 and 1. As mentioned earlier, following Relation 2.20, complete extinction happens at critical coupling when $\tau_{j,c} = \tau_{j,0}$ or $Q_{j,c} = Q_{j,0}$.

2.3.3 Q-factor measurement

The total Q-factor can be measured using the resonance's spectral full width at half maximum (FWHM), $\Delta\omega_j$, where $|s_L(z_1,t)|^2/|s_L(z_0,t)|^2 = (1 + T_{j,0})/2$:

$$\frac{1+T_{j,0}}{2} = \frac{(\frac{1}{2\tau_j} - \frac{1}{\tau_{j,c}})^2 + (\omega_{\mathrm{FWHM}} - \omega_j)^2}{\frac{1}{4\tau_j^2} + (\omega_{\mathrm{FWHM}} - \omega_j)^2} \Rightarrow (\omega_{\mathrm{FWHM}} - \omega_j)^2 = \frac{1}{4\tau_j^2}$$

$$\Rightarrow \Delta\omega_j = 2(\omega_{\mathrm{FWHM}} - \omega_j) = \frac{1}{\tau_j}$$

$$\Rightarrow Q_{j,T} = \frac{\omega_j}{\Delta\omega_j} \equiv \frac{\lambda_j}{\Delta\lambda_j}. \tag{2.21}$$

This is not surprising since the resonance is a Lorentzian curve in the frequency domain, i.e. the Fourier transform of a decaying exponential curve in time. It is important to note that only a Lorentzian curve can be characterized using its FWHM value. When modal coupling or any resonance's asymmetry is observed, more complicated numerical fits are mandatory.

Once $T_{j,0}$ and $Q_{j,T}$ are known, it is possible to retrieve $Q_{j,0}$ and $Q_{j,c}$ except for one detail : Relation 2.20 is symmetric in view of $Q_{j,c}$ and $Q_{j,0}$ and we usually do not know which is larger. We have

$$Q_{j,c} = \frac{2Q_{j,T}}{1 \pm \sqrt{T_{j,0}}} \quad \text{et} \quad Q_{j,0} = \frac{2Q_{j,T}}{1 \mp \sqrt{T_{j,0}}} \tag{2.22}$$

where the upper and lower signs correspond to the *overcoupled regime* and *undercoupled regime*. To solve this issue, it is possible to take multiple transmission measurements with different coupling conditions, hence different $Q_{j,c}$. It is also possible to use a technique developed during the master's thesis based on a Stokes parameters measurement [241].

2.3.4 Coupled power

In this thesis, many terms are used to describe power flows : the input power, the output power and the coupled power. The input power terms were already defined as $|s_L(z_0,t)|^2$ and $|s_{-L}(z_1,t)|^2$. They describe the power in the waveguide at the entrance of the coupling area. Similarly, the output power terms are $|s_L(z_1,t)|^2$ and $|s_{-L}(z_0,t)|^2$. They describe the power in the waveguide at the exit of the coupling area. When $|s_{-L}(z_0,t)|^2$ and $|s_{-L}(z_1,t)|^2$ are null, input and output powers can be defined uniquely as

$$\textbf{Input power} \quad P_{in} = |s_L(z_0,t)|^2$$
$$\textbf{Output power} \quad P_{out} = |s_L(z_1,t)|^2.$$

The coupled power P_{coup} is defined as the total power transfered from the waveguide to the cavity. In other words, it is the power that is not transmitted through the waveguide. It is written as

$$\textbf{Coupled power} \quad P_{coup} = (1 - T_j)P_{in}$$

where T_j is the transmission coefficient. Considering a linear regime and no modal coupling, T_j is defined using Relation 2.19 :

$$P_{coup} = \frac{1}{\tau_{j,0}} \frac{1}{\tau_{j,c}} \frac{P_{in}}{\frac{1}{4\tau_j^2} + (\omega_L - [\omega_j - \Gamma_{jj}])^2}. \tag{2.23}$$

The coupled power term is directly obtained from the transmission spectrum. Furthermore, it carries the detuning term $\omega_L - [\omega_j - \Gamma_{jj}]$ which appears in linear output power definitions, but also in the stimulated Raman scattering output power terms (Section 2.5.1) and the laser signal output power terms (Section 2.6). The use of P_{coup} allows the direct comparison between the theoretical framework of this thesis and the nonlinear output power measurements.

Other terms such as the intracavity power or the circulating power in the mode j and the accumulation factor are often seen in the literature. Explicit definitions are found in Section B.2.2, but are not discussed here as they are not used in the following chapters of this thesis.

2.4 Eigenmodes of microspheres

The WGM microcavity structure used in this thesis is the microsphere. Usually made from high-purity optical fiber, microspheres are made using simple melting techniques and they offer excellent Q-factors, regularly $> 10^7$. Furthermore, the vectorial solutions of the wave equation (Eq. 2.5) are known. In this section, we will discuss the spatial distributions of the eigenmodes but their explicit mathematical formulations are described in Section B.3.

The solutions are written for the spherical coordinates (ρ, θ, ϕ) shown in Fig. 2.7 using the form

$$\begin{aligned}
\mathbf{E}_j(\mathbf{r}, t) &= \frac{a_j(t) e^{-i\omega_j t} \mathbf{e}_j(\mathbf{r})}{2\sqrt{N_j}} + \text{c.c.} \\
\mathbf{e}_j(\mathbf{r}) &= \left[e_\rho(\rho, \theta, \phi)\hat{\rho} + e_\theta(\rho, \theta, \phi)\hat{\theta} + e_\phi(\rho, \theta, \phi)\hat{\phi} \right] \\
&= \left[e_\rho(\rho, \theta)\hat{\rho} + e_\theta(\rho, \theta)\hat{\theta} + e_\phi(\rho, \theta)\hat{\phi} \right] e^{im_j \phi}
\end{aligned}$$

The solutions are separated as transverse-electric (TE) and transverse-magnetic (TM) solutions where the ρ components of the electric and magnetic fields are null respectively. The mode frequencies, wavelengths or wavenumbers are determined by their characteristic equations :

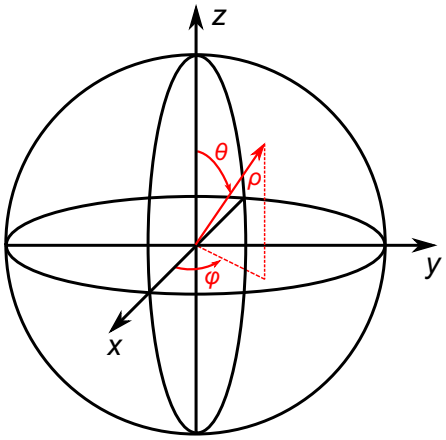

Figure 2.7 : Spherical coordinates for a microsphere.

TE characteristic equation

$$\frac{n_c}{n_a}\frac{J_{l_j-1+1/2}(n_c k_j R_c)}{J_{l_j+1/2}(n_c k_j R_c)} = \frac{H^{(1)}_{l_j-1+1/2}(n_a k_j R_c)}{H^{(1)}_{l_j+1/2}(n_a k_j R_c)}$$

TM characteristic equation

$$\frac{1}{n_c}\frac{J_{l_j-1+1/2}(n_c k_j R_c)}{J_{l_j+1/2}(n_c k_j R_c)} - \frac{1}{n_a}\frac{H^{(1)}_{l_j-1+1/2}(n_a k_j R_c)}{H^{(1)}_{l_j+1/2}(n_a k_j R_c)} = \frac{l_j}{k_j R_c}\left(\frac{1}{n_c^2} - \frac{1}{n_a^2}\right)$$

where $J_{l_j+1/2}(x)$ is the Bessel function of the first kind and $H^{(1)}_{l_j+1/2}(x)$ is the Hankel function of the first kind [242]. R_c and n_c are the sphere radius and refractive index. n_a is the surrounding medium refractive index. l_j and m_j are the polar and azimuthal integers numbers of the jth mode, similarly to the hydrogen atom solutions of the Schrödinger equation.

The WGM solutions are represented by the first solutions (smallest k_j, largest λ_j) of the characteristic equations for a particular l_j and typically for $m_j = l_j$. Figure 2.8 shows the TE spatial distribution of $|\mathbf{e}_j|^2$ for an As_2S_3 microsphere. The mode $l_j = m_j = 139$ has a single lobe centered at $\theta = \pi/2$ and its confinement inside the sphere is assured by the high refractive index of As_2S_3.

An eigenmode with a $m_j = l_j - q$ has $q+1$ lobes along the polar direction. Figure 2.9 presents the spatial distribution of $|\mathbf{e}_j|^2$ for a similar wavelength, but for $l_j = 132$ and $m_j = l_j - 2$. The mode has now two lobes radially meaning that a wavelength of 1547 nm is the second solution of the TE characteristic equation for $l_j = 132$. It also has 3 lobes along the polar direction caused by the $l_j - m_j$ difference.

For a perfect sphere, the characteristic equations do not depend on m_j. All the m_j solutions

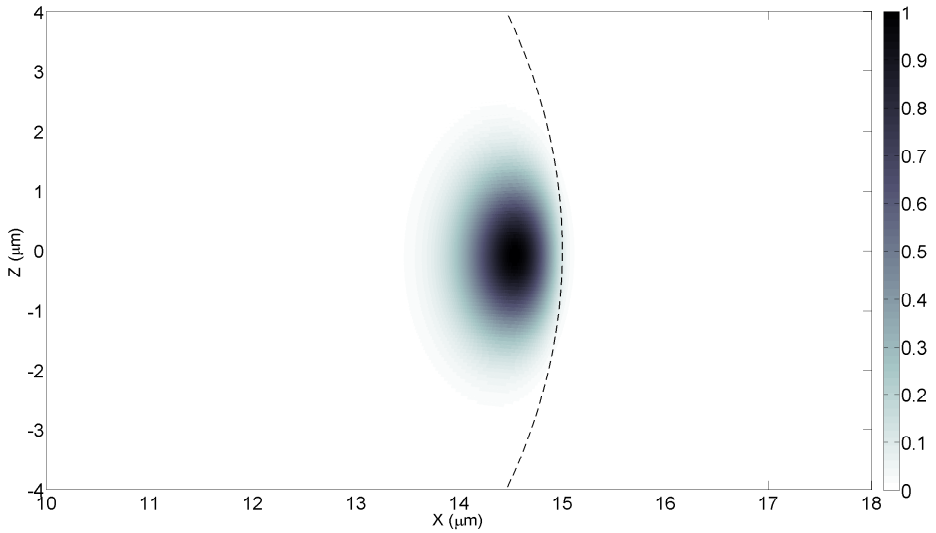

Figure 2.8 : Spatial distribution of TE solutions $|\mathbf{e}_j|^2$ for an As_2S_3 sphere with a radius of 15 μm. The wavelength is 1550 nm, $l_j = 139$ and $m_j = l_j$. The dashed line is the cavity's boundary.

are degenerate and have the same frequency ω_j. They also have the same round-trip time since the additional time spent in the polar direction is compensated by a longer trip along the equator ($\theta = \pi/2$). Approximated solutions for k_j or ω_j associated to a mode l_j can be

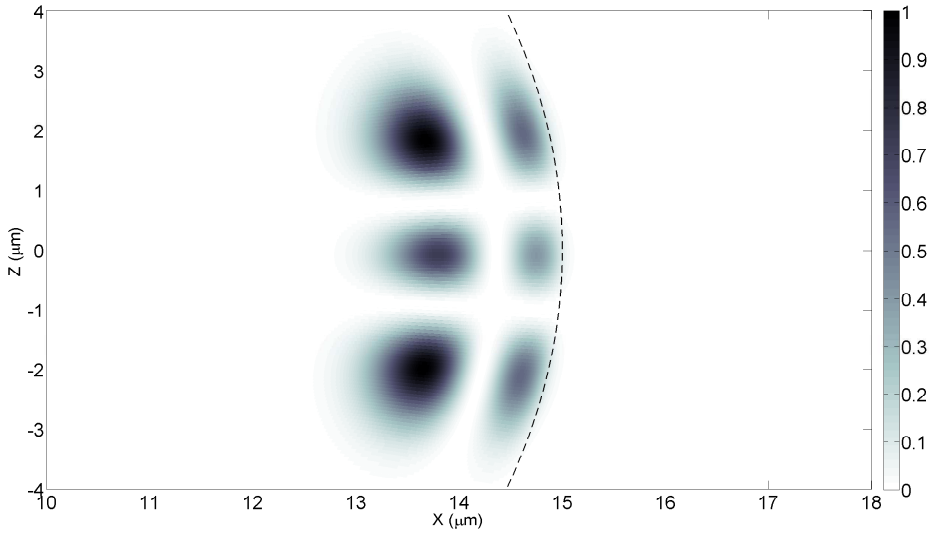

Figure 2.9 : Spatial distribution of TE solutions $|\mathbf{e}_j|^2$ for an As_2S_3 sphere with a radius of 15 μm. The wavelength is 1547 nm, $l_j = 132$ and $m_j = l_j - 2$. The dashed line is the cavity's boundary.

found in [14, 16].

The TE and TM mode spectra are determined by their characteristic equation solutions $k_j = 2\pi/\lambda_j$. Figure 2.10 shows the resonance positions for each $l_j = m_j$ number for an As_2S_3 sphere with a radius of 15 μm. The top series in red are the 1st radial order solutions. The density of modes can be quite large as the input signal can also couple to modes $> 2^{nd}$ order. The density increases with the resonator size as shown in Fig. 2.11 for a sphere with a radius of 150 μm. The spectral distance between successive l_j numbers is called the Free Spectral Range (FSR) and is ~ 1 nm for a sphere radius of 150 μm.

Furthermore, the solutions shown in Fig. 2.10 and 2.11 are valid for $l_j = m_j$ as m_j solutions are degenerate. In practice, the microspheres are not perfect and a difference between the major axis and minor axis radius ΔR_c lifts this degeneracy as [21]

$$\frac{\omega_j^{(l_j \neq m_j)}}{\omega_j^{(l_j = m_j)}} \approx 1 - \frac{\Delta R_c}{R_c}\left(2 + 3\frac{l_j^2 - m_j^2}{l_j^2}\right).$$

This usually causes the mode density to double, to triple or even more. Fortunately, large Q-factors are associated with narrow resonance linewidths, following Relation 2.21. A resonance with a Q-factor of 1×10^6 has a linewidth of 1.5 pm at a wavelength of 1.5 μm. Resonances are usually well separated in the spectra and measurements can be done on single lines without

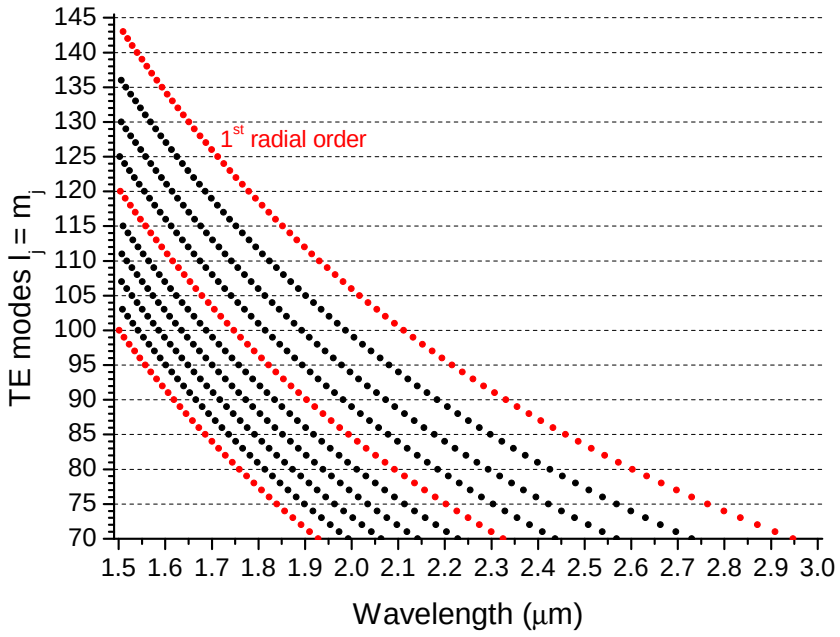

Figure 2.10 : TE mode wavelengths and their associated l_j numbers for an As_2S_3 sphere with a radius of 15 μm. Red dots denote the 1st, 5th and 10th radial order.

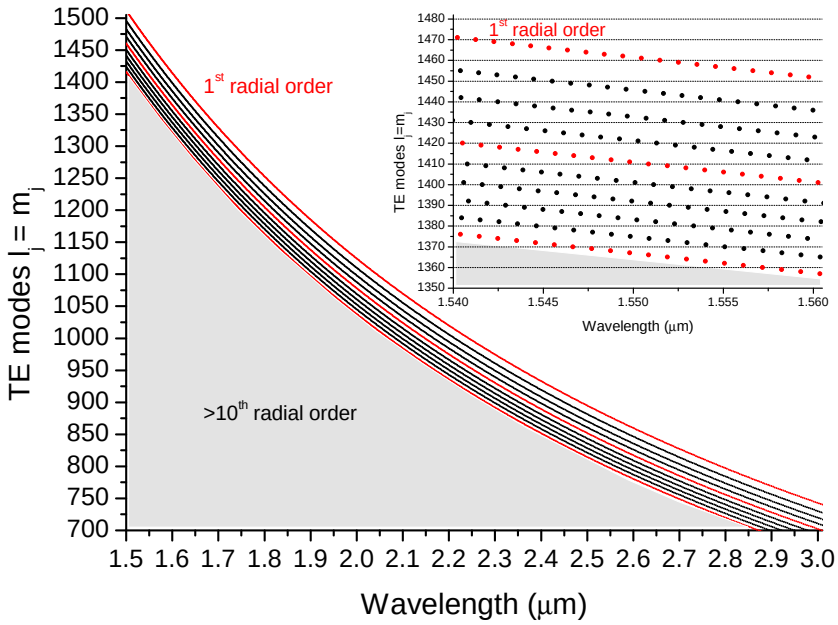

Figure 2.11 : TE mode wavelengths and their associated l_j numbers for an As_2S_3 sphere with a radius of 150 μm. Red dots denote the 1st, 5th and 10th radial order. Mode wavelengths of radial order $> 10^{th}$ are located in the shaded area. Inset : Zoom on the C-band section to show the high density of modes.

difficulty.

Dispersion of microspheres

The sphere dispersion – the mode frequencies as a function of their azimuthal number m_j – is especially important for phase-matched nonlinear processes such as parametric frequency mixing. As an example, four-wave mixing processes depend on coupling terms proportional to

$$e^{i(\omega_1+\omega_2+\omega_3+\omega_4)t}e^{i(m_1+m_2+m_3+m_4)\phi}.$$

The first part is linked by the energy conservation $\hbar\omega_1+\hbar\omega_2+\hbar\omega_3+\hbar\omega_4 \to 0$ and the second part is related to the WGM microcavity phase matching conditions $m_1+m_2+m_3+m_4 \to 0$.

The most studied case is the degenerate four-wave mixing (FWM) where two pump photons are added to give one signal photon and one idler photon. The total frequency dispersion is given by [97]

$$\Delta\omega_T = 2\omega_p - (\omega_s+\omega_i) - \frac{2n_2 I_p \omega_p^2 R_c}{m_p c} = \Delta\omega_{lin} - \frac{2n_2 I_p \omega_p^2 R_c}{m_p c} \to 0$$

where the last term is the nonlinear shift caused by the self-phase modulation and the cross-phase modulation. n_2 is the nonlinear Kerr index. Degenerate FWM is the basic principle of parametric amplification and frequency combs generation in WGM microcavities, as seen in Table 1.1. In WGM microcavities, successive azimuthal orders must obey

$$2m_j - m_{j-1} - m_{j+1} = 2m_p - m_s - m_i = 0$$

The linear dispersion $\Delta\omega_{lin}$ depends on the material and structure dispersions, and is defined by the characteristic equation solutions. In the case of silica microspheres, both conditions are fulfilled near a wavelength of 1550 nm for a diameter of 150 μm [97]. However, for As_2S_3, the material dispersion pushes the zero-dispersion wavelength to longer wavelength. Figure 2.12 shows the linear dispersion $\Delta\omega_{lin}$ for an As_2S_3 microsphere with a radius of 150 μm.

To successfully generate signal and idler photons in As_2S_3 spheres, the total dispersion $\Delta\omega_T$ needs to fall inside the resonance linewidth as shown in Fig. 2.12. Additionally, the nonlinear dispersion shift is negative for As_2S_3. Pump wavelengths > 4 μm are then needed. A smaller sphere radius pushes the zero-dispersion wavelength further to the IR. Consequently, degenerate FWM for As_2S_3 spheres is limited to mid-IR wavelengths. This explains why it was not observed during this thesis experiments : pump wavelengths were limited to $\lambda_p < 2$ μm.

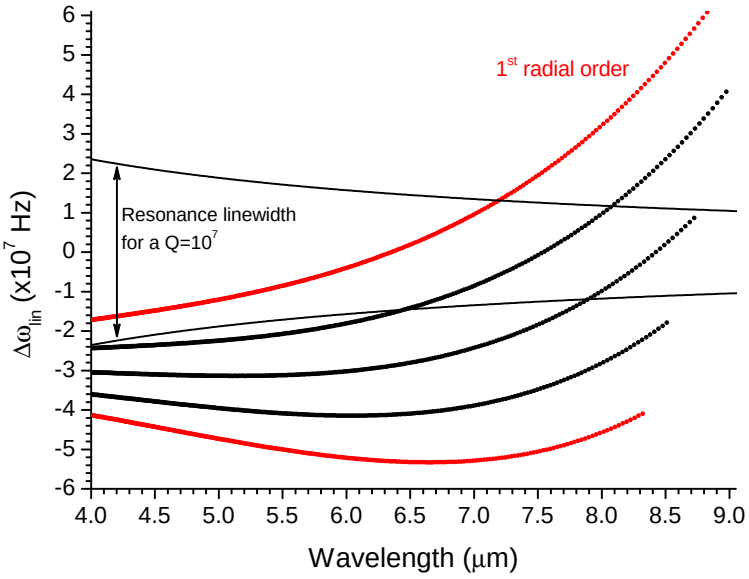

Figure 2.12 : Linear sphere dispersion $\Delta\omega_{lin}$ for an As_2S_3 sphere with a radius of 150 μm. Two black lines indicate the resonance linewidth for a Q-factor of 1×10^7.

2.5 Nonlinear coupled-modes equations

The material response to an external optical field $\mathbf{E}(\mathbf{r},t)$ is described by the electric polarization vector $\mathbf{P}(\mathbf{r},t)$. When the field intensity is small, the response varies linearly with the field :

$$\mathbf{P}(\mathbf{r},t) \propto \chi^{(1)}\mathbf{E}(\mathbf{r},t)$$

where $\chi^{(1)}$ is the first order electric susceptibility. If the field intensity is large, this linear description may not fully describe the material response and the electric polarization vector needs to be rewritten :

$$\mathbf{P}(\mathbf{r},t) \propto \chi^{(1)}\mathbf{E}(\mathbf{r},t) + \chi^{(2)}\mathbf{E}(\mathbf{r},t)\mathbf{E}(\mathbf{r},t) + \chi^{(3)}\mathbf{E}(\mathbf{r},t)\mathbf{E}(\mathbf{r},t)\mathbf{E}(\mathbf{r},t) + \dots$$

where $\chi^{(2)}$ and $\chi^{(3)}$ describe the second and third order nonlinear responses. The optical field can interact nonlinearly with itself and other fields, leading to interesting and useful phenomena. For example, the field can interact with itself and modify its own phase through self-phase modulation, a third order process. Frequency mixing processes such as second and third harmonic generations are also possible and widely used.

The material response is dictated by the electronic dipoles, ions dipoles, photon-phonon interactions or free charges. The dominating process depends mainly on the material composition, and the optical field frequency and its strength. Parametric processes such as self-phase modulation and third harmonic generation result from electronic dipoles response. For some materials, such as chalcogenide glasses used in this thesis, the optical field also strongly interacts with the material's lattice through photon-phonon interactions or Raman scattering.

This interaction can be modeled through the nonlinear coupled-modes equations, similar to the linear coupled-modes equations of Section 2.2. The following sections highlight the main relations used in this thesis and are based on the explicit derivation of Section B.4.

2.5.1 Stimulated Raman scattering

Raman scattering comes from the inelastic scattering of an optical signal photon and a material phonon. Figure 2.13 shows the energy transfer of two processes. The incoming photon with an energy $\hbar\omega_p$ loses an energy quanta $\hbar\Omega_v$ to the material's lattice. The outgoing Stokes photon has a residual energy $\hbar\omega_s < \hbar\omega_p$. When the incoming photon gains an energy quanta from the lattice, the outgoing photon (anti-Stokes) goes out with an energy $\hbar\omega_a > \hbar\omega_p$.

Classically, the material is viewed as N diatomic molecules that vibrate with a frequency Ω_v. The atom distance from their equilibrium positions is described by the vector $\mathbf{Q}_v(\mathbf{r},t)$

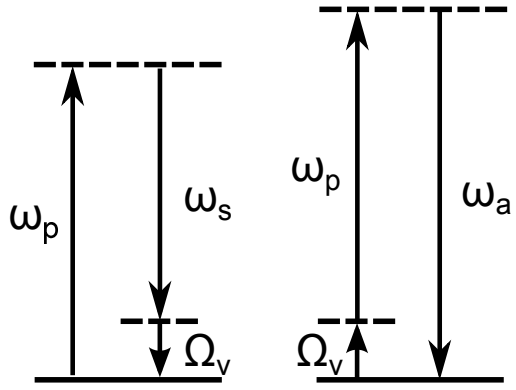

Figure 2.13 : Stokes photon $\hbar\omega_s$ and anti-Stokes photon $\hbar\omega_a$ creation through Raman scattering of a pump signal photon $\hbar\omega_p$.

following the definition in [243]. The material's polarizability α - not to be confused with the linear attenuation coefficient - quantifies its reaction to an external optical field. In linear optics, the sole contribution from the electrons α_{el}, linked to $\chi^{(1)}$, is usually considered. Here, we will also consider the nucleus contribution when it moves out of his equilibrium position. Its contribution is added using a linear expansion [243, 244]

$$\alpha = \alpha_{el} + \sum_i \left(\frac{\partial\alpha}{\partial Q_{v,i}}\right)_0 Q_{v,i}(\mathbf{r},t) \;\rightarrow\; \alpha_{el} + \left(\frac{\partial\alpha}{\partial Q_v}\right)_0 Q_v(\mathbf{r},t)$$

where we summed the ith vector component. To simplify, we can consider that the molecule oscillates along one direction, parallel to the external electric field. The polarizability is now scalar.

The vibration $Q_v(\mathbf{r},t)$ influences the optical field through the polarizability and the electric polarization vector

$$\mathbf{P}(\mathbf{r},t) = N\alpha\mathbf{E} = N\left[\alpha_0 + \left(\frac{\partial\alpha}{\partial Q_v}\right)_0 Q_v(\mathbf{r},t)\right]\mathbf{E}(\mathbf{r},t) = \underbrace{\epsilon_0\chi^{(1)}\mathbf{E}(\mathbf{r},t)}_{\mathbf{P}^{(1)}(\mathbf{r},t)} + \underbrace{N\left(\frac{\partial\alpha}{\partial Q_v}\right)_0 Q_v(\mathbf{r},t)\mathbf{E}(\mathbf{r},t)}_{\mathbf{P}_{Raman}(\mathbf{r},t)}.$$

It splits into a linear part $\mathbf{P}^{(1)}(\mathbf{r},t)$ and the nonlinear part of Raman scattering $\mathbf{P}_{Raman}(\mathbf{r},t)$.

Linear coupled-modes equations 2.7 to 2.10 can be rewritten to take into account the Raman gain for a single pump signal and a single Stokes signal. Inside the cavity, we have

$$\frac{\partial a_p(t)}{\partial t} = \left(i\left[\omega_L - \omega_p\right] - \frac{1}{2\tau_{p,0}} - \frac{1}{2\tau_{p,c}}\right)a_p(t)$$

$$- g_R \frac{\omega_p}{\omega_s} \left(|a_s(t)|^2 + |a_{-s}(t)|^2 \right) a_p(t) + i\kappa_{pL} s_L(z_0, t) \tag{2.24}$$

$$\frac{\partial a_s(t)}{\partial t} = - \left(\frac{1}{2\tau_{s,0}} + \frac{1}{2\tau_{s,c}} \right) a_s(t) + g_R |a_p(t)|^2 a_s(t) \tag{2.25}$$

$$\frac{\partial a_{-s}(t)}{\partial t} = - \left(\frac{1}{2\tau_{s,0}} + \frac{1}{2\tau_{s,c}} \right) a_{-s}(t) + g_R |a_p(t)|^2 a_{-s}(t). \tag{2.26}$$

where the perturbation losses and modal coupling are considered negligible and the clockwise a_s and counterclockwise mode a_{-s} are equally pumped by the Raman scattering process [123–125]. The anti-Stokes signal is left out since the phase matching conditions were not met in our experiments.

The output signals are given by

$$s_L(z_1, t) = s_L(z_0, t) + i\kappa_{Lp}(z_1) a_p(t) \approx s_L(z_0, t) + i \frac{a_p(t)}{\sqrt{\tau_{p,c}}}$$

$$s_S(z_1, t) = i\kappa_{Ss}(z_1) a_s(t) \approx i \frac{a_s(t)}{\sqrt{\tau_{s,c}}}$$

$$s_{-S}(z_0, t) = i\kappa_{-S-s}(z_0) a_{-s}(t) \approx i \frac{a_{-s}(t)}{\sqrt{\tau_{s,c}}}.$$

The cavity Raman gain g_R ($\mathrm{J}^{-1}\mathrm{s}^{-1}$) is defined as

$$g_R = \frac{c^2 g_R^{(b)}}{2 n_p n_s V_{ppss}} \tag{2.27}$$

where

$$V_{ppss} = \frac{\int_V |\mathbf{e}_p|^2 dV \int_V |\mathbf{e}_s|^2 dV}{\int_V |\mathbf{e}_p|^2 |\mathbf{e}_s|^2 dV} \tag{2.28}$$

quantifies the mode fields overlap. $g_R^{(b)}$ is the material Raman gain or *bulk* Raman gain expressed in m/W.

The material Raman gain $g_R^{(b)}$ amplitude depends greatly on the material composition as seen in Table 1.2. Following the Fermi golden rule, the Raman gain is larger if the probability of transition from a ground vibrational state to a virtual excited state and back to a higher level vibrational state is also larger. The classical model developed in Section B.4 shows that it depends on $\left(\frac{\partial \alpha}{\partial Q_v}\right)_0^2$. This value is linked to the transition dipole moment between the ground vibrational state and a virtual excited state and to the transition dipole moment between the virtual excited state and a higher energy level vibrational state [243]. A larger Raman gain in silicon is understandable as the higher level vibrational state energy is the same everywhere due to the crystalline layout. In amorphous materials, the higher level vibrational state energy

changes with the local atomic configuration, hence distributing the Raman response over a broader energy spectrum.

The coupled-modes equations 2.24 to 2.26 can be solved for a CW regime. The threshold conditions for stimulated Raman scattering (SRS) are given by Eq. 2.25 or 2.26, when the Stokes mode losses are compensated by the pump gain :

$$g_R|a_p(t)|^2 = \frac{1}{2\tau_s}$$

The conditions are similar for the clockwise and the counterclockwise Stokes modes : they start lasing at the same time. Furthermore, the pump mode energy is fixed by this condition, meaning that the excess energy is converted to the Raman signal.

The link between the energy of both Stokes mode $|a_s(t)|^2$ and $|a_{-s}(t)|^2$ and the input power $P_{in} = |s_L(z_0,t)|^2$ is given by Eq. 2.24 :

$$a_p(t) = \frac{1}{\sqrt{\tau_{p,c}}} \frac{s_L(z_0,t)}{\frac{1}{2\tau_p} + \frac{\omega_p}{\omega_s} g_R \left(|a_s(t)|^2 + |a_{-s}(t)|^2\right) - i\left[\omega_L - \omega_p\right]}.$$

The total SRS power P_S leaving though the waveguide is the summation of the forward and backward SRS power, $|s_S(t)|^2$ and $|s_{-S}(t)|^2$ respectively :

$$\begin{aligned} P_S = |s_S(t)|^2 + |s_{-S}(t)|^2 &= \frac{|a_s(t)|^2 + |a_{-s}(t)|^2}{\tau_{s,c}} \\ &= \frac{1}{2\tau_p \tau_{s,c} g_R} \frac{\omega_s}{\omega_p} \left[\sqrt{\frac{P_{in}}{P_{in,th}^{\Delta_L=0}} - (2\tau_p)^2 \Delta_L^2} - 1 \right] \\ \text{with} \quad \Delta_L &= \omega_L - \omega_p \end{aligned} \tag{2.29}$$

where the threshold pump power with and without laser frequency detuning Δ_L, $P_{in,th}$ and $P_{in,th}^{\Delta_L=0}$, are

$$P_{in,th} = \left[1 + (2\tau_p)^2 \Delta_L^2\right] \frac{\tau_{p,c}}{(2\tau_p)^2 (2\tau_s) g_R} \;\Rightarrow\; P_{in,th}^{\Delta_L=0} = \frac{\tau_{p,c}}{(2\tau_p)^2 (2\tau_s) g_R} = \frac{\pi^2 n_p n_s V_{ppss} Q_{p,c}}{\lambda_p \lambda_s g_R^{(b)} Q_{p,T}^2 Q_{s,T}} \tag{2.30}$$

As it is seen from Eq. 2.29, the total SRS power depends on the laser detuning. This feature is hard to quantify, especially when the measurements are dynamic or when thermo-optic effects are present. To remove its dependency to Δ_L, we express P_S as a function of the coupled pump power $P_{L,coup} = P_{in}(1 - T_p)$ where T_p is the transmission of the pump resonance at the

position ω_L :

$$P_{in,coup} = \frac{1}{2\tau_s g_R}\left[\frac{1}{\tau_p}\sqrt{\frac{P_{in}}{P_{in,th}^{\Delta_L=0}} - (2\tau_p)^2\Delta_L^2} - \frac{1}{\tau_{p,c}}\right]$$

The coupled power is different from the linear coupled power of Eq. 2.23 because the Raman gain contribution is added. We get

$$P_S = \frac{\omega_s}{\omega_p}\frac{\tau_s}{\tau_{s,c}}\left[P_{in,coup} - \frac{1}{2\tau_s\tau_{p,0}g_R}\right] \tag{2.31}$$

It is worth noting that the total SRS power P_S follows a square-root dependency of P_{in}. As the input power grows and the Stokes signal get stronger, the pump signal suffers a larger loss to the Stokes signal, limiting the power conversion. In other words, it saturates. This also results in a variation of the extrinsic/intrinsic losses ratio and the transmission T_p. The coupled power notation includes this square-root dependency and the transmission variation, thus P_S is proportional to $P_{in,coup}$.

Finally, external and internal power conversion efficiencies at threshold conditions are defined as

$$\begin{aligned}\eta_{ex} &= \frac{dP_S}{dP_{in}}|_{P_{in,th}} = 2\frac{\omega_s}{\omega_p}\frac{\tau_p}{\tau_{p,c}}\frac{\tau_s}{\tau_{s,c}} = 2\frac{\omega_s}{\omega_p}\frac{Q_{p,T}Q_{s,T}}{Q_{p,c}Q_{s,c}}\\ \eta_{in} &= \frac{dP_S}{dP_{in,coup}} = \frac{\omega_s}{\omega_p}\frac{\tau_s}{\tau_{s,c}} = \frac{\omega_s}{\omega_p}\frac{Q_{s,T}}{Q_{s,c}}\end{aligned} \tag{2.32}$$

The former gives the efficiency of the device as a whole and the latter removes the contribution of the pump signal coupling. If the external efficiency is much smaller than the internal efficiency, it means that the device suffers from non optimal pump coupling conditions.

2.5.2 Cascaded Raman scattering

As shown in Section B.4, the generation of a Stokes signal through Raman scattering is not limited by phase matching conditions, but follows mainly the energy conservation condition. Practically, this means that if a first Stokes signal is strong enough, it can pump a second Stokes signal with photon energy $\hbar\omega_p - 2\hbar\Omega_v$, as shown in Fig. 1.2. If the threshold conditions allow it, multiple Raman orders can be observed. As an example, Chapter 5 shows the measurements of Raman emissions up to the 5th order with a pump wavelength of 1550 nm. More specifically, it presents the Raman power growth as a function of the input pump power for the first three orders. Similarly to a single Raman order emission, these measurements can be understood using nonlinear coupled-modes equations.

Single pump & 3 Raman orders

To describe cascaded Raman emission up to the 3rd order, we need 7 coupled-modes equations for the cavity modes :

$$\begin{aligned}
\frac{\partial a_p(t)}{\partial t} &= \left(i\left[\omega_L-\omega_p\right]-\frac{1}{2\tau_p}\right)a_p(t)-g_{R1}\frac{\omega_p}{\omega_{s1}}\left(|a_{s1}(t)|^2+|a_{-s1}(t)|^2\right)a_p(t)+i\kappa_{pL}s_L(z_0,t)\\
\frac{\partial a_{s1}(t)}{\partial t} &= -\frac{1}{2\tau_{s1}}a_{s1}(t)-g_{R2}\frac{\omega_{s1}}{\omega_{s2}}\left(|a_{s2}(t)|^2+|a_{-s2}(t)|^2\right)a_{s1}(t)+g_{R1}|a_p(t)|^2a_{s1}(t) \qquad (2.33)\\
\frac{\partial a_{-s1}(t)}{\partial t} &= -\frac{1}{2\tau_{s1}}a_{-s1}(t)-g_{R2}\frac{\omega_{s1}}{\omega_{s2}}\left(|a_{s2}(t)|^2+|a_{-s2}(t)|^2\right)a_{-s1}(t)+g_{R1}|a_p(t)|^2a_{-s1}(t)\\
\frac{\partial a_{s2}(t)}{\partial t} &= -\frac{1}{2\tau_{s2}}a_{s2}(t)-g_{R3}\frac{\omega_{s2}}{\omega_{s3}}\left(|a_{s3}(t)|^2+|a_{-s3}(t)|^2\right)a_{s2}(t)+g_{R2}\left(|a_{s1}(t)|^2+|a_{-s1}(t)|^2\right)a_{s2}(t)\\
\frac{\partial a_{-s2}(t)}{\partial t} &= -\frac{1}{2\tau_{s2}}a_{-s2}(t)-g_{R3}\frac{\omega_{s2}}{\omega_{s3}}\left(|a_{s3}(t)|^2+|a_{-s3}(t)|^2\right)a_{-s2}(t)+g_{R2}\left(|a_{s1}(t)|^2+|a_{-s1}(t)|^2\right)a_{-s2}(t)\\
\frac{\partial a_{s3}(t)}{\partial t} &= -\frac{1}{2\tau_{s3}}a_{s3}(t)+g_{R3}\left(|a_{s2}(t)|^2+|a_{-s2}(t)|^2\right)a_{s3}(t)\\
\frac{\partial a_{-s3}(t)}{\partial t} &= -\frac{1}{2\tau_{s3}}a_{-s3}(t)+g_{R3}\left(|a_{s2}(t)|^2+|a_{-s2}(t)|^2\right)a_{-s3}(t).
\end{aligned}$$

with

$$g_{R1}=\frac{c^2g_R^{(b)}}{2n_pn_{s1}V_{pps1s1}},\quad g_{R2}=\frac{c^2g_R^{(b)}}{2n_{s1}n_{s2}V_{s1s1s2s2}},\quad \text{and}\quad g_{R3}=\frac{c^2g_R^{(b)}}{2n_{s2}n_{s3}V_{s2s2s3s3}}.$$

Each Raman order has a clockwise and a counterclockwise mode and they each have similar gain and loss terms related to the previous and the following order respectively.

The output signals are given by

$$\begin{aligned}
s_L(z_1,t) &= s_L(z_0,t)+i\kappa_{Lp}(z_1)a_p(t)\\
s_{S1}(z_1,t) &= i\kappa_{S1s1}(z_1)a_{s1}(t) & s_{-S1}(z_0,t) &= i\kappa_{-S1-s1}(z_0)a_{-s1}(t)\\
s_{S2}(z_1,t) &= i\kappa_{S2s2}(z_1)a_{s2}(t) & s_{-S2}(z_0,t) &= i\kappa_{-S2-s2}(z_0)a_{-s2}(t)\\
s_{S3}(z_1,t) &= i\kappa_{S3s3}(z_1)a_{s3}(t) & s_{-S3}(z_0,t) &= i\kappa_{-S3-s3}(z_0)a_{-s3}(t).
\end{aligned}$$

Again, it is possible to solve theses equations for a CW regime. The clockwise and counterclockwise equations of a specific Raman order give the same threshold conditions and dependencies :

$$g_{R3}\left(|a_{s2}(t)|^2+|a_{-s2}(t)|^2\right)=\frac{1}{2\tau_{s3}} \tag{2.34}$$

$$g_{R2}\left(|a_{s1}(t)|^2+|a_{-s1}(t)|^2\right)=\frac{1}{2\tau_{s2}}+\frac{\omega_{s2}}{\omega_{s3}}g_{R3}\left(|a_{s3}(t)|^2+|a_{-s3}(t)|^2\right) \tag{2.35}$$

$$g_{R1}|a_p(t)|^2=\frac{1}{2\tau_{s1}}+\frac{\omega_{s1}}{\omega_{s2}}g_{R2}\left(|a_{s2}(t)|^2+|a_{-s2}(t)|^2\right) \tag{2.36}$$

$$a_p(t)=\frac{1}{\sqrt{\tau_{p,c}}}\frac{s_L(z_0,t)}{\frac{1}{2\tau_p}+\frac{\omega_p}{\omega_{s1}}g_{R1}\left(|a_{s1}(t)|^2+|a_{-s1}(t)|^2\right)-i\left[\omega_L-\omega_p\right]}. \tag{2.37}$$

Relation 2.34 is the threshold condition for the stimulated emission of the 3rd Raman order and Relations 2.35 to 2.37 displays the mode energy dependencies. Raman emissions of odd and even orders are linked as shown in Fig. 2.14, and their mode energies are clamped simultaneously [123, 124]. When the first Raman order emission grows, the pump signal energy is clamped. When the second Raman order starts, the first order is clamped and the pump signal power increases. Finally, when the third order is observed, the second order and the pump signal stop increasing as the first order grows again.

The total power of the 3rd order emission P_{S3} is given by

$$P_{S3}=|s_{S3}(t)|^2+|s_{-S3}(t)|^2=\frac{|a_{s3}(t)|^2+|a_{-s3}(t)|^2}{\tau_{s3,c}} \tag{2.38}$$

$$=\frac{1}{\tau_{s3,c}}\left(\frac{\omega_{s1}\omega_{s3}}{\omega_p\omega_{s2}}\frac{g_{R2}}{g_{R1}g_{R3}}\right)\left(\frac{1}{2\tau_p}+\frac{1}{2\tau_{s2}}\frac{\omega_p}{\omega_{s1}}\frac{g_{R1}}{g_{R2}}\right)\left[\sqrt{\frac{P_{in}}{P_{in,th}^{\Delta_L=0}}-\Delta_L^2\left(\frac{1}{2\tau_p}+\frac{1}{2\tau_{s2}}\frac{\omega_p}{\omega_{s1}}\frac{g_{R1}}{g_{R2}}\right)^{-2}}-1\right]$$

where

$$P_{in,th}^{\Delta_L=0}=\tau_{p,c}\left(\frac{1}{2\tau_p}+\frac{1}{2\tau_{s2}}\frac{\omega_p}{\omega_{s1}}\frac{g_{R1}}{g_{R2}}\right)^2\left(\frac{1}{2\tau_{s1}g_{R1}}+\frac{1}{2\tau_{s3}}\frac{\omega_{s1}}{\omega_{s2}}\frac{g_{R2}}{g_{R1}g_{R3}}\right) \tag{2.39}$$

$$P_{in,th}=\left[1+\Delta_L^2\left(\frac{1}{2\tau_p}+\frac{1}{2\tau_{s2}}\frac{\omega_p}{\omega_{s1}}\frac{g_{R1}}{g_{R2}}\right)^{-2}\right]P_{in,th}^{\Delta_L=0}$$

We also find the total power of the 1st and 2nd order using Eq. 2.35 and 2.34 respectively :

$$P_{S1}=\frac{|a_{s1}(t)|^2+|a_{-s1}(t)|^2}{\tau_{s1,c}}=\frac{1}{\tau_{s1,c}}\left(\frac{1}{2\tau_{s2}g_{R2}}+\frac{\omega_{s2}}{\omega_{s3}}\frac{g_{R3}}{g_{R2}}\tau_{s3,c}P_{S3}\right) \tag{2.40}$$

$$P_{S2}=\frac{|a_{s2}(t)|^2+|a_{-s2}(t)|^2}{\tau_{s2,c}}=\frac{1}{2\tau_{s2,c}\tau_{s3}g_{R3}} \tag{2.41}$$

showing that P_{S1} grows with P_{S3} while P_{S2} is clamped.

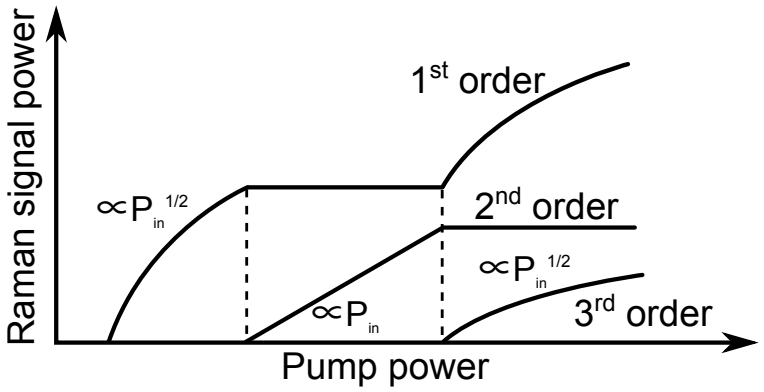

Figure 2.14 : Schematic of the first three Raman order evolution.

Single pump & 2 Raman orders

The simpler case, limited to two Raman orders, is obtained by setting $a_{s3}(t) = 0$ and $a_{-s3}(t) = 0$ in Eq. 2.33 and 2.35.

The resulting total power of the 2nd order emission in CW regime, P_{S2}, is

$$P_{S2} = \frac{|a_{s2}(t)|^2 + |a_{-s2}(t)|^2}{\tau_{s2,c}} \tag{2.42}$$
$$= \frac{1}{\tau_{s2,c}\tau_{p,c}} \frac{\omega_{s2}}{\omega_{s1}} \frac{g_{R1}}{g_{R2}} \frac{1}{\left[\left(\frac{1}{2\tau_p} + \frac{1}{2\tau_{s2}} \frac{\omega_p}{\omega_{s1}} \frac{g_{R1}}{g_{R2}}\right)^2 + \Delta_L^2\right]} \left(P_{in} - \frac{\tau_{p,c}}{2\tau_{s1} g_{R1}} \left[\left(\frac{1}{2\tau_p} + \frac{1}{2\tau_{s2}} \frac{\omega_p}{\omega_{s1}} \frac{g_{R1}}{g_{R2}}\right)^2 + \Delta_L^2\right]\right)$$

while P_{S1} is clamped to

$$P_{S1} = \frac{|a_{s1}(t)|^2 + |a_{-s1}(t)|^2}{\tau_{s1,c}} = \frac{1}{2\tau_{s1,c}\tau_{s2} g_{R2}}. \tag{2.43}$$

Relation 2.42 shows that, for a fixed Δ_L, the 2nd order Raman emission is proportional to the input pump power P_{in}, as shown in Fig. 2.14.

2.6 Quasi-two level laser modeling

Many rare-earth dopants are used for laser applications. In their trivalent forms, optical transitions of rare-earth ions such as Er^{3+} or Tm^{3+} happen between $4f$ levels at near-IR and mid-IR frequencies. Lower level electrons ($5s$ and $5p$) shields the $4f$ electrons from its host material electronic and phonon interactions [246], meaning that host material only changes the ions absorption and emission properties slightly. Figure 2.15 shows energy levels of Er^{3+} and Tm^{3+} that are typically used for near-IR emission. Electrons from the lowest levels are first excited to a higher level. Fast non radiative decay takes place within the upper level manifold before the electron goes back to the ground state. Each level are Stark-split through ions-lattice interactions. In the case of the thulium ions, this Stark-splitting allows the signal amplification at a wavelength of 1800 nm with a pump at 1550-1600 nm between ${}^3F_4 \leftrightarrow {}^3H_6$ levels. This is similar to the transition between the ${}^4I_{13/2} \leftrightarrow {}^4I_{15/2}$ levels of erbium ions with a pump wavelength of 1480 nm.

To achieve population inversion for lasing behavior, the transition rate from levels $1 \rightarrow 2$ has to equal the transition rate from $2 \rightarrow 1$. The rate of these transitions in presence of optical signals is related to the signal intensities (number of photons) and to the ions absorption

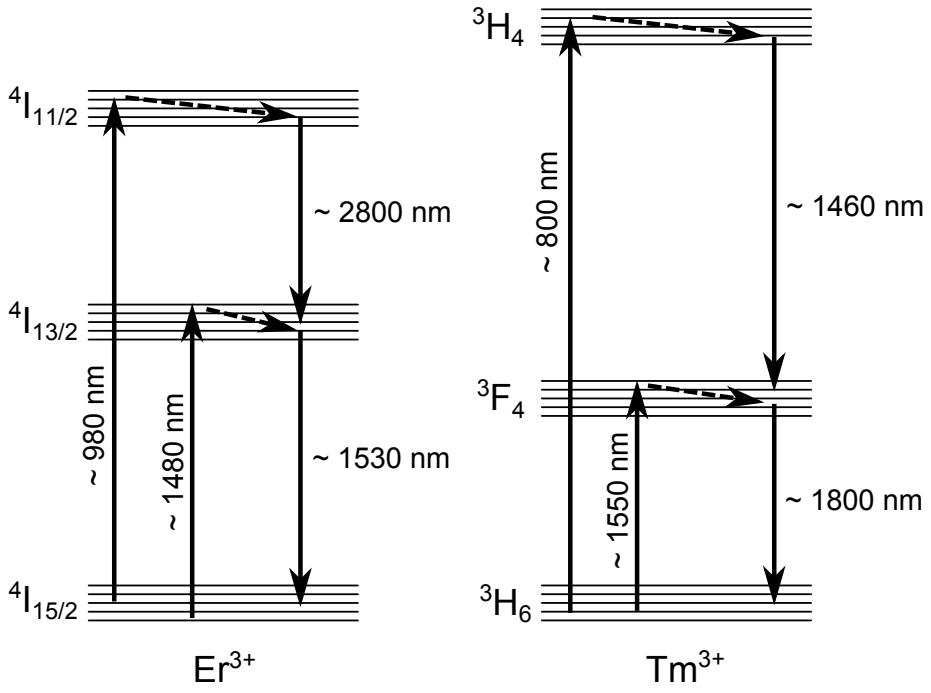

Figure 2.15 : Typical energy level path for Er^{3+} and Tm^{3+} ions. Lines and dashed lines express radiative and non radiative decays.

and emission effective cross sections[1] $\sigma_{a,e}(\omega)$ which depend, among others, on the signal frequencies. The ${}^3F_4 \leftrightarrow {}^3H_6$ transition of thulium ions can be represented as a quasi two-level system because of the fast non radiative decay in the ${}^3F_4$ manifold.

A simplified two-level rate equations for thulium-doped optical fibers are expressed as [247]

$$\frac{dN_2(\mathbf{r},t)}{dt} = \frac{I_p}{\hbar\omega_p}\left(\sigma_{ap}N_1(\mathbf{r},t) - \sigma_{ep}N_2(\mathbf{r},t)\right) + \frac{I_s}{\hbar\omega_s}\left(\sigma_{as}N_1(\mathbf{r},t) - \sigma_{es}N_2(\mathbf{r},t)\right) - \frac{N_2(\mathbf{r})}{\tau_{Tm}} \tag{2.44}$$

$$\text{with } N_T(\mathbf{r}) = N_1(\mathbf{r}) + N_2(\mathbf{r}), \tag{2.45}$$

$$\frac{dP_p(z,t)}{dz} = \sigma_{ep}\int_A I_p(\rho,\theta,t)N_2(\mathbf{r},t)dA - \sigma_{ap}\int_A I_p(\rho,\theta,t)N_1(\mathbf{r},t)dA, \tag{2.46}$$

$$\frac{dP_s(z,t)}{dz} = \sigma_{es}\int_A I_s(\rho,\theta,t)N_2(\mathbf{r},t)dA - \sigma_{as}\int_A I_s(\rho,\theta,t)N_1(\mathbf{r},t)dA. \tag{2.47}$$

N_1 and N_2 are the ions density (ions/m^3) in the ground and upper levels respectively at a position $\mathbf{r}$. The total ions density N_T is fixed and is considered to be constant in the cavity, $N_T(\mathbf{r}) \to N_T$. The amplified spontaneous emission noise is set to zero for simplicity, as spontaneously emitted photons with frequencies $\omega \neq \omega_s$ do not propagate for long in the cavity. τ_{Tm} is the decay time of the spontaneous emission of the thulium ${}^3F_4 \to {}^3H_6$ transition and is related to the ions concentration [248].

The rate equations that rule over the laser dynamics in fibers are not optimized for WGM microcavities [249], and need to be modified to take into account mode overlap which is not always the case for WGM laser models [40].

To solve Eq. 2.45 to 2.47, $N_2(\mathbf{r},t)$ distribution has to be known. Unfortunately, it depends on the mode field distributions, the pump power, and the signal power. To deal with this issue, we approximate N_2 as

$$N_2(\rho,\theta,t) \to N_2^{max}\frac{I_p(\rho,\theta,t)}{I_p^{max}}$$

where N_2^{max} is the N_2 value at the spatial position where the pump intensity I_p is maximum. Therefore, $N_2(\rho,\theta,t)$ follows the pump field distribution. This is valid for a low signal power regime, for example near lasing threshold, where the signal field distribution slightly modifies $N_2(\mathbf{r},t)$ distribution.

Following Section B.5 derivation, Relations 2.45 to 2.47 can be adapted to WGM microcavities coupled-modes equations formalism. For the microsphere TE solutions of Section B.3, no

1. Effective cross sections account for the transition between multiple Stark-split levels

modal coupling, and no perturbation loss, we have

$$\frac{dN_2^{max}}{dt}A_p|a_p(t)|^2\frac{B_p}{C^{max}} = \tag{2.48}$$
$$N_T\left[\frac{\sigma_{ap}}{\hbar\omega_p}A_p|a_p|^2B_p+\frac{\sigma_{as}}{\hbar\omega_s}A_s|a_s|^2B_s\right]-\frac{N_2^{max}}{\tau_{Tm}}\frac{B_p}{C^{max}}-\frac{(\sigma_{ep}+\sigma_{ap})}{\hbar\omega_p}A_p|a_p|^2N_2^{max}\frac{B_{pp}}{C^{max}}$$
$$-\frac{(\sigma_{es}+\sigma_{as})}{\hbar\omega_s}A_s|a_s|^2N_2^{max}\frac{B_{ps}}{C^{max}}$$
$$\frac{da_p}{dt} = g_{Tm}^{(p)}a_p(t)-\frac{1}{2\tau_p}a_p(t)+i(\omega_L-\omega_p)a_p(t)+i\kappa_{pL}s_L(z_0,t) \tag{2.49}$$
$$\frac{da_s}{dt} = g_{Tm}^{(s)}a_s(t)-\frac{1}{2\tau_s}a_s(t) \tag{2.50}$$

with

$$g_{Tm}^{(p)} = \frac{\omega_p}{2m_p}\left[(\sigma_{ep}+\sigma_{ap})N_2^{max}\frac{B_{pp}}{B_p'C^{max}}-\sigma_{ap}N_T\frac{B_p}{B_p'}\right]$$
$$g_{Tm}^{(s)} = \frac{\omega_s}{2m_s}\left[(\sigma_{es}+\sigma_{as})N_2^{max}\frac{B_{ps}}{B_s'C^{max}}-\sigma_{as}N_T\frac{B_s}{B_s'}\right]$$
$$A_{p/s} = \frac{m_{p/s}}{2\omega_{p/s}\mu_0N_{p/s}},\ C^{max} = \frac{|e_{p/s,\theta}^{max}(t)|^2}{(\rho\sin\theta)|_{max}},$$
$$B_{p/s} = \int_A\frac{|e_{p/s,\theta}(\rho,\theta,t)|^2}{\rho\sin\theta}\rho dA,\ B_{p/s}' = \int_A\frac{|e_{p/s,\theta}(\rho,\theta,t)|^2}{\rho\sin\theta}dA$$
$$B_{pp} = \int_A\frac{|e_{p,\theta}(\rho,\theta,t)|^4}{\rho^2\sin^2\theta}\rho dA \text{ and } B_{ps} = \int_A\frac{|e_{p,\theta}(\rho,\theta,t)|^2|e_{s,\theta}(\rho,\theta,t)|^2}{\rho^2\sin^2\theta}\rho dA$$

where $e_{p/s,\theta}$ are the e_θ components of the pump and signal fields respectively. $|e_{p/s,\rho}|^2$ are used for TM modes.

Equations 2.48 to 2.50 can be solved for steady-state conditions. In a low pump power regime, the pump rate is not large enough and electrons in the upper energy levels have time to return to the lower levels through spontaneous emission. Having $N_2 \to 0$, Relation 2.49 changes to

$$\begin{aligned}\frac{da_p}{dt} &= -\frac{\omega_p}{2m_p}\sigma_{ap}N_T\frac{B_p}{B_p'}a_p(t)-\frac{1}{2\tau_p}a_p(t)+i(\omega_L-\omega_p)a_p(t)+i\kappa_{pL}s_L(z_0,t)\\ &= -\frac{1}{2\tau_{p,Tm}}a_p(t)-\frac{1}{2\tau_p}a_p(t)+i(\omega_L-\omega_p)a_p(t)+i\kappa_{pL}s_L(z_0,t)\\ \Rightarrow Q_{p,Tm} &= \omega_p\tau_{p,Tm} = \frac{m_p}{\sigma_{ap}N_T}\frac{B_p'}{B_p}\end{aligned} \tag{2.51}$$

where $Q_{p,Tm}$ is the Q-factor contribution due ions absorption at low pump power.

When N_2 is not negligible, N_2^{max} value is determined by the pump and signal mode energies

$|a_p|^2$ and $|a_s|^2$, and is given by Relation 2.48 :

$$N_2^{max} = N_T C^{max} \frac{\left[\frac{\sigma_{ap}}{\hbar\omega_p} A_p |a_p|^2 B_p + \frac{\sigma_{as}}{\hbar\omega_s} A_s |a_s|^2 B_s\right]}{\frac{B_p}{\tau_{Tm}} - \frac{(\sigma_{ep}+\sigma_{ap})}{\hbar\omega_p} A_p |a_p|^2 B_{pp} - \frac{(\sigma_{es}+\sigma_{as})}{\hbar\omega_s} A_s |a_s|^2 B_{ps}}. \tag{2.52}$$

The threshold conditions for SRS signal emission are given by Relation 2.50, fixing $N_2^{max} \to N_{2,th}^{max}$ and $g_{Tm}^{(p)} \to g_{Tm,th}^{(p)}$,

$$\begin{aligned} g_{Tm,th}^{(s)} &= \frac{1}{2\tau_s} \\ \Rightarrow N_{2,th}^{max} &= \frac{\frac{m_s B_s'}{\omega_s \tau_s} + \sigma_{as} N_T B_s}{(\sigma_{es}+\sigma_{as}) B_{ps}} C^{max} \qquad (2.53) \\ \Rightarrow g_{Tm,th}^{(p)} &= -\frac{1}{2\tau_s} \frac{m_s \omega_p}{m_p \omega_s} \frac{(\sigma_{ep}+\sigma_{ap})}{(\sigma_{es}+\sigma_{as})} \frac{B_{pp} B_s'}{B_{ps} B_p'} \left(\frac{N_T \omega_s \tau_s}{m_s B_s'} \left[\frac{B_p B_{ps}}{B_{pp}} \sigma_{ap} \frac{(\sigma_{es}+\sigma_{as})}{(\sigma_{ep}+\sigma_{ap})} - \sigma_{as} B_s \right] - 1 \right). \qquad (2.54) \end{aligned}$$

Putting 2.52 equals to 2.53, we get the relation between the pump and signal mode energies, $|a_p|^2$ and $|a_s|^2$,

$$|a_s(t)|^2 = 2\tau_s \frac{m_p^2}{m_s^2} \frac{\omega_s^3}{\omega_p^3} \frac{B_p'}{B_s'} \frac{N_s}{N_p} (-g_{Tm,th}^{(p)}) |a_p(t)|^2 - \frac{2}{\tau_{Tm}} \frac{\hbar\omega_s^2 \mu_0 N_s}{m_s(\sigma_{es}+\sigma_{as})} \frac{B_p}{B_{ps}} \left(\frac{N_T \omega_s \tau_s}{m_s} \frac{B_s}{B_s'} \sigma_{as} + 1 \right).$$

The output signal power $P_{S,out}(t) = |s_S(z_1,t)|^2$ is linked to the input pump power $P_{in} = |s_L(z_0,t)|^2$ using Relation 2.49 in steady-state regime and $|\kappa_{pL}|^2 \approx 1/\tau_{p,c}$:

$$\begin{aligned} P_{S,out}(t) &= \frac{|a_s(t)|^2}{\tau_{s,c}} \\ &= 2\frac{\tau_s}{\tau_{s,c}} \frac{m_p^2}{m_s^2} \frac{\omega_s^3}{\omega_p^3} \frac{B_p'}{B_s'} \frac{N_s}{N_p} \frac{P_{L,in}}{\tau_{p,c}} \frac{-g_{Tm,th}^{(p)}}{(\omega_L - \omega_p)^2 + (\frac{1}{2\tau_p} - g_{Tm,th}^{(p)})^2} \\ &\quad - \frac{2}{\tau_{s,c}\tau_{Tm}} \frac{\hbar\omega_s^2 \mu_0 N_s}{m_s(\sigma_{es}+\sigma_{as})} \frac{B_p}{B_{ps}} \left(\frac{N_T \omega_s \tau_s}{m_s} \frac{B_s}{B_s'} \sigma_{as} + 1 \right). \end{aligned} \tag{2.55}$$

Similarly to Section 2.5.1, we can remove the laser detuning dependency by introducing the coupled pump power

$$P_{coup}(t) = P_{in}(t)(1-T_p) = P_{in}(t) \frac{2}{\tau_{p,c}} \frac{\frac{1}{2\tau_{p,0}} - g_{Tm,th}^{(p)}}{(\omega_L - \omega_p)^2 + (\frac{1}{2\tau_p} - g_{Tm,th}^{(p)})^2},$$

giving

$$P_{S,out}(t) = \frac{\tau_s}{\tau_{s,c}} \frac{m_p^2}{m_s^2} \frac{\omega_s^3}{\omega_p^3} \frac{B'_p}{B'_s} \frac{N_s}{N_p} \frac{-g^{(p)}_{Tm,th}}{\left(\frac{1}{2\tau_{p,0}} - g^{(p)}_{Tm,th}\right)} P_{coup}(t) \\ - \frac{2}{\tau_{s,c}\tau_{Tm}} \frac{\hbar\omega_s^2\mu_0 N_s}{m_s(\sigma_{es}+\sigma_{as})} \frac{B_p}{B_{ps}} \left(\frac{N_T\omega_s\tau_s}{m_s} \frac{B_s}{B'_s}\sigma_{as} + 1 \right). \tag{2.56}$$

The output signal power is proportional to both $P_{L,in}$ and P_{coup}.

CHAPTER 3 EXPERIMENTATION

3.1 Microspheres fabrication

The fabrication of As_2S_3 and tellurite glass microspheres is based on a CO_2 laser melting method and are made from high purity optical fibers. This technique was successfully used to produce silica spheres with large Q-factors [250], but was not used for chalcogenide glass resonators yet. Previous melting methods rely on heating plates to transform an optical fiber into a tapered tip and to melt this tip to form a sphere [154, 220]. The resulting Q-factors $< 2 \times 10^5$ indicate that these methods could be improved. Glass contamination, slow melting time and poor spherical shape may be to blame. On the contrary, laser melting offers many benefits : fast forming time < 250 ms, no material contact during the fabrication, and homogeneous heat distribution resulting from the volume absorption of the laser light.

The fabrication steps are depicted in Fig. 3.1. First, the polymer coating of a high purity optical fiber is removed and the fiber is cleaned using isopropanol and acetone. Remaining dust particles or polymer debris could stick on the melting glass or diffuse into it and cause undesirable optical losses. The fiber is illuminated by a high power CO_2 laser with a wavelength of 10.6 μm (Fig. 3.1(a)). For an As_2S_3 fiber with a diameter of 200 μm, a laser intensity of ~ 50 MW/m^2 over a 300 μm beam waist at the fiber level is necessary to slowly melt and pull the fiber into a tapered fiber. To continuously pull the fiber, the laser power needs to be increased as the fiber diameter decreases, since the absorbing glass volume is smaller. When the fiber diameter reaches 10-20 μm, it usually breaks into a narrow tip (Fig. 3.1(b)). At this point, the laser intensity has to be $\sim 400 - 500$ MW/m^2 to reflow the tip into a microsphere. The melted glass naturally forms a spherical shape through surface tension (Fig. 3.1(c)). This process leaves a smooth surface that minimizes scattering losses. The sphere diameter can be increased using successive laser exposures.

Images of As_2S_3 and tellurite microspheres obtained with the laser reflow technique are shown in Fig. 3.2. Microspheres with diameters between 20 μm and 400 μm were fabricated using this method. The visible images of Fig. 3.2(a) and 3.2(b) show the good symmetry and eccentricity of the As_2S_3 spheres. The tellurite spheres, as displayed in Fig. 3.2(d), share the same properties. The scanning electron microscope image of Fig. 3.2(c) shows the smoothness and cleanness of the sphere's surface. All these characteristics are mandatory to achieve large Q-factors.

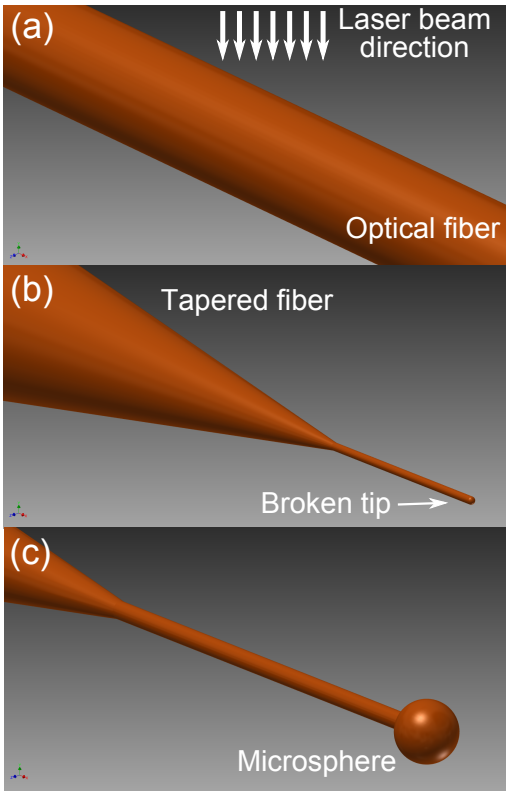

Figure 3.1 : Microsphere fabrication steps : (a) A high purity optical fiber is placed under the CO_2 laser illumination. (b) The fiber is heated by the laser beam and is pulled into a tapered fiber until it breaks. A narrow tip is left. (c) A microsphere is obtained by heating the fiber tip. The surface tension of the molten glass naturally forms a spherical shape.

3.1.1 Laser melting setup

To execute the previous fabrication steps, the laser setup has to be able to pull an optical fiber into a tapered fiber and to produce spheres. Our setup is composed of two main parts : the fiber pulling system and the focusing region.

The focusing region shown in Fig. 3.3(a) is designed to monitor an object while it is illuminated by the laser beam. The latter enters at the top of the setup, passes through a beamsplitter and is focused by the bottom lens. Both the beamsplitter and the concave lens are made of ZnSe glass, transparent at a wavelength of 10.6 μm. An object placed on the 3-axis stage is imaged using visible optics and a camera. The beamsplitter is coated to obtain a reflection coefficient of 99 % in the visible spectrum and a transmission coefficient of 99 % at 10.6 μm for an incident angle of 45°. The laser power can be modified manually and it is stabilized by an internal control loop. A CW or pulsed illumination is obtained using a shutter unit. A gate time of 250 ms was used during this thesis based on its practicality. A object in focus on

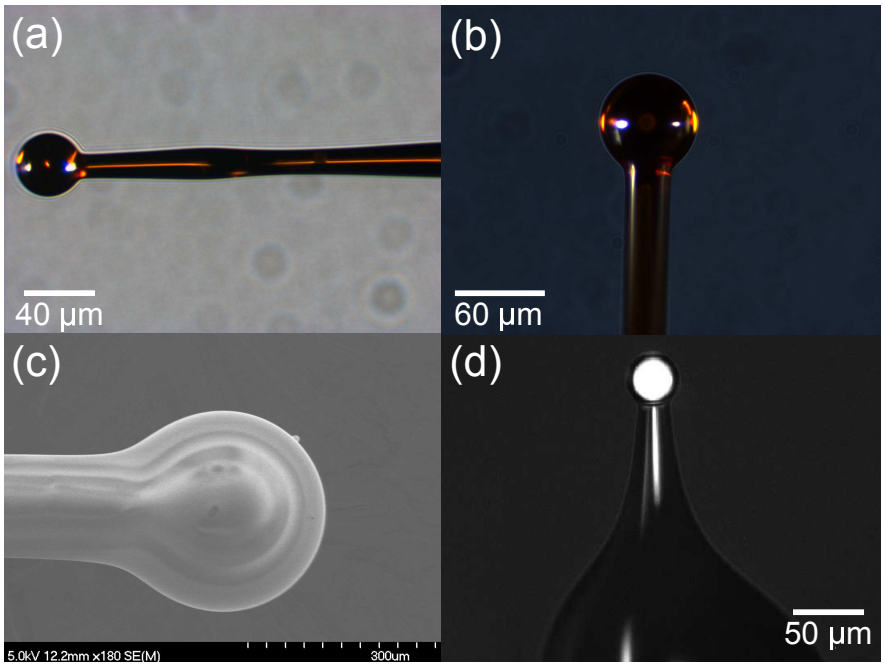

Figure 3.2 : Typical microspheres produced using the laser reflow technique - (a) and (b) Images of As_2S_3 spheres. (c) Scanning electron microscope image of an As_2S_3 sphere. (d) Visible image of a tellurite sphere.

the monitoring camera insures a reproducible laser intensity over time at the specific imaging height.

A setup photograph is presented in Fig. 3.3(b). The red LED ring light illuminates the imaging region when the outer protective box is closed. Nitrogen is sent to the imaging region to reduce its oxygen content. It is intend to minimize oxidation during the melting processes which could induce optical losses. A vacuum vent tube is also used to remove vapors produced during the glass reflow. These vapors could condensate back on the sphere or other optics elements of the setup and deteriorate them.

The fiber pulling system is placed under the laser beam as shown in Fig. 3.3(a). Figures 3.4(a) presents its components. It is made of four aluminum blocks, two of them clamp an optical fiber on one side while another one can be moved on two transversal rods. The moving block is pulled using a rope linked to weights. It keeps the optical fiber stretched before laser exposure. The drilled fourth block holds the rods and keeps the pulling rope parallel to the rods, but is not clamped to the optical fiber. Grooves are carved in the blocks to keep the fiber straight at all time.

The pulling process is shown in Fig. 3.4(b)-(e). Under laser illumination, the weights pull on the block and the fiber starts its tapering process. With a constant pulling force, the tapered

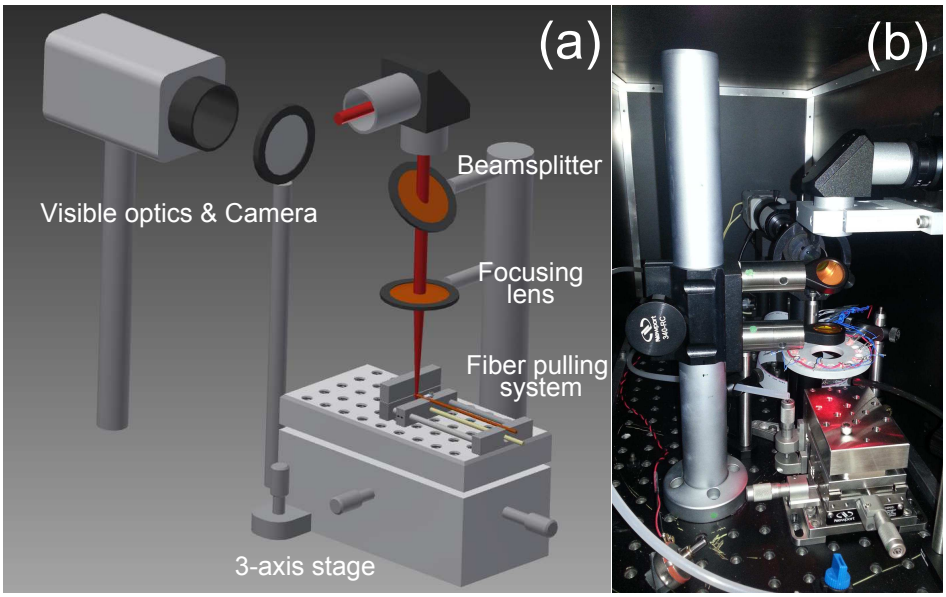

Figure 3.3 : (a) Laser setup - The CO_2 laser beam, depicted in a false red color, is focused on a fiber pulling system positioned by a 3-axis stage. A beamsplitter allows the simultaneous monitoring of the focusing spot and the target using visible optics and a camera. (b) Photograph of the setup. Additional components are present : red LED ring light for visible imaging, a nitrogen flow (white tube) pointing toward the focused region, and a vacuum vent (black tube) to extract vapors from the melting.

fiber diameter can be brought to 10-20 μm before it breaks, leaving two glass tips on each side of the pulling system. These tips are directly heated afterward to form spheres as shown in Fig. 3.4(f).

For a glass tip size of few microns, the laser illumination with a beam waist of 300 μm can be considered homogeneous and the heat transfer is quasi instantaneous. This results in a homogeneous heating of the tip and leads to a symmetric sphere shape. Experience showed that successive laser exposures produce larger spheres, but of lesser quality. This phenomenon suggests that contaminants and oxidation incorporate the sphere each time it is reflowed. Large sphere melting is also less homogeneous, resulting in larger asymmetrical spheres.

3.1.2 Raman spectroscopy on As_2S_3 melted glass

The linear and nonlinear optical properties of glasses are given by their structural composition and their impurity content. The latter can be minimized by working in a controlled and clean environment. The former is affected by the physical treatment the glass undergoes such as heat. The multiple heating and melting steps of the laser reflow technique may impact the

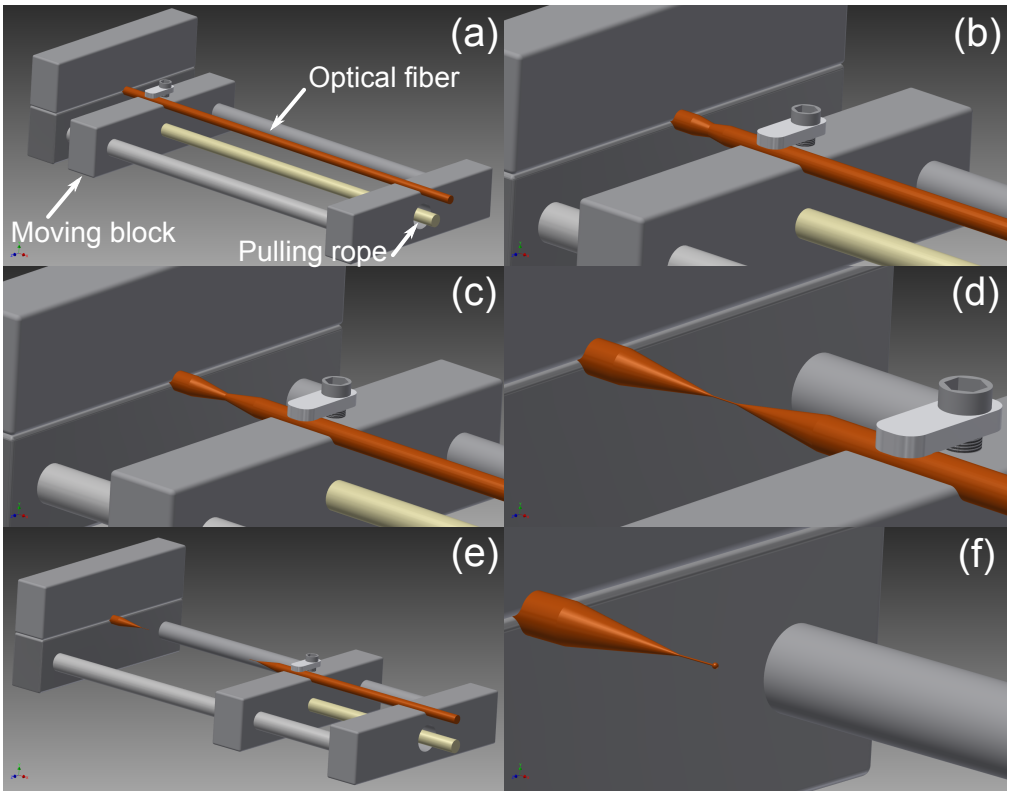

Figure 3.4 : Fiber pulling and tapering system used in the laser setup. (a) An optical fiber is clamped at two locations : a fixed block on the left side and a moving block in the middle. The moving block is linked to weights with a pulling rope. (b) While the laser beam heats the fiber, it is pulled and a tapered shape forms. (c) The tapered shape can be reduced to the required diameter. (d) A narrow glass filament eventually forms. (e) The tapered fiber finally breaks into a glass tip. (f) The glass tip is heated again to form a sphere.

structural composition of the optical fiber glass. Furthermore, As_2S_3 glass is characterized by a relatively low glass transition temperature $T_g \sim 180 - 215°C$ [147, 178, 191]. Crystallization or detrimental group formation during the fabrication steps could impair the glass properties. For example, the presence of As_4S_4 groups, observed in As_2S_3 thin films [251], is suspected to increase the photosensitivity of the glass, even at telecommunication wavelengths [188].

To verify that the glass structure stays amorphous during the pulling and melting processes, we performed Raman spectroscopy measurements on three locations : the unaffected fiber, the tapered fiber and the microsphere itself. Raman spectroscopy probes the material vibration energies of its constituent bonds. Sharp peaks indicate the presence of single vibration modes and suggest a crystalline layout. Broader peaks can be attributed to groups of vibration modes usually found in amorphous materials. Results are presented in Fig. 3.5, the spectra are normalized and are offset vertically for clarity. The main broad peak is located at a Raman

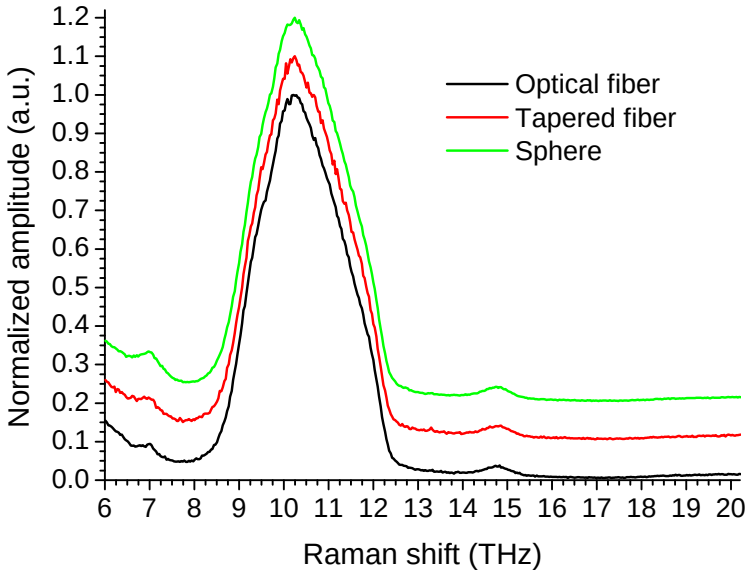

Figure 3.5 : Raman spectra of As_2S_3 glass for three locations : the optical fiber, the tapered fiber part and the microsphere. The spectra are normalized and are offset vertically for clarity.

shift of 10.3 THz and the spectra are similar to other work measurements [184, 191, 251]. The absence of sharp peaks indicates that the glass structure stays amorphous during the fabrication steps. Two factors mainly contribute to these results. First, thanks to the high purity of the glass, crystallization centers such as contaminants are reduced in number. Second, the melting and cooling times are below 200 ms and crystal formation is thus limited.

More measurements were made near the optical mode area on an As_2S_3 sphere and are shown in Fig. 3.6. The spectra were taken along a line perpendicular to the equatorial region of the sphere, separated by a distance of 0.5 μm. The spectra in red are taken in the optical mode region. Again, every sphere regions favorably share the same amorphous structure.

Raman spectroscopy probes the material surface over few microns deep only. Fortunately, the optical modes also propagate few microns from the surface as shown in Fig. 2.8 and 2.9. Consequently, it is safe to say that the optical modes occupy the amorphous glass region.

3.1.3 Tapered silica fiber fabrication

Many guiding structures are used to couple light in and out of WGM microcavities : mainly integrated waveguides, prisms, and tapered optical fibers. The latter is well suited for microspheres as it is highly compatible with common fiber optic components and provides low loss monomodal coupling. This last properties is sometimes called coupling ideality [252] and it defines how well a cavity mode couples uniquely to a single waveguide mode.

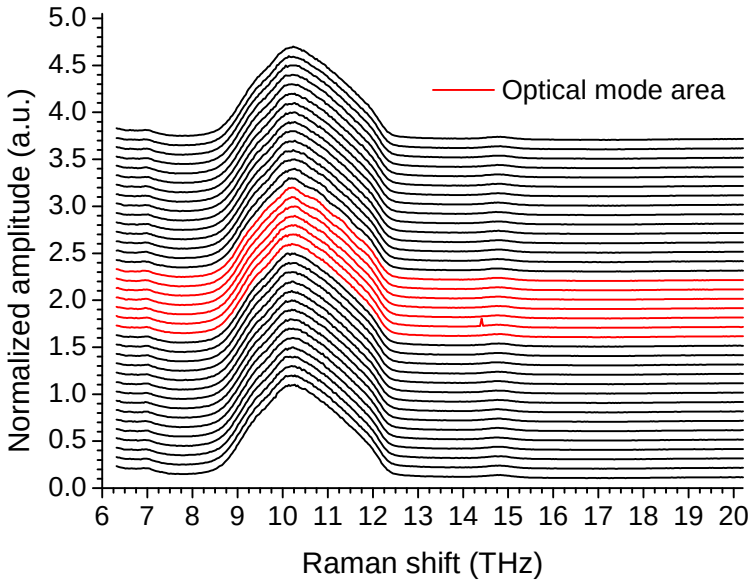

Figure 3.6 : Raman spectroscopy spectra of an As_2S_3 microsphere taken along a line perpendicular to the optical mode area. The spectra locations are separated by 0.5 μm. The optical mode area is denoted by red lines. The spectra are normalized and are offset vertically for clarity.

In this thesis, we used silica tapered fibers made from single mode Corning's SMF-28 optical fibers. With a diameter of $\sim 2\mu$m, silica tapered fibers are simple to make and they are relatively sturdy. They are pulled adiabatically, keeping much of the power into a single mode, and they provide quasi single mode guiding over their entire length. They were made using the facilities of the *Laboratoire des fibres optiques* of *École Polytechnique de Montréal*. The pulling setup is shown in Fig. 3.7. A cleaned optical fiber is clamped on two 1-axis motorized stages. A third 3-axis motorized stage controls the displacement of an oxygen-propane flame. The flame is swept along the fiber while both stages pull the fiber apart resulting in an adiabatic profile. The stages movements are controlled and monitored by a NI LabVIEW program.

3.1.4 Cavity encapsulation

To keep optical losses as low as possible, it is crucial to fabricate and manipulate the microspheres in a clean environment. Trials and errors show that it is difficult to clean microspheres once they have been contaminated by dust particles. Only few micron size contaminants are needed to decrease the Q-factor to $10^3 - 10^4$. An image of a spoiled microsphere is shown in Fig. 3.8. The presence of particles in the mode field, nearby the equator line, increases coupling to radiative modes and modal coupling. Manipulations show that the durability of

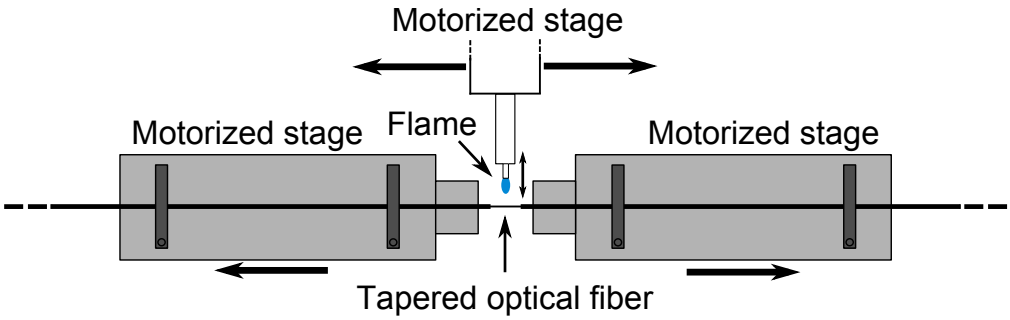

Figure 3.7 : Pulling setup used to fabricate silica tapered optical fiber. A flame is swept along the optical fiber while two motorized stages are pulling it apart.

the spheres decreases after a few hours only in the laboratory environment without a proper cleanroom ventilation system. To obtain similar measurement results over time, the microsphere and the coupled silica tapered fiber have to be protected, mainly from surrounding air flows. To solve this issue, both are encapsulated in a silica glass tube with a fixed coupling position. Figure 3.9(a) presents the assembly parts. The silica tapered fiber is transfered from its pulling setup to two half-rod blocks glued to a bottom half-tube. The tube is closed with the upper half-tube. A small opening on the tube's side allows the positioning of the sphere inside. Once the coupling conditions are optimized, the fiber tip holding the sphere is glued to the tube's side. All the parts are made of silica glass to follow the thermal expansion of the silica tapered fiber. The sphere and the fiber have to be aligned within the micron range to optimize the coupling conditions. Any displacement caused by the thermal expansion of different materials would be critical.

A photograph of the encapsulated system is shown in Fig. 3.9(b). The device is 6 cm long and 5 mm wide. The fixed As_2S_3 microsphere can be seen inside the tube. Using this protection,

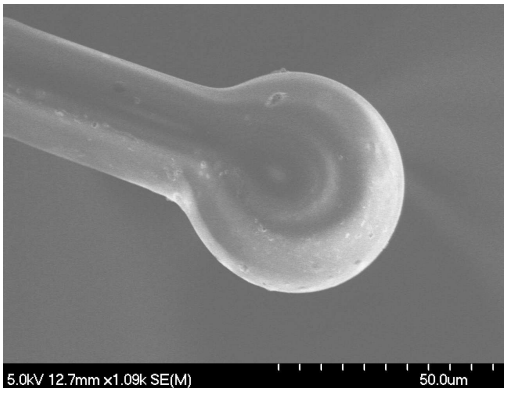

Figure 3.8 : An As_2S_3 microsphere contaminated by dust.

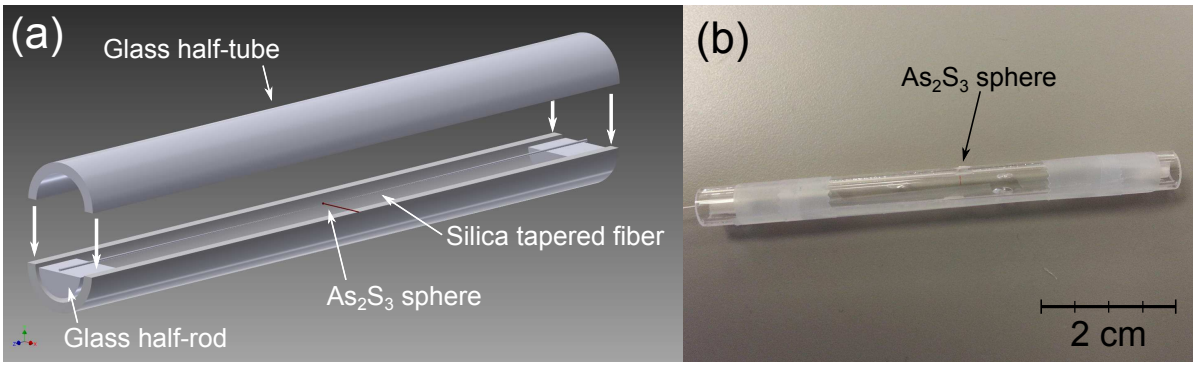

Figure 3.9 : Packaged tapered fiber and microsphere. (a) 3D model of the silica glass tube. The silica tapered fiber is fixed to two glass half-rod blocks. The fiber tip holding the sphere is glued on the half-tube side. (b) Photograph of an encapsulated system.

similar results could be obtained over a long period. For example, cascaded Raman spectra similar to Fig 5.4 were obtained two weeks apart. Furthermore, the sphere quality is not affected by the process as no glue or contaminant touches the sphere. Using this packaging technique, the fragile fiber-sphere system becomes a portable in-line fiber device.

3.2 Linear and nonlinear signals measurements

3.2.1 Transmission measurement setup

The linear characteristics of WGM microcavities are usually measured through their transmission spectra. The simplest setup needed for these measurements is presented in Fig. 3.10 and is composed of five main elements. A tunable laser source (TLS) is used to scan across a specific wavelength range. Its laser linewidth $\sim$ 300 kHz allows measurements of narrow cavity resonances without convolution problem. The polarization controller (PC) optimizes the polarization for the selection of TE or TM cavity modes. The signal passes through the tapered fiber and is coupled to the microsphere via evanescent coupling. The intensity of the transmission signal is measured by a photodiode detector (DET) and is monitored on an oscilloscope (OSC). A trigger signal synchronizes the tunable laser sweep and the oscilloscope monitoring. The time axis becomes the wavelength axis using $\lambda_1 = \lambda_0 + v_{scan}\Delta t$ where λ_0 and λ_1 are the initial and current wavelength positions respectively, Δt is the elapsed time since the trigger signal, and v_{scan} is the laser sweeping speed. The latter is usually kept low $\sim$ 1 nm/s to simulate a CW input signal. The advantage of this simple technique is the achievable resolution only limited by the tunable laser linewidth. The use of a broadband source and an optical spectrum analyzer is limited to the latter's resolution of 0.05 nm, not enough

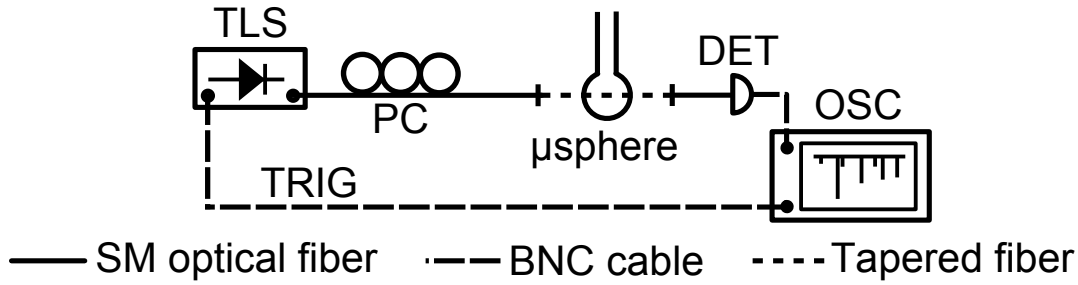

Figure 3.10 : Basic setup for transmission spectra measurements - TLS : Tunable laser source, PC : Polarization controller, DET : Photodiode detector, OSC : Oscilloscope, TRIG : Trigger signal, and SM : Single mode.

for cavity resonance linewidth < 1 pm. Furthermore, the setup contains only optical fiber compatible elements. More complex setups were used during this thesis and are presented in the next chapters, but their data acquisition principle remains the same.

Figure 3.11 presents typical spectra taken with a scanning range of 1 nm for an As_2S_3 sphere with a diameter ~ 30 μm and for three coupling conditions. The input power is kept constant. The waveguide coupling is increased by approaching the silica tapered fiber near the sphere inside its mode fields. The top spectrum shows the lower coupling case. Despite the narrow scanning range, more than a dozen high Q-factor resonances are visible. Those resonances are not successive azimuthal orders as the free spectral range is 10.5 nm for this sphere's size. They are multiple radial modes and possibly polar modes that successfully couple to the waveguide mode. As the coupling level increases, the peak transmission coefficients decrease, a manifestation of a decreasing coupling Q-factor $Q_{j,c}$ based on Relation 2.20. This also means those resonances are in a undercoupled regime $Q_{j,0} < Q_{j,c}$.

The smaller gap between the tapered fiber and the sphere allows more cavity modes to overlap with the waveguide mode. This results in an increasing number of visible resonances in the spectrum. The bottom spectrum is taken when the silica tapered fiber is in contact with the sphere : at the maximal coupling conditions for this configuration. Peaks that were not visible now reach transmission level below 80 %. Other peaks like those located at a wavelength of 1552.08 nm and 1552.82 nm are now deformed, suggesting that they possess the highest Q-factor of the region. The deformation is caused by thermal drifting and will be discussed in Section 3.2.2.

As mentioned earlier, despite the large number of resonances, their individual measurement is not affected by the presence of others, thanks to their narrow linewidth. Typical transmission spectra of single resonances are shown in Fig. 3.12. Lorentzian curve fits in red are in good agreement with the resonance shapes. Following Section 2.3.3 and Relation 2.21, the curve

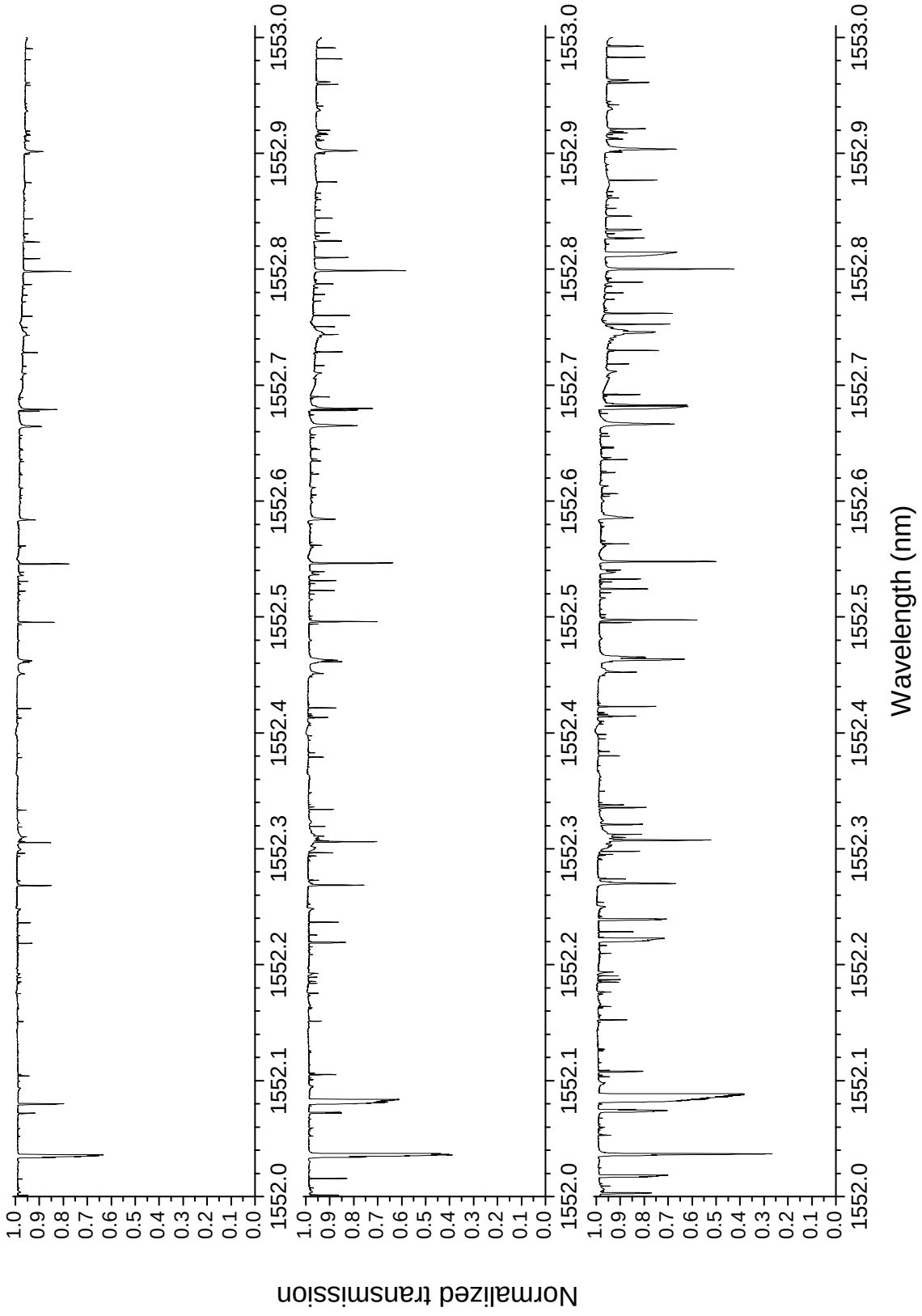

Figure 3.11 : Evolution of transmission spectra taken with an increasing waveguide coupling. The input power is kept constant. Top spectrum has the lowest waveguide coupling. The bottom spectrum has the largest waveguide coupling when the tapered fiber touches the sphere.

full width at half maximum (FWHM) is linked to the resonance's total Q-factor $Q_{j,T}$. The left and right plots present peaks with FWHM of 0.5 pm and 0.22 pm, giving total Q-factors of 3.1×10^6 and 7.0×10^6 respectively at a wavelength of 1550 nm.

The right plot of Fig. 3.12 presents a peak with a transmission near unity. Being in an overcoupled regime, the total Q-factor $Q_{j,T}$ is dominated by the intrinsic losses and its value approaches the intrinsic Q-factor $Q_{j,0}$. Following the lower sign Relation 2.22, its center transmission $T_{j,0}$ of 0.955 leads to $(Q_{j,0}, Q_{j,c}) = (7.08 \times 10^6, 6.2 \times 10^8)$. In comparison, the left resonance Q-factors are $(Q_{j,0}, Q_{j,c}) = (4.2 \times 10^6, 1.2 \times 10^7)$ where $Q_{j,T}$ can no longer be approximated by $Q_{j,0}$. This example also shows the large range of values the coupling Q-factor can take, and how sensitive it can be to coupling condition variations.

The single Lorentzian shapes indicate negligible modal coupling between clockwise and counterclockwise modes. However, the peak splitting is easier to measure when the resonance linewidth (Q-factor) is narrower (larger). Figure 3.13 presents two resonances affected by modal coupling. The red curves based on Relation B.68 are fitted with good agreement. The theoretical model allows the extraction of the resonance characteristics for $\Gamma'_{jj} \neq \mathbf{\Gamma'_{j-j}}$ and $\Gamma'_{jj} = \mathbf{\Gamma'_{j-j}}$. In both cases, the fitted curve agreements are similar with R^2 values above 0.985. The extracted values are shown in Table 3.1. All fits indicate an undercoupled regime with a slightly larger coupling load for the right plot, leading to a smaller peak transmission. The notable difference is the peak separations $\sim 2\Gamma_{j-j}$ of 180 MHz and 400 MHz for the left and right plot respectively, relatively lower and larger than $1/\tau_{j,T}$.

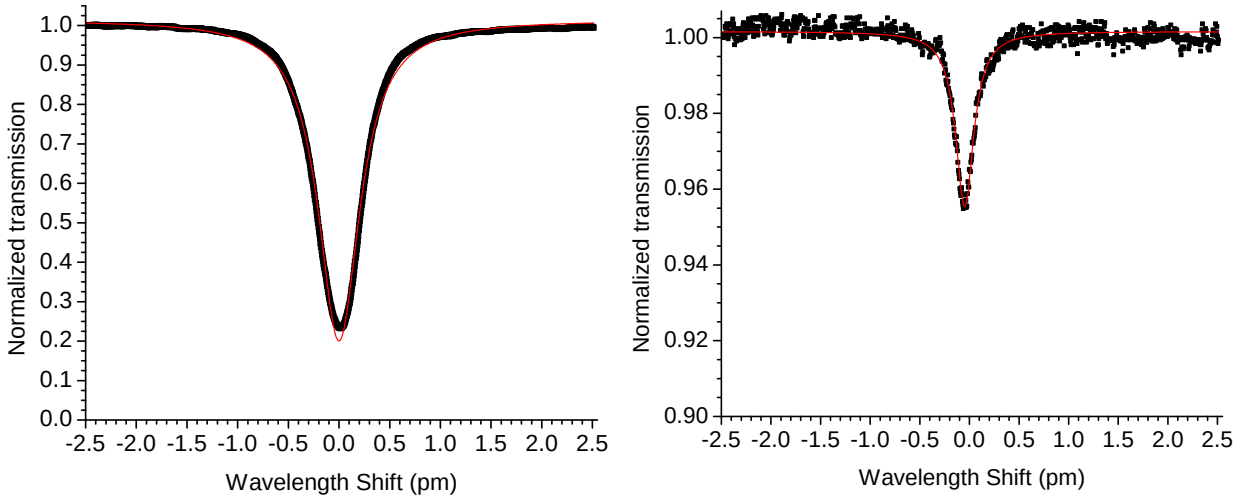

Figure 3.12 : Transmission measurement spectra for two As_2S_3 sphere resonances. Lorentzian curve fits are used in red to extract the resonance FWHM. The resonance total Q-factors are 3.1×10^6 (left) and 7.0×10^6 (right).

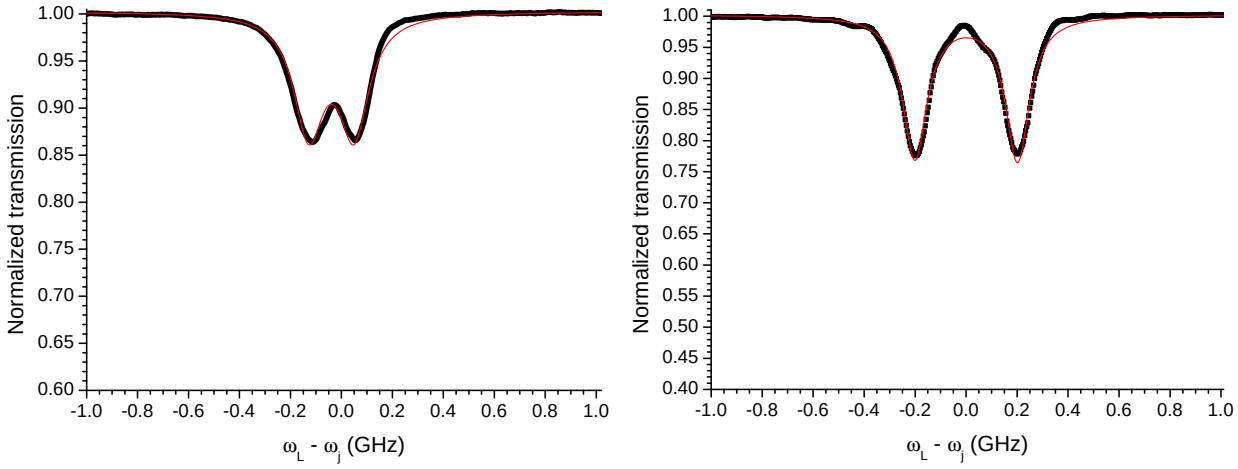

Figure 3.13 : Transmission measurement spectra for two As_2S_3 sphere resonances with notable modal coupling. The fitted double peak curves in red are based on Relation B.68.

Finally, the losses analysis is more tricky and shows the limit of the fitted curve extraction, mainly due to the peak symmetry. Both cases $\Gamma'_{jj} \neq \Gamma'_{j-j}$ and $\Gamma'_{jj} = \Gamma'_{j-j}$ give realistic and similar values. The intrinsic and perturbation losses, represented by $\tau_{j,0}$, Γ'_{jj}, and Γ'_{j-j}, can be modified while the coupling losses remain stable without important curve shape modification. Additional measurements are needed to settle this issue.

Table 3.1 : Extracted linear resonance characteristics of Fig. 3.13.

		Left plot	**Right plot**	**Left plot**	**Right plot**
	Unit	$\boldsymbol{\Gamma'_{jj} \neq \Gamma'_{j-j}}$		$\boldsymbol{\Gamma'_{jj} = \Gamma'_{j-j}}$	
$\tau_{j,c}$	**ns**	108	70.5	108	70.4
$\tau_{j,0}$	**ns**	10.4	19.5	7.7	10.34
$1/\tau_{j,T}$	**MHz**	105	66	140	111
Γ_{jj}	**MHz**	-39.8	0.2	-39.6	0.2
Γ'_{jj}	**MHz**	18.7	24.8	0.6	1.3
Γ_{j-j}	**MHz**	89.4	202	89.6	202
Γ'_{j-j}	**MHz**	0	0.5	0.6	1.3

3.2.2 Thermal drifting

The position of WGM resonances is very sensitive to the environment, especially to variations of thermal origin. Even if the surrounding medium temperature can be stabilized, heating mechanisms that take place inside the cavity can hardly be avoided when the optical power is large enough. Almost every WGM microcavities are affected by the heat generated by the material absorption, leading to thermorefractive variations dn/dT and thermal expansion of the mode region [131]. Both effects increase the optical path and red-shift the cavity resonances. Figure 3.14 shows the main heat transfer paths inside a microsphere. The heat builds up in the mode region due to optical absorption and is transfered to the whole sphere through conduction. The microcavity size limits the heat outflow through convection because the surface area is small. This results in a noticeable temperature increase that affects the transmission spectrum of the cavity.

This phenomenon is particularly important when the transmission spectrum is measured using a tunable laser sweeping toward longer wavelengths, for example using the setup of Fig. 3.10. Typical thermal drifting behavior is shown in Fig. 3.15 for an As_2S_3 sphere. The black, red and green curves are the transmission spectra of the same resonance with an increasing input optical power. The resonance's position is shifted toward longer wavelengths because the thermorefractive coefficient $dn/dT > 0$. The trailing behavior comes from the combination of the simultaneous laser sweeping and the resonance red-shifting : the resonance is dragged with the tunable laser line. Multiple works have studied thermal nonlinearities in WGM microcavities which can be used as an efficient stabilization method or for its bistability

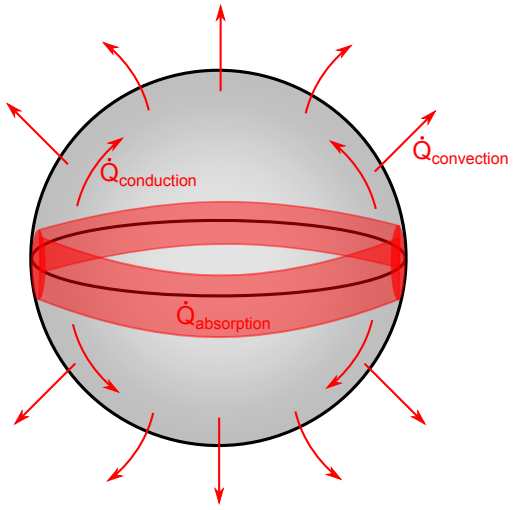

Figure 3.14 : Heat propagation in a microsphere. The optical mode is located on the equatorial line.

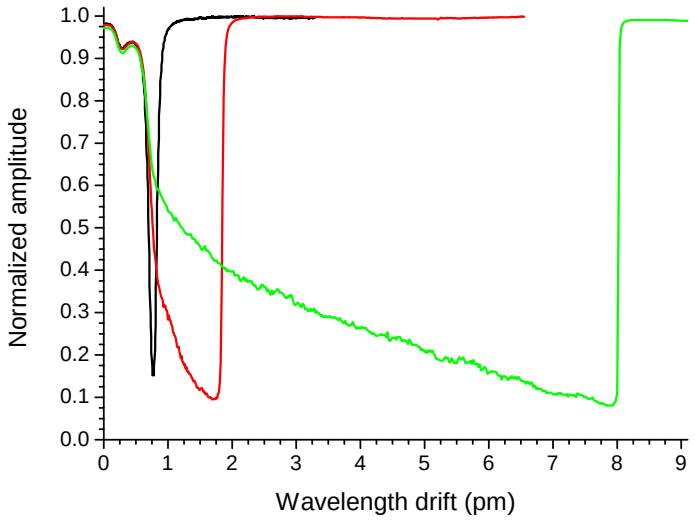

Figure 3.15 : Thermal drifting of a resonance as the tunable laser line is swept toward longer wavelengths for an increasing optical power. The black and green lines represent the lowest and largest power respectively.

behavior [1, 130, 131].

The trail appearance depends on the resonance Q-factor and transmission coefficient, and on the laser tuning speed and its power. It can extend easily to ten or a hundred times the resonance original linewidth. When performing a Q-factor measurement, the input power has to be low enough to not deform the Lorentzian curve. Only 10 μW of input power is sometimes enough to distort the spectrum in the case of an As_2S_3 sphere and a resonance with a $Q \sim 10^7$.

3.2.3 Raman and laser signal measurements through thermal drifting

To measure the Raman or laser signals generated inside the microspheres, one could use a tunable laser emission, tune its wavelength on a resonance and monitor the emitted signal with an optical spectrum analyzer or an optical powermeter. However, this method is difficult to apply. The stable positioning of the laser emission at a precise location inside resonances with sub-pm linewidths has to rely on stabilization techniques. Furthermore, even for a stabilized laser line, the thermal shifting of the resonance pushes it away from the laser line as shown in Fig. 3.16. This results in a varying coupled pump power with an increasing input pump power. Consequently, any signal power measurements as a function of input pump power has to account for this wavelength detuning. Finally, in the case of As_2S_3, thermal shifting happens at power levels below the Raman and laser power threshold values.

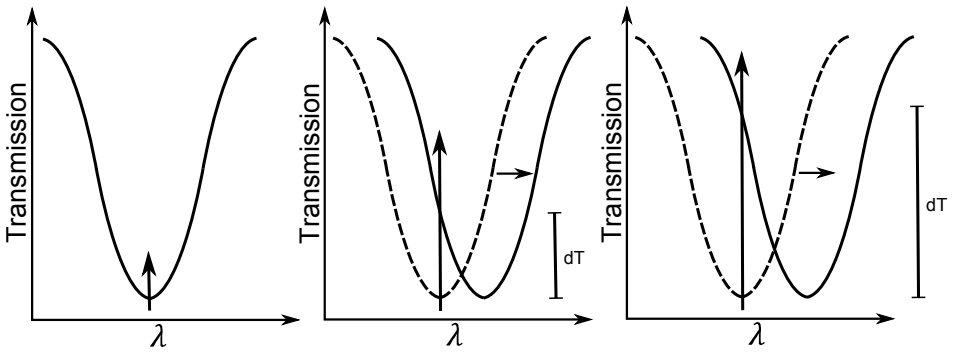

Figure 3.16 : Thermal drifting of a resonance for a fixed laser line with an increasing pump power and transmission shift dT. This effect is particularly important for As_2S_3 WGM microcavities.

To solve this issue, it is easier to use thermal drifting as part of the measurement technique [253]. When the resonance is dragged with the laser line, coupled pump power increases slowly as the laser line moves. Additionally, the input pump power can remain constant. This principle is depicted in Fig. 3.17 left plot. The coupled power in blue is deduced from the output and input power difference $P_{coup} = P_{in} - P_{out} = P_{in}(1 - T_j)$. This method allows scanning over a large range of power values. Furthermore, the pump and generated signals can be recorded simultaneously using a single spectral scan. The theoretical model developed in Sections 2.5 and 2.6 can be directly linked to the measurements, especially to Eq. 2.31 and 2.56.

To measure the generated signals, a setup similar to the transmission measurement setup can be used. It is presented in Fig. 3.18. Only the detection part is modified. A wavelength division multiplexer (WDM) is needed to record the transmitted pump signal and the generated

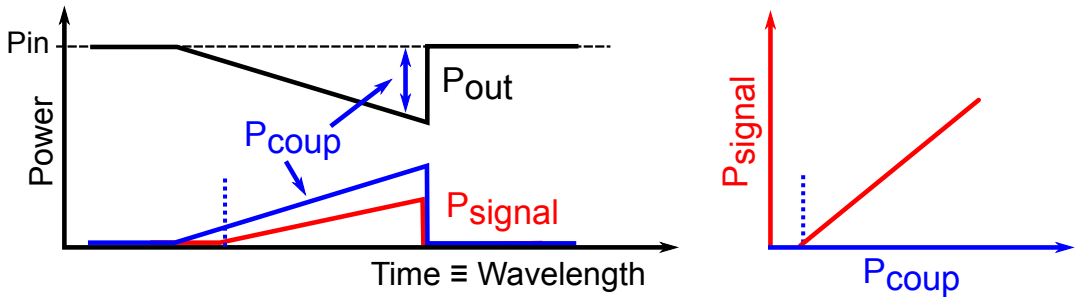

Figure 3.17 : Left plot - Increasing coupled power during thermal drifting. If the coupled power threshold is achieved, the nonlinear or laser signal starts increasing. The constant input power and the threshold are shown as dotted black and blue lines respectively. Right plot - Signal power as a function of the coupled power.

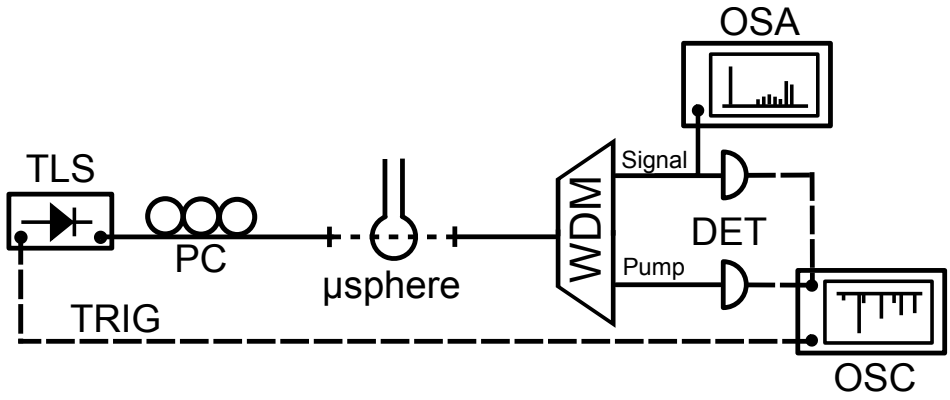

Figure 3.18 : Basic setup for nonlinear and laser measurements - TLS : Tunable laser source, PC : Polarization controller, DET : Photodiode detector, OSC : Oscilloscope, OSA : Optical spectrum analyzer, TRIG : Trigger signal and WDM : Wavelength division multiplexer.

nonlinear signal simultaneously. Using two optical detectors, the measured traces as a function of time will look like the black and red curves of Fig. 3.17 left plot. The threshold curve is plotted by comparing the signal power in red and the coupled power in blue, shown in Fig 3.17 right plot. For Raman emission, the threshold curve slope $dP_S/dP_{in,coup}$ is the internal conversion efficiency as defined by Eq. 2.32.

The setup can be modified further using an optical spectrum analyzer (OSA) to spectrally discriminate multiple emission peaks excited by a single pump resonance. The gain bandwidths from Raman scattering and rare-earth ions are large enough to overlap multiple high Q-factor resonances. Stimulated Raman emission and laser emission start when the threshold conditions are achieved. These conditions can be simultaneously fulfilled by multiple modes.

To measure the complete and cumulative emission spectrum generated during the tunable laser scan, the *Hold Max* feature of the OSA is used. As its name indicates, this feature records the largest power value for each wavelength increment. The emission spectrum builds up with each spectral sweep of the pump laser. The spectra presented in Fig. 4.3(a) and 6.3 were obtained using this method.

However, the main advantage of the OSA is its use in the temporal domain [1] in combination with its built-in filtering capability. Similarly to an oscilloscope, the OSA can follow the transmitted pump and generated signal evolutions. The OSA spectral bandwidth can be positioned on a specific emission wavelength to study. Its bandwidth can be adjusted to measure a single emission peak among others.

1. The temporal domain is reached by setting the wavelength span option to 0.

3.2.4 Self-frequency locking setup

As expressed in the previous sections, the wavelength red-shift caused by thermorefractive changes and thermal expansion is part of any measurement using an external source tuned on a WGM resonance. This is especially true for cavities made of As_2S_3 glass that has a thermal expansion coefficient $\sim 20 \times 10^{-6}$ K^{-1}, approximately 40 times the silica's coefficient [147]. It also decreases the effectiveness of thermal stabilization method commonly used for silica microcavities [131]. This method is based on the principle shown in Fig. 3.16 : a laser line with a constant power will stabilize on the blue side of the resonance. In the case of large Q-factor resonances in As_2S_3, the stabilization point is rapidly pushed in the upper part of the resonance for 10-50 μW of input power, leading to a decreased coupled power.

To obtain a stable pump signal, a microcavity can be used as part of the laser medium to filter the gain instead of being an external component. The oscillating frequency is selected by the cavity most suitable resonance and is able to follow the thermal drifting. A typical setup is shown in Fig. 3.19. Similar setups were used for silica microspheres excitation [61, 254]. The gain from an optical amplifier (AMP) first passes through a tunable bandpass filter (TF). This first filtering step is used to select a spectral region where lasing will occur. The filter bandwidth controls the number of resonances the gain overlaps. If the bandwidth is too large or too narrow, multiple or none of the resonances interact with the gain signal. A single interacting resonance is preferred. The gain propagates to the microsphere using a circulator (CIRC). Optical modes whose resonances are located inside the bandpass filter bandwidth accumulate energy. The modes affected by modal coupling also concentrate energy in their counterclockwise modes and couple light back in the laser loop. The reflected gain signal is polarization-filtered using polarization controllers (PC) and a linear polarizer (POL) before returning to the amplifier. When the threshold conditions are realized, laser emission starts

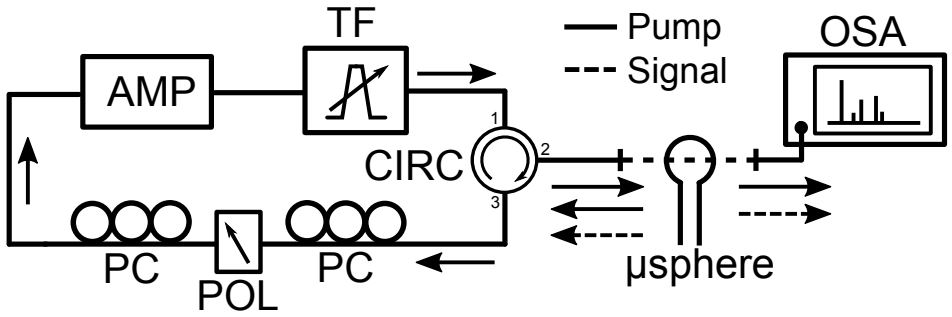

Figure 3.19 : Basic self-frequency locking setup - AMP : Optical amplifier, TF : Tunable bandpass filter, CIRC : Circulator, PC : Polarization controller, POL : Linear polarizer, and OSA : Optical spectrum analyzer.

in the loop. If the circulating power in the cavity's mode is large enough, nonlinear signal is generated. Both the pump and signal lines are measured using an OSA.

This setup is based on the reflective filtering of the WGM microcavity. This can only happen if a mode is affected by modal coupling. Fortunately, larger Q-factor modes are more affected by perturbations and modal coupling is achieved more easily. They are also the preferred modes for nonlinear signal generation.

Measurements of cascaded Raman emissions and their threshold curves shown in Chapter 5 were obtained using a similar setup. When there is no generated signal in the cavity, at low pump power, the pump emission is stable over several minutes. Over time, slow polarization variations inside the loop cause pump power deviations at the output.

Stable emission is also achievable when there is a single pump peak and a single signal peak. The setup is designed to stabilize the pump emission but it does not filter the signal emission generated inside the microcavity. The latter can be multimode if many modes reach the threshold conditions. Mode competition over the available gain may then cause power fluctuation and unstable emission. This issue was observed during the work presented in Chapter 5 and is discussed in Chapter 7.

CHAPTER 4 RAMAN LASING IN AS_2S_3 HIGH-Q WHISPERING GALLERY MODE RESONATORS

Published in F. Vanier, M. Rochette, N. Godbout, and Y.-A. Peter, Optics Letters, vol. 32, issue 23, pp.4966-4969 (2013).

4.1 Authors and Affiliation

Francis Vanier[1], Martin Rochette[2], Nicolas Godbout[1], and Yves-Alain Peter[1]

[1] Department of Engineering Physics, École Polytechnique de Montréal, Montréal (QC), H3C 3A7 Canada

[2] Department of Electrical and Computer Engineering, McGill University, Montréal (QC), H3A 2A7 Canada

4.2 Abstract

We report the first observation of a nonlinear process in a chalcogenide microresonator. Raman scattering and stimulated Raman scattering leading to laser oscillation is observed in microspheres made of As_2S_3. The coupled pump power threshold is as low as 13 μW using a pump wavelength of 1550 nm. The quality factor of the chalcogenide microresonator is also the highest ever reported with $Q > 7 \times 10^7$.

4.3 Introduction

The process of Stimulated Raman Scattering (SRS) is significant for the operation of lasers. In contrast with the electronic processes involved in typical rare-earth doped glasses, SRS provides gain at essentially all wavelengths for which a glass is transparent. SRS and cascaded SRS are specifically important for the generation of mid-IR light required in spectroscopy and biosensing applications.

Chalcogenide glasses such as As_2S_3 and As_2Se_3 are advantageous in view of SRS emission. As_2S_3 has a high Raman gain coefficient almost 100 times that encountered in silica and has a transparency window that extends up to 6 μm in the mid-infrared [184]. SRS-based lasers have already been demonstrated in As_2Se_3 fibers and microwires [197, 255–257].

Whispering gallery mode (WGM) optical microcavities such as microspheres, microdisks, and

microtoroids offer good possibilities for SRS emission thanks to their high quality factors and small mode volume. Threshold powers as low as 74 μW and 15 μW were respectively observed in silica microtoroids [125] and CaF_2 microdisks [126], thanks to their quality factor $Q > 10^8$. Many chalcogenide glasses WGM microcavities were reported in litterature. Ga :La :S and Ga :La :S :O glass microspheres with $Q = 8 \times 10^4$ were first produced by Elliot *et al.* [216]. As_2S_3 racetrack resonators and disks, As_2S_3 and As_2Se_3 microspheres and others were reported [153, 154, 207–209, 217–220]. The highest Q measured was 2.3×10^6 in As_2Se_3 [154]. However, no demonstration of SRS emission has ever been reported in a chalcogenide glass WGM microcavity.

In this Letter, we present the first observation of a nonlinear process in a chalcogenide microresonator, using stimulated Raman scattering in high-Q As_2S_3 microspheres. The microspheres used for this experiment possess the highest quality factors reported yet with chalcogenide glass. Using microspheres with loaded Q factors above 1×10^7, stimulated Raman scattering was measured for a threshold pump power of 35 μW with a power conversion efficiency of 11 %.

4.4 Sphere Fabrication

To fabricate the microspheres, a CO_2 laser reflow process is used, similar to the technique used for silica microspheres. For this purpose, a high purity As_2S_3 fiber provided by CorActive High-Tech is cleaned with acetone to remove the polymer cladding. The fiber is melted and pulled into a tapered fiber tip under a 3 W CO_2 laser illumination. With a diameter between 10 μm and 20 μm, the broken tip is melted again under CO_2 laser illumination to form a sphere from surface tension. Successive illuminations allow the production of spheres with diameters of 40 μm and above. The inset of Fig. 4.1 shows a typical microsphere produced with this technique.

The quality factor of spheres under test is determined from transmission spectra using evanescent coupling of a silica tapered fiber. The tapered fiber has a diameter of 2 μm. The probe laser that propagates in the tapered fiber is scanned around a wavelength of 1550 nm and the transmitted power is measured with a photodiode (Thorlabs DET01CFC). The transmission spectra are recorded over time with an oscilloscope. The time scale of the oscilloscope is converted into a wavelength scale based on the scan speed of the tunable laser. A polarization controler is used to optimize the coupling conditions. Fig. 4.1 shows the transmitted spectrum of a resonance peak measured in a sphere having a diameter of 80 μm. The full width at half maximum indicates a loaded quality factor $Q_L = 7 \times 10^7$ and an intrinsic quality factor $Q_0 = 7.2 \times 10^7$ assuming an undercoupled regime [241].

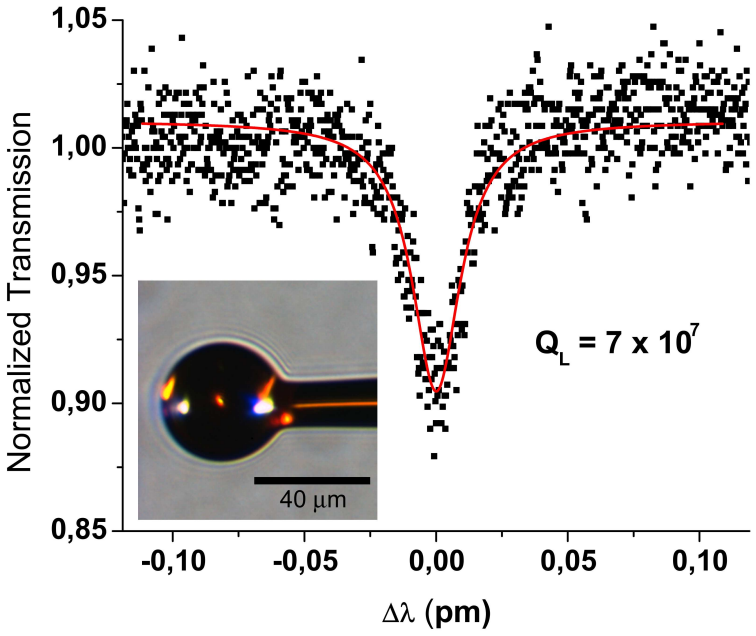

Figure 4.1 : Transmission spectrum of a resonance with a $Q_L = \ 7 \times 10^7$. Inset : Micrograph of a typical microsphere produced with the laser melting process.

The attenuation coefficient of an As_2S_3 fiber prior to the sphere fabrication provides a lower bound on the maximum achievable quality factor. Using the attenuation value of $\alpha \approx 0.115\ \mathrm{m}^{-1}$ at a wavelength of 1550 nm, the corresponding quality factor is $Q_0^{max} = \frac{2\pi n}{\lambda\alpha} \approx 8.6\times 10^7$. The measured quality factor indicates that the quality of the spheres produced by laser melting approaches the limit imposed by the material attenuation. Using this technique, quality factors above 10^6 and 10^7 are regularly achieved. These values are up to 100 times larger than values previously measured in an As_2S_3 microresonator and the highest reported for a chalcogenide glass [153, 154, 208].

4.5 Stimulated Raman scattering measurements

With the combination of a high quality factor and a high Raman gain of $g_R^{(b)} \sim 4.4 \times 10^{-10}$ cm/W [184], these As_2S_3 spheres are good candidates for stimulated Raman scattering (SRS) and laser oscillation from a low pump power and with a high conversion efficiency. Fig. 4.2 shows the experimental setup used to characterize SRS. In a first experiment, the output from an Agilent 81600B tunable laser source (TLS) is evanescently coupled to the sphere with a silica tapered fiber having a diameter of 2 μm. The transmitted Raman emission is measured using an Agilent 86146B optical spectrum analyzer (OSA). The tunable laser is periodically scanned over a span of 1 nm around a central wavelength of 1549 nm. The forward

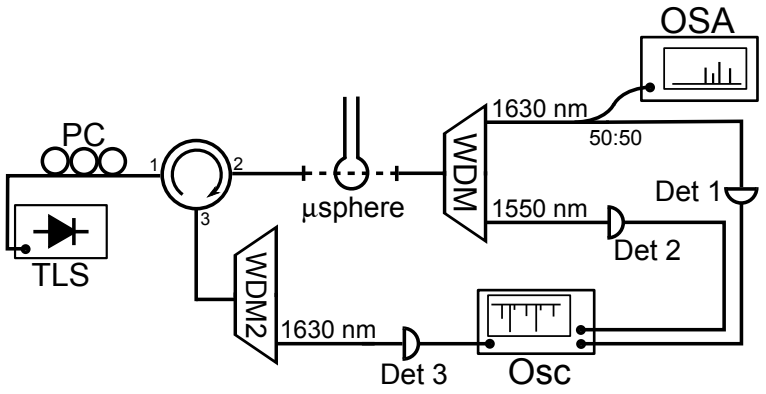

Figure 4.2 : Experimental setup for Raman laser emission measurements - TLS : Tunable Laser Source, PC : Polarization Controler, WDM : Wavelength Division Multiplexer, OSA : Optical Spectrum Analyzer, Det : Detector, Osc : Oscilloscope.

Raman spectrum is measured from several scan periods by using the *Hold Max* feature of the OSA. The SRS emission is expected to be shifted 10.3 THz away from the pump and to be around 1635 nm [184, 251]. A microsphere with a diameter of 71 μm is used.

Fig. 4.3(a) shows in black the measured spectrum for an input pump power in the tapered fiber $P_{in} = 123$ μW. The forward Raman emission has a peak power of 407 nW and is located at 1636.47 nm, as expected. Only one Raman emission peak was detected at this pump power. The spectrum fluctuations are artifacts caused by the mismatched scanning synchronization of the OSA and the pump laser. The red curve shows the spectrum of a continuous wave laser line tuned to 1636.47 nm, much narrower than the resolution limit of the OSA. The red curve fits well the black one and thus the Raman laser emission spectrum from the microsphere is expected to be much narrower than the experimental acquisition profile. Forward Raman emission powers are plotted for different input pump powers in Fig. 4.3(b). The measurements shows a linear dependency and indicate an input power threshold power $P_{in}^{th} = 61.3$ μW with a forward external conversion efficiency of 0.7 %.

To obtain the internal conversion efficiency of the process, the Raman emission in the temporal domain was measured . In a second experiment, the transmitted Raman emission and pump powers are measured with photodiodes. The backward Raman emission generated in the sphere is collected by the tapered fiber and is sent to a third photodiode. All optical powers are corrected for insertion loss of the components : PC, WDM, circulator and tapered fiber. The pump power line is repeatedly scanned near 1552 nm over a 1 nm span and all signals are recorded with an oscilloscope. The optical spectrum analyzer is set in zero-span mode to measure temporal profiles and allows us to identify the Raman emission wavelength. Using this setup, it is possible to plot the threshold curve in a single scan.

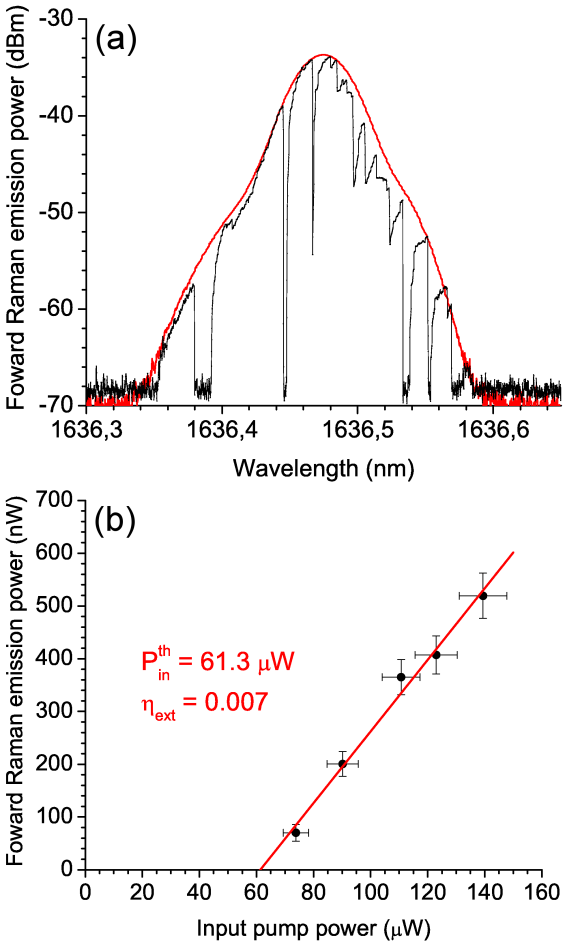

Figure 4.3 : **(a)** Raman laser emission with an input pump power of 123 μW(black curve). Superimposed (red curve) is the bandwidth-limited spectrum of a narrow cw laser, indicating that the Raman laser emission spectrum is also bandwidth-limited by the OSA. **(b)** Maxima of Raman emission spectra as a function of the input pump power. The Raman lasing threshold power is 61.3 μW.

Fig. 4.4 illustrates the principle of the measurement. As the pump laser line shifts to gradually superimpose with a resonance from the microsphere (black line), the increase of intra-cavity power heats the cavity and leads to a thermal drift of the resonance, resulting in a redshift of the transmitted spectrum as shown in Fig. 4.4(a) [131]. At threshold (dotted line), the power coupled inside the cavity becomes large enough so that the Raman emission power (red line) turns into laser oscillation. The coupled pump power P_{coup} is related to the input pump power P_{in} in the tapered fiber by $P_{coup} = (1-T)P_{in}$ where T is the transmission value at a particular wavelength. The Raman emission power P_R increases as long as the power inside the optical mode increases. A higher input pump power results in a longer thermal drift and a higher Raman emission power while the threshold coupled power P_{coup}^{th} is maintained.

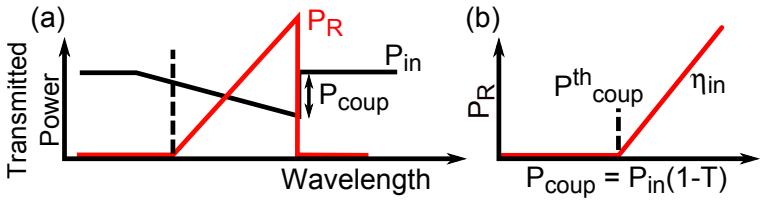

Figure 4.4 : Scheme of the measurements. **(a)** Oscilloscope view of transmitted pump and Raman emission power P_R. **(b)** Raman emission power against coupled pump power P_{coup} gives the coupled pump threshold power P_{coup}^{th} and the internal conversion efficiency η_{in} of the Raman process. P_{in} and T are the input pump power and the transmission value respectively.

By plotting the SRS emission power versus the coupled pump power, a threshold curve is obtained as shown in Fig. 4.4(b). The slope of the curve is the internal conversion efficiency of the process η_{in} [124].

Fig. 4.5 shows the transmitted pump power P_{out}, the forward Raman emission P_R^{Forw} and the backward Raman emission P_R^{Back} in black, red and blue respectively as a function of wavelength detuning. A resonance at a wavelength of 1552.5 nm with $Q_L = 3{\times}10^7$ is used. The input pump power is 49 μW. The Raman emission wavelength is 1640.7 nm and corresponds to the Raman shift. The forward and backward SRS emission start simultaneously at a wavelength detuning of 2 pm when the coupled pump power reaches threshold. The forward and backward Raman emission powers become similar as soon as the pump threshold power

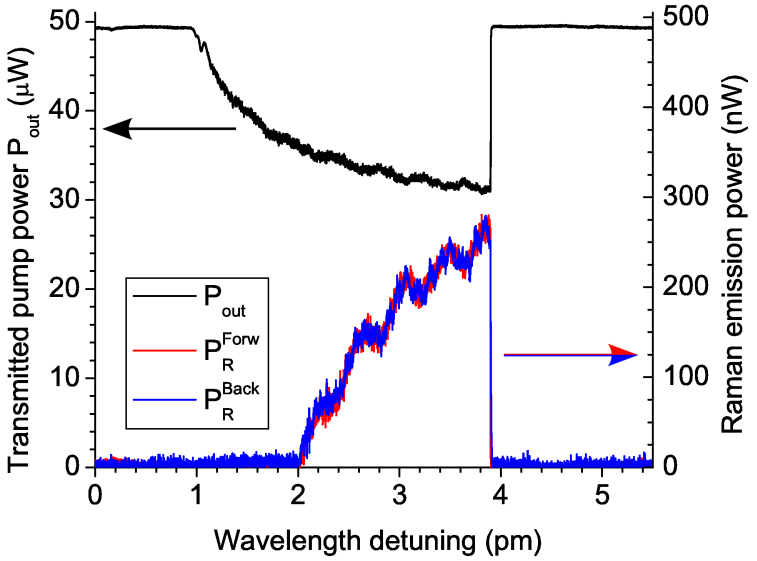

Figure 4.5 : Temporal domain measurements of SRS emission for an input pump power of 49 μW with transmitted pump power in black, forward Raman emission in red and backward Raman emission in blue. Raman lasing starts at a detuning of 2 pm.

is exceeded, as expected.

Fig. 4.6 shows total SRS emission power as a function of the coupled pump power P_{coup} for a constant input pump power $P_{in} = 49\ \mu$W. $P_{coup}^{th} = 12.9\ \mu$W and an internal conversion efficiency of 10.7 % are obtained. SRS emissions up to 1.1 μW were measured with $P_{coup} > 100\ \mu$W.

The center transmittivity of the resonance used in this experiment equals 63 % and leads to $P_{in}^{th} = 34.9\ \mu$W. This threshold value is comparable to the values showed in CaF_2 disks, silica microspheres and silica microtoroids. The transmission value also indicates a coupling quality factor $Q_c = 2.9 \times 10^8$ considering an undercoupled regime and a lossless and ideal coupling [252]. Using

$$\eta_{in} = \frac{\omega_R}{\omega_P}\frac{Q_L}{Q_c} \tag{4.1}$$

where ω_P and ω_R are the pump and Raman emission frequencies, $\eta_{in} = 9.8$ % assuming that the Raman mode quality factors are similar to the pump mode quality factors. This value agrees with the measurements and indicates an external conversion efficiency $\eta_{ext} = 2$ %. In order to improve these external conversion efficiencies, a larger coupling coefficient is needed. A possible solution is to use As_2S_3 tapered fibers which produce better phase matching conditions compared to silica tapered fibers. The observation of higher orders Raman emission

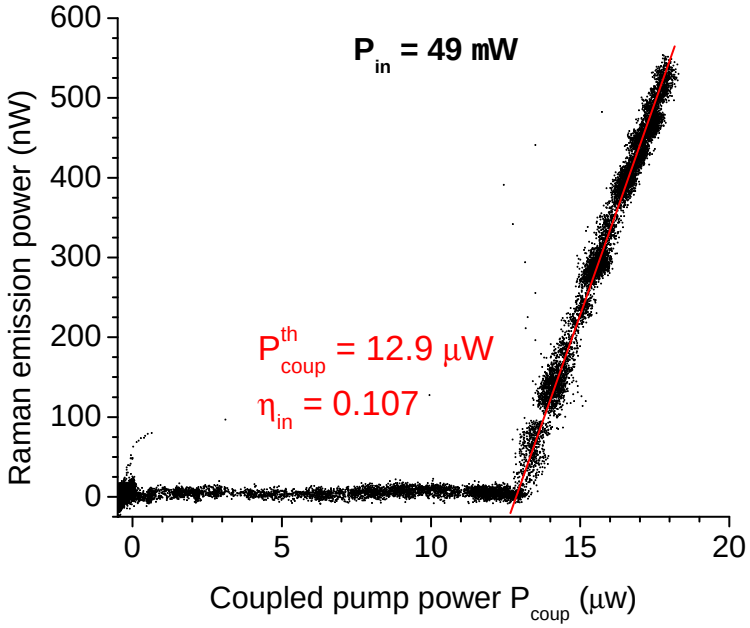

Figure 4.6 : Raman emission power versus coupled pump power for an input pump power of 49 μW. Raman lasing starts at 12.9 μW of coupled power with an internal conversion efficiency of 10.7 %.

peaks should be possible and it is currently under investigation.

4.6 Conclusion

To conclude, we have presented As_2S_3 microspheres fabricated using CO_2 laser melting. These spheres regularly presents quality factors in the $10^6 - 10^7$ range and up to 7×10^7, more than two order magnitude higher than reported in litterature for As_2S_3 microcavities. It also represents the highest value reported for a chalcogenide glass. Raman laser emissions were observed with coupled pump power down to 12.9 μW and internal conversion efficiency of 10.7 %. These results show the first observation of a nonlinear process in a chalcogenide microcavity. The threshold values measured in this work are comparable to that obtained in silica and CaF_2 WGM microcavities despite smaller Q_L. Considering a transparency window up to 6 μm, As_2S_3 microspheres are good candidates for mid-IR Raman-based microlaser applications.

4.7 Complementary results

4.7.1 Back on the Raman signal measurements

The previous sections highlight the measurements of low pump power Raman emission. Figures 4.5 and 4.6 are especially important since they show the evolution of the Raman emission as the coupled power increases. It was measured using a constant input pump power of 49 μW but similar results can be obtained with different input powers. For example, the measurements were repeated for input powers of 33 μW, 82 μW and 100 μW. Their threshold curves are shown in Fig. 4.7 along the results of Fig. 4.6. As the input power increases, more power is coupled to the mode. All the curves show the same Raman signal evolution up to a larger coupled power value. The threshold and slope values are the same. Acquisition through thermal drifting do not depend on the input power and need one scan

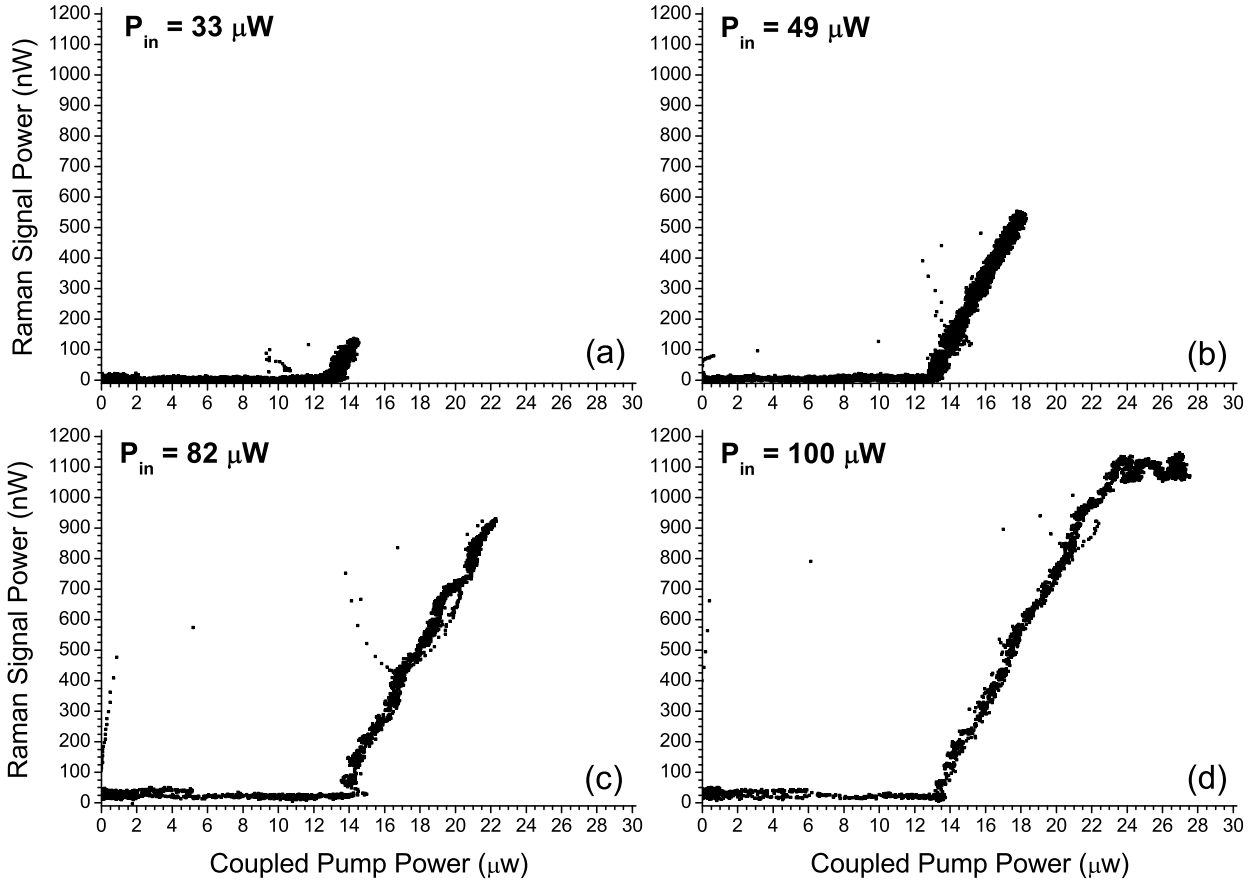

Figure 4.7 : Raman emission power curves taken with four input pump powers : (a) 33 μW, (b) 49 μW, (c) 82 μW and (d) 100 μW.

to plot the threshold curve. It is possible to measure the Raman emission evolution fully by setting the input power high enough. The similitude between traces also indicates that this kind of measurement is reproducible over many laser scans and over time. Finally, clamping behavior is even observable in the case of an input power of 100 μW in Fig. 4.7(d) for a coupled power of 23 μW. This behavior is a sign of 2nd Raman order emission and is studied in the next chapter.

Another feature of Fig. 4.5 is the forward and backward Raman signal similitude shown in red and blue respectively. The setup losses were considered and the photodiodes, represented by *Det 1* and *Det 3* in Fig. 4.2, were calibrated using the same optical powermeter. Both curves even follow the variation of the pump signal due to rapid thermal fluctuations. Figure 4.8 shows the ratio of the forward power over the total Raman power. At the threshold value, half of the power is launched forward and the other half is sent backward. Similar results are measured with different input pump powers as well. The theoretical model presented in Section 2.5.1 and explicitly in Section B.4 also follows this symmetric behavior. This is due to the fulfillment of the phase matching conditions for Stokes wavevectors pointing in the opposite direction .

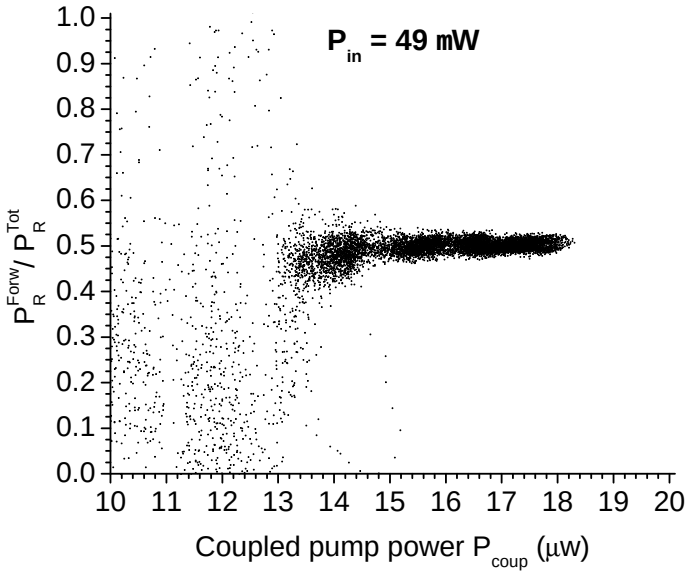

Figure 4.8 : Ratio of the forward Raman emission power over the total Raman power. The input pump power is 49 μW.

4.7.2 Theoretical analysis

The theoretical model, especially Relation 2.31, is easily applicable to the results of Fig. 4.6. The predicted linear dependency on the coupled power is observable for each input power in Fig. 4.7. The slope of the threshold curves is the internal conversion of Relation 2.32 and reveals the signal total and coupling Q-factors ratio. The threshold value is given by

$$P_{in,coup}^{th} = \frac{1}{\tau_s \tau_{p,0} g_R} = \frac{2\omega_p \omega_s n_p n_s V_{ppss}}{Q_{s,T} Q_{p,0} c^2 g_R^{(b)}} \qquad V_{ppss} = \frac{\int_V |\mathbf{e}_p|^2 dV \int_V |\mathbf{e}_s|^2 dV}{\int_V |\mathbf{e}_p|^2 |\mathbf{e}_s|^2 dV}$$

where Definitions 2.27 and 2.28 were used. It links together both mode Q-factors and the effective mode volume quantifying the mode overlap. The latter can be deduced numerically using the sphere solutions of Section 2.4. Figure 4.9 shows the first radial TE solution of the pump and Raman signal modes associated to a wavelength of 1552.5 nm and 1640.7 nm respectively. The sphere diameter is 71 μm. Both modes are similar and occupy approximately the same volume : $V_p = 712$ μm^3 and $V_s = 759$ μm^3. Numerical calculations give an effective mode volume $V_{ppss} = 1454$ μm^3. Based on the experimental threshold value and internal efficiency in Fig. 4.6, signal Q-factors are deduced :

Table 4.1 : Measured pump Q-factors and extracted Raman signal Q-factors.

	Pump mode	**Raman mode**
$Q_{j,T}$	3×10^7	7×10^7
$Q_{j,0}$	3.3×10^7	7.9×10^7
$Q_{j,c}$	2.9×10^8	6.2×10^8
$T_{j,0}$	63 %	60 %

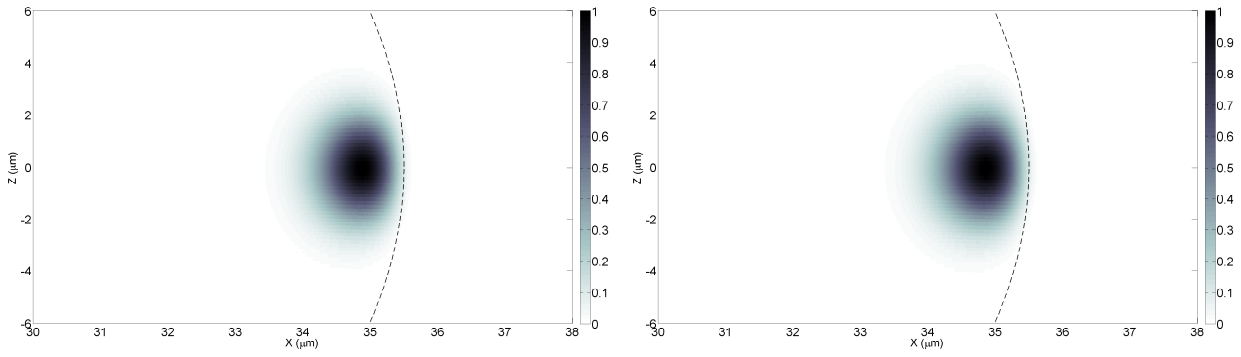

Figure 4.9 : Transverse view of the pump (left) and signal (right) TE modes corresponding to a wavelength of 1552.5 nm and 1640.7 nm respectively. The first radial pump mode is linked to $m_p = l_p = 338$. The signal mode is associated to $m_p = l_p = 319$.

Those values are realistic and fall within the limit provided by the attenuation value of the As_2S_3 fiber. To fit the measurements with the use of higher order radial or polar modes, the increase of the effective mode volume pushes the signal Q-factors above the attenuation limit. This suggests that the modes depicted in Fig. 4.9 are the right ones. The theoretical results are similar using TM modes and offer no new insight.

Furthermore, the extracted Q-factor values can be used to deduce the external power conversion efficiency shown in Relation 2.32 :

$$\eta_{ex} = 2\frac{\omega_s}{\omega_p}\frac{Q_{p,T}Q_{s,T}}{Q_{p,c}Q_{s,c}} = 0.022.$$

Compared to the internal power conversion efficiency of 10.7 %, most of the efficiency is lost during the pump coupling process.

CHAPTER 5 CASCADED RAMAN LASING IN PACKAGED HIGH QUALITY AS_2S_3 MICROSPHERES

Published in F. Vanier, Y.-A. Peter, and M. Rochette, Optics Express, vol. 22, issue 23, pp.28731-28739 (2014).

5.1 Authors and Affiliation

Francis Vanier[1], Yves-Alain Peter[1], and Martin Rochette[2]

[1] Department of Engineering Physics, École Polytechnique de Montréal, Montréal (QC), H3C 3A7 Canada

[2] Department of Electrical and Computer Engineering, McGill University, Montréal (QC), H3A 2A7 Canada

5.2 Abstract

We report the observation of cascaded Raman lasing in high-Q As_2S_3 microspheres. Cascaded stimulated Raman scattering emission is obtained up to the 5th order for a pump wavelength of 1557 nm and up to the 3rd order for a pump wavelength of 1880 nm. High-Q As_2S_3 microspheres are used in a self-frequency locking laser setup without an external laser source. Threshold curves measurements are presented and follow the expected coupled mode theory behavior with a sub-mW threshold pump power.

5.3 Introduction

Stimulated Raman scattering (SRS) and cascaded SRS are important nonlinear optical phenomena for signal generation at wavelengths that are not accessible by conventional semiconductor and rare-earth doped sources. This is due to the fact that Raman gain is available over the entire transparency window of the host material. This can be especially important for the $2 - 12$ μm mid-IR region for molecular spectroscopy and biosensing applications.

Chalcogenide glasses such as As_2S_3 are ideal materials in this regard as they provide a wide transparency window over the mid-IR. Widespread under the form of high purity fibers, chalcogenide glasses are also known for their high Raman gain typically more than 100 times the gain of silica [184, 185]. SRS and cascaded SRS processes were already observed in As_2S_3 and As_2Se_3 fibers, tapered fibers and suspended core fibers [185, 186, 197, 255–262].

Whispering gallery modes (WGM) microcavities such as spheres, disks and toroids are excellent structures for SRS emission thanks to their high Q-factors and small modal volumes. SRS and cascaded SRS emission were also demonstrated in silica spheres and toroids, CaF_2 disks and $LiNbO_3$ disks [106, 122–124, 126]. Typical input power threshold < 100 μW were obtained for the first Raman order emission due to the cavity high Q-factor $> 10^8$ [122, 126].

Chalcogenide WGM cavities such as As_2S_3 and $Ge_{23}Sb_7S_{70}$ racetracks [208–210], As_2S_3 and As_2Se_3 disks [207, 263], As_2S_3 microfibers [219] and Ga :La :S, As_2S_3 and As_2Se_3 spheres [153, 154, 216–218, 220, 264, 265] were also fabricated. Despite the high potential of chalcogenide glasses as a SRS medium, it was not until recently that SRS emission was observed in chalcogenide WGM cavities. First order SRS emission with a threshold pump power of 35 μW was shown in As_2S_3 microspheres with a Q-factor of 7×10^7 [265].

In this article, we demonstrate cascaded SRS emission in As_2S_3 high-Q microspheres up to the 5th Raman order pumped at a wavelength of 1557 nm. Threshold power measurements show the expected coupled mode theory dynamics for the first three Raman order emission. A laser pumping setup without an external source is presented together with a packaging technique for the microsphere and the tapered fiber. Testing was also performed using a pump wavelength of 1880 nm. SRS emission up to the 3rd order was obtained at a wavelength of 2350 nm. These results show the potentiel of As_2S_3 high-Q microspheres to act as sub-mW pump power cascaded SRS sources in the telecommunication band and in the $2 - 6$ μm mid-IR range.

5.4 Self-frequency locking laser setup

Chalcogenide glasses such as As_2S_3 have a relatively high thermorefractive coefficient $\frac{dn}{dT}$. This property makes it difficult to couple an external signal to a high-Q optical mode because the resonance rapidly shifts away as the mode region heats up, and limits the optical power coupled inside the cavity. To mitigate this behavior, we used a self-frequency locking laser setup shown Fig. 5.1 [254]. The amplified signal of an Er-doped fiber amplifier (EDFA) is sent through a tunable band-pass filter (TBF) with a bandwidth of 0.2 nm and tunable throughout the telecommunication C-band. An isolator (Iso) prevents any back-reflection to be amplified and ensures the signal direction in the fiber cavity. The filtered optical signal goes through a circulator and is evanescently coupled to an As_2S_3 microsphere using a silica tapered fiber with a diameter of 2 μm. The microspheres are fabricated from reshaping the tip of a fine As_2S_3 wire using a CO_2 laser. The Q-factors of the spheres typically reach 10^7 [265]. Some high-Q resonances act as narrow band mirror when they are mode-splitted by a small perturbation such as surface roughness or a dust particle. A single laser line is typically

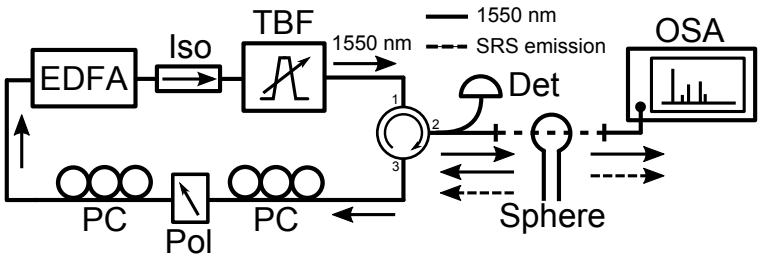

Figure 5.1 : Self-frequency locking laser setup - The gain signal from a Er-doped fiber amplifer is filtered using a 0.2 nm bandwidth tunable band-pass filter. An As_2S_3 microsphere acts as a narrow-band mirror and sends back a single line emission in the fiber loop. The transmitted pump signal and the forward Raman signal is measured by the OSA. A powermeter measures the injected pump power in the tapered fiber.

reflected back in the fiber cavity. The bandwidth of a high-Q resonance is usually below 1 pm at a wavelength of 1550 nm. The polarization controllers (PCs) and a polarizer (Pol) are used to optimize the coupling conditions to the microsphere. When the pump signal power is strong enough, SRS emission builds-up in the microsphere. The emitting pump signal and forward Raman signal are measured using a Yokogawa AQ6375 optical spectrum analyzer (OSA). The optical power sent to the microsphere is measured using an optical powermeter (Det). In this configuration, the signal is forced to propagate inside a high-Q mode of the microcavity and the lasing frequency is determined by the resonances of the microcavity.

5.5 Sphere Encapsulation

Dust particles on the sphere surface increase the scattering losses and thus decrease the Q-factor. To avoid such detrimental contamination, the microsphere and the tapered silica fiber are packaged in a closed glass tube. Figure 5.2 shows the glass tube packaging process. First, glass half-rods are glued inside of the lower half of a 6 cm long glass tube with a low-expansion UV-polymer (Fig. 5.2(a)). The tapered silica fiber is fabricated and is glued on the half-rods (Fig. 5.2(b)). The fiber tip of the microsphere is then attached to the glass tube once the coupling condition and the transmission spectrum are optimized. Finally, the upper half of the glass tube is placed on top to complete the assembly (Fig. 5.2(c)). An image of a typical As_2S_3 high-Q microsphere is presented in Fig. 5.3(a).

It was recently shown that an As_2S_3 microsphere and a silica tapered fiber can be packaged in a UV-curable polymer [153]. Unfortunately, the additional loss caused by the polymer touching the sphere reduces the Q-factor of the sphere. Q-factors up to 2×10^5 were measured

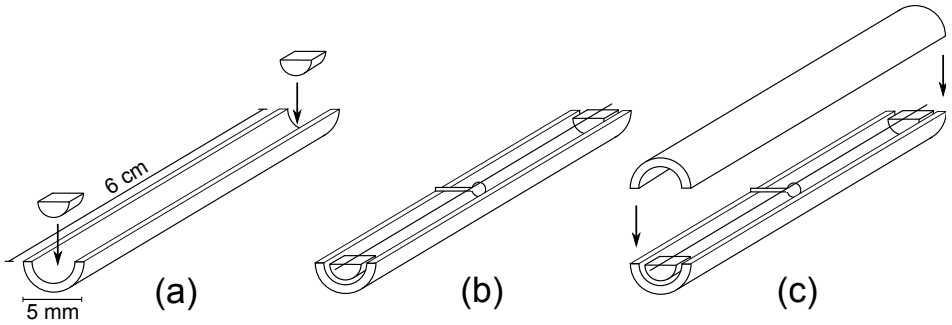

Figure 5.2 : Glass tube packaging - (a) Glass half-rods are installed in the lower half of a glass tube. (b) The tapered fiber is attached to the glass half-rods. While the microsphere is in a optimal coupling condition, its fiber tip is glued to the side of the half-tube. (c) The upper half of the glass tube is placed on top.

using this method.

In contrast, the glass tube packaging method leaves the tapered fiber and the microsphere suspended in air. The transmission of the tapered fiber and the high Q-factor of the sphere are not affected by this method. Resonances with a loaded Q-factor Q_L up to 10^7 are measured at a wavelength of 1550 nm after the packaging process. A high-Q resonance transmission spectrum is shown in Fig. 5.3(b) for a sphere with a diameter of 40 μm. Once sealed, the glass tube could be used as a gas chamber for gas sensing measurements if a mid-IR source were to be used.

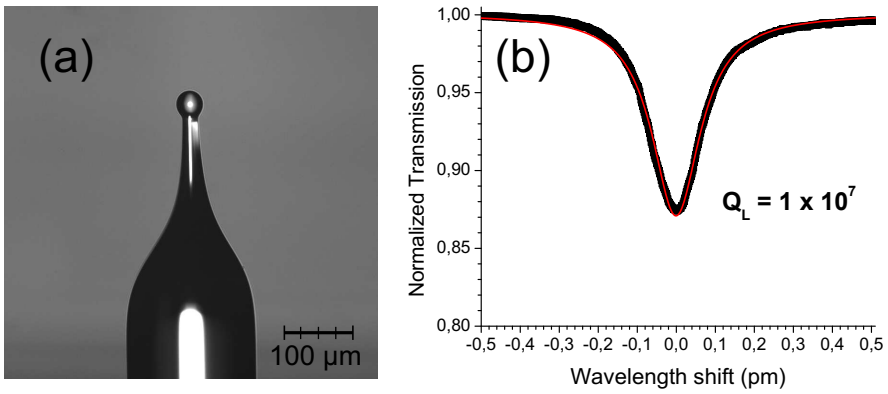

Figure 5.3 : (a) Image of a typical packaged As_2S_3 microsphere. (b) Transmission spectrum of a high-Q resonance from a packaged As_2S_3 microsphere. The loaded Q-factor $Q_L = 1 \times 10^7$.

5.6 Cascaded SRS emission from the 1550 nm wavelength region

Cascaded SRS emission is obtained when the gain provided by the previous Raman orders exceeds the losses of the present Raman order. Whispering gallery modes of cavities such as microspheres are ideal for cascaded SRS emission since they present high Q-factors, small mode volumes and a good mode overlap. A spectrum of the forward Raman signal power is presented in Fig. 5.4. The sphere used has a diameter of 50 μm and is in contact with the silica tapered fiber. SRS emission up to 5th order is observed while pumping at a wavelength of 1557 nm and with a pump power of 6.3 mW. Raman emission peaks are located in multimode bands centered on wavelengths of 1646 nm, 1747 nm, 1861 nm, 1991 nm and 2140 nm respectively. The Raman shift of each successive Raman order corresponds to a value of ~ 10.5 THz. This value is in agreement with an in-house Raman spectroscopy measurement on the surface of our As_2S_3 spheres. A typical Raman spectroscopy measurement is shown in the inset of Fig. 5.4. This Raman shift for As_2S_3 was also predicted in [184, 251].

The SRS emission is multimode due to the large Raman gain bandwidth of As_2S_3 glass and the large number of high-Q cavity modes present across the spectrum. However, a single

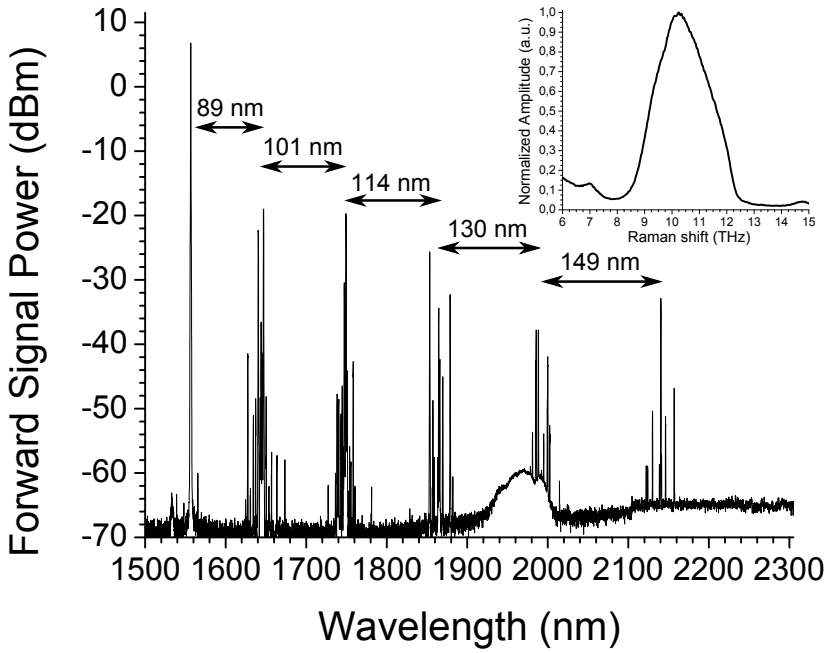

Figure 5.4 : Spectrum of a cascaded SRS emission of an As_2S_3 microsphere including 5 Raman orders generated from a pump wavelength of 1557 nm. The injected pump power in the tapered fiber is 6.3 mW. Each Raman order bands are centered on wavelengths of 1646 nm, 1747 nm, 1861 nm, 1991 nm and 2140 nm respectively. The inset shows a typical Raman spectroscopy measurement made on an As_2S_3 sphere surface.

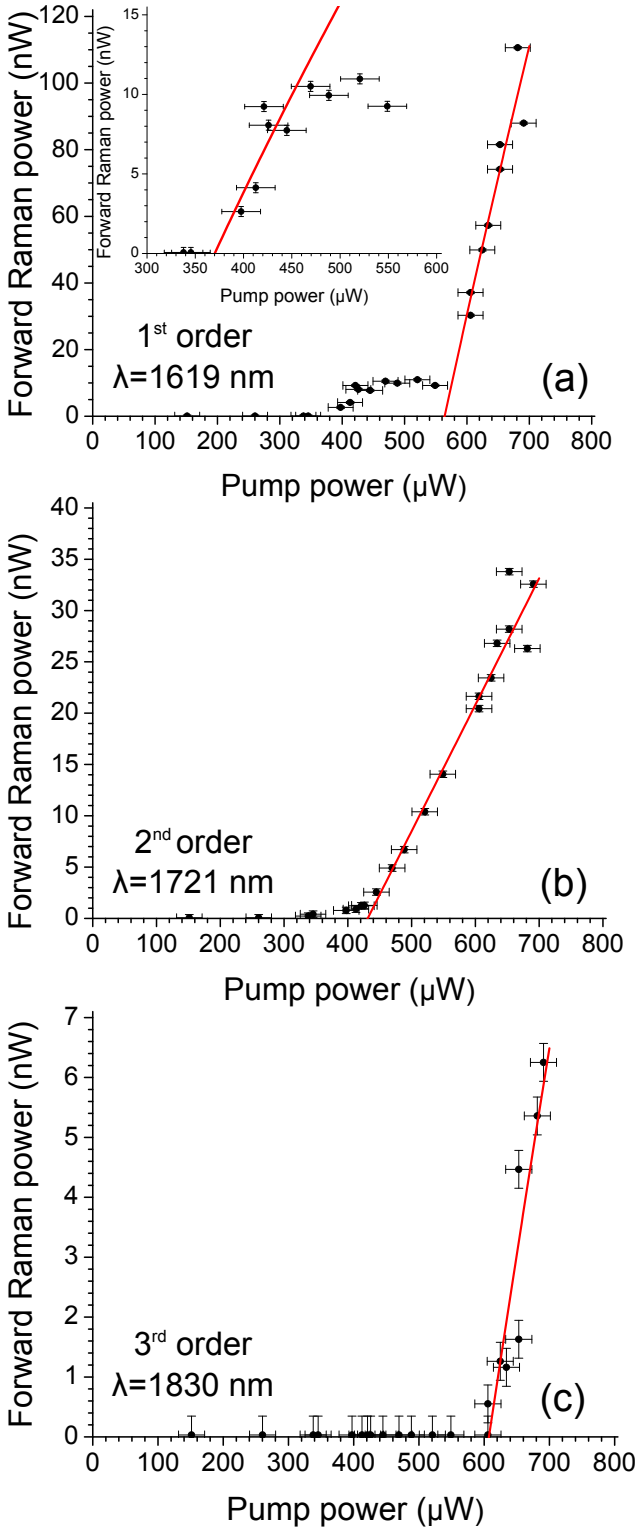

Figure 5.5 : Forward Raman signal power measurements for the (a) 1st (b) 2nd and (c) 3rd Raman order. In the inset of (a), SRS threshold pump power is 370 μW. In (b), the threshold pump power of the second order Raman emission is 430 μW. The first order Raman signal saturates when the second order SRS emission power increases between 450 μW and 600 μW of pump power. In (c), the threshold power of the third Raman order is 607 μW. The first order Raman signal increases again when the third order Raman signal is getting stronger.

pump mode contributes to the gain of all the first Raman order emission peaks. Each peak can then provide gain for the successive Raman order emission peaks. In this multimode regime, mode competition causes fluctuation of the output Raman power. To get a reliable power measurement, a regime where each Raman order emission is monomode is preferred.

Figure 5.5 shows the forward Raman signal power as a function of the injected pump power for three Raman orders. Each data point are extracted from a spectral measurement for different injected pump power values. The pump and the three Raman orders wavelengths are 1536 nm, 1619 nm, 1721 nm and 1830 nm respectively. In Fig. 5.5(a), as the pump power is increased, the first Raman order emission starts at an injected pump power of 370 μW and it follows a square root dependency as expected [123]. In the inset of Fig. 5.5(a), a square root curve fit shows that the first Raman order emission saturates at a pump power of ~ 450 μW. The saturation is caused by the SRS emission of a second Raman order presented in Fig. 5.5(b). The growth of the second order follows an expected linear dependency as the pump power increases. A linear curve fit indicates a threshold pump power of 430 μW. The first Raman order saturation is maintained until a pump power of ~ 600 μW where the first order emission increases again for a higher pump power. It coincides with the SRS emission of a third Raman order shown in Fig. 5.5(c). Again, the Raman signal power of the first and third order are in agreement with a square root tendency [123]. A square root curve fit shows a threshold pump power of 607 μW. The error on pump power measurement is limited by the fluctuation of the pump power circulating in the fiber cavity. The error on the forward Raman signal power is based on the noise level of the OSA.

The forward external efficiency $\eta_{ext} = dP_{Ri}/dP_{in}$, where P_{Ri} is the ith Raman order signal power and P_{in} is the injected pump power, are $(1.3 \pm 0.8) \times 10^{-2}$ %, $(1.23 \pm 0.02) \times 10^{-2}$ % and $(7 \pm 2) \times 10^{-3}$ % for the first, second and third Raman order respectively. These relatively low values are attibuted to a low coupling phase matching between the optical modes of the cavity and the silica tapered fiber, hence being in a undercoupling condition $Q_c >> Q_0$ with the coupling Q-factor Q_c and the intrinsic Q-factor Q_0. The use of an As_2S_3 tapered fiber would greatly increase the coupling coefficient and the Raman signal extraction.

5.7 Cascaded SRS emission from the 1880 nm wavelength region

An important property of As_2S_3 glass is its tranparency window across the $2-6$ μm spectral range. Combining this property, a high Raman gain and the high Q-factor of As_2S_3 microspheres could lead to low power mid-IR sources. To test this idea, we replaced the Er-doped fiber amplifier in Fig. 5.1 with a Tm-doped fiber amplifier to shift the Raman pump wavelength near 2 μm. The setup is shown in Fig. 5.6. A pump signal at a wavelength of 1550 nm

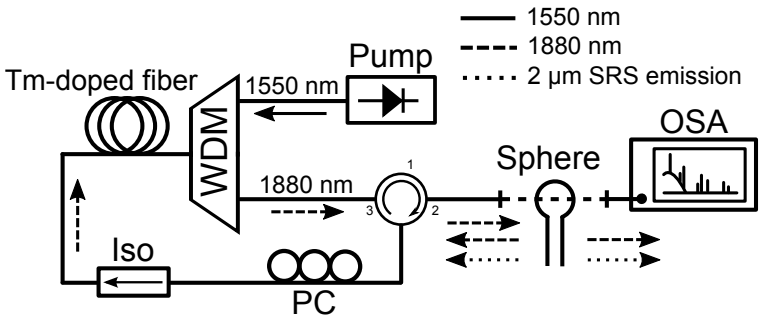

Figure 5.6 : Self-frequency locking laser setup at 1880 nm - The gain of a Tm-doped fiber is sent to the microsphere which acts as a narrow band mirror. The reflected signal is amplified in the fiber loop. The spectra are measured using an OSA.

is sent to a 32-cm long Tm-doped fiber. The gain signal in the 1800-1900 nm spectral region propagates to an As_2S_3 microsphere. Again, this setup uses the microsphere as a narrow band mirror. The reflected signal is sent back to the Tm-doped fiber. The isolator (Iso) forces the propagation direction. The polarization controller (PC) is used to optimize the coupling conditions and to select a preferred resonance group. The spectra are measured with an OSA.

In Fig. 5.7, a typical spectrum is presented for a multimode pump emission centered around a wavelength of 1880 nm. The signal power at a wavelength of 1550 nm that pumps the gain in the Tm-doped fiber is approximately 875 mW. The multimode 1880 nm pump signal in the microcavity leads to cascaded SRS emission up to the third order. The generated SRS signal is also multimode. SRS emission peaks are grouped around a wavelength of 2015 nm, 2170 nm and 2350 nm for the first, second and third order respectively. Again, the Raman shift is in agreement with the value of 10.3 THz.

These measurements show that As_2S_3 microspheres are good candidates for low power cascaded Raman sources. Furthermore, the transparency window of chalcogenide glasses such as As_2S_3 offers the possibility to extend the emission wavelength to the $2-6$ μm region. The As_2S_3 glass provided by CorActive High-Tech has an attenuation value below 1 dB/m across this spectral region. An upper Q-factor limit of 1×10^7 could be achieved if this attenuation value is considered. Provided that the laser fabrication technique produced microspheres with intrinsic Q-factors near this limit [265], the realisation of mid-IR As_2S_3 cascaded Raman sources with sub-mW of pump power seems possible.

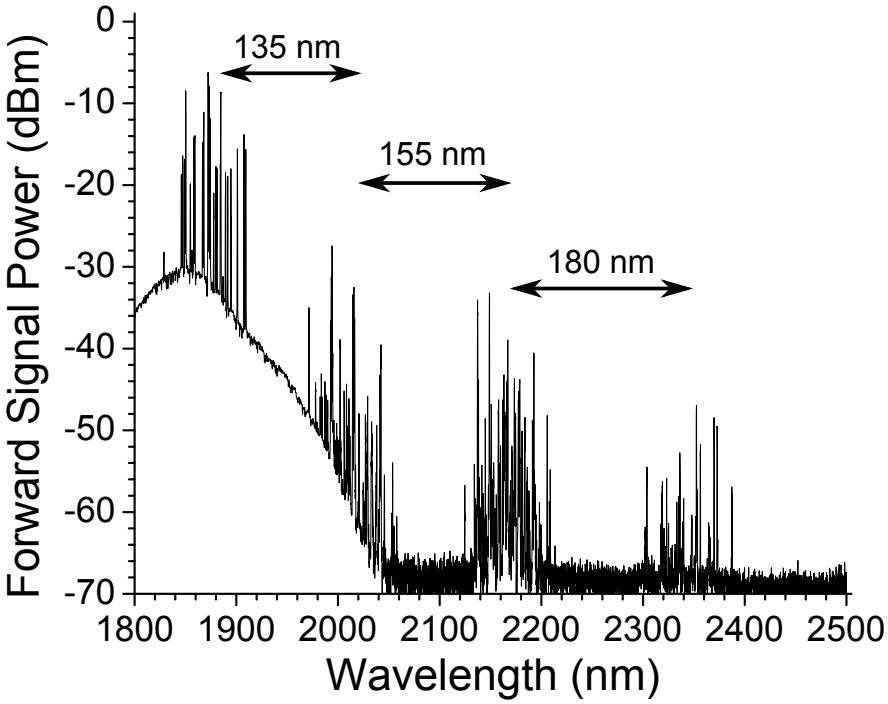

Figure 5.7 : Spectrum of a cascaded SRS emission with 3 Raman orders with a pump wavelength band centered on 1880 nm. Multimode Raman emission band positions are 2015 nm, 2170 nm and 2350 nm respectively.

5.8 Conclusion

In this work, we presented measurements of cascaded stimulated Raman scattering emission in As_2S_3 microspheres. Due to the high Raman gain of As_2S_3 and the high Q-factor resonances of the microspheres, SRS emissions up to the 5th order were observed with a pump wavelength of 1557 nm. A self-frequency locking laser setup was used to mitigate the thermal drift of high Q-factor resonances. We introduced a packaging technique for an As_2S_3 sphere and a tapered fiber which preserves the high Q-factors of the cavities. The measurements of the Raman signal power as a function of the input pump power were shown for the first three Raman orders. These measurements are in agreement with the expected theoretical behavior. Another setup was built to pump the microsphere at a wavelength of 1880 nm using a Tm-doped fiber amplifier. SRS emissions up to the 3rd order were measured. These results reveal the potential of As_2S_3 microspheres as low power cascaded Raman sources at telecommunication wavelengths and in the $2-6$ μm mid-IR range.

5.9 Complementary results

5.9.1 Theoretical analysis : cascaded Raman with a pump wavelength of 1536 nm

The measurements shown in Fig. 5.5 display the intricate evolution of three Raman order emissions. The theoretical model presented in Section 2.5.1 agrees with the dependencies of these emission versus the pump power. It is especially true from the visible clamping of the 1st Raman order when the 2nd order starts increasing. It is possible to push the theoretical analysis further and to extract the properties of the Raman modes. The top part of Table 5.1 shows the threshold powers, the external efficiencies, and the clamped powers measured for each Raman order of Fig. 5.5. Those values are represented by Relations 2.29, 2.32 and 2.38 to 2.43. They depend explicitly on four total Q-factors $Q_{j,T}$ and four coupling Q-factors $Q_{j,c}$ of each modes. Unfortunately, solving these relations for the eight missing variables is limited by the fact $Q_{p,T}$ and $Q_{p,c}$ are always combined and cannot be solved completely. In other words, two of the eight relations are redundant. However, it is possible to find realistic ranges following the attenuation level of the glass. The extracted Q-factors are shown in the bottom half of Table 5.1. The mode volumes and V_{jjii} are also shown for a sphere with a diameter of 50 μm.

Those values may look strange at first, but they are in agreement with the low external efficiencies. Following the efficiency definition for the 1st Raman order (Eq. 2.32), such efficiencies are only obtained for severe undercoupled regime case where $Q_{j,c} \gg Q_{0,T}$. The fact that Raman emissions build up in these modes is not surprising. The small external coupling load allows Raman emission power to increase rapidly and to oscillate. This also explains

Table 5.1 : Measured (top) and extracted (bottom) characteristic values of the Raman emission modes.

	Pump mode	1st **Raman mode**	2nd **Raman mode**	3rd **Raman mode**
λ (nm)	1536	1619	1721	1830
$P_{in,th}^{\Delta_L=0}$ (μW)	-	370	430	607
η_{ex} (%)	-	1.3×10^{-2}	1.23×10^{-2}	7×10^{-3}
$P_S^{clamped}$ (nW)	-	~ 9	~ 30	-
V_j (μm^3)	367	390	420	451
V_{jjii} (μm^3)	748	797	858	
$Q_{j,T}$ ($\times 10^7$)	$0.3 - 0.7$	$1.2 - 2.5$	$3.2 - 6.4$	$3.3 - 6.4$
$Q_{j,c}$ ($\times 10^7$)	$2 - 4$	$1300 - 2600$	$530 - 1000$	$1400 - 2700$
$Q_{j,0}$ ($\times 10^7$)	$0.35 - 0.7$	$1.2 - 2.5$	$3.2 - 6.4$	$3.3 - 6.4$
$T_{j,0}$	50 %†	99.6 %	97.6 %	99 %

† Measured

why the emissions of the first and second Raman orders are visible almost simultaneously. Photons associated with the first Raman order only have a small chance to be coupled out of the cavity and have time to interact with the glass lattice.

This behavior was regularly observed with other resonances and spheres. For example, Fig. 5.8 shows a second set of measurements for a pump wavelength of 1550 nm where the first and second Raman order emissions starts almost simultaneously. The first three Raman order emissions are shown and they exhibit better threshold pump powers. A square-root dependency is observed for the first Raman order shown in the inset of Fig. 5.8(a). Furthermore, clamping is seen for the first and second Raman orders but the emission behaviors are less clear. Notably, the second Raman order emission clamps and decreases for increasing pump power. This evolution is not predicted by the theoretical model developed in this thesis but it may be attributed to the presence of multiple emission lines associated with the second and third Raman orders.

The setup used in this work is designed to select the pump mode only. However, the nonlinear interactions between the sphere modes are not constrained. Consequently, only the most suitable modes can build Raman emission. By letting the sphere choose which modes can sustain Raman emission, the pump energy is rapidly transfered to higher order Raman modes according to the limits fixed by the mode overlap and the Raman gain. External efficiencies and output powers suffer from this behavior. Combined with the large number of high quality modes, the unfiltered Raman emission is also visible for multiple modes and can cause stabilization issues. This will be discussed in Chapter 7.

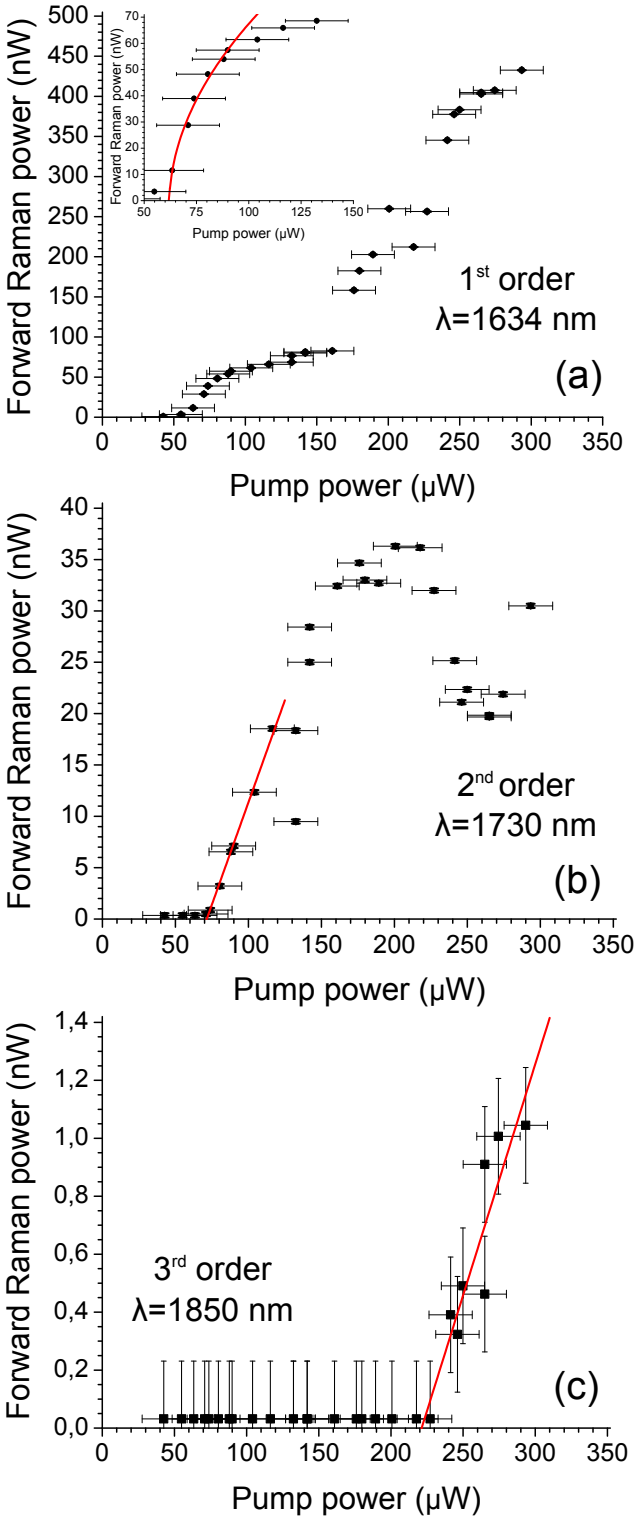

Figure 5.8 : Forward Raman signal power measurements for the (a) 1st (b) 2nd and (c) 3rd Raman order. In the inset of (a), SRS threshold pump power is $\sim$ 70 μW. The inset shows a close-up view near the threshold. In (b), the threshold pump power of the second order Raman emission is also $\sim$ 70 μW. In (c), the threshold power of the third Raman order is 220 μW.

CHAPTER 6 LOW-THRESHOLD LASING AT 1975 NM IN THULIUM-DOPED TELLURITE GLASS MICROSPHERES

Published in F. Vanier, F. Côté, M. El Amraoui, Y. Messaddeq, Y.-A. Peter, and M. Rochette, Optics Letters, vol. 40, issue 22, pp.5227-5230 (2015).

6.1 Authors and Affiliation

Francis Vanier[1], François Côté[2], Mohammed El Amraoui[2], Younès Messaddeq[2], Yves-Alain Peter[1], and Martin Rochette[3]

[1] Department of Engineering Physics, École Polytechnique de Montréal, Montréal (QC), H3C 3A7 Canada

[2] Center for Optics, Photonics and Lasers (COPL), Laval University, Québec City (QC), G1V 0A6, Canada

[3] Department of Electrical and Computer Engineering, McGill University, Montréal (QC), H3A 2A7 Canada

6.2 Abstract

Thulium-doped (Tm-doped) tellurite glass microspheres are used as laser media. Emission lines at wavelengths near 1975 nm are observed. The onset of laser emission is achieved with 8.6 μW and 30 μW of coupled pump power and injected pump power respectively at a wavelength of 1554 nm. To the authors' knowledge, these are the lowest laser threshold values recorded for a Tm-doped tellurite glass microcavity. Intrinsic Q-factors above 10^6 for the undoped tellurite glass microspheres assert the quality of the fabrication processes. Optical intrinsic Q-factors comparison between Tm-doped tellurite and undoped tellurite microspheres shows that ions absorption is the dominant loss source at pump wavelengths. Lower lasing threshold powers and higher power conversion are observed at longer pump wavelengths in agreement with theoretical models.

6.3 Introduction

Thulium-based lasers emitting near a wavelength of 2 μm are used in many applications such as laser-assisted medical interventions [266–268], material analysis [269], gas detection [270], and optical telecommunications [271].

To support these applications, the use of tellurite glasses as an host material is attractive owing to its transparency in the 1.8-2.1 μm region. Tellurite glasses also enable dissolving a larger concentration of thulium ions compared to other mid-IR glasses such as chalcogenides. As a tellurite glass, Tm-doped TeO_2-ZnO-Na_2O-$ZnCl_2$ glass has previously shown larger absorption and emission cross sections in the $^3F_4 \rightarrow {}^3H_6$ transition region compared to silica glass [248, 272, 273]. Most of the Tm-doped tellurite glass laser media are fiber-based and provide relatively high power output but exhibit high power threshold [273].

Whispering gallery mode (WGM) cavities such as microspheres are ideal laser media as they are compact, they can achieve high Q-factors, and they have small optical mode volumes. Lasing in doped WGM cavities was previously shown for example in Er-doped silica and tellurite glass [40, 79, 274], and Er-Yb codoped tellurite glass [152], among others. While WGM lasers' output power is usually below 1 mW, they exhibit threshold power of few microwatts and efficient power conversion.

Threshold pump powers of 0.5 mW and up were shown in Tm-doped tellurite microspheres [227–229]. It is expected that the cavity Q-factor could be increased by using spheres of improved glass transmittance, leading to a laser threshold of few μW typically observed in doped WGM microcavities [40, 79]. In Tm-doped silica microspheres, for example, estimated threshold pump power of 50 μW was reported for near 2 μm emission [226].

In this paper, we report lasing emission at 1975 nm of Tm-doped tellurite glass microspheres. The threshold pump power of 30 μW for a pump wavelength of 1554 nm is the lowest ever reported for a Tm-doped tellurite microcavity by at least an order of magnitude [227–229]. Microwatts laser threshold values were achieved from microspheres with intrinsic Q-factors above 10^6, owing to the high purity and transparency of the host glass.

6.4 Tellurite fiber and sphere fabrication

The microspheres are made from a Tm-doped tellurite glass fiber. The glass is produced from high purity oxide and carbonate (Na_2CO_3) powders ($> 99.99\%$) dried separately at high temperature and mixed together as $74TeO_2$-$15ZnO$-$5Na_2O$-$5ZnCl_2$-$1Tm_2O_3$ (mol%). A second drying step is performed where the $ZnCl_2$ compound acts as a drying agent. The glass synthesis is done at 800°C during 1 hour. The melted glass is then transfered to a fiber preform and is slowly cooled down to 290°C to prevent crystallization. The preform is finally pulled into a monoindex optical fiber with a diameter of 210 μm. An undoped fiber and microspheres were also fabricated using similar techniques for comparison. The dopant concentration N_T is $(4.2 \pm 0.3) \times 10^{20}$ ions/cm^3.

The microspheres are fabricated using a two-step process. The tellurite fiber is first tapered to a 10 μm tip using a high power CO_2 laser. With additional laser pulses, the tip transforms into a microsphere due to surface tension. A silica tapered fiber is used to couple light in and out of the microsphere. The microsphere and the tapered fiber are encapsulated in a glass tube to prevent contamination and the reduction of the Q-factor as shown in [275].

Figure 6.1(a) presents the setup used to measure the Q-factors and the laser emission of the microspheres. The emission of a tunable laser source (TLS, Keysight 81600B) is sent to the microsphere using a silica tapered fiber with a diameter of 2 μm. An optical spectrum analyzer (OSA, Yokogawa AQ6375) measures the transmitted pump signal and the forward laser emission. A part of the injected pump signal is measured with an optical detector (DET). Finally, a polarization controller (PC) is used to optimize the coupling conditions. Figure 6.1(b) shows the image of a typical tellurite glass microsphere.

To measure the transmission spectra and the loaded Q-factors, the wavelength of the tunable laser is scanned over 1 nm near the wavelengths of 1504 nm, 1554 nm, 1585 nm, and 1629 nm. The OSA is set to zero span mode with a bandwidth of 2 nm. The narrower resonances were identified for each spectral regions, and a Lorentzian fit was used to determine the loaded Q-factors. A low power pump signal of 800 nW was used to prevent any thermal drifting. For the doped microspheres, additional care was taken to ensure that the Q-factor measurements were not affected by the ions absorption intensity dependence, i.e., with an injected power 25 times lower than the threshold power. The diameters of the doped and undoped spheres are approximately 30 μm.

Figure 6.2 presents the intrinsic Q-factors, Q_0, of undoped (black diamonds) and doped (red circles) microspheres for an undercoupled regime. The undoped microspheres resonances exhibit similar Q_0 of $\sim 2 \times 10^6$ between 1500 nm and 1630 nm, as expected. On the contrary, the doped spheres resonances suffer increasing losses at longer wavelengths. The comparison between the doped tellurite and the undoped tellurite Q-factors shows that the losses can

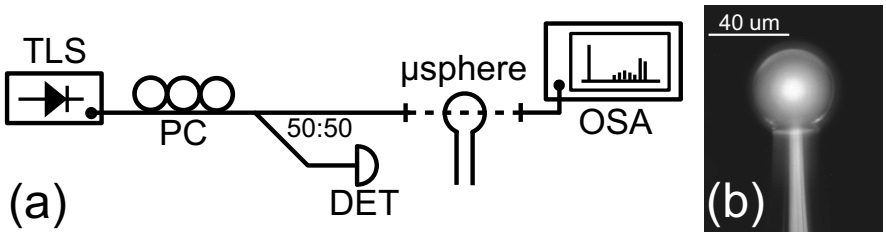

Figure 6.1 : (a) Experimental setup for Tm-doped tellurite glass microsphere laser emission - TLS : Tunable laser source, PC : Polarization controller, DET : Optical detector and OSA : Optical spectrum analyzer. (b) Microscope image of a typical tellurite microsphere.

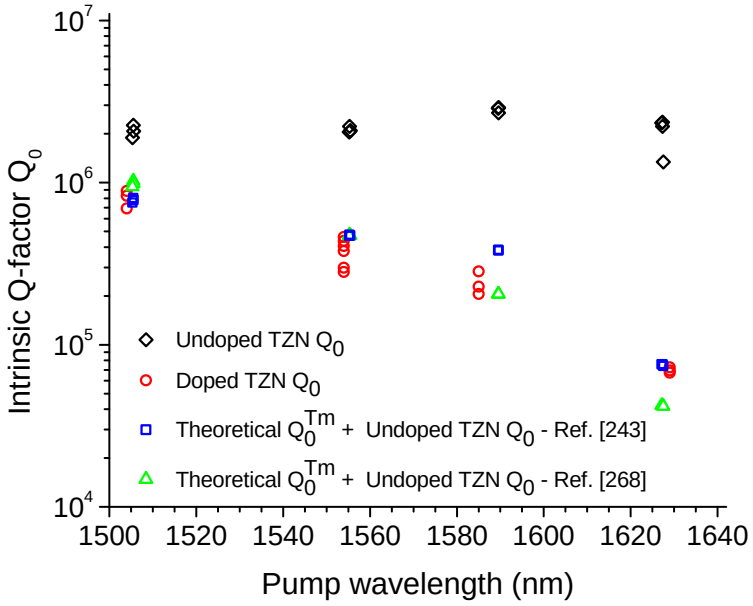

Figure 6.2 : Intrinsic Q-factor Q_0 for undoped tellurite spheres (black diamonds) and Tm-doped tellurite spheres (red circles) for an undercoupled regime. Theoretical intrinsic Q_0^{Tm} following absorption cross section values of [248, 273] are also shown.

be attributed to the dopant absorption. Following the WGM laser model of [40, 247], the intrinsic Q-factor, Q_0^{Tm}, related to the low pump power losses caused by the ions absorption can be calculated as

$$Q_0^{\mathrm{Tm}} = \frac{m_p}{R_c \sigma_{a,p}} \frac{\int_S |\vec{e}_p|^2 dS}{\int_S N_T |\vec{e}_p|^2 dS} \approx \frac{m_p}{R_c \sigma_{a,p} N_T} \tag{6.1}$$

where m_p is the azimuthal number of pump mode, $\sigma_{a,p}$ is the ions absorption cross section at the pump wavelength, R_c is the sphere radius, and N_T is the ions concentration. The approximation is valid since the evanescent field outside the cavity is negligible compared to the optical field inside. Using Eq. 6.1, the absorption cross section values of [248, 273], and the undoped tellurite Q_0 values, theoretical Q_0 can be found for $R_c = 15$ μm and $N_T = 4.2 \times 10^{20}$ ions/cm^3. They are plotted in Fig. 6.2 (blue rectangles and green triangles). The decreasing Q-factor with longer wavelengths arises mainly from the increasing absorption cross section of thulium [248, 273] as presented in Fig. 6.6.

6.5 Tm-doped sphere laser emission

Figure 6.3 shows the forward emission spectrum of a Tm-doped microsphere using the *Hold Max* feature of the OSA as the pump wavelength is continuously scanned from 1554 nm to 1555 nm with a pump power of 86 μW. The *Hold Max* feature cumulates the emission

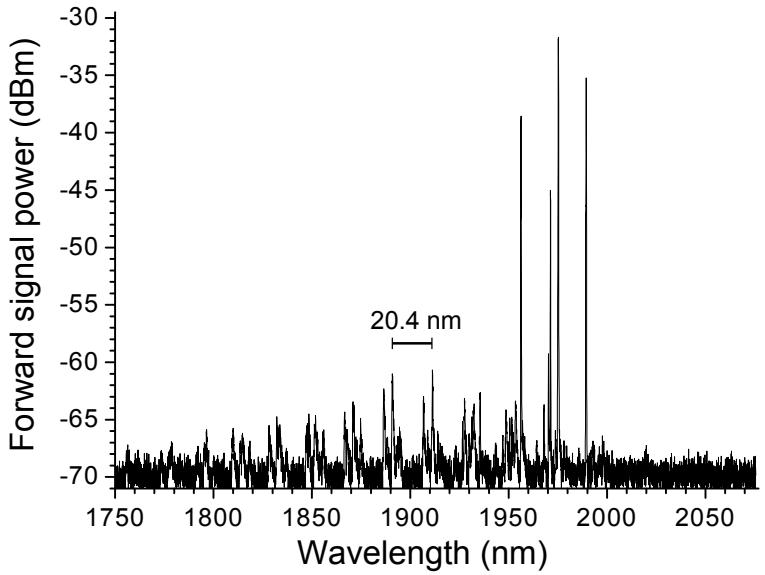

Figure 6.3 : Forward emission spectrum of a Tm-doped tellurite glass microsphere. The photoluminescence of the Tm ions is filtered by the cavity resonances. Multimode laser emission lines are also visible and are centered at a wavelength of 1975 nm.

spectra resulting from the successive excitation of resonances scanned by the pump laser. The photoluminescence of the Tm ions is filtered by the cavity resonances. It is visible from 1775 nm to 2000 nm and is centered around a wavelength of 1900 nm. It displays a free spectral range of successive azimuthal order modes of 20.4 nm which is associated with a cavity radius of ~ 14 μm, in agreement with visual inspection of the sphere. Laser emission lines are also measured and are centered at wavelengths around 1975 nm. The emission is multimode because many modes achieve lasing threshold conditions. These modes usually have high Q-factors and a good field overlap with the pump mode. Laser lines occur at the long-wavelength side of the photoluminescence spectrum due to the large thulium ions concentration. The laser signal gets absorbed and re-emits to longer wavelengths following a non radiative decay in the $^3\mathrm{F}_4$ band [229, 276].

Three threshold curves are presented in Fig. 6.4 for three different pump resonances near a wavelength of 1554 nm. The measurement technique is similar to [253, 265]. Similarly to the Q-factor measurements, the OSA is used in zero span mode, and its measurement bandwidth of 2 nm is centered on the strongest emission peak at a wavelength of 1975 nm . Linear fit are used to extract the lasing threshold coupled power and the efficiency of the emission process. Each curve has a different threshold value $P_{p,th}^{coup}$ of 8.6 μW, 17.2 μW, and 25 μW and internal efficiency $\eta_{in} = dP_s/dP_p^{coup}$ of 4 %, 3 %, and 1.6 % respectively. This is due to their different intrinsic Q-factors, coupling conditions, and mode overlaps with the signal mode at 1975 nm.

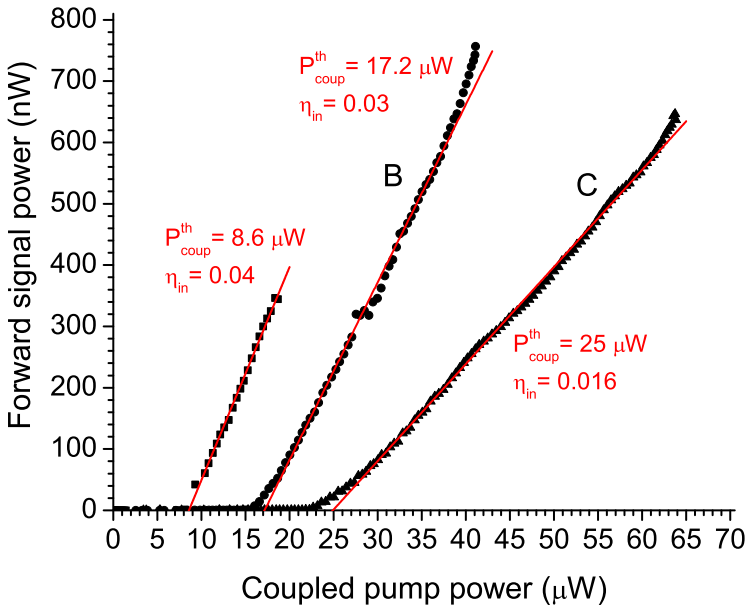

Figure 6.4 : Forward signal power at a wavelength of 1975 nm versus the coupled pump power. The input pump power is 86 μW. Curve A, B and C represent different pump resonances near a wavelength of 1554 nm.

Based on their resonance's transmission T, all the curves have similar threshold injected powers $P_p^{in} = P_p^{coup}/(1-T)$ of ~ 30 μW. These coupled and injected power values are the lowest measured for a Tm-doped tellurite glass microcavity to the authors' knowledge.

Since the ions absorption cross section depends strongly on the pump wavelength, it is interesting to see how it affects the threshold power and the lasing efficiency. Figure 6.5 presents the forward signal power as a function of the coupled pump power for three different pump modes, each near different pump wavelengths of 1504 nm, 1554 nm, 1585 nm, and 1629 nm. The threshold coupled pump power $P_{p,th}^{coup}$ and the internal efficiency η_{in} tend to be lower and higher respectively at a longer wavelength where the ions absorption cross section is more important.

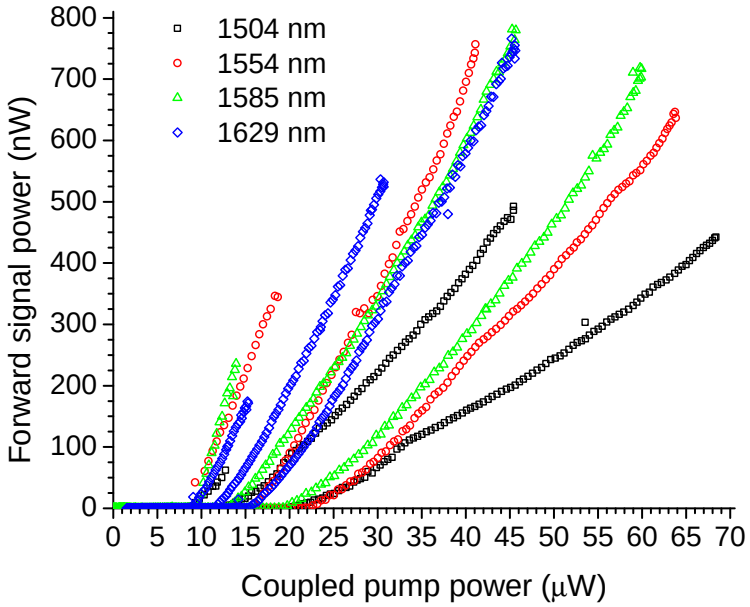

Figure 6.5 : Forward signal power at a wavelength of 1975 nm versus the coupled pump power near wavelengths of 1504 nm (black squares), 1554 nm (red circles), 1585 nm (green triangles), and 1629 nm (blue diamond). For each pump wavelength regions, three curves represent different pump resonances.

Both can be calculated as [40, 247] [1]

$$\eta_{in} = \frac{m_p^2\omega_s^3}{m_s^2\omega_p^3}\frac{N_s|\vec{e}_p|^2_{max}}{N_p|\vec{e}_s|^2_{max}}\frac{\tau_s}{\tau_{s,c}}\frac{\gamma_p^{Tm}}{\left(\gamma_p^{Tm}+\frac{1}{2\tau_{p,0}}\right)} \tag{6.2}$$

$$P_{p,th}^{coup} = \frac{2\hbar R_c}{c^2\tau_{Tm}\left[\sigma_{a,s}+\sigma_{e,s}\right]}\left(\frac{N_T\omega_s\tau_s R_c\sigma_{a,s}}{m_s}+1\right)\frac{\omega_s^2}{m_s\tau_{s,c}}\frac{N_s}{|\vec{e}_s|^2_{max}}\frac{1}{\eta_{in}} \tag{6.3}$$

where $N_{p,s} = \int_V n_0^2(\vec{r})|\vec{e}_{p,s}|^2 dV$ are the normalization factors and $|\vec{e}_{p,s}|^2_{max}$ are the maximum values of $|\vec{e}_{p,s}|^2$ for the pump and emitted signal respectively, $n_0(\vec{r})$ is the refractive index profile and $\omega_{p,s}$ are the pump/signal frequencies. $\tau_{s,c}$, $\tau_{p,0}$ and $\tau_{Tm} \approx 1.35$ ms are the decay time of the signal coupling losses, the decay time of the pump intrinsic losses, and the ions lifetime of the $^3F_4 \rightarrow {}^3H_6$ transition related to the ions concentration [248]. $\tau_s = (1/\tau_{s,0} + 1/\tau_{s,c})^{-1}$ is the total decay time of the signal resonance without the gain of the ions.

1. This chapter is the reproduction of the submitted article to Optics Letters and the revised laser model of chapter 2.6 was developed afterward. It is more accurate as it takes into account mode overlap for a N_2 distribution that follows the pump signal distribution. The relations 6.2 and 6.3 given in this chapter are found using a fixed N_2 distribution and the maximum values $|\vec{e}_{p,s}|^2_{max}$. This approximated model is valid if both the pump and signal modes have similar field distributions and the N_2 population is located near these maxima. In microspheres, this happen when both modes are first order radial modes with $l_j = m_j$ for large resonators. These modes are used for the calculations of Fig. 6.6

$\sigma_{a(e),p(s)}$ are the ions absorption (emission) cross sections of the pump (signal) respectively. $\hbar$ and c are the Planck constant and the speed of light in vacuum. Finally, γ_p^{Tm} is the clamped pump loss rate due to the ions absorption above the lasing threshold, and it is defined by

$$\gamma_p^{Tm} = -\frac{1}{2\tau_s}\frac{m_s\omega_p}{m_p\omega_s}\left(\frac{N_T\omega_s\tau_s R_c\left[\sigma_{a,s}\sigma_{e,p}-\sigma_{a,p}\sigma_{e,s}\right]}{m_s\left[\sigma_{a,s}+\sigma_{e,s}\right]}+\frac{\left[\sigma_{a,p}+\sigma_{e,p}\right]}{\left[\sigma_{a,s}+\sigma_{e,s}\right]}\right).$$

As it can be seen from Fig. 6.2, the pump mode losses are dominated by the ions absorption while the intrinsic resonator losses such as scattering are constant. This means that γ_p^{Tm} increases while $\tau_{p,0}$ remains constant at longer wavelengths. Following Eq. 6.2 and Eq. 6.3, for similar lasing signal modes characteristics, η_{in} should increase and $P_{p,th}^{coup}$ should decrease at longer wavelengths where the thulium absorption cross section is larger, this is in agreement with the experimental results of Fig. 6.5.

Figure 6.5 shows the emission power for a signal mode located at 1975 nm pumped by different pump modes. The signal mode characteristic values such as the coupling Q-factors Q_c and the intrinsic Q-factor Q_0 that excludes the ions gain can be extracted from these curves using Eq. 6.2 and Eq. 6.3. Fig. 6.6 shows the extracted Q_0 and Q_c for each pump wavelength. As expected, the intrinsic and the coupling Q-factors share similar values near $\sim\ 6\times10^4$ and $\sim\ 8\times10^5$ respectively. The larger variation of the Q_c values can be linked

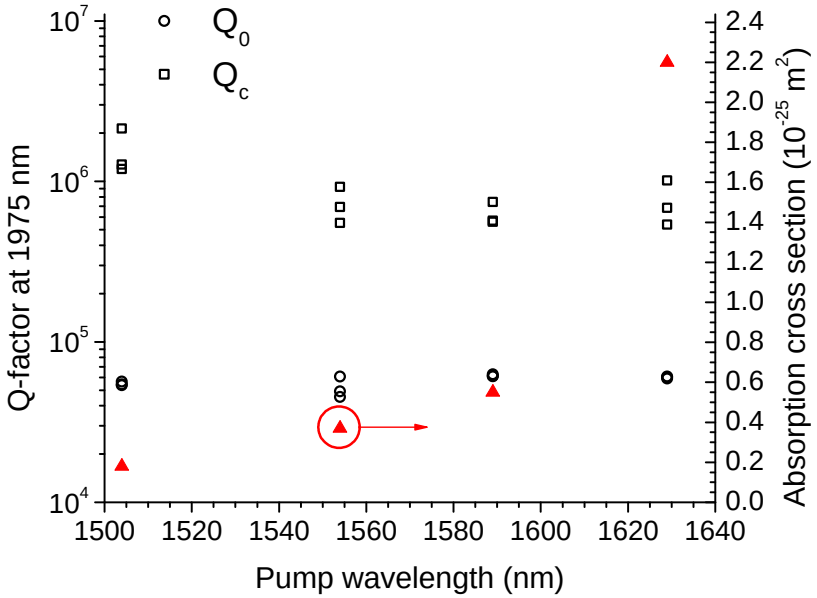

Figure 6.6 : Signal resonance Q_0 (black circles) and Q_c (black squares) at 1975 nm obtained by fitting their threshold curves at different pump wavelengths for 1st order radial modes. The fitted absorption cross sections (red triangles) are also shown.

to the undercoupled regime conditions where small variations of the Q_0 values cause large variations of the associated Q_c values. The best results were obtained by using the pump absorption cross section also shown in Fig. 6.6. These values are in good agreement with the values from [248, 273].

6.6 Conclusion

In conclusion, we presented measurements of low threshold laser emissions at a wavelength of 1975 nm of Tm-doped tellurite glass microspheres. The threshold pump power of 30 μW is the lowest value reported for a Tm-doped microcavity and at least a tenfold improvement for a Tm-doped tellurite microcavity. Different pump wavelengths were used, and the results show better lasing performances at longer pump wavelengths where ions absorption cross section is larger, in agreement with the theoretical models.

CHAPTER 7 GENERAL DISCUSSION

The broad goal of this thesis is to study As_2S_3 microspheres as potential mid-IR sources for emission above the wavelength of 2 μm. Stimulated and cascaded Raman scattering processes were chosen because of their broad applicability across the entire transparency window of materials. Additionally, cascaded Raman generation is naturally suitable to WGM microcavities such as microspheres. To extend the emission further in the infrared, the idea of combining ions-doped glass laser emission and Raman emission inside the same cavity was tested. Tm-doped tellurite glass was used due to the unavailability of good quality ions-doped As_2S_3. It represents a good alternative to As_2S_3 since it can be produced with high purity and possesses a good Raman gain coefficient (Table 1.2).

Chapters 4 to 6 present the results that were obtained in this thesis. The main achievements and novelties are summarized here :

1. Fabrication of As_2S_3 microspheres with the largest quality factors reported for a chalcogenide cavity.
2. Generation of stimulated Raman scattering emission in As_2S_3 microspheres with few tens of μW of input power at a wavelength of 1550 nm.
3. Generation of cascaded Raman scattering emission in As_2S_3 microspheres :
   - up to the fifth Raman order at a wavelength of 2140 nm from a pump wavelength at 1550 nm.
   - up to the third Raman order at a wavelength of 2350 nm from a pump wavelength at 1880 nm.
4. Generation of laser emission at a wavelength of 1975 nm based on high Q-factors Tm-doped tellurite microspheres with few μW of input power.

It is important to compare this thesis work to other Raman and cascaded Raman WGM sources to put it in its context. Some aspects need to be discussed to explain why important results were not obtained. Notably, it was not possible to

1. Generate long-term stable cascaded Raman emissions above the third Raman order in As_2S_3 microspheres.
2. Generate simultaneous ions-doped laser and Raman emissions in Tm-doped tellurite microspheres.

Finally, for the sake of future works, a discussion on the feasibility of Raman lasing in ions-doped cavities is undertaken.

7.1 Are As_2S_3 microspheres good Raman WGM sources ?

It is interesting to compare the Raman emission characteristics with other WGM Raman sources. Table 7.1 gives an overview of the current SRS performances reported in WGM microcavities, including the results presented in this thesis. Favorably, input threshold power levels are comparable to the values obtained in SiO_2 and CaF_2 resonators despite the smaller Q-factors. However, the external power conversion efficiency lacks behind.

Both internal and external efficiencies are improved if the $Q_{j,T}/Q_{j,c}$ ratio are increased for the pump and the Raman signal modes. Two solutions are possible : reducing the coupling Q-factors or increasing the intrinsic Q-factors.

The first solution is to bring down the coupling Q-factors values closer to the intrinsic Q-factors. To do so, the coupling load between the cavity and waveguide modes has to be increased by reducing the gap or changing the waveguide properties. The former is not possible in our case since the tapered fiber is in contact with the sphere. The problem resides mainly in the refractive index difference between the sphere As_2S_3 (n=2.43) and the waveguide silica (n=1.45). The phase matching conditions between the sphere and tapered fiber modes are not optimized. For example, better conversion efficiencies are obtained for SiO_2 cavities and silica tapered fibers as shown in the first two lines of Table 7.1. The effective mode index n_{eff} would increase from ~ 1.36 for a single mode silica tapered fiber ($\varnothing \sim 2$ μm) to ~ 2.2 for a single mode As_2S_3 tapered fiber ($\varnothing \sim 1$ μm), closer to the sphere's modes effective index.

The fabrication of single mode As_2S_3 tapered fibers with a diameter of $\varnothing \sim 1$ μm is possible despite their fragility [196]. The use of multimode waveguides with larger diameters would

Table 7.1 : SRS performances of reported WGM microcavities.

Material	$\boldsymbol{\lambda}$ **(μm)**	**Length** $\boldsymbol{L_c}$ **(μm)**	$\boldsymbol{Q}$	**Threshold power(μW)**	**Conversion efficiency**	**Reference**
SiO_2	1.55	40π	1×10^8	62	36 %$^{(b)}$	[122]
	1.55	55π	6×10^7	$74 - 250$	45 %$^{(b)}$	[124]
Ti-SiO_2	0.765	-	2.4×10^7	52.6	-	[277]
Si	1.55	30000	$3.4 \times 10^{6\dagger}$	80000	6 %	[278]
CaF_2	1.064	5000π	2.6×10^{10}	3	5 %	[126]
	1.064	100π	1×10^8	15$^{(e)}$	-	[126]
	1.064	5000π	6.9×10^9	78	32 %	[127]
As_2S_3	1.55	71π	3×10^7	35	2.2 %$^{(b)}$	This work

$^{(e)}$ Estimated, $^{(b)}$ Bidirectional, † Evaluated from the waveguide losses.

cause mode mixing between the input and output modes, and reduce the overall coupling efficiencies. Rigorous simulations such as [37] that include effects of the waveguide RI, diameter and distance are needed in addition of precise fabrication techniques.

It is important to note that the performances of As_2S_3 WGM Raman sources presented in this thesis cannot be significantly improved using the current glass purity of the fiber. Figure 7.1 displays how decreasing $Q_{p,c}$ affects the input threshold power and the external efficiency. The Raman mode properties found in Section 4.7.2 are kept constant. The input threshold power can be reduced from 35 μW to 13 μW only if critical coupling is achieved. At this coupling condition, the external efficiency increases from 2.2 % to match the internal efficiency value of 10.7 %.

The second solution is to increase $Q_{j,0}$ while the coupling Q-factors remain constant. It improves $Q_{j,T}$, the threshold power and the conversion efficiency. It is the best solution but it is hard to realize. A larger $Q_{j,0}$ implies the improvement of the As_2S_3 fiber purity, a feature that was out of our control. It is however a realistic option for future works. Glass attenuation values $\sim$ 30dB/km at 1.5 μm were obtained by others [174, 193], pushing the Q-factor limit above 10^9. Based on the results of Chapter 4 and Section 4.7.2, Figure 7.2 shows how an increase of $Q_{p,0}$ improves the input threshold power and the external efficiency. The input threshold power drops drastically and could even reach the μW level when $Q_{p,0} = Q_{p,c}$ at critical coupling. The external efficiency also increases to equal the internal efficiency of

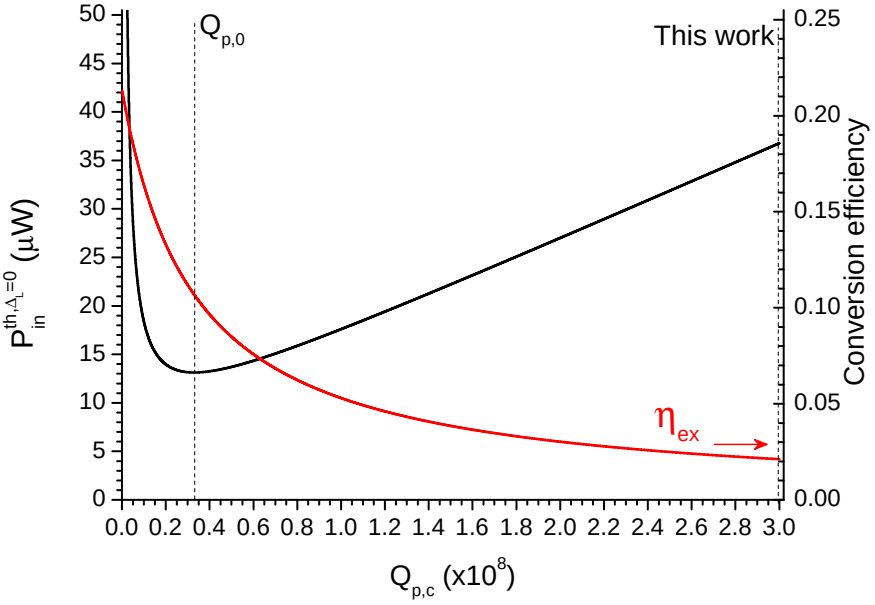

Figure 7.1 : Consequence of a smaller coupling Q-factor $Q_{p,c}$ for the pump mode. The Raman mode Q-factors remain constant and are based on the results of Chapter 4.

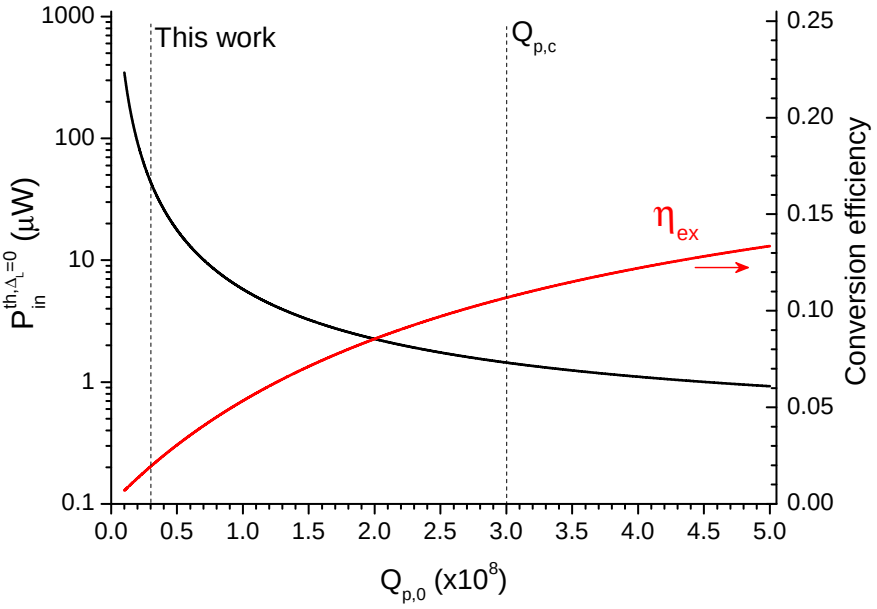

Figure 7.2 : Consequence of a larger intrinsic Q-factor $Q_{p,0}$ for the pump mode. The Raman mode Q-factors remain constant and are based on the results of Chapter 4.

10.7 %.

By comparing both solutions in Fig. 7.1 and 7.2, it is obvious that a large change of $Q_{p,c}$ is equivalent to a small change of $Q_{p,0}$ when the threshold power is considered. Furthermore, improving the purity of the glass will, in all likelihood, increase the Raman mode intrinsic Q-factor as well. Figure 7.3 displays the case where $Q_{p,0} = Q_{s,0}$ are increased while $Q_{p,c} = Q_{s,c} = 3 \times 10^8$ are kept constant. Despite the small reduction of the input threshold power, both the external and internal efficiencies are largely improved and reach ~ 50 % for critical coupling.

Following these remarks, the improvement of the As_2S_3 glass purity should be the next step of future works to improve the WGM Raman source performances.

7.2 Are As_2S_3 microspheres good cascaded Raman WGM sources ?

A few works on cascaded Raman WGM sources were published [106, 123, 124, 126, 279]. Table 7.2 regroups the best performances of different materials. The performances of As_2S_3 and SiO_2 microcavities are comparable : they present the same number of observed Raman orders and their threshold pump powers are of the same order. A larger number of Raman orders were demonstrated in CaF_2 WGM resonators with better threshold powers. This is largely due to their superior Q-factors. Additionally, the mode overlap is better when both

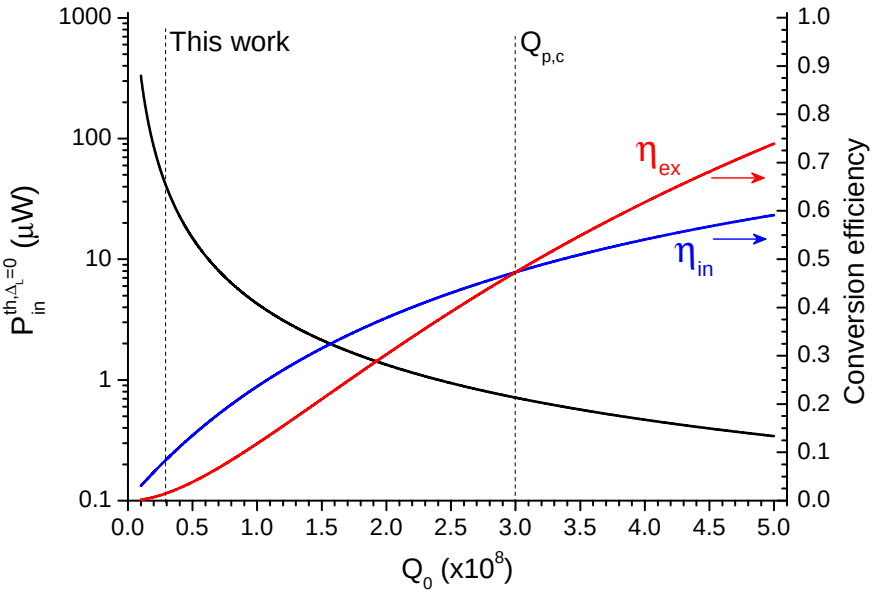

Figure 7.3 : Consequence of a larger intrinsic Q-factor $Q_{j,0}$ for the pump and the signal modes. The couping Q-factors $Q_{p,c} = Q_{s,c}$ remain constant.

modes have closer resonance wavelengths, but the Raman shift is larger at longer wavelengths. The Raman shift is ~ 40 nm for CaF_2 resonators at a pump wavelength of 1064 nm. In comparison, Raman shifts are ~ 100 nm and ~ 160 nm at pump wavelengths of 1550 nm and 1880 nm for As_2S_3 spheres. Yet, both materials have similar Raman shift frequencies. This limits the number of observed Raman orders in our case.

However, signal generation at wavelengths above 2 μm is only demonstrated in this thesis work. The observed output power of few μW for both pump wavelengths of 1550 nm and 1880 nm indicates that cascaded Raman performances are similar for the first two Raman orders at least. Furthermore, the setup used for the pump emission at 1880 nm, shown in Fig. 5.6, lacked important optical components. More specifically, with the absence of a narrow tunable band-pass filter and a polarizer, the pump emission becomes largely multimode, leading to mode competition over the available gain and to emission instability. The large number of pump modes can then feed more Raman modes, as seen by comparing the emission bandwidth of each Raman order in Fig. 5.4 and Fig. 5.7. Moreover, multimode Raman emission is observed for both setups and makes it difficult to clearly characterize the behavior of each Raman order.

For both pump wavelengths, second and third Raman order emissions were regularly observed in high Q-factors As_2S_3 microspheres, supporting their natural ability for cascaded emission. Fourth Raman order lines were also frequently generated with a pump wavelength of 1550 nm.

Table 7.2 : Reported cascaded Raman performances in WGM microcavities.

Material	**Ref.**	**Q**	**Pump λ (μm)**	**Raman order**	**Raman λ (μm)**	**Threshold power**[†] **(μW)**	**Maximum power**[‡] **(μW)**
SiO_2	[123]	1×10^8	0.980	1	1.025	54 | 425	25 μW
				2	1.060	75 | 450	10 μW
				3	1.120	120 | 490	400 nW
				4	1.180	180 | 575	50 nW
				5	1.225	- | 900	0.3 nW
CaF_2	[126]	2.6×10^{10}	1.064	1	1.102	3	6 μW
				2	1.142	7.5	2 μW
				3	1.186	-	3 nW
				4	1.234	-	3 nW
				5	1.284	-	6 nW
				6	1.340	-	3 nW
				7	1.400	-	600 pW
				8	1.466	-	30 pW
As_2S_3	This work	$10^6 - 10^7$	1.55	1	1.646	370 | 70	13 μW
				2	1.746	430 | 70	11 μW
				3	1.861	607 | 220	3 μW
				4	1.991	-	300 nW
				5	2.140	-	500 nW
			1.88	1	2.015	-	2 μW
				2	2.170	-	500 nW
				3	2.350	-	20 nW

[†] Multiple values are attributed to different sets of measurements
[‡] Not related to the threshold powers

This suggests that the observation of a fourth Raman order with a pump wavelength of 1880 nm may be limited only by the optical spectrum analyzer detection range of 2500 nm.

Despite their smaller Q-factors, As_2S_3 microspheres perform well as cascaded Raman WGM sources. The improvement of glass purity will certainly increase those performances by reducing the threshold power of each Raman order and boosting their power conversion efficiencies. Additionally, future efforts should be focused on the stability of Raman emissions. This issue is discussed in the next section and setup modifications are proposed.

7.3 Stabilization issues of the self-frequency locking laser setup

One issue of this work is the emission stabilization when multiple Raman lines are generated. The setup presented in Fig. 5.1 filters and stabilizes the pump emission but does not affect

the generated signals as shown in Fig. 5.4 and Fig. 5.7. Power fluctuation in each mode can influence the whole cascading process. For example, if the first Raman order emission has a single line, the gain available for the second Raman order emission comes from a unique source. If the first Raman order emission is multimode, the second Raman order emission feeds on the gain of two different sources, causing power fluctuation. This issue is transfered to each successive Raman order and is worsened when multiple emission lines appear in each order group. This not only renders the emission unpredictable but it also diminishes the available Raman gain for every line.

For As_2S_3 spheres, many high Q-factor modes are available within the Raman gain bandwidth. Three emission lines or more belonging to the first Raman order are regularly seen when a third Raman order starts lasing. This random behavior prevented accurate measurements of the emission power above the third Raman order, as depicted in Fig. 5.5.

A potential solution is to use multiple filtering steps for each Raman order. The simplest method is to place the microsphere between Bragg mirrors as shown in Fig. 7.4. The advantages are twofold : the emission wavelength of each Raman order can be selected within the filters bandwidth and stable single line emissions would be possible. However, to optimize the cascaded Raman emission, tunable filters are required to select the best modes sequence. Additionally, to achieve efficient emission at wavelengths above 2 μm, silica fibers components need to be replaced by ones transparent in the mid-IR, especially between the backward Bragg mirrors and the forward output. Fortunately, chalcogenide glass tapered fibers [196] and fiber Bragg gratings written in As_2S_3 [280] were demonstrated in the recent years. The latter are already used as part of efficient Raman and cascaded Raman fiber lasers [257, 262]. The setup implementation shown in Fig. 7.4 follows naturally the work presented in this thesis and is conceivable within the next years.

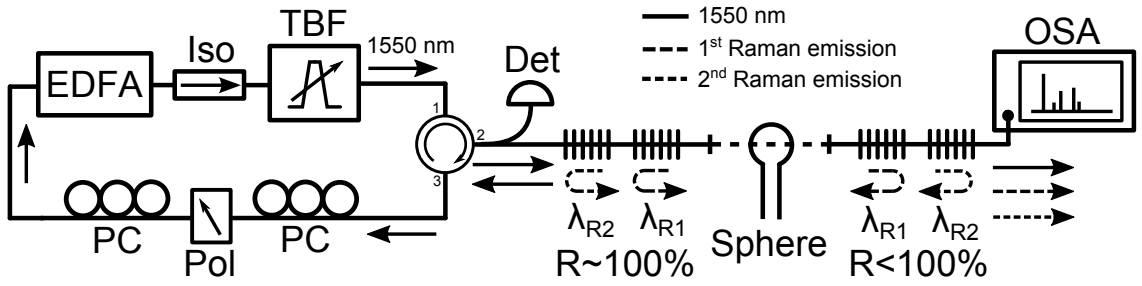

Figure 7.4 : Modified self-frequency locking laser setup including additional filtering steps. EDFA : Erbium Doped Fiber Amplifier, Iso : Isolator, TBF : Tunable Bandpass Filter, PC : Polarization Controler, Pol : Polarizer, OSA : Optical Spectrum Analyzer, Det : Photodiode detector.

7.4 Raman emission in Tm-doped tellurite glass WGM lasers

As mentioned previously, ions doped tellurite glasses are promising materials for combining laser and Raman emissions. In view of mid-IR emission, lasers sources at wavelengths near 2.8 μm based on erbium ions are conceivable in tellurite glasses, unlike silica glass. Compared to chalcogenide glasses, tellurite glasses also have better resistance to crystallization when they are doped with rare-earth ions [233, 234], meaning that larger ions concentrations are possible. The realization of Tm-doped tellurite WGM lasers near wavelengths of 2 μm with a few μW of input pump power improved the current performances of tellurite microcavity lasers. However, it was not possible to generate Raman lines combined with the laser emission of the Tm ions.

This issue comes from the glass purity of the microspheres. Figure 6.2 displayed the measured intrinsic Q-factors for the doped and undoped tellurite glass microspheres. The undoped microspheres exhibit $Q_0 \sim 2 \times 10^6$ at pump wavelengths between 1500 nm and 1630 nm, at least an order of magnitude smaller than Q_0 measured for As_2S_3 microspheres. Since the input threshold power goes as $\propto (g_R^{(b)} Q^2)^{-1}$, it is expected to be $\sim$ 200 times larger for tellurite glass spheres, near 6 mW. This value is far from the μW power levels that were used in Chapter 6. For example, Raman emission measurements at input power of 1 mW were unsuccessful. The same conclusions remain valid in the case of doped tellurite glass since the fabrication steps were similar. Raman threshold conditions are expected to be even harder to reach as the extracted Q_0 at 1975 nm are $\sim 6 \times 10^4$.

Again, the purification of the glass is the key element to improve. Intrinsic Q-factors $\sim 2 \times 10^6$ are related to attenuation coefficients $\alpha_{lin} \sim 4.4$ m^{-1} or $\sim$ 19 dB/m at a wavelength of 1550 nm. Fortunately, tellurite fibers of similar compositions with attenuation below 1-2 dB/m were demonstrated [281, 282] [1], pushing the intrinsic Q-factor limit to 4×10^7.

Compared to the attenuation of bulk glass samples, the current glass purity is not decreased by the sphere fabrication steps, at least for the C-band wavelengths. Extracted $Q_0 \sim 6 \times 10^4$ at 1975 nm, however, show a large drop in quality down to $\sim$ 500 dB/m that cannot be attributed to the ions absorption. The melting process in an 'open-air/nitrogen' environment during the fiber pulling steps and the sphere formation may have contributed to the glass degradation with the incorporation of water and other contaminants. Future works should focus not only on better purification steps, but also on studying effects of the melting environment on the glass degradation.

1. Commercial tellurite optical fibers display an attenuation below 0.5 dB/m for wavelengths between 1 μm and 4 μm.

7.5 Achieving Raman lasing in ions doped WGM microcavities

To push the emission wavelength toward the mid-IR, the idea to generate Raman emission pumped by the laser signal of an ions doped cavity is worth studying. The following section is intended to give predictions on the pump power levels needed to generate hybrid sources and is based on the Tm-doped sphere laser characteristics.

As presented in Table 1.2, the Raman shift of tellurite glass is $\sim$ 19.9 THz, pushing the Raman emission almost twice as far as the As_2S_3 shift. Following Chapter 6 results, a pump wavelength of $\lambda_p = 1554\ nm$ feeds the laser signal with a wavelength of $\lambda_s \sim 1975$ nm. Raman scattering pushes the Raman lines to wavelengths $\lambda_R \sim 2270$ nm. Figure 7.5 presents their modal distributions for a sphere radius of 14 μm. Despite the large wavelength gap between the three signals, their field distributions are similar. Additionally, the sphere dimensions confine the optical energy into small mode volumes : $V_p = 157\ \mu m^3$, $V_s = 207\ \mu m^3$ and $V_R = 243\ \mu m^3$. The mode overlap of the laser signal and Raman modes is $V_{ssRR} = 451\ \mu m^3$.

To predict the input threshold power needed to generate a Raman signal through the laser emission, the coupled-modes equations of the Raman emission, Eq. 2.24 to 2.26, are combined with the laser CM relations, Eq. 2.49 and 2.50 :

$$\frac{da_p}{dt} = g_{Tm}^{(p)} a_p(t) - \frac{1}{2\tau_p} a_p(t) + i(\omega_L - \omega_p) a_p(t) + i\kappa_{pL} s_L(z_0, t) \tag{7.1}$$

$$\frac{da_s}{dt} = g_{Tm}^{(s)} a_s(t) - \frac{1}{2\tau_s} a_s(t) - g_R \frac{\omega_s}{\omega_R} \left(|a_R(t)|^2 + |a_{-R}(t)|^2 \right) a_s(t) \tag{7.2}$$

$$\frac{\partial a_R(t)}{\partial t} = -\frac{1}{2\tau_R} a_R(t) + g_R |a_s(t)|^2 a_R(t) \tag{7.3}$$

$$\frac{\partial a_{-R}(t)}{\partial t} = -\frac{1}{2\tau_R} a_{-R}(t) + g_R |a_s(t)|^2 a_{-R}(t). \tag{7.4}$$

with

$$g_{Tm}^{(p)} = \frac{\omega_p}{2m_p} \left[(\sigma_{ep} + \sigma_{ap}) N_2^{max} \frac{B_{pp}}{B'_p C^{max}} - \sigma_{ap} N_T \frac{B_p}{B'_p} \right]$$

$$g_{Tm}^{(s)} = \frac{\omega_s}{2m_s} \left[(\sigma_{es} + \sigma_{as}) N_2^{max} \frac{B_{ps}}{B'_s C^{max}} - \sigma_{as} N_T \frac{B_s}{B'_s} \right]$$

$$gR = \frac{c^2 g_R^{(b)}}{2 n_s n_R V_{ssRR}},\ V_{ssRR} = \frac{\int_V |\mathbf{e}_s|^2 dV \int_V |\mathbf{e}_R|^2 dV}{\int_V |\mathbf{e}_s|^2 |\mathbf{e}_R|^2 dV},\ C^{max} = \frac{|e_{p/s,\theta}^{max}(t)|^2}{(\rho \sin\theta)|_{max}}$$

$$B_{p/s} = \int_A \frac{|e_{p/s,\theta}(\rho,\theta,t)|^2}{\rho \sin\theta} \rho dA,\ B'_{p/s} = \int_A \frac{|e_{p/s,\theta}(\rho,\theta,t)|^2}{\rho \sin\theta} dA$$

$$B_{pp} = \int_A \frac{|e_{p,\theta}(\rho,\theta,t)|^4}{\rho^2 \sin^2\theta} \rho dA \text{ and } B_{ps} = \int_A \frac{|e_{p,\theta}(\rho,\theta,t)|^2 |e_{s,\theta}(\rho,\theta,t)|^2}{\rho^2 \sin^2\theta} \rho dA.$$

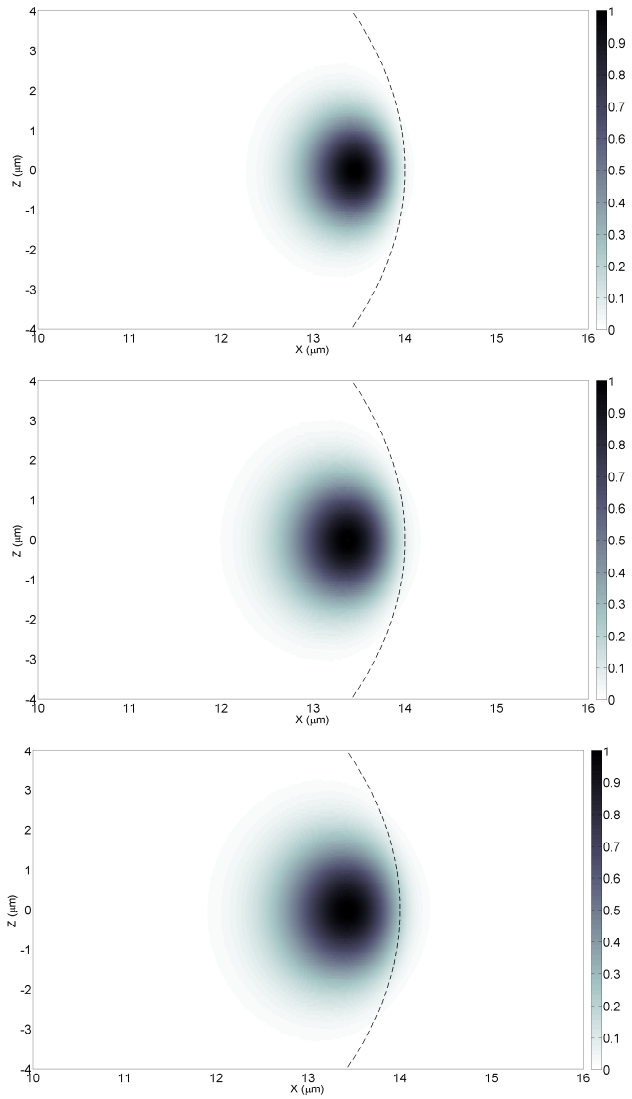

Figure 7.5 : Transverse view of the pump (top), laser signal (center) and Raman signal (bottom) TE modes corresponding to a wavelength of 1554 nm ($m_p = l_p = 106$), 1975 nm ($m_p = l_p = 82$), and 2270 nm ($m_p = l_p = 71$) respectively.

The laser signal mode $a_s(t)$ can now transfer energy to the clockwise and counterclockwise Raman modes, $a_R(t)$ and $a_{-R}(t)$.

In a CW regime, the threshold condition for laser emission is the same :

$$g_{Tm}^{(s)} = \frac{1}{2\tau_s}.$$

The Raman threshold condition is achieved afterward when

$$|a_s(t)|^2 = \frac{1}{2\tau_R g_R} \quad \text{or} \quad P_{S,out}(t) = \frac{|a_s(t)|^2}{\tau_{s,c}} = \frac{1}{2\tau_{s,c}\tau_R g_R}.$$

Relation 2.55 gives directly the necessary input power level

$$P_{in,th} = \frac{\dfrac{1}{2\tau_R g_R} + \dfrac{2}{\tau_{Tm}} \dfrac{\hbar\omega_s^2 \mu_0 N_s}{m_s(\sigma_{es}+\sigma_{as})} \dfrac{B_p}{B_{ps}} \left(\dfrac{N_T \omega_s \tau_s}{m_s} \dfrac{B_s}{B'_s} \sigma_{as} + 1 \right)}{\dfrac{2\tau_s}{\tau_{p,c}} \dfrac{m_p^2}{m_s^2} \dfrac{\omega_s^3}{\omega_p^3} \dfrac{B'_p}{B'_s} \dfrac{N_s}{N_p} \dfrac{}{(\omega_L - \omega_p)^2 + (\frac{1}{2\tau_p} - g_{Tm,th}^{(p)})^2} - g_{Tm,th}^{(p)}}$$

where $g_{Tm,th}^{(p)}$ is defined by Eq. 2.54.

Figure 7.6 shows the evolution of the input power threshold for the laser signal (black lines) and the successive Raman signal (blue lines) as the intrinsic Q-factors of each mode are increased. The coupling Q-factor for the pump mode is fixed to 5×10^6, a typical value measured with Tm-doped tellurite spheres. For both signals, the improvement of Q_0 based on better glass purification has a drastic effect on the threshold powers. The laser signal only need few μW of pump power to oscillate at realistic $Q_0 \sim 10^7$, a tenfold improvement over

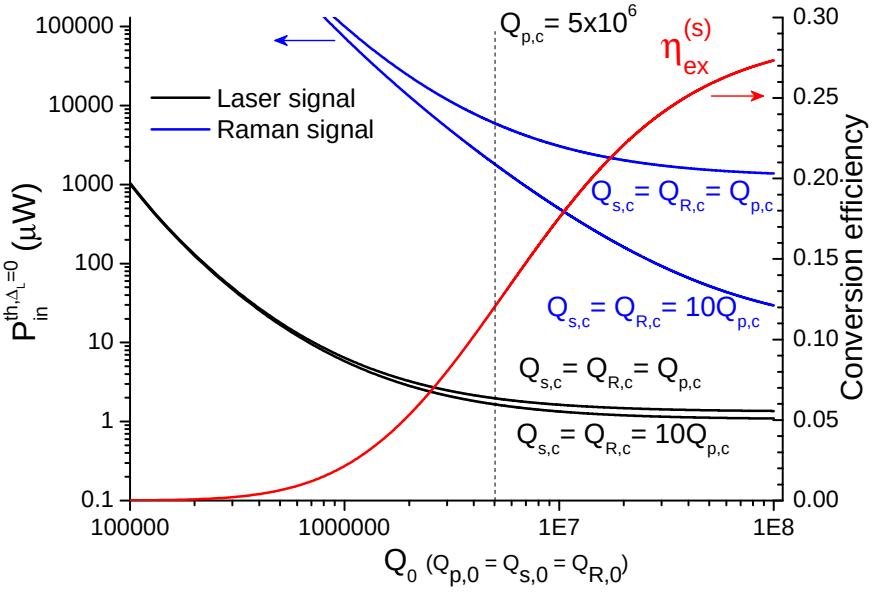

Figure 7.6 : Input pump threshold power to achieve lasing (black lines) and simultaneous first order Raman emission (blue lines). For each case, two curves are shown and represent two coupling conditions : $Q_{s,c} = Q_{R,c} = Q_{p,c}$ and $Q_{s,c} = Q_{R,c} = 10Q_{p,c}$. The laser signal external power conversion efficiency, $\eta_{ex}^{(s)}$, is shown in red.

the current threshold values.

However, the Raman signal needs a few milliwatts of pump power to start if the coupling Q-factors are equal. The large gap between both threshold powers is explained by the relatively small power conversion efficiency and coupling Q-factors of the laser signal and Raman modes. The effect of an increasing conversion efficiency is clearly seen for Q_0 between 10^6 and 10^7. For an almost constant threshold power value, the excess pump power is transfered to the laser signal more rapidly as the external conversion efficiency $\eta_{ex}^{(s)}$ increases (red line). This means $|a_s(t)|^2$ reaches the threshold conditions with a smaller amount of excess pump power.

The impacts of a coupling Q-factor modification are visible through the second set of pump threshold evolution where $Q_{s,c} = Q_{R,c} = 10Q_{p,c}$. While its impact on the the laser signal pump threshold is small, the Raman pump threshold drops. For example, for $Q_0 \sim 4 \times 10^7$, it decreases from 2 mW to 100 μW. The combined reduction of the coupling losses for the laser signal and Raman modes improves the power accumulation in each mode and threshold conditions are quickly reached. Furthermore, the improvement is also larger for each Q_0 increment.

If ions doped As_2S_3 glass is successfully fabricated with purity level of the undoped glass, the threshold powers would improve slightly through a larger Raman gain, better mode confinement and smaller mode overlap. However, the previous discussion is still valid.

These results suggest that hybrid laser and Raman sources are realistic within the current limitations of the glass fabrication and purification steps. The realization of these hybrid laser microcavities would certainly open new possibilities for the generation of mid-IR frequencies.

CHAPTER 8 CONCLUSIONS & RECOMMENDATIONS

This thesis compiles the results of my efforts done toward the development of mid-IR Raman sources based on As_2S_3 and tellurite glasses microspheres. Along the main experimental results of Chapters 4 to 6, basic concepts of WGM microcavities are exposed. Additionally, measurements are related to theoretical models based on coupled-modes equations. Experimental setups and challenges are also addressed. Finally, this thesis' results are compared to the literature and possible improvements are discussed. This thesis improves the state of art of chalcogenide and tellurite glasses microcavities with several contributions.

The first contribution of this work was to successfully fabricate As_2S_3 microcavities with Q-factors $> 5 \times 10^7$. It represents a tenfold improvement for a chalcogenide microcavity. It is more than two orders of magnitude larger than previously reported in As_2S_3 microcavities. This result is important since the threshold power needed to generate Raman scattering processes is reduced quadratically with the Q-factor. The microspheres are made from high purity As_2S_3 optical fibers using a laser shaping technique. The glass quality of the fibers limits the attenuation of the microspheres to $\sim 9 \times 10^7$. The fabricated sphere Q-factors approach this limit and confirm the laser shaping technique suitability. Furthermore, a packaging procedure is demonstrated. A narrow tubular structure prevents dust particles from degrading the spheres quality. Enclosed with a tapered optical fiber to couple light in and out of the microspheres, packaged microcavities can now be used as in-line fiber devices.

The second thesis contribution is the generation of Raman lasing in As_2S_3 microspheres with threshold coupled pump powers ~ 13 μW at a wavelength of 1550 nm. Raman lasing performances are comparable to other WGM Raman sources, being held back only by lower Q-factors. The results shown in Chapter 4 are the first demonstrations of nonlinear interactions in chalcogenide microcavities. Larger losses of previously reported chalcogenide WGM microcavities limit threshold power levels to tens of milliwatts. As discussed in Chapter 7, future works should aim at the improvement of As_2S_3 glass purity. Threshold pump powers could be reduced to sub-μW levels if intrinsic Q-factors were larger. Power conversion efficiencies are expected to improve as well. The performances of As_2S_3 microspheres as Raman sources in the near-IR suggest similar performances in the mid-IR region. Glass purification techniques provide relatively constant optical attenuation across the transparency window, thus similar Q-factors are expected.

Generation of cascaded Raman scattering in As_2S_3 microspheres naturally follows as the third thesis contribution. Using a pump wavelength of 1560 nm, Raman emission lines up

to the fifth order were observed at wavelengths of 1645 nm, 1750 nm, 1860 nm, 1990 nm, and 2140 nm. Additionally, the Raman power was monitored for the first three orders. Their behaviors are in agreement with the theoretical models. The self-frequency locking laser setup used in Chapter 5 successfully maintains a single pump emission line but does not modify the available Raman gain inside the microsphere. Simultaneous Raman emission lines are regularly observed and cause power instability. Future improvements should include feedback mechanisms to stabilize the emission signals and select the emission wavelengths.

To push the emission wavelengths further above 2 μm, a pumping scheme at wavelengths $\sim$ 1880 nm is developed based on a thulium-doped optical amplifier. Emission bands centered on wavelengths of 2015 nm, 2170 nm, and 2350 nm are observed. This is the first demonstration of cascaded Raman lasing above a wavelength of 2 μm in WGM microcavities. Previously reported measurements were limited to telecommunication bands. The microspheres' ability to generate cascaded Raman lasing with pump powers $<$ 1 mW strengthens their potential use as compact Raman sources in the mid-IR.

The fourth thesis contribution is the generation of laser emission at wavelengths $\sim$ 1975 nm in tellurite microspheres. This demonstration is a first step toward the development of hybrid sources based on ions-doped laser emission and Raman emission. Measured threshold pump powers of $\sim$ 30 μW represent a tenfold improvement over the reported performances in thulium-doped tellurite microcavities, thanks to larger Q-factors. Improvements of the glass purification steps could increase the Q-factors even more. A tenfold improvement of the Q-factors would decrease hybrid Raman lasing threshold powers below the milliwatt level. If high quality ions doped As_2S_3 microspheres were obtained, the larger Raman gain could increase the performances even more.

In view of these thesis results, few important challenges remain, but could be addressed within the next years :

- Realistic improvement of the chalcogenide and tellurite glasses purity could enhance the performances significantly.
- The use of chalcogenide tapered optical fibers to couple light in and out of As_2S_3 microspheres could increase the power conversion efficiencies of the Raman sources.
- Filtering mechanisms are needed for the development of stabilized and efficient cascaded Raman sources based on As_2S_3 microspheres.

By addressing these challenges, chalcogenide and tellurite microspheres could be used as low power cascaded Raman and laser sources near a wavelength of 2 μm and further in the mid-IR. These microsources are suitable for portable detection applications such as molecular spectroscopy. Precise molecular vibration spectra could be obtained considering the narrow

emission linewidth of WGM microcavities. The packaging tube can readily be modified as a miniature gas chamber for this purpose. Furthermore, multiplexed detection channels for different molecules sharing the same low power pump signal could be developed in a compact manner.

Several research paths can alternatively be explored in extension to this thesis. The realization of high Q-factor As_2S_3 microspheres opens the way for multiple applications not tested during this project. Some of these are mentioned in Table 1.1. WGM microcavities are suitable for nonlinear signal generation, not only for Raman scattering processes, but also for parametric frequency conversion processes. As it is depicted in Fig. 2.12, the dispersion of As_2S_3 microspheres pushes degenerate four-wave mixing processes and frequency combs generation to the mid-IR region. These processes can efficiently convert the pump signal to dozens of emission lines, of interest for sensing applications. In combination with external mid-IR sources, As_2S_3 microspheres could simply be used as passive components such as narrow band optical filters or highly sensitive biodetection devices. Additionally, the packaging tube can act as a gas chamber for molecular sensing.

Finally, it could be interesting to test other chalcogenide glasses such as As_2Se_3. Table 1.2 indicates that threshold pump powers could reach a few hundreds of nanowatts only. Despite thermal instabilities expected with input powers of tens of μW, stable Raman lasing could be possible below this level.

BIBLIOGRAPHY

[1] V. Braginsky, M. Gorodetsky, and V. Ilchenko, "Quality-factor and nonlinear properties of optical whispering-gallery modes," *Physics Letters A*, vol. 137, pp. 393–397, may 1989.

[2] K. J. Vahala, "Optical microcavities," *Nature*, vol. 424, pp. 839–846, 2003.

[3] A. B. Matsko and V. S. Ilchenko, "Optical resonators with whispering-gallery modes-part I : basics," *IEEE Journal of Selected Topics in Quantum Electronics*, vol. 12, pp. 3–14, jan 2006.

[4] A. Chiasera, Y. Dumeige, P. Féron, M. Ferrari, Y. Jestin, G. Nunzi Conti, S. Pelli, S. Soria, and G. Righini, "Spherical whispering-gallery-mode microresonators," *Laser & Photonics Reviews*, vol. 4, pp. 457–482, apr 2010.

[5] L. Rayleigh, "CXII. The problem of the whispering gallery," *Philosophical Magazine Series 6*, vol. 20, pp. 1001–1004, dec 1910.

[6] R. D. Richtmyer, "Dielectric Resonators," *Journal of Applied Physics*, vol. 10, pp. 391–398, 1938.

[7] J. A. Stratton, *Electromagnetic Theory*. McGraw-Hill Book Company, Inc., 1941.

[8] R. S. Elliott, "Azimuthal Surface Waves on Circular Cylinders," *Journal of Applied Physics*, vol. 26, no. 4, pp. 368–376, 1955.

[9] C. Garrett, W. Kaiser, and W. Bond, "Stimulated Emission into Optical Whispering Modes of Spheres," *Physical Review*, vol. 124, pp. 1807–1809, dec 1961.

[10] M. Brambilla and U. Finzi, "Electro-Magnetic Eigenmodes of the Toroidal Cavity," *IEEE Transactions on Plasma Science*, vol. 2, no. 3, pp. 112–114, 1974.

[11] F. Cap and R. Deutsch, "Toroidal Resonators for Electromagnetic Waves," *IEEE Transactions on Microwave Theory and Techniques*, vol. MTT-26, no. 7, pp. 478–486, 1978.

[12] M. Janaki and B. Dasgupta, "Eigenmodes for electromagnetic waves propagating in a toroidal cavity," *IEEE Transactions on Plasma Science*, vol. 18, no. 1, pp. 78–85, 1990.

[13] H. Lai, P. Leung, K. Young, P. Barber, and S. Hill, "Time-independent perturbation for leaking electromagnetic modes in open systems with application to resonances in microdroplets," *Physical Review A*, vol. 41, pp. 5187–5198, may 1990.

[14] C. C. Lam, P. T. Leung, and K. Young, "Explicit asymptotic formulas for the positions, widths, and strengths of resonances in Mie scattering," *Journal of the Optical Society of America B*, vol. 9, pp. 1585–1592, sep 1992.

[15] B. R. Johnson, "Theory of morphology-dependent resonances : shape resonances and width formulas," *Journal of the Optical Society of America A*, vol. 10, pp. 343–352, feb 1993.

[16] S. Schiller, "Asymptotic expansion of morphological resonance frequencies in Mie scattering," *Applied Optics*, vol. 32, no. 12, pp. 2181–2185, 1993.

[17] P. C. Y. Lee and J. S. Yang, "Vibrations of circular disk dielectric resonators," *Journal of Applied Physics*, vol. 73, no. 11, pp. 7083–7092, 1993.

[18] P. C. Y. Lee and J. D. Yu, "Guided electromagnetic waves in anisotropic dielectric plates," *Journal of Applied Physics*, vol. 74, no. 8, pp. 4823–4839, 1993.

[19] D. W. Vernooy and H. J. Kimble, "Quantum structure and dynamics for atom galleries," *Physical Review A*, vol. 55, pp. 1239–1261, feb 1997.

[20] B. E. Little, J. Laine, H. A. Haus, and L. Fellow, "Analytic Theory of Coupling from Tapered Fibers and Half-Blocks into Microsphere Resonators," *Journal of Lightwave Technology*, vol. 17, no. 4, pp. 704–715, 1999.

[21] A. Oraevsky, H. Search, C. Journals, A. Contact, M. Iopscience, Q. Electron, and I. P. Address, "Whispering-gallery waves," *Quantum Electronics*, vol. 377, no. 5, pp. 377–400, 2002.

[22] B. Min, L. Yang, and K. Vahala, "Perturbative analytic theory of an ultrahigh-Q toroidal microcavity," *Physical Review A*, vol. 76, pp. 1–10, jul 2007.

[23] V. Braginsky, M. Gorodetsky, and V. Ilchenko, "Quality-factor and nonlinear properties of optical whispering-gallery modes," *Physics Letters A*, vol. 137, pp. 393–397, may 1989.

[24] M. L. Gorodetsky, A. A. Savchenkov, and V. S. Ilchenko, "Ultimate Q of optical microsphere resonators," *Optics Letters*, vol. 21, no. 7, pp. 453–455, 1996.

[25] B. E. Little and S. T. Chu, "Estimating surface-roughness loss and output coupling in microdisk resonators," *Optics Letters*, vol. 21, pp. 1390–1392, sep 1996.

[26] M. L. Gorodetsky, A. D. Pryamikov, and V. S. Ilchenko, "Rayleigh scattering in high-Q microspheres," *Journal of the Optical Society of America B*, vol. 17, no. 6, pp. 1051–1057, 2000.

[27] S. Bittner, B. Dietz, M. Miski-Oglu, P. Iriarte, a. Richter, and F. Schäfer, "Experimental test of a two-dimensional approximation for dielectric microcavities," *Physical Review A*, vol. 80, no. 2, pp. 1–9, 2009.

[28] D. R. Rowland and J. D. Love, "Evanescent wave coupling of whispering gallery modes of a dielectric cylinder," *Optoelectronics, IEE Proceedings J*, vol. 140, pp. 177–188, 1993.

[29] G. Griffel, S. Arnold, D. Taskent, A. Serpengüzel, J. Connolly, and N. Morris, "Morphology-dependent resonances of a microsphere-optical fiber system," *Optics Letters*, vol. 21, pp. 695–697, may 1996.

[30] B. Little, S. Chu, H. Haus, J. Foresi, and J.-P. Laine, "Microring resonator channel dropping filters," *Journal of Lightwave Technology*, vol. 15, no. 6, pp. 998–1005, 1997.

[31] B. E. Little, J.-P. Laine, and S. T. Chu, "Surface-roughness-induced contradirectional coupling in ring and disk resonators," *Optics Letters*, vol. 22, pp. 4–6, jan 1997.

[32] M. L. Gorodetsky and V. S. Ilchenko, "Optical microsphere resonators : optimal coupling to high-Q whispering-gallery modes," *Journal of the Optical Society of America B*, vol. 16, no. 1, pp. 147–154, 1999.

[33] C. Manolatou, M. Khan, S. Fan, P. Villeneuve, H. Haus, and J. Joannopoulos, "Coupling of modes analysis of resonant channel add-drop filters," *IEEE Journal of Quantum Electronics*, vol. 35, no. 9, pp. 1322–1331, 1999.

[34] Y. Xu, Y. Li, R. Lee, and A. Yariv, "Scattering-theory analysis of waveguide-resonator coupling," *Physical Review E*, vol. 62, pp. 7389–7404, nov 2000.

[35] A. Yariv, "Universal relations for coupling of optical power between microresonators and dielectric waveguides," *Electronics Letters*, vol. 36, no. 4, pp. 321–322, 2000.

[36] T. J. Kippenberg, S. M. Spillane, and K. J. Vahala, "Modal coupling in traveling-wave resonators," *Optics Letters*, vol. 27, pp. 1669–1671, oct 2002.

[37] M. J. Humphrey, E. Dale, A. T. Rosenberger, and D. K. Bandy, "Calculation of optimal fiber radius and whispering-gallery mode spectra for a fiber-coupled microsphere," *Optics Communications*, vol. 271, pp. 124–131, mar 2007.

[38] T. Harayama and P. Davis, "Nonlinear Whispering Gallery Modes," *Physical Review Letters*, vol. 82, pp. 3803–3806, may 1999.

[39] T. Harayama, P. Davis, and K. S. Ikeda, "Whispering Gallery Mode Lasers," *Progress of Theoretical Physics*, no. 139, pp. 363–374, 2000.

[40] B. Min, T. J. Kippenberg, L. Yang, and K. J. Vahala, "Erbium-implanted high-Q silica toroidal microcavity laser on a silicon chip," *Physical Review A*, vol. 70, pp. 1–12, sep 2004.

[41] M. M. Mazumder, S. C. Hill, D. Q. Chowdhury, and R. K. Chang, "Dispersive optical bistability in a dielectric sphere," *Journal of the Optical Society of America B*, vol. 12, pp. 297–310, feb 1995.

[42] D. Braunstein, A. Khazanov, G. Koganov, and R. Shuker, "Lowering of threshold conditions for nonlinear effects in a microsphere.," *Physical review. A*, vol. 53, pp. 3565–3572, may 1996.

[43] F. C. Blom, D. R. van Dijk, H. J. W. M. Hoekstra, A. Driessen, and T. J. A. Popma, "Experimental study of integrated-optics microcavity resonators : Toward an all-optical switching device," *Applied Physics Letters*, vol. 71, no. 6, pp. 747–749, 1997.

[44] H. Rokhsari and K. J. Vahala, "Observation of Kerr nonlinearity in microcavities at room temperature," *Optics Letters*, vol. 30, no. 4, pp. 427–429, 2005.

[45] I. Agha, J. Sharping, M. Foster, and a.L. Gaeta, "Optimal sizes of silica microspheres for linear and nonlinear optical interactions," *Applied Physics B*, vol. 83, pp. 303–309, mar 2006.

[46] A. Rodriguez, M. Soljacic, J. D. Joannopoulos, and S. G. Johnson, "Xhi(2) and Xhi(3) harmonic generation at a critical power in inhomogeneous doubly resonant cavities," *Optics Express*, vol. 15, no. 12, pp. 7303–7318, 2007.

[47] P. Andalib and N. Granpayeh, "All-optical ultracompact photonic crystal AND gate based on nonlinear ring resonators," *Journal of the Optical Society of America B*, vol. 26, pp. 10–16, dec 2008.

[48] I. S. Grudinin and K. J. Vahala, "Thermal instability of a compound resonator," *Optics Express*, vol. 17, pp. 14088–14097, jul 2009.

[49] Y. Chembo and N. Yu, "Modal expansion approach to optical-frequency-comb generation with monolithic whispering-gallery-mode resonators," *Physical Review A*, vol. 82, pp. 1–18, sep 2010.

[50] L. G. Helt, Z. Yang, M. Liscidini, and J. E. Sipe, "Spontaneous four-wave mixing in microring resonators.," *Optics Letters*, vol. 35, pp. 3006–3008, sep 2010.

[51] A. B. Matsko, A. A. Savchenkov, W. Liang, V. S. Ilchenko, D. Seidel, and L. Maleki, "Mode-locked Kerr frequency combs," *Optics Letters*, vol. 36, pp. 2845–2847, jul 2011.

[52] B. Sturman and I. Breunig, "Generic description of second-order nonlinear phenomena in whispering-gallery resonators," *JOSA B*, vol. 28, no. 10, pp. 2465–2471, 2011.

[53] B. A. Daniel, D. N. Maywar, and G. P. Agrawal, "Dynamic mode theory of optical resonators undergoing refractive index changes," *Journal of the Optical Society of America B*, vol. 28, pp. 2207–2215, aug 2011.

[54] W.-J. Chen, F.-W. Sun, C.-L. Zou, and G.-C. Guo, "Integrated entangled photons source from microcavity parametric down conversion," *Journal of the Optical Society of America B*, vol. 29, pp. 1884–1888, jul 2012.

[55] N. Sakhnenko and A. Nerukh, "Rigorous analysis of whispering gallery mode frequency conversion because of time variation of refractive index in a spherical resonator.," *Journal of the Optical Society of America. A, Optics, image science, and vision*, vol. 29, pp. 99–104, jan 2012.

[56] C. Bao, L. Zhang, A. Matsko, Y. Yan, Z. Zhao, G. Xie, A. M. Agarwal, L. C. Kimerling, J. Michel, L. Maleki, and A. E. Willner, "Nonlinear conversion efficiency in Kerr frequency comb generation," *Optics Letters*, vol. 39, no. 21, pp. 6126–6129, 2014.

[57] B. Little, J. Foresi, G. Steinmeyer, E. Thoen, S. Chu, H. Haus, E. Ippen, L. Kimerling, and W. Greene, "Ultra-compact Si-SiO2 microring resonator optical channel dropping filters," *IEEE Photonics Technology Letters*, vol. 10, pp. 549–551, apr 1998.

[58] A. Savchenkov, V. Ilchenko, A. Matsko, and L. Maleki, "Kilohertz optical resonances in dielectric crystal cavities," *Physical Review A*, vol. 70, pp. 1–4, nov 2004.

[59] J. K. Poon, L. Zhu, G. A. DeRose, and A. Yariv, "Transmission and group delay of microring coupled-resonator optical waveguides," *Optics Letters*, vol. 31, no. 4, pp. 456–458, 2006.

[60] F. Xia, L. Sekaric, and Y. Vlasov, "Ultracompact optical buffers on a silicon chip," *Nature Photonics*, vol. 1, no. 1, pp. 65–71, 2007.

[61] K. Kieu and M. Mansuripur, "Self-Locked Excitation Scheme for Microsphere Resonators," *IEEE Photonics Technology Letters*, vol. 19, pp. 100–102, jan 2007.

[62] F. Morichetti, A. Melloni, A. Breda, A. Canciamilla, C. Ferrari, and M. Martinelli, "A reconfigurable architecture for continuously variable optical slow-wave delay lines.," *Optics Express*, vol. 15, pp. 17273–82, dec 2007.

[63] Q. Huang, X. Zhang, J. Xia, and J. Yu, "Dual-band optical filter based on a single microdisk resonator," *Optics Letters*, vol. 36, pp. 4494–4496, nov 2011.

[64] H. Lee, T. Chen, J. Li, O. Painter, and K. J. Vahala, "Ultra-low-loss optical delay line on a silicon chip," *Nature Communications*, vol. 3, p. 867, may 2012.

[65] H. Lee, T. Chen, J. Li, K. Y. Yang, S. Jeon, O. Painter, and K. J. Vahala, "Chemically etched ultrahigh-Q wedge-resonator on a silicon chip," *Nature Photonics*, vol. 6, pp. 369–373, may 2012.

[66] F. Vollmer, D. Braun, A. Libchaber, M. Khoshsima, I. Teraoka, and S. Arnold, "Protein detection by optical shift of a resonant microcavity," *Applied Physics Letters*, vol. 80, no. 21, pp. 4057–4059, 2002.

[67] S. Arnold, M. Khoshsima, I. Teraoka, S. Holler, and F. Vollmer, "Shift of whispering-gallery modes in microspheres by protein adsorption.," *Optics Letters*, vol. 28, pp. 272–4, feb 2003.

[68] A. M. Armani, R. P. Kulkarni, S. E. Fraser, R. C. Flagan, and K. J. Vahala, "Label-free, single-molecule detection with optical microcavities.," *Science*, vol. 317, pp. 783–787, aug 2007.

[69] I. M. White and X. Fan, "On the performance quantification of resonant refractive index sensors," *Optics Express*, vol. 16, pp. 1020–1028, jan 2008.

[70] F. Vollmer and S. Arnold, "Whispering-gallery-mode biosensing : label-free detection down to single molecules," *Nature Methods*, vol. 5, pp. 591–596, jul 2008.

[71] J. Zhu, S. K. Ozdemir, Y.-F. Xiao, L. Li, L. He, D.-R. Chen, and L. Yang, "On-chip single nanoparticle detection and sizing by mode splitting in an ultrahigh-Q microresonator," *Nature Photonics*, vol. 4, no. 1, pp. 46–49, 2009.

[72] S. Arnold, S. I. Shopova, and S. Holler, "Whispering gallery mode bio-sensor for label-free detection of single molecules : thermo-optic vs reactive mechanism," *Optics Express*, vol. 18, pp. 281–287, dec 2009.

[73] H. K. Hunt and A. M. Armani, "Label-free biological and chemical sensors.," *Nanoscale*, vol. 2, pp. 1544–59, sep 2010.

[74] L. He, S. K. Ozdemir, J. Zhu, W. Kim, and L. Yang, "Detecting single viruses and nanoparticles using whispering gallery microlasers.," *Nature Nanotechnology*, vol. 6, pp. 428–32, jul 2011.

[75] F. Vollmer and L. Yang, "Label-free detection with high-Q microcavities : a review of biosensing mechanisms for integrated devices," *Nanophotonics*, vol. 1, pp. 267–291, 2012.

[76] B. Sprenger, H. G. L. Schwefel, and L. J. Wang, "Whispering-gallery-mode-resonator-stabilized narrow-linewidth fiber loop laser," *Optics Letters*, vol. 34, pp. 3370–3372, oct 2009.

[77] B. Sprenger, H. G. L. Schwefel, Z. H. Lu, S. Svitlov, and L. J. Wang, "CaF2 whispering-gallery-mode-resonator stabilized-narrow-linewidth laser," *Optics Letters*, vol. 35, pp. 2870–2872, aug 2010.

[78] M. Peccianti, a. Pasquazi, Y. Park, B. Little, S. Chu, D. Moss, and R. Morandotti, "Demonstration of a stable ultrafast laser based on a nonlinear microcavity," *Nature Communications*, vol. 3, p. 765, apr 2012.

[79] V. Sandoghdar, F. Treussart, J. Hare, V. Lefèvre-Seguin, J. Raimond, and S. Haroche, "Very low threshold whispering-gallery-mode microsphere laser," *Physical Review A*, vol. 54, no. 3, pp. R1777–R1780, 1996.

[80] M. Cai, O. Painter, K. J. Vahala, and P. C. Sercel, "Fiber-coupled microsphere laser," *Optics Letters*, vol. 25, no. 19, pp. 1430–1432, 2000.

[81] A. Polman, B. Min, J. Kalkman, T. J. Kippenberg, and K. J. Vahala, "Ultralow-threshold erbium-implanted toroidal microlaser on silicon," *Applied Physics Letters*, vol. 84, no. 7, pp. 1037–1039, 2004.

[82] L. He, S. K. Özdemir, and L. Yang, "Whispering gallery microcavity lasers," *Laser & Photonics Reviews*, vol. 7, pp. 60–82, jan 2013.

[83] L. Yang, D. K. Armani, and K. J. Vahala, "Fiber-coupled erbium microlasers on a chip," *Applied Physics Letters*, vol. 83, no. 5, pp. 825–826, 2003.

[84] L. Yang and K. J. Vahala, "Gain functionalization of silica microresonators," *Optics Letters*, vol. 28, no. 8, pp. 592–594, 2003.

[85] J. Verbert, F. Mazen, T. Charvolin, E. Picard, V. Calvo, P. Noé, J.-M. Gérard, and E. Hadji, "Efficient coupling of Er-doped silicon-rich oxide to microdisk whispering gallery modes," *Applied Physics Letters*, vol. 86, no. 11, p. 111117, 2005.

[86] L. Yang, T. Carmon, B. Min, S. M. Spillane, and K. J. Vahala, "Erbium-doped and Raman microlasers on a silicon chip fabricated by the sol-gel process," *Applied Physics Letters*, vol. 86, no. 9, p. 091114, 2005.

[87] E. P. Ostby, L. Yang, and K. J. Vahala, "Ultralow-threshold Yb3+ : SiO2 glass laser fabricated by the solgel process," *Optics Letters*, vol. 32, no. 18, pp. 2650–2652, 2007.

[88] L. Liu, R. Kumar, K. Huybrechts, T. Spuesens, G. Roelkens, E.-j. Geluk, T. de Vries, P. Regreny, D. Van Thourhout, R. Baets, and G. Morthier, "An ultra-small, low-power, all-optical flip-flop memory on a silicon chip," *Nature Photonics*, vol. 4, pp. 182–187, jan 2010.

[89] A. Pasquazi, R. Ahmad, M. Rochette, M. Lamont, B. E. Little, S. T. Chu, R. Morandotti, and D. J. Moss, "All-optical wavelength conversion in an integrated ring resonator.," *Optics Express*, vol. 18, pp. 3858–3863, feb 2010.

[90] M. Pöllinger and A. Rauschenbeutel, "All-optical signal processing at ultra-low powers in bottle microresonators using the Kerr effect.," *Optics Express*, vol. 18, pp. 17764–17775, aug 2010.

[91] Y. H. Wen, O. Kuzucu, T. Hou, M. Lipson, and A. L. Gaeta, "All-optical switching of a single resonance in silicon ring resonators.," *Optics Letters*, vol. 36, pp. 1413–1415, apr 2011.

[92] D. O'Shea, C. Junge, M. Pöllinger, A. Vogler, and A. Rauschenbeutel, "All-optical switching and strong coupling using tunable whispering-gallery-mode microresonators," *Applied Physics B*, vol. 105, pp. 129–148, sep 2011.

[93] F. Li, M. Pelusi, D.-X. Xu, R. Ma, S. Janz, B. J. Eggleton, and D. J. Moss, "All-optical wavelength conversion for 10 Gb/s DPSK signals in a silicon ring resonator.," *Optics Express*, vol. 19, pp. 22410–22416, nov 2011.

[94] T. J. Kippenberg, S. M. Spillane, and K. J. Vahala, "Kerr-Nonlinearity Optical Parametric Oscillation in an Ultrahigh-Q Toroid Microcavity," *Physical Review Letters*, vol. 93, pp. 18–21, aug 2004.

[95] T. Carmon and K. J. Vahala, "Visible continuous emission from a silica microphotonic device by third-harmonic generation," *Nature Physics*, vol. 3, pp. 430–435, may 2007.

[96] D. O'Shea, J. Ward, B. Shortt, and S. Nic Chormaic, "An All-Fiber Coupled Multicolor Microspherical Light Source," *IEEE Photonics Technology Letters*, vol. 19, pp. 1720–1722, nov 2007.

[97] I. Agha, Y. Okawachi, M. Foster, J. Sharping, and A. Gaeta, "Four-wave-mixing parametric oscillations in dispersion-compensated high-Q silica microspheres," *Physical Review A*, vol. 76, pp. 1–4, oct 2007.

[98] A. A. Savchenkov, A. B. Matsko, M. Mohageg, D. V. Strekalov, and L. Maleki, "Parametric oscillations in a whispering gallery resonator," *Optics Letters*, vol. 32, no. 2, pp. 157–159, 2007.

[99] M. Ferrera, L. Razzari, D. Duchesne, R. Morandotti, Z. Yang, M. Liscidini, J. E. Sipe, S. Chu, B. E. Little, and D. J. Moss, "Low-power continuous-wave nonlinear optics in doped silica glass integrated waveguide structures," *Nature Photonics*, vol. 2, pp. 737–740, nov 2008.

[100] I. H. Agha, Y. Okawachi, and A. L. Gaeta, "Theoretical and experimental investigation of broadband cascaded four-wave mixing in high-Q microspheres.," *Optics Express*, vol. 17, pp. 16209–16215, aug 2009.

[101] J. Fürst, D. Strekalov, D. Elser, a. Aiello, U. Andersen, C. Marquardt, and G. Leuchs, "Low-Threshold Optical Parametric Oscillations in a Whispering Gallery Mode Resonator," *Physical Review Letters*, vol. 105, pp. 2–5, dec 2010.

[102] G. Kozyreff, J. Dominguez-Juarez, and J. Martorell, "Nonlinear optics in spheres : from second harmonic scattering to quasi-phase matched generation in whispering gallery modes," *Laser & Photonics Reviews*, vol. 5, pp. 737–749, nov 2011.

[103] J. S. Levy, M. a. Foster, A. L. Gaeta, and M. Lipson, "Harmonic generation in silicon nitride ring resonators.," *Optics Express*, vol. 19, pp. 11415–11421, jun 2011.

[104] J. Moore, M. Tomes, and T. Carmon, "Continuous-wave ultraviolet emission through fourth-harmonic generation in a whispering-gallery resonator," *Optics Express*, vol. 19, no. 24, pp. 24139–24146, 2011.

[105] M. T. Simons and I. Novikova, "Observation of second-order hyper-Raman generation in LiNbO3 whispering-gallery mode disk resonators.," *Optics Letters*, vol. 36, pp. 3027–3029, aug 2011.

[106] J. Moore, M. Tomes, T. Carmon, and M. Jarrahi, "Continuous-wave cascaded-harmonic generation and multi-photon Raman lasing in lithium niobate whispering-gallery resonators," *Applied Physics Letters*, vol. 99, no. 22, p. 221111, 2011.

[107] W. H. P. Pernice, C. Xiong, C. Schuck, and H. X. Tang, "Second harmonic generation in phase matched aluminum nitride waveguides and micro-ring resonators," *Applied Physics Letters*, vol. 100, no. 22, p. 223501, 2012.

[108] T. Herr, V. Brasch, J. D. Jost, C. Y. Wang, N. M. Kondratiev, M. L. Gorodetsky, and T. J. Kippenberg, "Temporal solitons in optical microresonators," *Nature Photonics*, vol. 8, pp. 145–152, dec 2013.

[109] P. Del'Haye, A. Schliesser, O. Arcizet, T. Wilken, R. Holzwarth, and T. J. Kippenberg, "Optical frequency comb generation from a monolithic microresonator.," *Nature*, vol. 450, pp. 1214–1217, dec 2007.

[110] P. Del'Haye, O. Arcizet, A. Schliesser, R. Holzwarth, and T. Kippenberg, "Full Stabilization of a Microresonator-Based Optical Frequency Comb," *Physical Review Letters*, vol. 101, pp. 1–4, jul 2008.

[111] I. S. Grudinin, N. Yu, and L. Maleki, "Generation of optical frequency combs with a CaF2 resonator," *Optics Letters*, vol. 34, pp. 878–880, mar 2009.

[112] J. S. Levy, A. Gondarenko, M. A. Foster, A. C. Turner-Foster, A. L. Gaeta, and M. Lipson, "CMOS-compatible multiple-wavelength oscillator for on-chip optical interconnects," *Nature Photonics*, vol. 4, pp. 37–40, dec 2009.

[113] W. Liang, A. A. Savchenkov, A. B. Matsko, V. S. Ilchenko, D. Seidel, and L. Maleki, "Generation of near-infrared frequency combs from a MgF2 whispering gallery mode resonator," *Optics Letters*, vol. 36, pp. 2290–2292, jun 2011.

[114] M. A. Foster, J. S. Levy, O. Kuzucu, K. Saha, M. Lipson, and A. L. Gaeta, "Silicon-based monolithic optical frequency comb source," *Optics Express*, vol. 19, pp. 14233–14239, jul 2011.

[115] Y. Okawachi, K. Saha, J. S. Levy, Y. H. Wen, M. Lipson, and A. L. Gaeta, "Octave-spanning frequency comb generation in a silicon nitride chip.," *Optics Letters*, vol. 36, pp. 3398–400, sep 2011.

[116] T. J. Kippenberg, R. Holzwarth, and S. A. Diddams, "Microresonator-based optical frequency combs.," *Science*, vol. 332, pp. 555–559, apr 2011.

[117] A. A. Savchenkov, A. B. Matsko, W. Liang, V. S. Ilchenko, D. Seidel, and L. Maleki, "Kerr combs with selectable central frequency," *Nature Photonics*, vol. 5, pp. 293–296, apr 2011.

[118] A. Schliesser, N. Picqué, and T. W. Hänsch, "Mid-infrared frequency combs," *Nature Photonics*, vol. 6, pp. 440–449, jun 2012.

[119] C. Y. Wang, T. Herr, P. Del'Haye, A. Schliesser, J. Hofer, R. Holzwarth, T. W. Hänsch, N. Picqué, and T. J. Kippenberg, "Mid-infrared optical frequency combs at 2.5 um based on crystalline microresonators.," *Nature Communications*, vol. 4, p. 1345, jan 2013.

[120] S. Miller, K. Luke, Y. Okawachi, J. Cardenas, A. L. Gaeta, and M. Lipson, "On-chip frequency comb generation at visible wavelengths via simultaneous second- and third-order optical nonlinearities," *Optics Express*, vol. 22, pp. 26517–26525, oct 2014.

[121] A. R. Johnson, Y. Okawachi, M. R. E. Lamont, J. S. Levy, M. Lipson, and A. L. Gaeta, "Microresonator-based comb generation without an external laser source," *Optics Express*, vol. 22, pp. 1394–1401, jan 2014.

[122] S. M. Spillane, T. J. Kippenberg, and K. J. Vahala, "Ultralow-threshold Raman laser using a spherical dielectric microcavity.," *Nature*, vol. 415, pp. 621–623, feb 2002.

[123] B. Min, T. J. Kippenberg, and K. J. Vahala, "Compact, fiber-compatible, cascaded Raman laser," *Optics Letters*, vol. 28, no. 17, pp. 1507–1509, 2003.

[124] T. Kippenberg, S. Spillane, B. Min, and K. Vahala, "Theoretical and Experimental Study of Stimulated and Cascaded Raman Scattering in Ultrahigh-Q Optical Microcavities," *IEEE Journal of Selected Topics in Quantum Electronics*, vol. 10, pp. 1219–1228, sep 2004.

[125] T. J. Kippenberg, S. M. Spillane, D. K. Armani, and K. J. Vahala, "Ultralow-threshold microcavity Raman laser on a microelectronic chip," *Optics Letters*, vol. 29, no. 11, pp. 1224–1226, 2004.

[126] I. S. Grudinin and L. Maleki, "Ultralow-threshold Raman lasing with CaF2 resonators.," *Optics Letters*, vol. 32, pp. 166–168, jan 2007.

[127] I. S. Grudinin and L. Maleki, "Efficient Raman laser based on a CaF2 resonator," *Journal of the Optical Society of America B*, vol. 25, pp. 594–598, mar 2008.

[128] V. S. Ilchenko and M. L. Gorodetsky, "Thermal Nonlinear Effects in Optical Whispering Gallery Microresonators," *Laser Physics*, vol. 2, no. 6, pp. 1004–1009, 1992.

[129] D. Armani, B. Min, A. Martin, and K. J. Vahala, "Electrical thermo-optic tuning of ultrahigh-Q microtoroid resonators," *Applied Physics Letters*, vol. 85, no. 22, pp. 5439–5441, 2004.

[130] M. L. Gorodetsky and I. S. Grudinin, "Fundamental thermal fluctuations in microspheres," *Journal of the Optical Society of America B*, vol. 21, no. 4, pp. 697–705, 2004.

[131] T. Carmon, L. Yang, and K. J. Vahala, "Dynamical thermal behavior and thermal self-stability of microcavities," *Optics Express*, vol. 12, pp. 4742–4750, oct 2004.

[132] V. R. Almeida and M. Lipson, "Optical bistability on a silicon chip," *Optics Letters*, vol. 29, pp. 2387–2389, oct 2004.

[133] A. E. Fomin, M. L. Gorodetsky, I. S. Grudinin, and V. S. Ilchenko, "Nonstationary nonlinear effects in optical microspheres," *Journal of the Optical Society of America B*, vol. 22, no. 2, pp. 459–465, 2005.

[134] T. J. Johnson, M. Borselli, and O. Painter, "Self-induced optical modulation of the transmission through a high-Q silicon microdisk resonator," *Optics Express*, vol. 14, no. 2, pp. 817–831, 2006.

[135] K. Ikeda, R. E. Saperstein, N. Alic, and Y. Fainman, "Thermal and Kerr nonlinear properties of plasma-deposited silicon nitride/ silicon dioxide waveguides.," *Optics Express*, vol. 16, pp. 12987–12994, aug 2008.

[136] C. Schmidt, A. Chipouline, T. Pertsch, A. Tünnermann, O. Egorov, F. Lederer, and L. Deych, "Nonlinear thermal effects in optical microspheres at different wavelength sweeping speeds.," *Optics Express*, vol. 16, pp. 6285–6301, apr 2008.

[137] H. S. Choi and A. M. Armani, "Thermal nonlinear effects in hybrid optical microresonators," *Applied Physics Letters*, vol. 97, no. 22, p. 223306, 2010.

[138] I. Grudinin, H. Lee, T. Chen, and K. Vahala, "Compensation of thermal nonlinearity effect in optical resonators.," *Optics Express*, vol. 19, pp. 7365–7372, apr 2011.

[139] L. Zhang, Y. Fei, Y. Cao, X. Lei, and S. Chen, "Experimental observations of thermo-optical bistability and self-pulsation in silicon microring resonators," *Journal of the Optical Society of America B*, vol. 31, pp. 201–205, jan 2014.

[140] V. S. Ilchenko and A. B. Matsko, "Optical resonators with whispering-gallery modes-part II : applications," *IEEE Journal of Selected Topics in Quantum Electronics*, vol. 12, pp. 15–32, jan 2006.

[141] J. Ward and O. Benson, "WGM microresonators : sensing, lasing and fundamental optics with microspheres," *Laser & Photonics Reviews*, vol. 5, pp. 553–570, jul 2011.

[142] S. D. Jackson, "Towards high-power mid-infrared emission from a fibre laser," *Nature Photonics*, vol. 6, pp. 423–431, jun 2012.

[143] Y. Yao, A. J. Hoffman, and C. F. Gmachl, "Mid-infrared quantum cascade lasers," *Nature Photonics*, vol. 6, pp. 432–439, jun 2012.

[144] R. Soref, "Mid-infrared photonics in silicon and germanium," *Nature Photonics*, vol. 4, pp. 495–497, aug 2010.

[145] B. Way, R. K. Jain, and M. Hossein-Zadeh, "High-Q microresonators for mid-IR light sources and molecular sensors," *Optics Letters*, vol. 37, pp. 4389–4391, oct 2012.

[146] G. Lin and Y. K. Chembo, "On the dispersion management of fluorite whispering-gallery mode resonators for Kerr optical frequency comb generation in the telecom and mid-infrared range," *Optics Express*, vol. 23, no. 2, pp. 1594–1604, 2015.

[147] M. Weber, "Handbook of Optical Materials, Section 2 : Glasses," in *Handbook of Optical Materials*, ch. Glasses, CRC Press, 2003.

[148] A. G. Griffith, R. K. Lau, J. Cardenas, Y. Okawachi, A. Mohanty, R. Fain, Y. H. D. Lee, M. Yu, C. T. Phare, C. B. Poitras, A. L. Gaeta, and M. Lipson, "Silicon-chip mid-infrared frequency comb generation," *Nature Communications*, vol. 6, p. 6299, feb 2015.

[149] A. A. Savchenkov, V. S. Ilchenko, F. Di Teodoro, P. M. Belden, W. T. Lotshaw, A. B. Matsko, and L. Maleki, "Generation of Kerr combs centered at 4.5 μm in crystalline microresonators pumped with quantum-cascade lasers," *Optics Letters*, vol. 40, pp. 3468–3471, aug 2015.

[150] Y. Deng, R. K. Jain, and M. Hossein-Zadeh, "Demonstration of a cw room temperature mid-IR microlaser.," *Optics Letters*, vol. 39, no. 15, pp. 4458–4461, 2014.

[151] A. Griffith, J. Cardenas, C. B. Poitras, and M. Lipson, "High quality factor and high confinement silicon resonators using etchless process," *Optics Express*, vol. 20, pp. 21341–21345, sep 2012.

[152] Y. Ruan, K. Boyd, H. Ji, A. Francois, H. Ebendorff-Heidepriem, J. Munch, and T. M. Monro, "Tellurite microspheres for nanoparticle sensing and novel light sources.," *Optics Express*, vol. 22, pp. 11995–12006, may 2014.

[153] P. Wang, M. Ding, T. Lee, G. Senthil Murugan, L. Bo, Y. Semenova, Q. Wu, D. Hewak, G. Brambilla, and G. Farrell, "Packaged chalcogenide microsphere resonator with high Q-factor," *Applied Physics Letters*, vol. 102, no. 13, p. 131110, 2013.

[154] D. H. Broaddus, M. A. Foster, I. H. Agha, J. T. Robinson, M. Lipson, and A. L. Gaeta, "Silicon-waveguide-coupled high-Q chalcogenide microspheres," *Optics Express*, vol. 17, pp. 5998–6003, mar 2009.

[155] R. Frerichs, "New Optical Glasses with Good Transparency in the Infrared," *Journal of the Optical Society of America*, vol. 43, pp. 1153–1157, dec 1953.

[156] A. Zakery and S. R. Elliott, "Optical properties and applications of chalcogenide glasses : a review," *Journal of Non-Crystalline Solids*, vol. 330, pp. 1–12, nov 2003.

[157] B. J. Eggleton, B. Luther-davies, and K. Richardson, "Chalcogenide photonics," *Nature Photonics*, vol. 5, pp. 141–148, 2011.

[158] A. Zakery and S. R. Elliott, *Optical Nonlinearities in Chalcogenide Glasses and their Applications*. Springer, 2007.

[159] J.-F. Viens, *Optique intégrée en verres infrarouges chalcogénures*. PhD thesis, Université Laval, Québec, 1997.

[160] N. Hô, *Écriture de guides d'onde dans les couches minces de verre de chalcogénures et photosensibilité*. PhD thesis, Université Laval, 2004.

[161] K. Turcotte, *Microfabrication, caractérisation et applications de guides d'ondes intégrés en verres chalcogénures*. PhD thesis, Université Laval, Québec, 2006.

[162] W. S. Rodney, I. H. Malitson, and T. A. King, "Refractive Index of Arsenic Trisulfide," *Journal of the Optical Society of America*, vol. 48, pp. 633–636, sep 1958.

[163] E. Marquez, J. Ramirez-Malo, P. Villares, R. Jimenez-Garay, P. J. S. Ewen, and A. E. Owen, "Calculation of the thickness and optical constants of amorphous arsenic sulphide films from their transmission spectra," *Journal of Physics D : Applied Physics*, vol. 25, pp. 535–541, mar 1992.

[164] E. D. Palik, *Handbook of Optical Constants of Solids*. Elsevier, 1998.

[165] W. C. Tan, M. E. Solmaz, J. Gardner, R. Atkins, and C. Madsen, "Optical characterization of a-As2S3 thin films prepared by magnetron sputtering," *Journal of Applied Physics*, vol. 107, no. 3, p. 033524, 2010.

[166] J. S. McCloy, B. J. Riley, S. Sundaram, H. A. Qiao, J. V. Crum, and B. R. Johnson, "Structure-optical property correlations of arsenic sulfide glasses in visible, infrared, and sub-millimeter regions," *Journal of Non-Crystalline Solids*, vol. 356, pp. 1288–1293, jun 2010.

[167] N. Carlie, N. C. Anheier, H. A. Qiao, B. Bernacki, M. C. Phillips, L. Petit, J. D. Musgraves, and K. Richardson, "Measurement of the refractive index dispersion of As2Se3 bulk glass and thin films prior to and after laser irradiation and annealing using prism coupling in the near- and mid-infrared spectral range.," *The Review of scientific instruments*, vol. 82, p. 053103, may 2011.

[168] J. T. Edmond and M. W. Redfearn, "Infra-red Study of As2Se3-type Glasses in the Wavelength Range 1.25 to 25 um," *Proceedings of the Physical Society*, vol. 81, pp. 380–382, feb 1963.

[169] P. A. Young, "Optical properties of vitreous arsenic trisulphide," *Journal of Physics C : Solid State Physics*, vol. 4, pp. 93–106, jan 1971.

[170] M. F. Churbanov, I. V. Scripachev, G. E. Snopatin, V. S. Shiryaev, and V. G. Plotnichenko, "High-purity glasses based on arsenic chalcogenides," *Journal of Optoelectronics and Advanced Materials*, vol. 3, no. 2, pp. 341–349, 2001.

[171] J. S. Sanghera, L. Shaw, and I. D. Aggarwal, "Applications of chalcogenide glass optical fibers," *Comptes Rendus Chimie*, vol. 5, pp. 873–883, dec 2002.

[172] A. Zakery, "Low loss waveguides in pulsed laser deposited arsenic sulfide chalcogenide films," *Journal of Physics D : Applied Physics*, vol. 35, pp. 2909–2913, nov 2002.

[173] A. Zakery, Y. Ruan, A. V. Rode, M. Samoc, and B. Luther-Davies, "Low-loss waveguides in ultrafast laser-deposited As2S3 chalcogenide films," *Journal of the Optical Society of America B*, vol. 20, no. 9, pp. 1844–1852, 2003.

[174] M. Churbanov, G. Snopatin, V. Shiryaev, V. Plotnichenko, and E. Dianov, "Recent advances in preparation of high-purity glasses based on arsenic chalcogenides for fiber optics," *Journal of Non-Crystalline Solids*, vol. 357, pp. 2352–2357, jun 2011.

[175] M. Asobe, K. Suzuki, T. Kanamori, and K. Kubodera, "Nonlinear refractive index measurement in chalcogenide-glass fibers by self-phase modulation," *Applied Physics Letters*, vol. 60, no. 10, pp. 1153–1154, 1992.

[176] H. Kobayashi, H. Kanbara, M. Koga, and K. Kubodera, "Third-order nonlinear optical properties of As2S3 chalcogenide glass," *Journal of Applied Physics*, vol. 74, no. 6, pp. 3683–3687, 1993.

[177] F. Smektala, C. Quemard, L. Leneindre, J. Lucas, A. Barthélémy, and C. De Angelis, "Chalcogenide glasses with large non-linear refractive indices," *Journal of Non-Crystalline Solids*, vol. 239, pp. 139–142, oct 1998.

[178] K. A. Cerqua-Richardson, J. M. McKinley, B. Lawrence, and A. Villeneuve, "Comparison of nonlinear optical properties of sulfide glasses in bulk and thin film form," *Optical Materials*, vol. 10, pp. 155–159, may 1998.

[179] G. Lenz, J. Zimmermann, T. Katsufuji, M. E. Lines, H. Y. Hwang, S. Spälter, R. E. Slusher, S. W. Cheong, J. S. Sanghera, and I. D. Aggarwal, "Large Kerr effect in bulk Se-based chalcogenide glasses.," *Optics Letters*, vol. 25, pp. 254–256, feb 2000.

[180] F. Smektala, C. Quemard, V. Couderc, and A. Barthélémy, "Non-linear optical properties of chalcogenide glasses measured by Z-scan," *Journal of Non-Crystalline Solids*, vol. 274, pp. 232–237, sep 2000.

[181] J. M. Harbold, F. O. Ilday, F. W. Wise, J. S. Sanghera, V. Q. Nguyen, L. B. Shaw, and I. D. Aggarwal, "Highly nonlinear As-S-Se glasses for all-optical switching.," *Optics Letters*, vol. 27, pp. 119–121, jan 2002.

[182] J. M. Laniel, N. Hô, R. Vallée, and A. Villeneuve, "Nonlinear-refractive-index measurement in As2S3 channel waveguides by asymmetric self-phase modulation," *Journal of the Optical Society of America B*, vol. 22, no. 2, pp. 437–445, 2005.

[183] J. Sanghera, C. Florea, L. Shaw, P. Pureza, V. Nguyen, M. Bashkansky, Z. Dutton, and I. Aggarwal, "Non-linear properties of chalcogenide glasses and fibers," *Journal of Non-Crystalline Solids*, vol. 354, pp. 462–467, jan 2008.

[184] M. Asobe, T. Kanamori, K. Naganuma, H. Itoh, and T. Kaino, "Third-order nonlinear spectroscopy in As2S3 chalcogenide glass fibers," *Journal of Applied Physics*, vol. 77, no. 11, pp. 5518–5523, 1995.

[185] R. E. Slusher, G. Lenz, J. Hodelin, J. Sanghera, L. B. Shaw, and I. D. Aggarwal, "Large Raman gain and nonlinear phase shifts in high-purity As2Se3 chalcogenide fibers," *Journal of the Optical Society of America B*, vol. 21, no. 6, pp. 1146–1155, 2004.

[186] O. P. Kulkarni, C. Xia, D. J. Lee, M. Kumar, A. Kuditcher, M. N. Islam, F. L. Terry, M. J. Freeman, B. G. Aitken, S. C. Currie, J. E. McCarthy, M. L. Powley, and D. A. Nolan, "Third order cascaded Raman wavelength shifting in chalcogenide fibers and determination of Raman gain coefficient," *Optics Express*, vol. 14, no. 17, pp. 7924–7930, 2006.

[187] A. Tuniz, G. Brawley, D. J. Moss, and B. J. Eggleton, "Two-photon absorption effects on Raman gain in single mode As2Se3 chalcogenide glass fiber," *Optics Express*, vol. 16, pp. 18524–18534, oct 2008.

[188] N. Hô, J. M. Laniel, R. Vallée, and A. Villeneuve, "Photosensitivity of As2S3 chalcogenide thin films at 1.5 μm," *Optics Letters*, vol. 28, pp. 965–967, jun 2003.

[189] K. Petkov and P. Ewen, "Photoinduced changes in the linear and non-linear optical properties of chalcogenide glasses," *Journal of Non-Crystalline Solids*, vol. 249, pp. 150–159, jul 1999.

[190] Y. Ruan, B. Luther-Davies, W. Li, A. Rode, V. Kolev, and S. Madden, "Large phase shifts in As2S3 waveguides for all-optical processing devices.," *Optics Letters*, vol. 30, pp. 2605–2607, oct 2005.

[191] T. Cardinal, K. Richardson, H. Shim, a. Schulte, R. Beatty, K. Le Foulgoc, C. Meneghini, J. Viens, and a. Villeneuve, "Non-linear optical properties of chalcogenide glasses in the system AsâĂŞSâĂŞSe," *Journal of Non-Crystalline Solids*, vol. 256-257, pp. 353–360, oct 1999.

[192] J. S. Sanghera and I. D. Aggarwal, "Development of chalcogenide glass fiber optics at NRL," *Journal of Non-Crystalline Solids*, vol. 213-214, pp. 63–67, may 1997.

[193] I. D. Aggarwal and J. S. Sanghera, "Development and Applications of Chalcogenide Glass Optical Fibers at NRL," *Journal of Optolectronics and Advanced Materials*, vol. 4, no. 3, pp. 665–678, 2002.

[194] E. C. Mägi, L. B. Fu, H. C. Nguyen, M. R. Lamont, D. I. Yeom, and B. J. Eggleton, "Enhanced Kerr nonlinearity in sub-wavelength diameter As2Se3 chalcogenide fiber tapers.," *Optics Express*, vol. 15, pp. 10324–10329, aug 2007.

[195] H. C. Nguyen, E. C. Mägi, D.-I. Yeom, L. Fu, and B. J. Eggleton, "Enhanced Kerr nonlinearity in As2Se3 chalcogenide fibre tapers with sub-wavelength diameter," in *Proceedings of SPIE*, vol. 6588, pp. 65880O–65880O–8, SPIE, may 2007.

[196] C. Baker and M. Rochette, "Highly nonlinear hybrid AsSe-PMMA microtapers.," *Optics Express*, vol. 18, pp. 12391–12398, jun 2010.

[197] R. Ahmad and M. Rochette, "High efficiency and ultra broadband optical parametric four-wave mixing in chalcogenide-PMMA hybrid microwires.," *Optics Express*, vol. 20, pp. 9572–9580, apr 2012.

[198] R. Ahmad and M. Rochette, "Chalcogenide optical parametric oscillator," *Optics Express*, vol. 20, pp. 10095–10099, apr 2012.

[199] R. Ahmad, M. Rochette, and C. Baker, "Fabrication of Bragg gratings in subwavelength diameter As2Se3 chalcogenide wires," *Optics Letters*, vol. 36, pp. 2886–2888, jul 2011.

[200] T. Miyashita and T. Manabe, "Infrared optical fibers," *IEEE Journal of Quantum Electronics*, vol. 18, pp. 1432–1450, oct 1982.

[201] K. Petkov, G. Vassilev, and V. Vassilev, "Dry etching of thin chalcogenide films," *Journal of Physics : Conference Series*, vol. 223, p. 012011, apr 2010.

[202] D. Choi, S. Maden, A. Rode, R. Wang, and B. Lutherdavies, "Plasma etching of As2S3 films for optical waveguides," *Journal of Non-Crystalline Solids*, vol. 354, pp. 3179–3183, jun 2008.

[203] J.-F. Viens, C. Meneghini, A. Villeneuve, T. Galstian, E. Knystautas, M. Duguay, K. Richardson, and T. Cardinal, "Fabrication and characterization of integrated optical waveguides in sulfide chalcogenide glasses," *Journal of Lightwave Technology*, vol. 17, pp. 1184–1191, jul 1999.

[204] J. Hu, V. Tarasov, N. Carlie, N. Feng, L. Petit, A. Agarwal, K. Richardson, and L. Kimerling, "Si-CMOS-compatible lift-off fabrication of low-loss planar chalcogenide waveguides," *Optics Express*, vol. 15, pp. 11798–11807, sep 2007.

[205] Z. G. Lian, W. Pan, D. Furniss, T. M. Benson, A. B. Seddon, T. Kohoutek, J. Orava, and T. Wagner, "Embossing of chalcogenide glasses : monomode rib optical waveguides in evaporated thin films.," *Optics Letters*, vol. 34, pp. 1234–1236, apr 2009.

[206] C. Tsay, E. Mujagić, C. K. Madsen, C. F. Gmachl, and C. B. Arnold, "Mid-infrared characterization of solution-processed As2S3 chalcogenide glass waveguides," *Optics Express*, vol. 18, pp. 15523–15530, jul 2010.

[207] J. Hu, N. Carlie, N.-N. Feng, L. Petit, A. Agarwal, K. Richardson, and L. Kimerling, "Planar waveguide-coupled, high-index-contrast, high-Q resonators in chalcogenide glass for sensing," *Optics Letters*, vol. 33, pp. 2500–2502, oct 2008.

[208] J. Hu, N. Carlie, L. Petit, A. Agarwal, K. Richardson, and L. Kimerling, "Demonstration of chalcogenide glass racetrack microresonators.," *Optics Letters*, vol. 33, pp. 761–763, apr 2008.

[209] M. Solmaz, D. Adams, W. Tan, W. Snider, and C. Madsen, "Vertically integrated As2S3 ring resonator on LiNbO3.," *Optics Letters*, vol. 34, pp. 1735–1737, may 2009.

[210] L. Li, H. Lin, S. Qiao, Y. Zou, S. Danto, K. Richardson, J. D. Musgraves, N. Lu, and J. Hu, "Integrated flexible chalcogenide glass photonic devices," *Nature Photonics*, vol. 8, pp. 643–649, jun 2014.

[211] P. Ma, D.-Y. Choi, Y. Yu, Z. Yang, K. Vu, T. Nguyen, A. Mitchell, B. Luther-Davies, and S. Madden, "High Q factor chalcogenide ring resonators for cavity-enhanced MIR spectroscopic sensing," *Optics Express*, vol. 23, pp. 19969–19979, jul 2015.

[212] S. J. Madden, D.-Y. Choi, D. a. Bulla, a. V. Rode, B. Luther-Davies, V. G. Ta'eed, M. D. Pelusi, and B. J. Eggleton, "Long, low loss etched As2S3 chalcogenide waveguides for all-optical signal regeneration," *Optics Express*, vol. 15, pp. 14414–14421, oct 2007.

[213] V. Ta'eed, N. J. Baker, L. Fu, K. Finsterbusch, M. R. E. Lamont, D. J. Moss, H. C. Nguyen, B. J. Eggleton, D.-Y. Choi, S. Madden, and B. Luther-Davies, "Ultrafast all-optical chalcogenide glass photonic circuits," *Optics Express*, vol. 15, no. 15, pp. 9205–9221, 2007.

[214] M. R. Lamont, B. Luther-Davies, D.-Y. Choi, S. Madden, and B. J. Eggleton, "Supercontinuum generation in dispersion engineered highly nonlinear As2S3 chalcogenide planar waveguide.," *Optics Express*, vol. 16, pp. 14938–14944, sep 2008.

[215] M. R. E. Lamont, B. Luther-Davies, D.-Y. Choi, S. Madden, X. Gai, and B. J. Eggleton, "Net-gain from a parametric amplifier on a chalcogenide optical chip.," *Optics Express*, vol. 16, pp. 20374–20381, dec 2008.

[216] G. Elliott, D. Hewak, G. Murugan, and J. Wilkinson, "Chalcogenide glass microspheres ; their production, characterization and potential," *Optics Express*, vol. 15, pp. 17542–17553, dec 2007.

[217] C. Grillet, S. N. Bian, E. C. Magi, and B. J. Eggleton, "Fiber taper coupling to chalcogenide microsphere modes," *Applied Physics Letters*, vol. 92, no. 17, p. 171109, 2008.

[218] G. R. Elliott, G. S. Murugan, J. S. Wilkinson, M. N. Zervas, and D. W. Hewak, "Chalcogenide glass microsphere laser.," *Optics Express*, vol. 18, pp. 26720–26727, dec 2010.

[219] F. Luan, E. Magi, T. Gong, I. Kabakova, and B. J. Eggleton, "Photoinduced whispering gallery mode microcavity resonator in a chalcogenide microfiber," *Optics Letters*, vol. 36, pp. 4761–4763, dec 2011.

[220] P. Wang, G. S. Murugan, G. Brambilla, M. Ding, Y. Semenova, Q. Wu, and G. Farrell, "Chalcogenide Microsphere Fabricated From Fiber Tapers Using Contact With a High-Temperature Ceramic Surface," *IEEE Photonics Technology Letters*, vol. 24, pp. 1103–1105, jul 2012.

[221] C.-R. Li, S.-X. Dai, Q.-Y. Zhang, X. Shen, X.-S. Wang, P.-Q. Zhang, L.-W. Lu, Y.-H. Wu, and S.-Q. Lv, "Low threshold fiber taper coupled rare earth ion-doped chalcogenide microsphere laser," *Chinese Physics B*, vol. 24, no. 4, p. 044208, 2015.

[222] D. Faucher, M. Bernier, N. Caron, and R. Vallée, "Erbium-doped all-fiber laser at 2.94 um," *Optics Letters*, vol. 34, pp. 3313–3315, nov 2009.

[223] K. Richardson, L. Petit, N. Carlie, B. Zdyrko, I. Luzinov, J. Hu, A. Agarwal, L. Kimerling, T. Anderson, and M. Richardson, "Progress on the Fabrication of on-Chip, Integrated Chalcogenide Glass (Chg)-Based Sensors," *Journal of Nonlinear Optical Physics & Materials*, vol. 19, no. 01, pp. 75–99, 2010.

[224] K. Yin, B. Zhang, G. Xue, L. Li, and J. Hou, "High-power all-fiber wavelength-tunable thulium doped fiber laser at 2 μm," *Optics Express*, vol. 22, pp. 19947–19952, aug 2014.

[225] V. Fortin, M. Bernier, S. T. Bah, and R. Vallée, "30 W fluoride glass all-fiber laser at 2.94 μm," *Optics Letters*, vol. 40, no. 12, pp. 2882–2885, 2015.

[226] A. Pal, S. Y. Chen, R. Sen, T. Sun, and K. T. V. Grattan, "A high- Q low threshold thulium-doped silica microsphere laser in the 2 μm wavelength region designed for gas sensing applications," *Laser Physics Letters*, vol. 10, p. 085101, aug 2013.

[227] K. Sasagawa, Z. O. Yonezawa, R. Iwai, J. Ohta, and M. Nunoshita, "S-band Tm3+-doped tellurite glass microsphere laser via a cascade process," *Applied Physics Letters*, vol. 85, no. 19, pp. 4325–4327, 2004.

[228] J. Wu, S. Jiang, and N. Peyghambarian, "1.5-um-band thulium-doped microsphere laser originating from self-terminating transition.," *Optics Express*, vol. 13, no. 25, pp. 10129–10133, 2005.

[229] J. Wu, S. Jiang, T. Qua, M. Kuwata-Gonokami, and N. Peyghambarian, "2 um lasing from highly thulium doped tellurite glass microsphere," *Applied Physics Letters*, vol. 87, no. 21, p. 211118, 2005.

[230] P. Bia, A. Di Tommaso, and M. De Sario, "Modeling of mid-IR amplifier based on an erbium-doped chalcogenide microsphere," *International Journal of Optics*, vol. 2012, p. 808679, 2012.

[231] L. Mescia, P. Bia, M. De Sario, A. Di Tommaso, and F. Prudenzano, "Design of mid-infrared amplifiers based on fiber taper coupling to erbium-doped microspherical resonator," *Optics Express*, vol. 20, no. 7, pp. 7616–7629, 2012.

[232] Zhaohong Han, Lin Zhang, L. C. Kimerling, and A. M. Agarwal, "Integrated Midinfrared Laser Based on an Er-Doped Chalcogenide Microresonator," *IEEE Journal of Selected Topics in Quantum Electronics*, vol. 21, pp. 311–317, jan 2015.

[233] M. F. Churbanov, a. N. Moiseev, a. V. Chilyasov, V. V. Dorofeev, and I. a. Kraev, "Production of high-purity TeO2-ZnO and TeO2-WO3 glasses with the reduced content of ĐđĐİ-groups," *Journal of Optoelectronics and Advanced Materials*, vol. 9, no. 10, pp. 3229–3234, 2007.

[234] A. Galstyan, S. Messaddeq, V. Fortin, I. Skripachev, R. Vallée, T. Galstian, and Y. Messaddeq, "Tm3+ doped Ga-As-S chalcogenide glasses and fibers," *Optical Materials*, vol. 47, pp. 518–523, sep 2015.

[235] V. Grigoriev and F. Biancalana, "Coupled-mode theory for on-channel nonlinear microcavities," *Journal of the Optical Society of America B*, vol. 28, pp. 2165–2173, aug 2011.

[236] B. A. Daniel and G. P. Agrawal, "Design of phase-switched two-input Kerr flip-flops," *Journal of the Optical Society of America B*, vol. 29, pp. 2288–2296, aug 2012.

[237] A. W. Snyder and J. D. Love, *Optical waveguide theory.* London : Chapman and Hall, 1983.

[238] J. Bures, *Guided optics : optical fibers and all-fiber components.* Weinheim : Wiley-VCH, 2009.

[239] A. Mazzei, S. Götzinger, L. de S. Menezes, G. Zumofen, O. Benson, and V. Sandoghdar, "Controlled Coupling of Counterpropagating Whispering-Gallery Modes by a Single Rayleigh Scatterer : A Classical Problem in a Quantum Optical Light," *Physical Review Letters*, vol. 99, p. 173603, oct 2007.

[240] L. He, S. K. Ozdemir, J. Zhu, and L. Yang, "Scatterer induced mode splitting in poly(dimethylsiloxane) coated microresonators," *Applied Physics Letters*, vol. 96, no. 22, p. 221101, 2010.

[241] F. Vanier, C. La Mela, A. Hayat, and Y.-A. Peter, "Intrinsic quality factor determination in whispering gallery mode microcavities using a single Stokes parameters measurement.," *Optics Express*, vol. 19, pp. 23544–23553, nov 2011.

[242] M. Abramowitz and I. A. Stegun, *Handbook of Mathematical Functions with Formulas, Graphs, and Mathematical Tables.* U.S. Department of Commerce, 1972.

[243] Y. R. Shen and N. Bloembergen, "Theory of Stimulated Brillouin and Raman Scattering," *Physical Review*, vol. 137, pp. A1787–A1805, mar 1965.

[244] R. W. Boyd, *Nonlinear Optics, 3rd edition.* Academic Press, 2008.

[245] K. Rottwitt, J. Bromage, A. J. Stentz, L. Leng, M. E. Lines, and H. Smith, "Scaling of the Raman Gain Coefficient : Applications to Germanosilicate Fibers," *Journal of Lightwave Technology*, vol. 21, pp. 1652–1662, jul 2003.

[246] M. J. F. Digonnet, *Rare-Earth-Doped Fiber Lasers and Amplifiers.* New York : Marcel Dekker, Inc., 2 ed., 2001.

[247] C. R. Giles and E. Desurvire, "Modeling Erbium-Doped Fiber Amplifiers," *Journal of Lightwave Technology*, vol. 9, no. 2, pp. 271–283, 1991.

[248] H. Gebavi, D. Milanese, R. Balda, S. Chaussedent, M. Ferrari, J. Fernandez, and M. Ferraris, "Spectroscopy and optical characterization of thulium doped TZN glasses," *Journal of Physics D : Applied Physics*, vol. 43, no. 13, p. 135104, 2010.

[249] M. Borselli, *High-Q Microresonators as Lasing Elements for Silicon Photonics.* PhD thesis, California Institute of Technology, 2006.

[250] M. Cai, O. Painter, and K. J. Vahala, "Observation of Critical Coupling in a Fiber Taper to a Silica-Microsphere Whispering-Gallery Mode System," *Physical Review Letters*, vol. 85, pp. 74–77, jul 2000.

[251] A. Schulte, C. Rivero, K. Richardson, K. Turcotte, V. Hamel, A. Villeneuve, T. Galstian, and R. Vallee, "Bulk-film structural differences of chalcogenide glasses probed in situ by near-infrared waveguide Raman spectroscopy," *Optics Communications*, vol. 198, pp. 125–128, oct 2001.

[252] S. M. Spillane, T. J. Kippenberg, O. J. Painter, and K. J. Vahala, "Ideality in a Fiber-Taper-Coupled Microresonator System for Application to Cavity Quantum Electrodynamics," *Physical Review Letters*, vol. 91, pp. 2–5, jul 2003.

[253] G. Lin, Y. Candela, O. Tillement, Z. Cai, V. Lefèvre-Seguin, and J. Hare, "Thermal bistability-based method for real-time optimization of ultralow-threshold whispering gallery mode microlasers.," *Optics Letters*, vol. 37, pp. 5193–5195, dec 2012.

[254] K. Kieu and M. Mansuripur, "Fiber laser using a microsphere resonator as a feedback element," *Optics Letters*, vol. 32, no. 3, pp. 244–246, 2007.

[255] R. Ahmad and M. Rochette, "Raman lasing in a chalcogenide microwire-based Fabry-Perot cavity," *Optics Letters*, vol. 37, pp. 4549–4551, oct 2012.

[256] S. D. Jackson and G. Anzueto-Sanchez, "Chalcogenide glass Raman fiber laser," *Applied Physics Letters*, vol. 88, no. 22, p. 221106, 2006.

[257] M. Bernier, V. Fortin, N. Caron, M. El-Amraoui, Y. Messaddeq, and R. Vallée, "Mid-infrared chalcogenide glass Raman fiber laser," *Optics Letters*, vol. 38, pp. 127–129, jan 2013.

[258] C. Xiong, E. Magi, F. Luan, A. Tuniz, S. Dekker, J. S. Sanghera, L. B. Shaw, I. D. Aggarwal, and B. J. Eggleton, "Characterization of picosecond pulse nonlinear propagation in chalcogenide As2S3 fiber," *Applied Optics*, vol. 48, pp. 5467–5474, oct 2009.

[259] N. Ducros, F. Morin, K. Cook, A. Labruyère, S. Février, G. Humbert, F. Druon, M. Hanna, P. Georges, J. Canning, R. Buczynski, D. Pysz, and R. Stepien, "Frequency conversion from near-infrared to mid-infrared in highly nonlinear optical fibres," in *Proc. of SPIE*, vol. 7714, pp. 77140B–77140B–8, apr 2010.

[260] R. T. White and T. M. Monro, "Cascaded Raman shifting of high-peak-power nanosecond pulses in As2S3 and As2Se3 optical fibers.," *Optics Letters*, vol. 36, pp. 2351–2353, jun 2011.

[261] M. Duhant, W. Renard, G. Canat, T. N. Nguyen, F. Smektala, J. Troles, Q. Coulombier, P. Toupin, L. Brilland, P. Bourdon, and G. Renversez, "Fourth-order cascaded Raman shift in AsSe chalcogenide suspended-core fiber pumped at 2 μm.," *Optics Letters*, vol. 36, pp. 2859–2861, aug 2011.

[262] M. Bernier, V. Fortin, M. El-Amraoui, Y. Messaddeq, and R. Vallée, "3.77 μm fiber laser based on cascaded Raman gain in a chalcogenide glass fiber.," *Optics Letters*, vol. 39, no. 7, pp. 2052–5, 2014.

[263] H. Lin, L. Li, Y. Zou, S. Danto, J. D. Musgraves, K. Richardson, S. Kozacik, M. Murakowski, D. Prather, P. T. Lin, V. Singh, A. Agarwal, L. C. Kimerling, and J. Hu, "Demonstration of high-Q mid-infrared chalcogenide glass-on-silicon resonators," *Optics Letters*, vol. 38, pp. 1470–1472, apr 2013.

[264] O. Aktas, E. Ozgur, O. Tobail, M. Kanik, E. Huseyinoglu, and M. Bayindir, "A New Route for Fabricating On-Chip Chalcogenide Microcavity Resonator Arrays," *Advanced Optical Materials*, vol. 2, no. 7, pp. 618–625, 2014.

[265] F. Vanier, M. Rochette, N. Godbout, and Y.-A. Peter, "Raman lasing in As2S3 high-Q whispering gallery mode resonators," *Optics Letters*, vol. 38, pp. 4966–4969, nov 2013.

[266] N. S. Nishioka and Y. Domankevitz, "Comparison of tissue ablation with pulsed holmium and thulium lasers," *IEEE Journal of Quantum Electronics*, vol. 26, no. 12, pp. 2271–2275, 1990.

[267] N. J. Scott, C. M. Cilip, and N. M. Fried, "Thulium fiber laser ablation of urinary Stones through small-core Optical fibers," *IEEE Journal on Selected Topics in Quantum Electronics*, vol. 15, no. 2, pp. 435–440, 2009.

[268] R. L. Blackmon, P. B. Irby, and N. M. Fried, "Comparison of holmium :YAG and thulium fiber laser lithotripsy : ablation thresholds, ablation rates, and retropulsion effects.," *Journal of Biomedical Optics*, vol. 16, no. 7, p. 071403, 2011.

[269] M. Baudelet, C. C. C. Willis, L. Shah, and M. Richardson, "Laser-induced breakdown spectroscopy of copper with a 2 microm thulium fiber laser.," *Optics Express*, vol. 18, no. 8, pp. 7905–7910, 2010.

[270] K. Bremer, A. Pal, S. Yao, E. Lewis, R. Sen, T. Sun, and K. T. V. Grattan, "Sensitive detection of CO2 implementing tunable thulium-doped all-fiber laser," *Applied Optics*, vol. 52, no. 17, pp. 3957–3963, 2013.

[271] J. Li, H. Lee, and K. J. Vahala, "Microwave synthesizer using an on-chip Brillouin oscillator," *Nature Communications*, vol. 4, pp. 1–7, jun 2013.

[272] E. R. Taylor, L. N. Ng, N. P. Sessions, and H. Buerger, "Spectroscopy of Tm3+-doped tellurite glasses for 1470 nm fiber amplifier," *Journal of Applied Physics*, vol. 92, no. 1, pp. 112–117, 2002.

[273] B. Richards, A. Jha, Y. Tsang, D. Binks, J. Lousteau, F. Fusari, A. Lagatsky, C. Brown, and W. Sibbett, "Tellurite glass lasers operating close to 2 um," *Laser Physics Letters*, vol. 7, no. 3, pp. 177–193, 2010.

[274] X. Peng, F. Song, M. Kuwata-Gonokami, S. Jiang, and N. Peyghambarian, "Er[sup 3+]-doped tellurite glass microsphere laser : optical properties, coupling scheme, and lasing characteristics," *Optical Engineering*, vol. 44, no. 3, p. 034202, 2005.

[275] F. Vanier, Y.-A. Peter, and M. Rochette, "Cascaded Raman lasing in packaged high quality As2S3 microspheres," *Optics Express*, vol. 22, pp. 28731–28739, nov 2014.

[276] J. Li, Z. Sun, H. Luo, Z. Yan, K. Zhou, Y. Liu, and L. Zhang, "Wide wavelength selectable all-fiber thulium doped fiber laser between 1925 nm and 2200 nm.," *Optics Express*, vol. 22, no. 5, pp. 5387–5399, 2014.

[277] N. Deka, A. J. Maker, and A. M. Armani, "Titanium enhanced Raman microcavity laser," in *Optics Letters*, vol. 39, pp. 1354–1357, mar 2014.

[278] H. Rong, S. Xu, O. Cohen, O. Raday, M. Lee, V. Sih, and M. Paniccia, "A cascaded silicon Raman laser," *Nature Photonics*, vol. 2, no. March, pp. 170–174, 2008.

[279] M. V. Chistiakova and A. M. Armani, "Cascaded Raman microlaser in air and buffer.," *Optics Letters*, vol. 37, pp. 4068–4070, oct 2012.

[280] M. Bernier, J. F. Couillard, Y. Messaddeq, and R. Vallée, "Writing of Bragg gratings through the polymer jacket of low-loss As2S3 fibers using femtosecond pulses at 800 nm," *Optics Letters*, vol. 37, no. 18, pp. 3900–3902, 2012.

[281] H. Ebendorff-Heidepriem, K. Kuan, M. R. Oermann, K. Knight, and T. M. Monro, "Extruded tellurite glass and fibers with low OH content for mid-infrared applications," *Optical Materials Express*, vol. 2, no. 4, pp. 432–442, 2012.

[282] X. Feng, J. Shi, M. Segura, N. White, P. Kannan, L. Calvez, X. Zhang, L. Brilland, and W. Loh, "Towards Water-Free Tellurite Glass Fiber for 2-5 μm Nonlinear Applications," *Fibers*, vol. 1, pp. 70–81, nov 2013.

[283] L. D. Landau, *The classical theory of fields*. Oxford : Pergamon Press, 3rd ed., 1971.

[284] M. Born and E. Wolf, *Principles of Optics : Electromagnetic Theory of Propagation, Interference and Diffraction of Light, 7th edition*. Cambridge : Cambridge University Press, 7th ed., 1999.

[285] T. J. Kippenberg, S. M. Spillane, and K. J. Vahala, "Demonstration of ultra-high-Q small mode volume toroid microcavities on a chip," *Applied Physics Letters*, vol. 85, no. 25, p. 6113, 2004.

[286] D. S. Weiss, V. Sandoghdar, J. Hare, V. Lefèvre-Seguin, J.-M. Raimond, and S. Haroche, "Splitting of high-Q Mie modes induced by light backscattering in silica microspheres," *Optics Letters*, vol. 20, pp. 1835–1837, sep 1995.

[287] I. Teraoka and S. Arnold, "Theory of resonance shifts in TE and TM whispering gallery modes by nonradial perturbations for sensing applications," *Journal of the Optical Society of America B*, vol. 23, no. 7, pp. 1381–1389, 2006.

ANNEX A LIST OF SCIENTIFIC CONTRIBUTIONS

Refereed journal publications

- **F. Vanier**, F. Côté, M. El Amraoui, Y. Messaddeq, Y.-A. Peter, and M. Rochette, "Low threshold lasing at 1975 nm in thulium-doped tellurite glass microspheres" *Optics Letters*, vol. 40, n. 22, pp. 5227-5230, 2015.
- **F. Vanier**, Y.-A. Peter, et M. Rochette, "Cascaded Raman lasing in packaged high quality As_2S_3 microspheres," *Optics Express*, vol. 22, n. 23, pp. 28731-28739, 2014.
- **F. Vanier**, M. Rochette, Nicolas Godbout, et Y.-A. Peter, "Raman lasing in As_2S_3 high Q whispering gallery mode resonators," *Optics Letters*, vol. 38, n. 23, pp. 4966-4969, 2013.

Refereed journal publication not included in this thesis

- **F. Vanier**, C. La Mela, A. Hayat, et Y.-A. Peter, "Intrinsic quality factor determination in whispering gallery mode microcavities using a single Stokes parameters measurement," *Optics Express*, vol. 19, n. 23, pp. 23544-23553, 2011.
  (Selected paper in *Virtual Journal of Biomedical Optics*, vol. 7, no. 1, 2012)

Refereed conference publications

- **F. Vanier**†, Y.-A. Peter, et M. Rochette, "2 μm cascaded Raman scattering emission from As_2S_3 high-Q microspheres," *IEEE Intl. Conf. on Optical MEMS and Nanophotonics*, Glasgow, Scotland, pp. 15-16, 2014.
- **F. Vanier**†, M. Rochette, et Y.-A. Peter, "High-order Raman scattering emission in high-Q factor As_2S_3 microspheres," *Photonics Society Summer Topical Meeting Series*, Montréal, Canada, pp. 37-38, 2014.
- **F. Vanier**†, M. Rochette, et Y.-A. Peter, "Raman scattering emission in high Q factor As_2S_3 microspheres," *Conference on Lasers and Electro-Optics*, San Jose, USA, 2013.
- **F. Vanier**†, N. Godbout, M. Rochette, et Y.-A. Peter, "As_2S_3 Microspheres With Near Absorption-Limited Quality Factor," *IEEE Intl. Conf. on Optical MEMS and Nanophotonics*, Banff, Canada, pp. 45-46, 2012.
- M. I. Cheema, S. Mehrabani, A. Hayat, **F. Vanier**, Y.-A. Peter, A. M. Armani, et A. G.

Kirk, "Experimental demonstration of application of ring down measurement approach to microcavities for biosensing," Proc. SPIE 8212, Frontiers in Biological Detection : From Nanosensors to Systems IV, 2012.

- **F. Vanier***, C. La Mela, A. Hayat, et Y.-A. Peter, "Whispering Gallery Modes intrinsic quality factor and coupling regime extraction using stokes parameters," *IEEE Intl. Conf. on Optical MEMS and Nanophotonics*, Istanbul, Turkey, pp. 173-174, 2011.

- S. Bergeron, **F. Vanier**†, et Y.-A. Peter, "Silica microdisk coupled resonator optical waveguide," *IEEE Intl. Conf. on Optical MEMS and Nanophotonics*, Florida, USA, pp. 73-74, 2009.

† Oral presentation ∗ Poster presentation

ANNEX B EXPLICIT COUPLED-MODES EQUATIONS

B.1 Explicit linear coupled-modes theory in a WGM microcavity

This section details the steps needed to obtain important formulations and coupled-modes equations of Chapter 2.2. It offers a step-by-step description of the various constants and definitions found in the literature, starting from Maxwell equations to Q-factor explicit definitions.

B.1.1 Fields description and Maxwell equations

Vectors are written in bold : $\mathbf{E}(\mathbf{r},t) \equiv \vec{E}(\rho,\theta,\phi,t)$ or $\vec{E}(\rho,\theta,z,t)$

Fields notation

The total electric field is expressed as the linear combinaison of the electric fields of the cavity modes and the waveguide modes :

$$\begin{aligned}\mathbf{E}(\mathbf{r},t) &= \mathbf{E}_{\text{cavity}}(\mathbf{r},t) + \mathbf{E}_{\text{guide}}(\mathbf{r},t) \\ &= \sum_j \mathbf{E}_j(\mathbf{r},t) + \sum_L \mathbf{E}_L(\mathbf{r},t) \\ &= \sum_j \frac{a_j(t)e^{-i\omega_j t}\mathbf{e}_j(\mathbf{r})}{2\sqrt{N_j}} + \sum_L \frac{s_L(z,t)e^{-i\omega_L t}\mathbf{e}_L(\mathbf{r})}{2\sqrt{M_L}} + \text{c.c.}\end{aligned} \tag{B.1}$$

For cavity modes, $a_j(t)$ is the slowly varying component in time compared to $e^{-i\omega_j t}$. For waveguide modes, $s_L(z,t)$ is the slowly varying component in time and in space compared to the fast varying phase term $e^{i\beta_L z - i\omega_j t}$. $\mathbf{e}_j(\mathbf{r})$ and $\mathbf{e}_L(\mathbf{r})$ are representing the constant field distributions of the eigenmodes j and L of the cavity and the waveguide respectively. N_j is the cavity modes normalization constant, these modes are normalized so that $|a_j(t)|$ is the total confined energy of the jth mode. Similarly, M_L is the waveguide modes normalization constant and the modes are normalized so that $|s_L(z,t)|$ is the power propagating in the waveguide. Figure B.1 displays the different linear coupling processes such as external coupling and mode coupling (Section B.1.5).

The cavity field is expressed in spherical coordinates as seen in Section B.3 and the waveguide field is written using cylindrical coordinates with the z-direction along the waveguide. Computations of overlap integrals should be done using the right coordinate transformations

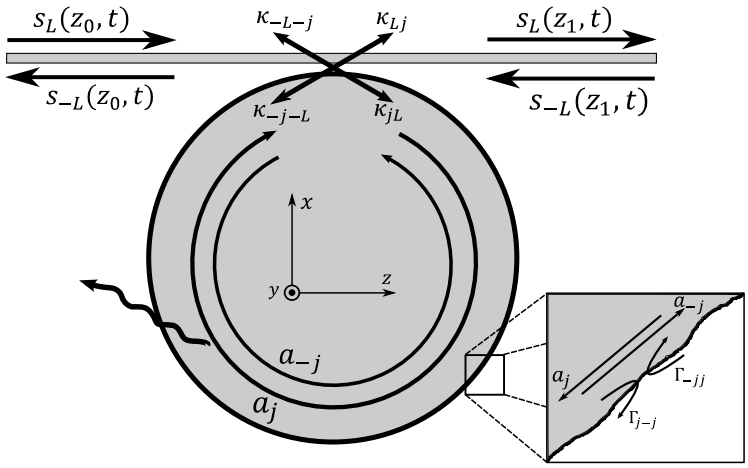

Figure B.1 : Schematic of the linear coupling processes between a waveguide and a WGM microcavity.

beforehand.

Maxwell equations

In a dielectric material, the propagation of monochromatic fields can be described by the macroscopic Maxwell equations without charge ($\rho = 0$) and current ($\mathbf{J} = 0$) :

$$\nabla \cdot \mathbf{D}(\mathbf{r},t) = 0 \tag{B.2}$$

$$\nabla \cdot \mathbf{B}(\mathbf{r},t) = 0 \tag{B.3}$$

$$\nabla \wedge \mathbf{E}(\mathbf{r},t) = -\frac{\partial \mathbf{B}(\mathbf{r},t)}{\partial t} = -\mu_0 \frac{\partial \mathbf{H}(\mathbf{r},t)}{\partial t} \tag{B.4}$$

$$\nabla \wedge \mathbf{H}(\mathbf{r},t) = \frac{\partial \mathbf{D}(\mathbf{r},t)}{\partial t} \tag{B.5}$$

where we considered that the material has a null magnetic response ($\mu_r = 0$) :

$$\mathbf{B}(\mathbf{r},t) = \mu_0 \mathbf{H}(\mathbf{r},t).$$

The electric displacement field $\mathbf{D}(\mathbf{r},t)$ is related to the electric field $\mathbf{E}(\mathbf{r},t)$ by

$$\mathbf{D}(\mathbf{r},t) = \epsilon_0 \mathbf{E}(\mathbf{r},t) + \mathbf{P}(\mathbf{r},t) \tag{B.6}$$

where $\mathbf{P}(\mathbf{r},t)$ is the polarization density vector or the electric polarization vector which describes the material reaction [1] in the presence of $\mathbf{E}(\mathbf{r},t)$. ϵ_0 and μ_0 are the vacuum permittivity

1. See the footnote of p.1 in M. Born & E. Wolf, *Principles of Optics 6th ed.*, Cambridge, 1980

and the vacuum permeability respectively.

Electric polarization and electric susceptibility

The material reaction in the presence of an electric field is due to different sources : the electronic dipoles, ions dipoles, photon-phonon interactions and free charges. The contribution of each source depends on the material composition and the field frequency. For example, in the visible region, electronic dipoles is the dominant response in transparent glasses such as silica.

The response is usually proportional to $\mathbf{E}(\mathbf{r},t)$. Nevertheless, when the field intensity is large, a nonlinear response may become important. In this case, $\mathbf{P}(\mathbf{r},t)$ depends on different field combinations. The x field component can affect the y component and can even influence itself. Phonon interactions are also possible for large field intensities.

The electric polarization vector depends on the applied electric field $\mathbf{E}(\mathbf{r},t)$ and can be written, in cartesian coordinates, as

$$\mathbf{P}(\mathbf{r},t) = \sum_{i=(x,y,z)} P_i(\mathbf{r},t)\hat{u}_i$$

with the unitary vector $\hat{u}_i$ for the $i=(x,y,z)$ components and

$$P_i(\mathbf{r},t) = P_i^{(1)}(\mathbf{r},t) + P_i^{(2)}(\mathbf{r},t) + P_i^{(3)}(\mathbf{r},t) + ...$$

where

$$P_i^{(1)}(\mathbf{r},t) = \epsilon_0 \sum_j \int\int_\infty \chi_{ij}^{(1)}(\mathbf{r}_1,t_1) E_j(\mathbf{r}-\mathbf{r}_1, t-t_1) dt_1 d\mathbf{r}_1$$

$$P_i^{(2)}(\mathbf{r},t) = \epsilon_0 \sum_j \sum_k \int\int\int\int_\infty \chi_{ijk}^{(2)}(\mathbf{r}_1,\mathbf{r}_2,t_1,t_2) E_j(\mathbf{r}-\mathbf{r}_1, t-t_1) E_k(\mathbf{r}-\mathbf{r}_2, t-t_2) dt_1 dt_2 d\mathbf{r}_1 d\mathbf{r}_2$$

$$\begin{aligned} P_i^{(3)}(\mathbf{r},t) = \epsilon_0 \sum_j \sum_k \sum_l \int\int\int\int\int\int_\infty \\ \chi_{ijkl}^{(3)}(\mathbf{r}_1,\mathbf{r}_2,\mathbf{r}_3,t_1,t_2,t_3) E_j(\mathbf{r}-\mathbf{r}_1, t-t_1) E_k(\mathbf{r}-\mathbf{r}_2, t-t_2) E_l(\mathbf{r}-\mathbf{r}_3, t-t_3) \\ dt_1 dt_2 dt_3 d\mathbf{r}_1 d\mathbf{r}_2 d\mathbf{r}_3. \end{aligned}$$

The linear response is described by $P^{(1)}$. Nonlinear responses such as second order processes and third order processes are described by $P^{(2)}$ and $P^{(3)}$ respectively. Higher order terms can be observed if the field intensity is large enough. The material reaction at ($\mathbf{r}$,t) depends on the past value of the surrounding electric fields. Two approximations are useful.

Local field approximation

The local field approximation considered that the response at $\mathbf{r}$ is not affected by its surrounding. In other words, the electric susceptibility is nonzero at $\mathbf{r}_1 = \mathbf{r}_2 = \mathbf{r}_3 = 0$. It is written as

$$\chi^{(3)}_{ijkl}(\mathbf{r}_1, \mathbf{r}_2, \mathbf{r}_3, t_1, t_2, t_3) = \chi^{(3)}_{ijkl}(\mathbf{r}, t_1, t_2, t_3)\delta(\mathbf{r}_1)\delta(\mathbf{r}_2)\delta(\mathbf{r}_3)$$

and gives

$$\begin{aligned}
P^{(1)}_i(\mathbf{r}, t) &= \epsilon_0 \sum_j \int_\infty \chi^{(1)}_{ij}(\mathbf{r}, t_1) E_j(\mathbf{r}, t - t_1) dt_1 \\
P^{(2)}_i(\mathbf{r}, t) &= \epsilon_0 \sum_j \sum_k \int \int_\infty \chi^{(2)}_{ijk}(\mathbf{r}, t_1, t_2) E_j(\mathbf{r}, t - t_1) E_k(\mathbf{r}, t - t_2) dt_1 dt_2 \\
P^{(3)}_i(\mathbf{r}, t) &= \epsilon_0 \sum_j \sum_k \sum_l \int \int \int_\infty \\
&\qquad \chi^{(3)}_{ijkl}(\mathbf{r}, t_1, t_2, t_3) E_j(\mathbf{r}, t - t_1) E_k(\mathbf{r}, t - t_2) E_l(\mathbf{r}, t - t_3) dt_1 dt_2 dt_3.
\end{aligned}$$

The spatial coordinate $\mathbf{r}$ is kept because it is imposed by the system geometry.

Fast response approximation

A fast response implies that the susceptibility decreases quickly around t. In our case, electric fields are written as Eq. B.1 :

$$\mathbf{E}(\mathbf{r}, t - t_1) \propto \mathbf{e}_p(\mathbf{r}) a_p(t - t_1) e^{-i\omega_p(t - t_1)} \approx \mathbf{e}_p(\mathbf{r}) a_p(t) e^{-i\omega_p(t - t_1)}. \tag{B.7}$$

where the slowly varying amplitude $a_p(t)$ is considered constant around t, where the electric susceptibility decreases quickly. $a_p(t)$ is then taken outside the integral and

$$\begin{aligned}
P^{(1)}_i(\mathbf{r}, t) &= \epsilon_0 \sum_j \int_\infty \left[\chi^{(1)}_{ij}(\mathbf{r}, t_1) e^{i\omega_p t_1} dt_1\right] a_p(t) e^{-i\omega_p t} \mathbf{e}_p(\mathbf{r}) \\
&= \epsilon_0 \sum_j \chi^{(1)}_{ij}(\mathbf{r}, \omega_p) a_p(t) e^{-i\omega_p t} \mathbf{e}_p(\mathbf{r}) \\
P^{(2)}_i(\mathbf{r}, t) &= \epsilon_0 \sum_j \sum_k \int \int_\infty \left[\chi^{(2)}_{ijk}(\mathbf{r}, t_1, t_2) e^{i\omega_p t_1} e^{i\omega_l t_2} dt_1 dt_2\right] a_p(t) a_l(t) e^{-i(\omega_p + \omega_l)t} \mathbf{e}_p(\mathbf{r}) \mathbf{e}_l(\mathbf{r}) \\
&= \epsilon_0 \sum_j \sum_k \chi^{(2)}_{ijk}(\mathbf{r}, \omega_p, \omega_l) a_p(t) a_l(t) e^{-i(\omega_p + \omega_l)t} \mathbf{e}_p(\mathbf{r}) \mathbf{e}_l(\mathbf{r}) \\
P^{(3)}_i(\mathbf{r}, t) &= \epsilon_0 \sum_j \sum_k \sum_l \int \int \int_\infty \\
&\qquad \left[\chi^{(3)}_{ijkl}(\mathbf{r}, t_1, t_2, t_3) e^{i\omega_p t_1} e^{i\omega_l t_2} e^{i\omega_m t_3} dt_1 dt_2 dt_3\right] a_p(t) a_l(t) a_m(t) e^{-i(\omega_p + \omega_l + \omega_m)t} \mathbf{e}_p(\mathbf{r}) \mathbf{e}_l(\mathbf{r}) \mathbf{e}_m(\mathbf{r})
\end{aligned}$$

$$= \epsilon_0 \sum_j \sum_k \sum_l \chi^{(3)}_{ijkl}(\mathbf{r}, \omega_p, \omega_l, \omega_m) a_p(t) a_l(t) a_m(t) e^{-i(\omega_p+\omega_l+\omega_m)t} \mathbf{e}_p(\mathbf{r}) \mathbf{e}_l(\mathbf{r}) \mathbf{e}_m(\mathbf{r}).$$

where $\chi^{(3)}_{ijkl}(\mathbf{r}, \omega_p, \omega_l, \omega_m) = \text{T.F.}\left\{\chi^{(3)}_{ijkl}(\mathbf{r}, t_1, t_2, t_3)\right\}$. With these approximations, the frequency response of the electric susceptibility can be used in the temporal propagation equations.

Isotropic medium : no slow-fast axis and $\chi^{(2)} = 0$

In opposition to crystalline materials, glasses or amorphous media are considered to be isotropic because of their lack of preferential axis on the macroscopic level. This means that the properties of a light beam such as the polarization is not modified if the medium is rotated. This simplifies the electric polarization vector.

On the first order, the linear response is now a scalar $\chi^{(1)}_{ij}(\mathbf{r}, \omega_p) \rightarrow \chi^{(1)}(\mathbf{r}, \omega_p)$ as each component of the electric field sees the same material response. The second order response $\chi^{(2)}_{ijk}$ vanishes in an isotropic medium as it is centrosymmetric [244].

For monochromatic fields of frequency ω, Relation B.6 becomes

$$\mathbf{D}(\mathbf{r}, t) = \epsilon_0 \mathbf{E}(\mathbf{r}, t) + \mathbf{P}(\mathbf{r}, t) = \epsilon_0 (1 + \chi^{(1)}(\mathbf{r}, \omega)) \mathbf{E}(\mathbf{r}, t) + \mathbf{P}^{(3)}(\mathbf{r}, t) = \epsilon_0 \epsilon_r(\mathbf{r}, \omega) \mathbf{E}(\mathbf{r}, t) + \mathbf{P}^{(3)}(\mathbf{r}, t)$$

where $\epsilon_r(\mathbf{r}, \omega) = 1 + \text{Re}[\chi^{(1)}(\mathbf{r}, \omega)] + i\text{Im}[\chi^{(1)}(\mathbf{r}, \omega)]$ is the dielectric constant of the medium. It can be written as $\epsilon_r = (n_0 + in_0')^2 = n_0^2 - n_0'^2 + i2n_0 n_0'$ where n_0 and n_0' are known as the refractive index and extinction coefficient respectively. They are usually defined as $n + ik$ in handbooks.

In a transparent material where $n_0 >> n_0'$, we have

$$n_0^2 \approx 1 + \text{Re}[\chi^{(1)}(\mathbf{r}, \omega)] \quad \text{and} \quad n_0' \approx \frac{\text{Im}[\chi^{(1)}(\mathbf{r}, \omega)]}{2n_0}.$$

This holds for silica or silicon at a wavelength of 1.5 μm. For example, for Si, at this wavelength, $n_0 \approx 3.45$ and $n_0' < 10^{-6}$ [164].

The linear absorption α_{lin} is expressed as

$$\alpha_{lin} = 2k_0 n_0' \approx \frac{k_0 \text{Im}[\chi^{(1)}(\mathbf{r}, \omega)]}{n_0}$$

with the wavenumber $k_0 = \frac{2\pi}{\lambda_0}$.

B.1.2 Energy density, power, intensity and mode normalization

How do we define the energy density, the power or the intensity of an optical mode ? In the literature, these concepts are defined using the Poynting's theorem developed in many references [244, 283, 284]. Considering an isotropic and linear medium without free charge ($\rho = 0$), no current ($\mathbf{J} = 0$) and no magnetic response :

$$\nabla \cdot \mathbf{D}(\mathbf{r}, t) = \epsilon_0 \epsilon_r \nabla \cdot \mathbf{E}(\mathbf{r}, t) = 0 \tag{B.8}$$

$$\nabla \cdot \mathbf{B}(\mathbf{r}, t) = \mu_0 \nabla \cdot \mathbf{H}(\mathbf{r}, t) = 0 \tag{B.9}$$

$$\nabla \wedge \mathbf{E}(\mathbf{r}, t) = -\frac{\partial \mathbf{B}(\mathbf{r}, t)}{\partial t} = -\mu_0 \frac{\partial \mathbf{H}(\mathbf{r}, t)}{\partial t} \tag{B.10}$$

$$\nabla \wedge \mathbf{H}(\mathbf{r}, t) = \frac{\partial \mathbf{D}(\mathbf{r}, t)}{\partial t} = \epsilon_0 \epsilon_r \frac{\partial \mathbf{E}(\mathbf{r}, t)}{\partial t} \tag{B.11}$$

Multiplying Eq. B.10 by $\mathbf{H}(\mathbf{r}, t)$ and Eq. B.11 by $\mathbf{E}(\mathbf{r}, t)$ on each side gives

$$\begin{aligned} \epsilon_0 \epsilon_r \frac{\partial \mathbf{E}}{\partial t} \mathbf{E} + \mu_0 \frac{\partial \mathbf{H}}{\partial t} \mathbf{H} &= -(\mathbf{H} \cdot \nabla \wedge \mathbf{E} - \mathbf{E} \cdot \nabla \wedge \mathbf{H}) = -\nabla(\mathbf{E} \wedge \mathbf{H}) \\ \Rightarrow \frac{\epsilon_0 \epsilon_r}{2} \frac{\partial \mathbf{E}^2}{\partial t} + \frac{\mu_0}{2} \frac{\partial \mathbf{H}^2}{\partial t} &= \frac{\partial}{\partial t} \left(\frac{\epsilon_0 \epsilon_r \mathbf{E}^2 + \mu_0 \mathbf{H}^2}{2} \right) = -\nabla(\mathbf{E} \wedge \mathbf{H}) \end{aligned}$$

where $(\mathbf{r}, t)$ is dropped for clarity. By integrating on a volume V and using the divergence theorem (Gauss theorem), we write

$$\begin{aligned} \frac{\partial}{\partial t} \int \left(\frac{\epsilon_0 \epsilon_r \mathbf{E}^2 + \mu_0 \mathbf{H}^2}{2} \right) \, dV &= -\int \nabla(\mathbf{E} \wedge \mathbf{H}) \, dV \\ &= -\oint \mathbf{E} \wedge \mathbf{H} \, d\mathbf{f} = -\oint (\mathbf{E} \wedge \mathbf{H}) \cdot \mathbf{n} \, df \end{aligned}$$

where $\mathbf{n}$ is the unitary vector perpendicular to the surface f around the integration volume V. By definition,

$$W = \int \left(\frac{\epsilon_0 \epsilon_r \mathbf{E}^2(\mathbf{r}, t) + \mu_0 \mathbf{H}^2(\mathbf{r}, t)}{2} \right) dV \text{ et } \mathbf{S}(\mathbf{r}, t) = \mathbf{E}(\mathbf{r}, t) \wedge \mathbf{H}(\mathbf{r}, t) \tag{B.12}$$

are the total electromagnetic energy in the volume and the Poynting vector respectively, and

$$\frac{\partial W}{\partial t} = -\oint \mathbf{S} \cdot \mathbf{n} df. \tag{B.13}$$

The Poynting vector is the energy flux density traveling through df per unit of time. This relation simply states that the change of energy in a volume V in a time dt is equal to ingoing and outgoing intensities that pass through the surface f — the ingoing and outgoing power.

Normalization

N_j and M_L are normalization factors and they are based on the Poynting's theorem results shown in Section B.1.2. For an unperturbed cavity, the average energy contained in an optical mode j can be written as [237]

$$\begin{aligned} W_j &= < \int_V \left(\frac{\epsilon_0 \epsilon_r \mathbf{E}_j^2(\mathbf{r},t) + \mu_0 \mathbf{H}_j^2(\mathbf{r},t)}{2} \right) dV > \\ &= \frac{|a_j(t)|^2}{2N_j} \int_V \epsilon_0 \epsilon_r |\mathbf{e}_j(\mathbf{r})|^2 dV \end{aligned}$$

Averaging using $< f(t) > \equiv \frac{1}{T}\int_0^T f(t)dt$ removes the time varying terms $\propto e^{-i2\omega t}$ which are oscillating rapidly compared to the time interval T. $a_j(t)$ and $s_L(z,t)$ are considered almost constant over T.

We wish to have $W_j = |a_j(t)|^2$, so

$$N_j = \frac{1}{2} \int_V \epsilon_0 (n_0^2|_c) |\mathbf{e}_j(\mathbf{r})|^2 dV$$

Similarly, for an unperturbed waveguide, the averaged power ΔP_L in the optical mode L entering or exiting a volume surrounded by a surface S can be written as [237] :

$$\begin{aligned} \Delta P_L &= < \oint_S (\mathbf{E}_L(\mathbf{r},t) \wedge \mathbf{H}_L(\mathbf{r},t)) \cdot \hat{\mathbf{n}} dS > \\ &= \frac{1}{4M_L} \oint_S |s_L(z,t)|^2 (\mathbf{e}_L(\mathbf{r}) \wedge \mathbf{h}_L^*(\mathbf{r}) + \mathbf{e}_L^*(\mathbf{r}) \wedge \mathbf{h}_L(\mathbf{r})) \cdot \hat{\mathbf{n}} dS \end{aligned}$$

where $\hat{n}$ is the unitary vector perpendicular to S and pointing outside.

For a waveguide parallel to the z axis, the field solution components are written as $e_{(r,\theta,z),L}(r,\theta,z) = e_{(r,\theta,z),L}(r,\theta)e^{i\beta_L z}$. Consequently, the cross product $\mathbf{e}_L^*(\mathbf{r}) \wedge \mathbf{h}_L(\mathbf{r})$ is independent of the z coordinate. Considering a large integration surface and the bounded field solutions, only the surfaces crossing the waveguide contribute to the integral so that

$$\Delta P_L = P_L(z_1,t) - P_L(z_0,t) = \frac{|s_L(z_1,t)|^2 - |s_L(z_0,t)|^2}{4M_L} \int_A (\mathbf{e}_L(\mathbf{r}) \wedge \mathbf{h}_L^*(\mathbf{r}) + \mathbf{e}_L^*(\mathbf{r}) \wedge \mathbf{h}_L(\mathbf{r})) \cdot \hat{\mathbf{z}} dA.$$

where $P_L(z,t)$ is the average power traveling through the $x-y$ plane at time t and position z.

We wish to have $P_L(z,t) = |s_L(z,t)|^2$, so

$$M_L = \frac{1}{4}\int_A (\mathbf{e}_L(\mathbf{r}) \wedge \mathbf{h}_L^*(\mathbf{r}) + \mathbf{e}_L^*(\mathbf{r}) \wedge \mathbf{h}_L(\mathbf{r})) \cdot \hat{\mathbf{z}} dA.$$

This normalization allows a direct link with the experiment : $|s_L(z_0,t)|^2$ and $|s_L(z_1,t)|^2$ are the injected power at the entrance and the measured power at the end of the coupling area respectively. As mentioned in [32], the energy normalization of N_j and M_L can be problematic since the irradiated energy blows up the integral. It is the imaginary part of the solutions that describes these radiation losses. However, these losses are negligible when the cavity radius is large (> 5 μm for $n \sim 1.45$). We can neglect this imaginary parts and describe the cavity modes as *bounded* so that the fields outside the cavity are evanescent.

Intensity and circulating power for the cavity's modes

The intensity I is usually defined as the amplitude of the time-averaged Poynting vector :

$$I = |\langle \mathbf{S} \rangle| \,. \tag{B.14}$$

In our case, cavity mode solutions of Eq. B.1

$$\mathbf{E}_{\text{cavity}}(\mathbf{r},t) = \sum_j \frac{a_j(t) e^{-i\omega_j t} \mathbf{e}_j(\mathbf{r})}{2\sqrt{N_j}} + \text{c.c.}$$
$$\mathbf{H}_{\text{cavity}}(\mathbf{r},t) = \sum_j \frac{a_j(t) e^{-i\omega_j t} \mathbf{h}_j(\mathbf{r})}{2\sqrt{N_j}} + \text{c.c.}$$

and the intensity of the jth mode is written as

$$\begin{aligned} I_j(\mathbf{r}) &= \frac{|a_j|^2}{4N_j} \left| (\mathbf{e}_j(\mathbf{r}) \wedge \mathbf{h}_j^*(\mathbf{r})) + (\mathbf{e}_j^*(\mathbf{r}) \wedge \mathbf{h}_j(\mathbf{r})) \right| \\ &= \frac{|a_j|^2}{4N_j} \left| \mathbf{e}_j(\mathbf{r}) \wedge \frac{\nabla \wedge \mathbf{e}_j^*(\mathbf{r})}{-i\omega_j \mu_0} + \mathbf{e}_j^*(\mathbf{r}) \wedge \frac{\nabla \wedge \mathbf{e}_j(\mathbf{r})}{i\omega_j \mu_0} \right|. \end{aligned}$$

The circulating power is the intensity integrated over the transverse area :

$$\begin{aligned} P_j &= \int_A I_j(\mathbf{r}) dA \\ &= \frac{|a_j|^2}{4N_j} \int_A \left| (\mathbf{e}_j(\mathbf{r}) \wedge \mathbf{h}_j^*(\mathbf{r})) + (\mathbf{e}_j^*(\mathbf{r}) \wedge \mathbf{h}_j(\mathbf{r})) \right| dA. \end{aligned}$$

Intensity and circulating power for the microsphere's modes

For a microsphere, the field is written as

$$\mathbf{e}_j(\mathbf{r}) = (e_\rho(\rho,\theta)\hat{\rho} + e_\theta(\rho,\theta)\hat{\theta} + e_\phi(\rho,\theta)\hat{\phi})e^{im_j\phi}.$$

Following the sphere TE and TM mode solutions of section B.3, we can apply the previous intensity relation

$$I_j^{TE}(\rho,\theta) \approx \frac{|a_j|^2}{4\omega_j\mu_0 N_j}\left|\frac{2m_j}{\rho\sin\theta}|e_\theta(\rho,\theta)|^2\hat{\phi}\right| = \frac{|a_j|^2}{2\omega_j\mu_0 N_j}\frac{m_j}{\rho\,|\sin\theta|}|e_\theta(\rho,\theta)|^2 \tag{B.15}$$

$$I_j^{TM}(\rho,\theta) \approx \frac{|a_j|^2}{4\omega_j\mu_0 N_j}\left|\frac{2m_j}{\rho\sin\theta}|e_\rho(\rho,\theta)|^2\hat{\phi}\right| = \frac{|a_j|^2}{2\omega_j\mu_0 N_j}\frac{m_j}{\rho\,|\sin\theta|}|e_\rho(\rho,\theta)|^2. \tag{B.16}$$

The intensity depends on the transversal coordinates. It is usually chosen near the maxima, $|\mathbf{e}_\theta^{max}|^2$ and $|\mathbf{e}_\rho^{max}|^2$, of the first radial order TE and TM modes $l_j = m_j$, located near $\rho \approx R_c$ and $\theta = \pi/2$.

$$I_j^{TE}(\rho \approx R_c, \theta = \pi/2) \approx \frac{|a_j|^2\epsilon_0 c^2}{2\omega_j N_j}\frac{m_j}{R_c}|\mathbf{e}_\theta^{max}|^2 \approx \frac{n_{eff}^{TE}\epsilon_0 c}{2N_j}|a_j|^2|\mathbf{e}_\theta^{max}|^2 \tag{B.17}$$

$$I_j^{TM}(\rho \approx R_c, \theta = \pi/2) \approx \frac{|a_j|^2\epsilon_0 c^2}{2\omega_j N_j}\frac{m_j}{R_c}|\mathbf{e}_\rho^{max}|^2 \approx \frac{n_{eff}^{TM}\epsilon_0 c}{2N_j}|a_j|^2|\mathbf{e}_\rho^{max}|^2 \tag{B.18}$$

where R_c is the sphere radius and we used the tangential wavenumber relation

$$k_{m_j} = \mathbf{k}_j \cdot \hat{\phi} \approx \frac{m_j}{R_c} \approx \frac{n_{eff}\omega_j}{c}.$$

Note that the approximation $\rho \approx R_c$ is valid for large resonators where $|e_\theta(\rho,\theta)|^2$ (TE) and $|e_\rho(\rho,\theta)|^2$ (TM) form a narrower Gaussian-like distribution that is pushed toward the sphere's boundaries.

These *intensity to field amplitude* relations B.17 and B.18 are similar to the plane wave intensity relation found in the literature :

$$I_{pw} = \frac{n\epsilon_0 c}{2} < |\mathbf{E}|^2 >$$

where where $< ... >$ is the time-averaged value and the factor $1/2$ comes from definition of the cavity mode solutions of Eq. B.1.

The previous circulating power definition can be applied to the microsphere's modes to give

$$P_j^{TE} \approx \frac{m_j|a_j|^2}{2\omega_j\mu_0 N_j}\int_A \frac{|e_\theta(\rho,\theta)|^2}{\rho\,|\sin\theta|}dA = |a_j|^2\frac{m_j c^2}{\omega_j}\frac{\int_A \frac{|e_\theta(\rho,\theta)|^2}{\rho|\sin\theta|}dA}{\int_V (n_0^2|_c)|\mathbf{e}_j(\mathbf{r})|^2 dV} \tag{B.19}$$

$$P_j^{TM} \approx \frac{m_j|a_j|^2}{2\omega_j\mu_0 N_j}\int_A \frac{|e_\rho(\rho,\theta)|^2}{\rho\,|\sin\theta|}dA = |a_j|^2\frac{m_j c^2}{\omega_j}\frac{\int_A \frac{|e_\rho(\rho,\theta)|^2}{\rho|\sin\theta|}dA}{\int_V (n_0^2|_c)|\mathbf{e}_j(\mathbf{r})|^2 dV} \tag{B.20}$$

where $dA \equiv \rho\sin(\theta)d\rho d\theta$.

Using the large resonator approximation for the first radial mode order where the field is located near $\rho \approx R_c$ and $\theta \approx \pi/2$, the integrals can be approximated and the circulating power can be written as

$$P_j^{TE} \approx |a_j|^2\frac{m_j c^2}{2\pi R_c^2\omega_j n_c^2} \tag{B.21}$$

$$P_j^{TM} \approx |a_j|^2\frac{m_j c^2}{2\pi R_c^2\omega_j n_c^2}. \tag{B.22}$$

where $|e_\theta(\rho,\theta)|$ and $|e_\rho(\rho,\theta)|$ are considered to be the dominant vector components of the TE and TM modes respectively and n_c is the cavity refractive index.

The round-trip time is typically written as $T_{rt} = 2\pi R_c n_{eff}/c$ where $R_c n_{eff}$ is viewed as an effective optical radius, hence having

$$P_j^{TE/TM} \approx \frac{|a_j|^2}{T_{rt}}\frac{n_{eff}^2}{n_c^2} \rightarrow P_j^{TE/TM} \approx \frac{|a_j|^2}{T_{rt}} \text{ for large cavities.} \tag{B.23}$$

For a fixed ω_j, a smaller m_j leads to a smaller number of nodes per round-trip, hence a smaller effective optical radius.

Mode area and mode volume

Many definitions of the mode area and mode volume are given in the literature. In this thesis, the definitions come directly from the intensity and power expressions B.15 to B.22. The transverse area and the volume occupied by the mode are given by

$$A_j = \frac{P_j}{I_j} \quad \text{and} \quad V_j = 2\pi R_c A_j.$$

Using the explicit expressions, we have

$$A_j^{TE}(\rho,\theta) = \frac{\rho\,|\sin\theta|}{|e_\theta(\rho,\theta)|^2}\int_A \frac{|e_\theta(\rho,\theta)|^2}{\rho\,|\sin\theta|}dA \tag{B.24}$$

$$A_j^{TM}(\rho,\theta) = \frac{\rho\,|\sin\theta|}{|e_\rho(\rho,\theta)|^2}\int_A \frac{|e_\rho(\rho,\theta)|^2}{\rho\,|\sin\theta|}dA \tag{B.25}$$

which are usually evaluated at the field maximum. For the first radial mode of large spheres, it simplifies to

$$A_j^{TE}(\rho\approx R_c,\theta=\pi/2) \approx \frac{1}{|\mathbf{e}_\theta^{max}|^2}\int_A |e_\theta(\rho,\theta)|^2 dA \tag{B.26}$$

$$A_j^{TM}(\rho\approx R_c,\theta=\pi/2) \approx \frac{1}{|\mathbf{e}_\rho^{max}|^2}\int_A |e_\rho(\rho,\theta)|^2 dA \tag{B.27}$$

and

$$V_j^{TE}(\rho\approx R_c,\theta=\pi/2) \approx \frac{2\pi R_c}{|\mathbf{e}_\theta^{max}|^2}\int_A |e_\theta(\rho,\theta)|^2 dA \approx \frac{1}{|\mathbf{e}_\theta^{max}|^2}\int_V |e_\theta(\rho,\theta)|^2 dV \tag{B.28}$$

$$V_j^{TM}(\rho\approx R_c,\theta=\pi/2) \approx \frac{2\pi R_c}{|\mathbf{e}_\rho^{max}|^2}\int_A |e_\rho(\rho,\theta)|^2 dA \approx \frac{1}{|\mathbf{e}_\rho^{max}|^2}\int_V |e_\rho(\rho,\theta)|^2 dV. \tag{B.29}$$

Similar results are obtained using Relations B.17, B.18, B.21 and B.22. These definitions are found in other works [125, 285].

B.1.3 General coupled-modes equations

The field propagation is dictated by Maxwell's equations (Eq.B.2-B.5) which give

$$\boldsymbol{\nabla}^2\mathbf{E}(\mathbf{r},t) - \nabla(\boldsymbol{\nabla}\cdot\mathbf{E}(\mathbf{r},t)) - \frac{1}{c^2}\frac{\partial^2\mathbf{E}(\mathbf{r},t)}{\partial t^2} = \mu_0\frac{\partial^2\mathbf{P}^{(1)}(\mathbf{r},t)}{\partial t^2} + \mu_0\frac{\partial^2\mathbf{P}^{(3)}(\mathbf{r},t)}{\partial t^2}$$

with the speed of light in vacuum $c = 1/\sqrt{\epsilon_0\mu_0}$.

Using the local field and the fast response approximations of Section B.1.1, we write the electric polarization components as

$$\begin{aligned}
P^{(1)(p1)}(\mathbf{r},t) &= \epsilon_0\sum_j\sum_{p2}\chi^{(1)}_{p1,p2}(\mathbf{r},\omega_l)E^{(p2)}_j(\mathbf{r},t)\\
P^{(3)(p1)}(\mathbf{r},t) &= \epsilon_0\sum_{l,m,p}\sum_{p2,p3,p4}\chi^{(3)}_{p1,p2,p3,p4}(\mathbf{r},\omega_l,\omega_m,\omega_p)E^{(p2)}_l(\mathbf{r},t)E^{(p3)}_m(\mathbf{r},t)E^{(p4)}_p(\mathbf{r},t)
\end{aligned}$$

where $(p1,p2,p3,p4)$ are one of the three spatial components (e.g. (x,y,z) or (ρ,θ,z)) and (l,m,p) represent the modes with frequencies ω_l, ω_m and ω_p respectively. For example, $\mathbf{E}^{(y)}_l$ is the y component of the electric field associated with the mode l.

For an isotropic medium (Section B.1.1), we have

$$\boldsymbol{\nabla}^2\mathbf{E}(\mathbf{r},t) - \nabla(\boldsymbol{\nabla}\cdot\mathbf{E}(\mathbf{r},t)) - \frac{\epsilon_r(\mathbf{r},\omega)}{c^2}\frac{\partial^2\mathbf{E}(\mathbf{r},t)}{\partial t^2} = \mu_0\frac{\partial^2\mathbf{P}^{(3)}(\mathbf{r},t)}{\partial t^2}$$

where $\epsilon_r(\mathbf{r},\omega) = 1+\chi^{(1)}(\mathbf{r},\omega)$. It can be simplified to

$$\boldsymbol{\nabla}^2\mathbf{E}(\mathbf{r},t) - \frac{\epsilon_r(\mathbf{r},\omega)}{c^2}\frac{\partial^2\mathbf{E}(\mathbf{r},t)}{\partial t^2} = \mu_0\frac{\partial^2\mathbf{P}^{(3)}(\mathbf{r},t)}{\partial t^2} \tag{B.30}$$

since

$$\begin{aligned}
\boldsymbol{\nabla}\cdot\mathbf{D}(\mathbf{r},t) &= \epsilon_0\nabla\cdot(\epsilon_r(\mathbf{r},\omega)\mathbf{E}(\mathbf{r},t)) + \boldsymbol{\nabla}\cdot\mathbf{P}^{(3)}(\mathbf{r},t) = 0\\
&= \epsilon_0[\epsilon_r(\mathbf{r},\omega)\boldsymbol{\nabla}\cdot\mathbf{E}(\mathbf{r},t) + (\nabla\epsilon_r(\mathbf{r},\omega))\cdot\mathbf{E}(\mathbf{r},t)] + \boldsymbol{\nabla}\cdot\mathbf{P}^{(3)}(\mathbf{r},t) = 0\\
&\Rightarrow \boldsymbol{\nabla}\cdot\mathbf{E}(\mathbf{r},t) = \frac{-\boldsymbol{\nabla}\cdot\mathbf{P}^{(3)}(\mathbf{r},t)}{\epsilon_0\epsilon_r(\mathbf{r},\omega)}
\end{aligned}$$

where we considered an isotropic medium $\nabla\epsilon_r(\mathbf{r},\omega) = 0$. Relation B.30 is obtained if we consider that

$$|\boldsymbol{\nabla}^2\mathbf{E}| \gg |\frac{\nabla(\boldsymbol{\nabla}\cdot\mathbf{P}^{(3)})}{\epsilon_0\epsilon_r}|,$$

which is valid when $\mathbf{P}^{(3)}$ is a small perturbation. ω is the frequency of the monochromatic signal. Using Eq.B.1 and Eq.B.30, we find

$$\sum_j \frac{a_j(t)e^{-i\omega_j t}}{2\sqrt{N_j}}[\boldsymbol{\nabla}^2\mathbf{e}_j(\mathbf{r})] - \frac{\epsilon_r(\mathbf{r},\omega)\mathbf{e}_j(\mathbf{r})}{2c^2\sqrt{N_j}}[-\omega_j^2 a_j(t) - i2\omega_j\frac{\partial a_j(t)}{\partial t} + \frac{\partial^2 a_j(t)}{\partial t^2}]e^{-i\omega_j t} +$$
$$\sum_L \frac{e^{-i\omega_L t}}{2\sqrt{M_L}}[\boldsymbol{\nabla}^2 s_L(z,t)\mathbf{e}_L(\mathbf{r})] - \frac{\epsilon_r(\mathbf{r},\omega)\mathbf{e}_L(\mathbf{r})}{2c^2\sqrt{M_L}}[-\omega_L^2 s_L(z,t) - i2\omega_L\frac{\partial s_L(z,t)}{\partial t} + \frac{\partial^2 s_L(z,t)}{\partial t^2}]e^{-i\omega_L t}$$
$$= \epsilon_0\mu_0 \sum_{i,j,k}\sum_{l,m,p} \frac{\partial^2}{\partial t^2}[\chi^{(3)}(\mathbf{r};\omega_l,\omega_m,\omega_p)\mathbf{E}_l^{(i)}(\mathbf{r},t)\mathbf{E}_m^{(j)}(\mathbf{r},t)\mathbf{E}_p^{(k)}(\mathbf{r},t)]. \tag{B.31}$$

where the term on the right side is summed over the different polarization components (i,q,k) associated with the modes (l,m,p).

The following approximation is made

$$\begin{aligned}\boldsymbol{\nabla}^2 s_L(z,t)\mathbf{e}_L(\mathbf{r}) &= s_L(z,t)\boldsymbol{\nabla}^2\mathbf{e}_L(\mathbf{r}) + i2\beta_L\mathbf{e}_L(\mathbf{r})\frac{\partial s_L(z,t)}{\partial z} + \mathbf{e}_L(\mathbf{r})\frac{\partial^2 s_L(z,t)}{\partial z^2} \\ &\approx s_L(z,t)\boldsymbol{\nabla}^2\mathbf{e}_L(\mathbf{r}) + i2\beta_L\mathbf{e}_L(\mathbf{r})\frac{\partial s_L(z,t)}{\partial z}\end{aligned}$$

where we considered that $e_{i,L}(r,\theta,z) = e_{i,L}(r,\theta)e^{i\beta_L z}$ and we neglected the second derivative compared to the first.

Finally, in Eq. B.31, we consider that $s_L(z,t)$ is quasi constant in time and $a_j(t)$ slowly change :

$$|i2\omega_j\frac{\partial a_j(t)}{\partial t}| \gg \frac{\partial^2 a_j(t)}{\partial t^2} \quad \text{et} \quad \omega_L^2 s_L(z,t) \gg |i2\omega_L\frac{\partial s_L(z,t)}{\partial t}|.$$

All these approximations result in a general coupling equation

$$\sum_j \frac{a_j(t)e^{-i\omega_j t}}{2\sqrt{N_j}}\boldsymbol{\nabla}^2\mathbf{e}_j(\mathbf{r}) - \frac{\epsilon_r(\mathbf{r},\omega)\mathbf{e}_j(\mathbf{r})}{2c^2\sqrt{N_j}}[-\omega_j^2 a_j(t) - i2\omega_j\frac{\partial a_j(t)}{\partial t}]e^{-i\omega_j t} +$$
$$\sum_L \frac{s_L(z,t)e^{-i\omega_L t}}{2\sqrt{M_L}}\boldsymbol{\nabla}^2\mathbf{e}_L(\mathbf{r}) + \frac{i\beta_L e^{-i\omega_L t}\mathbf{e}_L(\mathbf{r})}{\sqrt{M_L}}\frac{\partial s_L(z,t)}{\partial z} + \frac{\epsilon_r(\mathbf{r},\omega)\mathbf{e}_L(\mathbf{r})}{2c^2\sqrt{M_L}}\omega_L^2 s_L(z,t)e^{-i\omega_L t}$$
$$= \frac{1}{c^2}\sum_{i,j,k}\sum_{l,m,p} \frac{\partial^2}{\partial t^2}[\chi^{(3)}(\mathbf{r};\omega_l,\omega_m,\omega_p)\mathbf{E}_l^{(i)}(\mathbf{r},t)\mathbf{E}_m^{(j)}(\mathbf{r},t)\mathbf{E}_p^{(k)}(\mathbf{r},t)]. \tag{B.32}$$

It is important to note that complex conjugate terms (c.c.) are voluntarily omitted on the left side since they have no impact on linear coupling terms. These terms are function of the frequency difference $\omega_j - \omega_p$ and the phase mismatch. Some terms include $\mathbf{e}_j^*(\mathbf{r})\mathbf{e}_p^*(\mathbf{r})e^{i(\omega_j+\omega_p)}$. They are proportional to $e^{i2\omega}$ and they average to zero. Nevertheless, those terms are impor-

tant to describe nonlinear effects on the right side.

Decomposition of linear interaction

The linear interactions between modes can be described through a complex perturbative term $\epsilon_r(\mathbf{r},\omega) \rightarrow \epsilon_r(\mathbf{r},\omega) + \delta\epsilon_r(\mathbf{r},\omega)$ where ω is the signal frequency. The real and imaginary part of $\epsilon_r(\mathbf{r},\omega)$ are linked to the signal phase velocity and to the intrinsic losses in the material respectively. $\mathrm{Re}(\delta\epsilon_r(\mathbf{r},\omega)) = \delta\epsilon(\mathbf{r},\omega)$ describe the coupling processes to other modes p of the cavity and $\mathrm{Im}(\delta\epsilon_r(\mathbf{r},\omega)) = \delta\epsilon'(\mathbf{r},\omega)$ describe the losses to radiative modes during these coupling processes.

$$\begin{aligned}
\epsilon_r &= (n_0(\mathbf{r},\omega) + in_0'(\mathbf{r},\omega))^2 + \delta\epsilon_r(\mathbf{r},\omega) + i\delta\epsilon'(\mathbf{r},\omega) \\
\mathrm{Re}(\epsilon_r) &= n_0(\mathbf{r},\omega)^2 - n_0'(\mathbf{r},\omega)^2 + \delta\epsilon_r(\mathbf{r},\omega) \approx n_0(\mathbf{r},\omega)^2 + \delta\epsilon(\mathbf{r},\omega) \\
i\mathrm{Im}(\epsilon_r) &= i2n_0(\mathbf{r},\omega)n_0'(\mathbf{r},\omega) + i\delta\epsilon'(\mathbf{r},\omega).
\end{aligned}$$

n_0 et n_0' describe the refractive index profile and the absorption profile respectively :

$$\begin{aligned}
n_0(\mathbf{r}) &= n_c \text{ inside the cavity} \\
&= n_a \text{ in the surrounding medium} \\
&= n_g \text{ in the waveguide}
\end{aligned}$$

n_0' is considered to be small compared to n_0 and zero outside the cavity. $\delta\epsilon(\mathbf{r},\omega)$ can be linked to a local refractive index change such as surface roughness which allows the signal to scatter into other cavity modes or radiative modes [26]. Relation B.31 becomes

$$\begin{aligned}
\sum_j \frac{a_j(t)e^{-i\omega_j t}}{2\sqrt{N_j}}[\boldsymbol{\nabla}^2\mathbf{e}_j(\mathbf{r}) + \frac{n_0^2|_c}{c^2}\omega_j^2\mathbf{e}_j(\mathbf{r})] + \frac{a_j(t)e^{-i\omega_j t}}{2c^2\sqrt{N_j}}[n_0^2|_g - n_a^2]\omega_j^2\mathbf{e}_j(\mathbf{r}) + \\
\frac{a_j(t)e^{-i\omega_j t}}{2c^2\sqrt{N_j}}[\delta\epsilon(\mathbf{r}) + i\mathrm{Im}(\epsilon_r)]\omega_j^2\mathbf{e}_j(\mathbf{r}) + \frac{i\omega_j e^{-i\omega_j t}}{c^2\sqrt{N_j}}\frac{\partial a_j(t)}{\partial t}\epsilon_r(\mathbf{r})\mathbf{e}_j(\mathbf{r}) + \\
\sum_L \frac{s_L(z,t)e^{-i\omega_L t}}{2\sqrt{M_L}}[\boldsymbol{\nabla}^2\mathbf{e}_L(\mathbf{r}) + \frac{n_0^2|_g}{c^2}\omega_L^2\mathbf{e}_L(\mathbf{r})] + \frac{s_L(z,t)e^{-i\omega_L t}}{2c^2\sqrt{M_L}}[n_0^2|_c - n_a^2]\omega_L^2\mathbf{e}_L(\mathbf{r}) + \\
\frac{s_L(z,t)e^{-i\omega_L t}}{2c^2\sqrt{M_L}}[\delta\epsilon(\mathbf{r}) + i\mathrm{Im}(\epsilon_r)]\omega_L^2\mathbf{e}_L(\mathbf{r}) + \frac{i\beta_L e^{-i\omega_L t}}{\sqrt{M_L}}\frac{\partial s_L(z,t)}{\partial z}\epsilon_r(\mathbf{r})\mathbf{e}_L(\mathbf{r}) \\
= \frac{1}{c^2}\sum_{i,j,k}\sum_{l,m,p}\frac{\partial^2}{\partial t^2}[\chi^{(3)}(\mathbf{r};\omega_l,\omega_m,\omega_p)\mathbf{E}_l^{(i)}(\mathbf{r},t)\mathbf{E}_m^{(j)}(\mathbf{r},t)\mathbf{E}_p^{(k)}(\mathbf{r},t)]
\end{aligned}$$

where $n_0^2|_c$ and $n_0^2|_g$ are the squared refractive index profile of the cavity or the waveguide

alone in the surrounding medium, as shown in Fig. B.2.

We find a relation that shows the eigenmodes propagation equations explicitly for the cavity modes j and the waveguide modes L :

$$\boldsymbol{\nabla}^2\mathbf{e}_j(\mathbf{r}) + \frac{n_0^2|_c}{c^2}\omega_j^2\mathbf{e}_j(\mathbf{r}) = 0 \tag{B.33}$$

$$\boldsymbol{\nabla}^2\mathbf{e}_L(\mathbf{r}) + \frac{n_0^2|_g}{c^2}\omega_L^2\mathbf{e}_L(\mathbf{r}) = 0. \tag{B.34}$$

Furthermore, the coupling terms contain $[n_0^2|_g - n_a^2]$ and $[n_0^2|_c - n_a^2]$. Since the refractive index profiles depend on the signal frequency, the eigenmode equations are truly zero for ω_j and ω_L respectively. During an experiment, we control ω_L and we are interested in cases where the laser signal couples to cavity modes, meaning that $\omega_L \approx \omega_j$. The width of a WGM microcavity resonance is typically below 0.1 nm around a wavelength of 1550 nm. In that case, the refractive index difference is less than 0.00001 for As_2S_3. We can consider that these eigenmode equations are always zero when the coupled-modes equations are used.

We finally find

$$\begin{aligned}
&\frac{i\omega_j e^{-i\omega_j t}}{c^2\sqrt{N_j}}\frac{\partial a_j(t)}{\partial t}\epsilon_r(\mathbf{r})\mathbf{e}_j(\mathbf{r}) + \frac{a_j(t)e^{-i\omega_j t}}{2c^2\sqrt{N_j}}[n_0^2|_g - n_a^2]\omega_j^2\mathbf{e}_j(\mathbf{r}) \\
&\qquad + \frac{a_j(t)e^{-i\omega_j t}}{2c^2\sqrt{N_j}}[\delta\epsilon(\mathbf{r}) + i\mathrm{Im}(\epsilon_r)]\omega_j^2\mathbf{e}_j(\mathbf{r}) \\
&+ \sum_p \frac{i\omega_p e^{-i\omega_p t}}{c^2\sqrt{N_p}}\frac{\partial a_p(t)}{\partial t}\epsilon_r(\mathbf{r})\mathbf{e}_p(\mathbf{r}) + \frac{a_p(t)e^{-i\omega_p t}}{2c^2\sqrt{N_p}}[n_0^2|_g - n_a^2]\omega_p^2\mathbf{e}_p(\mathbf{r}) \\
&\qquad + \frac{a_p(t)e^{-i\omega_p t}}{2c^2\sqrt{N_p}}[\delta\epsilon(\mathbf{r}) + i\mathrm{Im}(\epsilon_r)]\omega_p^2\mathbf{e}_p(\mathbf{r}) \\
&+ \sum_L \frac{i\beta_L e^{-i\omega_L t}}{\sqrt{M_L}}\frac{\partial s_L(z,t)}{\partial z}\epsilon_r(\mathbf{r})\mathbf{e}_L(\mathbf{r}) + \frac{s_L(z,t)e^{-i\omega_L t}}{2c^2\sqrt{M_L}}[n_0^2|_c - n_a^2]\omega_L^2\mathbf{e}_L(\mathbf{r}) \\
&\qquad + \frac{s_L(z,t)e^{-i\omega_L t}}{2c^2\sqrt{M_L}}[\delta\epsilon(\mathbf{r}) + i\mathrm{Im}(\epsilon_r)]\omega_L^2\mathbf{e}_L(\mathbf{r}) \\
&= \frac{1}{c^2}\sum_{i,j,k}\sum_{l,m,p}\frac{\partial^2}{\partial t^2}[\chi^{(3)}(\mathbf{r};\omega_l,\omega_m,\omega_p)\mathbf{E}_l^{(i)}(\mathbf{r},t)\mathbf{E}_m^{(j)}(\mathbf{r},t)\mathbf{E}_p^{(k)}(\mathbf{r},t)].
\end{aligned} \tag{B.35}$$

We considered a main cavity mode j that is coupled to the waveguide modes L, and to other cavity modes p through linear and nonlinear processes.

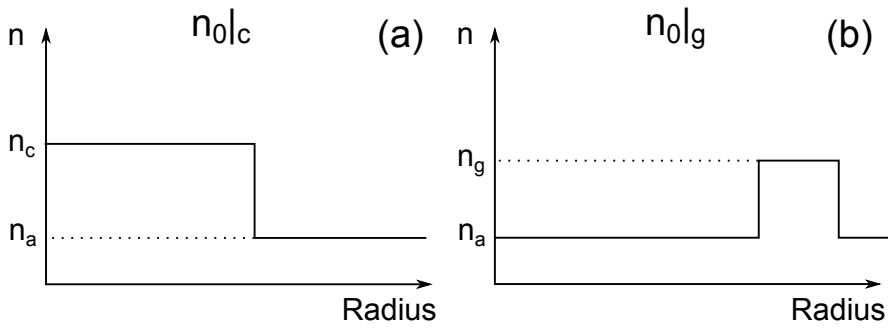

Figure B.2 : **(a)** The cavity refractive index profile $n_0|_c$. **(b)** The waveguide refractive index profile $n_0|_g$.

B.1.4 Waveguide and cavity coupled-modes equations

It is easier to start with the linear case where $\chi^{(3)} \to 0$.

Linear coupled-modes equations for the waveguide

To obtain the coupled-modes equations, we can isolate the spatial components into overlap integrals. We can retrieve the coupled-modes equation for the mode L from B.35 by multiplying $\wedge\mathbf{h}^*_{L'}$ from the right side and by integrating on the transverse area A, similarly to the previous power normalization :

$$\begin{aligned}
\frac{\partial s_L(z,t)}{\partial z} = & \frac{i s_L(z,t)\omega_L^2}{2\beta_L c^2}\frac{\int_A [n_0^2|_c - n_a^2 + \delta\epsilon(\mathbf{r})](\mathbf{e}_L \wedge \mathbf{h}_L^*)\cdot\hat{\mathbf{z}}dA}{\int_A (\mathbf{e}_L \wedge \mathbf{h}_L^*)\cdot\hat{\mathbf{z}}dA} \\
& - \frac{\partial a_j(t)}{\partial t} e^{-i(\omega_j-\omega_L)t}\frac{\omega_j}{\beta_L c^2}\sqrt{\frac{M_L}{N_j}}\frac{\int_A \epsilon_r(\mathbf{r})(\mathbf{e}_j \wedge \mathbf{h}_L^*)\cdot\hat{\mathbf{z}}dA}{\int_A (\mathbf{e}_L \wedge \mathbf{h}_L^*)\cdot\hat{\mathbf{z}}dA} \\
& + i a_j(t) e^{-i(\omega_j-\omega_L)t}\frac{\omega_j^2}{2\beta_L c^2}\sqrt{\frac{M_L}{N_j}}\frac{\int_A [n_0^2|_g - n_a^2 + \delta\epsilon(\mathbf{r})](\mathbf{e}_j \wedge \mathbf{h}_L^*)\cdot\hat{\mathbf{z}}dA}{\int_A (\mathbf{e}_L \wedge \mathbf{h}_L^*)\cdot\hat{\mathbf{z}}dA} \\
& - \sum_p \frac{\partial a_p(t)}{\partial t} e^{-i(\omega_p-\omega_L)t}\frac{\omega_p}{\beta_L c^2}\sqrt{\frac{M_L}{N_p}}\frac{\int_A \epsilon_r(\mathbf{r})(\mathbf{e}_p \wedge \mathbf{h}_L^*)\cdot\hat{\mathbf{z}}dA}{\int_A (\mathbf{e}_L \wedge \mathbf{h}_L^*)\cdot\hat{\mathbf{z}}dA} \\
& + \sum_p i a_p(t) e^{-i(\omega_p-\omega_L)t}\frac{\omega_p^2}{2\beta_L c^2}\sqrt{\frac{M_L}{N_p}}\frac{\int_A [n_0^2|_g - n_a^2 + \delta\epsilon(\mathbf{r})](\mathbf{e}_p \wedge \mathbf{h}_L^*)\cdot\hat{\mathbf{z}}dA}{\int_A (\mathbf{e}_L \wedge \mathbf{h}_L^*)\cdot\hat{\mathbf{z}}dA}.
\end{aligned} \tag{B.36}$$

By neglecting the modal coupling between the waveguide modes so that $L' \equiv L$, we obtain a first order inhomogeneous equation.

We usually know the input power $|s_L(z_0,t)|^2$ at z_0 where the coupling is negligible. We measure the output power $|s_L(z_1,t)|^2$ at z_1 where the coupling is also negligible. To find the

wave amplitude along the waveguide, we solve Eq. B.36 :

$$
\begin{aligned}
s_L(z,t) = s_L(z_0,t)e^{i\eta(z)} \\
&+ ia_j(t)e^{-i(\omega_j-\omega_L)t}\frac{\omega_j^2}{2\beta_L c^2}\sqrt{\frac{M_L}{N_j}}e^{i\eta(z)}\int_{z_0}^{z} e^{-i\eta(z')}\frac{\int_A [n_0^2|_g - n_a^2 + \delta\epsilon(\mathbf{r})](\mathbf{e}_j \wedge \mathbf{h}_L^*)\cdot\hat{\mathbf{n}}dA}{\int_A(\mathbf{e}_L\wedge\mathbf{h}_L^*)\cdot\hat{\mathbf{z}}dA}dz' \\
&- \frac{\partial a_j(t)}{\partial t}e^{-i(\omega_j-\omega_L)t}\frac{\omega_j}{\beta_L c^2}\sqrt{\frac{M_L}{N_j}}e^{i\eta(z)}\int_{z_0}^{z} e^{-i\eta(z')}\frac{\int_A \epsilon_r(\mathbf{r})(\mathbf{e}_j \wedge \mathbf{h}_L^*)\cdot\hat{\mathbf{z}}dA}{\int_A(\mathbf{e}_L\wedge\mathbf{h}_L^*)\cdot\hat{\mathbf{z}}dA}dz' \qquad \text{(B.37)} \\
&+ \sum_p ia_p(t)e^{-i(\omega_p-\omega_L)t}\frac{\omega_p^2}{2\beta_L c^2}\sqrt{\frac{M_L}{N_p}}e^{i\eta(z)}\int_{z_0}^{z} e^{-i\eta(z')}\frac{\int_A [n_0^2|_g - n_a^2 + \delta\epsilon(\mathbf{r})](\mathbf{e}_p \wedge \mathbf{h}_L^*)\cdot\hat{\mathbf{z}}dA}{\int_A(\mathbf{e}_L\wedge\mathbf{h}_L^*)\cdot\hat{\mathbf{z}}dA}dz' \\
&- \frac{\partial a_p(t)}{\partial t}e^{-i(\omega_p-\omega_L)t}\frac{\omega_p}{\beta_L c^2}\sqrt{\frac{M_L}{N_p}}e^{i\eta(z)}\int_{z_0}^{z} e^{-i\eta(z')}\frac{\int_A \epsilon_r(\mathbf{r})(\mathbf{e}_p \wedge \mathbf{h}_L^*)\cdot\hat{\mathbf{z}}dA}{\int_A(\mathbf{e}_L\wedge\mathbf{h}_L^*)\cdot\hat{\mathbf{z}}dA}dz'
\end{aligned}
$$

where

$$
\begin{aligned}
\eta(z) &= \frac{\omega_L^2}{2\beta_L c^2}\int_{z_0}^{z}\frac{\int_A [n_0^2|_c - n_a^2 + \delta\epsilon(\mathbf{r})](\mathbf{e}_L \wedge \mathbf{h}_L^*)\cdot\hat{\mathbf{z}}dA}{\int_A(\mathbf{e}_L\wedge\mathbf{h}_L^*)\cdot\hat{\mathbf{z}}dA}dz' \qquad \text{(B.38)} \\
\eta(z') &= \frac{\omega_L^2}{2\beta_L c^2}\int_{z_0}^{z'}\frac{\int_A [n_0^2|_c - n_a^2 + \delta\epsilon(\mathbf{r})](\mathbf{e}_L \wedge \mathbf{h}_L^*)\cdot\hat{\mathbf{z}}dA}{\int_A(\mathbf{e}_L\wedge\mathbf{h}_L^*)\cdot\hat{\mathbf{z}}dA}dz''
\end{aligned}
$$

are the phase changes induced by the cavity. All the overlap integrals are independent of the time component and they represent the sum of the fields overlap of the increment dz normalized by the power.

Linear coupled-modes equations for the cavity

For the cavity mode equations, linked to the energy normalization, we multiply by $\mathbf{e}_j^*(\mathbf{r})$ from the left and we integrate over a volume V which includes the cavity and the waveguide :

$$
\begin{aligned}
&\frac{i\omega_j e^{-i\omega_j t}}{c^2\sqrt{N_j}}\frac{\partial a_j(t)}{\partial t}\int_V \epsilon_r(\mathbf{r})|\mathbf{e}_j|^2 dV + \frac{a_j(t)e^{-i\omega_j t}}{2c^2\sqrt{N_j}}\omega_j^2\int_V [n_0^2|_g - n_a^2]|\mathbf{e}_j|^2 dV \\
&\quad + \frac{a_j(t)e^{-i\omega_j t}}{2c^2\sqrt{N_j}}\omega_j^2\int_V \delta\epsilon(\mathbf{r})|\mathbf{e}_j|^2 dV + \frac{a_j(t)e^{-i\omega_j t}}{2c^2\sqrt{N_j}}\omega_j^2\int_V i\mathrm{Im}(\epsilon_r)|\mathbf{e}_j|^2 dV \\
&+ \sum_p \frac{i\omega_p e^{-i\omega_p t}}{c^2\sqrt{N_p}}\frac{\partial a_p(t)}{\partial t}\int_V \epsilon_r(\mathbf{r})\mathbf{e}_j^*\mathbf{e}_p dV + \frac{a_p(t)e^{-i\omega_p t}}{2c^2\sqrt{N_p}}\omega_p^2\int_V [n_0^2|_g - n_a^2]\mathbf{e}_j^*\mathbf{e}_p dV \\
&\quad + \frac{a_p(t)e^{-i\omega_p t}}{2c^2\sqrt{N_p}}\omega_p^2\int_V \delta\epsilon(\mathbf{r})\mathbf{e}_j^*\mathbf{e}_p dV + \frac{a_p(t)e^{-i\omega_p t}}{2c^2\sqrt{N_p}}\omega_p^2\int_V i\mathrm{Im}(\epsilon_r)\mathbf{e}_j^*\mathbf{e}_p dV \\
&+ \sum_L \frac{i\beta_L e^{-i\omega_L t}}{\sqrt{M_L}}\int_V \frac{\partial s_L(z,t)}{\partial z}\epsilon_r(\mathbf{r})\mathbf{e}_j^*\mathbf{e}_L dV + \frac{e^{-i\omega_L t}}{2c^2\sqrt{M_L}}\omega_L^2\int_V s_L(z,t)[n_0^2|_c - n_a^2]\mathbf{e}_j^*\mathbf{e}_L dV
\end{aligned}
$$

$$+\frac{e^{-i\omega_L t}}{2c^2\sqrt{M_L}}\omega_L^2\int_V s_L(z,t)\delta\epsilon(\mathbf{r})\mathbf{e}_j^*\mathbf{e}_L dV+\frac{e^{-i\omega_L t}}{2c^2\sqrt{M_L}}\omega_L^2\int_V is_L(z,t)\mathrm{Im}(\epsilon_r)\mathbf{e}_j^*\mathbf{e}_L dV=0.$$

We now have multiple coupling terms but some are negligible. We can consider that the waveguide modes L are affected by the cavity's presence only. Furthermore, in the first term, we can change $\epsilon_r(\mathbf{r})$ for $n_0^2|_c$ since $|\mathbf{e}_j|^2$ is generally much higher inside the cavity. This gives

$$\begin{aligned}
&\frac{i\omega_j e^{-i\omega_j t}}{c^2\sqrt{N_j}}\frac{\partial a_j(t)}{\partial t}\int_V n_0^2|_c|\mathbf{e}_j|^2dV+\frac{a_j(t)e^{-i\omega_j t}}{2c^2\sqrt{N_j}}\omega_j^2\int_V[n_0^2|_g-n_a^2+\delta\epsilon(\mathbf{r})]|\mathbf{e}_j|^2dV\\
&\qquad+\frac{a_j(t)e^{-i\omega_j t}}{2c^2\sqrt{N_j}}\omega_j^2\int_V i\mathrm{Im}(\epsilon_r)|\mathbf{e}_j|^2dV\\
&+\sum_p\frac{i\omega_p e^{-i\omega_p t}}{c^2\sqrt{N_p}}\frac{\partial a_p(t)}{\partial t}\int_V\epsilon_r(\mathbf{r})\mathbf{e}_j^*\mathbf{e}_p dV+\frac{a_p(t)e^{-i\omega_p t}}{2c^2\sqrt{N_p}}\omega_p^2\int_V[n_0^2|_g-n_a^2+\delta\epsilon(\mathbf{r})]\mathbf{e}_j^*\mathbf{e}_p dV\\
&+\sum_L\frac{i\beta_L e^{-i\omega_L t}}{\sqrt{M_L}}\int_V\frac{\partial s_L(z,t)}{\partial z}\epsilon_r(\mathbf{r})\mathbf{e}_j^*\mathbf{e}_L dV+\frac{e^{-i\omega_L t}}{2c^2\sqrt{M_L}}\omega_L^2\int_V s_L(z,t)[n_0^2|_c-n_a^2+\delta\epsilon(\mathbf{r})]\mathbf{e}_j^*\mathbf{e}_L dV=0.
\end{aligned}$$

We can obtain the coupled-modes equations by moving all the terms on the right side :

$$\begin{aligned}
\frac{\partial a_j(t)}{\partial t}=&\frac{ia_j(t)\omega_j}{2}\frac{\int_V[n_0^2|_g-n_a^2+\delta\epsilon(\mathbf{r})]|\mathbf{e}_j|^2dV}{\int_V n_0^2|_c|\mathbf{e}_j|^2dV}\\
&-\frac{a_j(t)\omega_j}{2}\frac{\int_V\mathrm{Im}(\epsilon_r)|\mathbf{e}_j|^2dV}{\int_V n_0^2|_c|\mathbf{e}_j|^2dV}\\
&-\sum_p\frac{\partial a_p(t)}{\partial t}e^{-i(\omega_p-\omega_j)t}\frac{\omega_p}{\omega_j}\sqrt{\frac{N_j}{N_p}}\frac{\int_V\epsilon_r(\mathbf{r})\mathbf{e}_j^*\mathbf{e}_p dV}{\int_V n_0^2|_c|\mathbf{e}_j|^2dV}+\\
&+\sum_p\frac{ia_p(t)e^{-i(\omega_p-\omega_j)t}}{2}\frac{\omega_p^2}{\omega_j}\sqrt{\frac{N_j}{N_p}}\frac{\int_V[n_0^2|_g-n_a^2+\delta\epsilon(\mathbf{r})]\mathbf{e}_j^*\mathbf{e}_p dV}{\int_V n_0^2|_c|\mathbf{e}_j|^2dV}\\
&-\sum_L e^{-i(\omega_L-\omega_j)t}\frac{\beta_L c^2}{\omega_L}\sqrt{\frac{N_j}{M_L}}\frac{\int_V\frac{\partial s_L(z,t)}{\partial z}\epsilon_r(\mathbf{r})\mathbf{e}_j^*\mathbf{e}_L dV}{\int_V n_0^2|_c|\mathbf{e}_j|^2dV}\\
&+\sum_L\frac{ie^{-i(\omega_L-\omega_j)t}}{2}\frac{\omega_L^2}{\omega_j}\sqrt{\frac{N_j}{M_L}}\frac{\int_V s_L(z,t)[n_0^2|_c-n_a^2+\delta\epsilon(\mathbf{r})]\mathbf{e}_j^*\mathbf{e}_L dV}{\int_V n_0^2|_c|\mathbf{e}_j|^2dV}
\end{aligned}\tag{B.39}$$

The first term on the right side shows the j mode phase change due to the waveguide and $\delta\epsilon$. The second term describes the attenuation via the material absorption and diffusion, and via the scattering of $\delta\epsilon'(\mathbf{r})$. The third and fourth terms describe the coupling to other cavity modes p. The last two terms describe the coupling to waveguide modes.

To obtain an equation that depends on $s_L(z_0,t)$, we insert Eq. B.36 and Eq. B.37 in Eq. B.39 :

$$A_1\frac{\partial a_j(t)}{\partial t} = A_2 a_j(t) + \sum_p \left(A_3 a_p(t) + A_4\frac{\partial a_p(t)}{\partial t}\right) e^{-i(\omega_p-\omega_j)t} + \sum_L A_5 s_L(z_0,t) e^{-i(\omega_L-\omega_j)t} \quad \text{(B.40)}$$

where

$$A_1 =$$
$$1 - \sum_L \frac{\int_V \left[\frac{\int_A \epsilon_r(\mathbf{r})(\mathbf{e}_j\wedge\mathbf{h}_L^*)\cdot\hat{\mathbf{z}}dA}{\int_A(\mathbf{e}_L\wedge\mathbf{h}_L^*)\cdot\hat{\mathbf{z}}dA}\right]\epsilon_r(\mathbf{r})\mathbf{e}_j^*\mathbf{e}_L dV}{\int_V n_0^2|_c|\mathbf{e}_j|^2 dV}$$
$$+\sum_L i\frac{\omega_L^2}{2\beta_L c^2}\frac{\int_V e^{i\eta(z)}\left[\int_{z_0}^z e^{-i\eta(z')}\frac{\int_A \epsilon_r(\mathbf{r})(\mathbf{e}_j\wedge\mathbf{h}_L^*)\cdot\hat{\mathbf{z}}dA}{\int_A(\mathbf{e}_L\wedge\mathbf{h}_L^*)\cdot\hat{\mathbf{z}}dA}dz'\right][n_0^2|_c - n_a^2 + \delta\epsilon(\mathbf{r})]\mathbf{e}_j^*\mathbf{e}_L dV}{\int_V n_0^2|_c|\mathbf{e}_j|^2 dV}$$
$$-\sum_L i\frac{\omega_L^2}{2\beta_L c^2}\frac{\int_V e^{i\eta(z)}\left[\int_{z_0}^z e^{-i\eta(z')}\frac{\int_A \epsilon_r(\mathbf{r})(\mathbf{e}_j\wedge\mathbf{h}_L^*)\cdot\hat{\mathbf{z}}dA}{\int_A(\mathbf{e}_L\wedge\mathbf{h}_L^*)\cdot\hat{\mathbf{z}}dA}dz'\right]\left[\frac{\int_A[n_0^2|_c-n_a^2+\delta\epsilon(\mathbf{r})](\mathbf{e}_L\wedge\mathbf{h}_L^*)\cdot\hat{\mathbf{z}}dA}{\int_A(\mathbf{e}_L\wedge\mathbf{h}_L^*)\cdot\hat{\mathbf{z}}dA}\right]\epsilon_r(\mathbf{r})\mathbf{e}_j^*\mathbf{e}_L dV}{\int_V n_0^2|_c|\mathbf{e}_j|^2 dV}$$

$$A_2 =$$
$$-\frac{\omega_j}{2}\frac{\int_V \mathrm{Im}(\epsilon_r)|\mathbf{e}_j|^2 dV}{\int_V n_0^2|_c|\mathbf{e}_j|^2 dV}$$
$$+i\frac{\omega_j}{2}\frac{\int_V [n_0^2|_g - n_a^2 + \delta\epsilon(\mathbf{r})]|\mathbf{e}_j|^2 dV}{\int_V n_0^2|_c|\mathbf{e}_j|^2 dV}$$
$$-\sum_L i\frac{\omega_j}{2}\frac{\int_V\left[\frac{\int_A[n_0^2|_g-n_a^2+\delta\epsilon(\mathbf{r})](\mathbf{e}_j\wedge\mathbf{h}_L^*)\cdot\hat{\mathbf{z}}dA}{\int_A(\mathbf{e}_L\wedge\mathbf{h}_L^*)\cdot\hat{\mathbf{z}}dA}\right]\epsilon_r(\mathbf{r})\mathbf{e}_j^*\mathbf{e}_L dV}{\int_V n_0^2|_c|\mathbf{e}_j|^2 dV}$$
$$-\sum_L \frac{\omega_L^2\omega_j}{4\beta_L c^2}\frac{\int_V e^{i\eta(z)}\left[\int_{z_0}^z e^{-i\eta(z')}\frac{\int_A[n_0^2|_g-n_a^2+\delta\epsilon(\mathbf{r})](\mathbf{e}_j\wedge\mathbf{h}_L^*)\cdot\hat{\mathbf{n}}dA}{\int_A(\mathbf{e}_L\wedge\mathbf{h}_L^*)\cdot\hat{\mathbf{z}}dA}dz'\right][n_0^2|_c - n_a^2 + \delta\epsilon(\mathbf{r})]\mathbf{e}_j^*\mathbf{e}_L dV}{\int_V n_0^2|_c|\mathbf{e}_j|^2 dV}$$
$$+\sum_L \frac{\omega_L^2\omega_j}{4\beta_L c^2}\frac{\int_V e^{i\eta(z)}\left[\int_{z_0}^z e^{-i\eta(z')}\frac{\int_A[n_0^2|_g-n_a^2+\delta\epsilon(\mathbf{r})](\mathbf{e}_j\wedge\mathbf{h}_L^*)\cdot\hat{\mathbf{n}}dA}{\int_A(\mathbf{e}_L\wedge\mathbf{h}_L^*)\cdot\hat{\mathbf{z}}dA}dz'\right]\left[\frac{\int_A[n_0^2|_c-n_a^2+\delta\epsilon(\mathbf{r})](\mathbf{e}_L\wedge\mathbf{h}_L^*)\cdot\hat{\mathbf{z}}dA}{\int_A(\mathbf{e}_L\wedge\mathbf{h}_L^*)\cdot\hat{\mathbf{z}}dA}\right]\epsilon_r(\mathbf{r})\mathbf{e}_j^*\mathbf{e}_L dV}{\int_V n_0^2|_c|\mathbf{e}_j|^2 dV}$$

$$A_3 =$$
$$i\frac{\omega_p^2}{2\omega_j}\sqrt{\frac{N_j}{N_p}}\frac{\int_V [n_0^2|_g - n_a^2 + \delta\epsilon(\mathbf{r})]\mathbf{e}_j^*\mathbf{e}_p dV}{\int_V n_0^2|_c|\mathbf{e}_j|^2 dV}$$

$$
\begin{aligned}
&- \sum_L i\frac{\omega_p^2}{2\omega_j}\sqrt{\frac{N_j}{N_p}}\frac{\int_V \left[\frac{\int_A [n_0^2|_g - n_a^2 + \delta\epsilon(\mathbf{r})](\mathbf{e}_p \wedge \mathbf{h}_L^*)\cdot\hat{\mathbf{z}}dA}{\int_A (\mathbf{e}_L \wedge \mathbf{h}_L^*)\cdot\hat{\mathbf{z}}dA}\right]\epsilon_r(\mathbf{r})\mathbf{e}_j^*\mathbf{e}_L dV}{\int_V n_0^2|_c|\mathbf{e}_j|^2 dV} \\
&- \sum_L \frac{\omega_L^2\omega_p^2}{4\omega_j\beta_L c^2}\sqrt{\frac{N_j}{N_p}}\frac{\int_V e^{i\eta(z)}\left[\int_{z_0}^z e^{-i\eta(z')}\frac{\int_A [n_0^2|_g - n_a^2 + \delta\epsilon(\mathbf{r})](\mathbf{e}_p \wedge \mathbf{h}_L^*)\cdot\hat{\mathbf{n}}dA}{\int_A (\mathbf{e}_L \wedge \mathbf{h}_L^*)\cdot\hat{\mathbf{z}}dA}dz'\right][n_0^2|_c - n_a^2 + \delta\epsilon(\mathbf{r})]\mathbf{e}_j^*\mathbf{e}_L dV}{\int_V n_0^2|_c|\mathbf{e}_j|^2 dV} \\
&+ \sum_L \frac{\omega_L^2\omega_p^2}{4\omega_j\beta_L c^2}\sqrt{\frac{N_j}{N_p}}\times \\
&\left(\frac{\int_V e^{i\eta(z)}\left[\int_{z_0}^z e^{-i\eta(z')}\frac{\int_A [n_0^2|_g - n_a^2 + \delta\epsilon(\mathbf{r})](\mathbf{e}_p \wedge \mathbf{h}_L^*)\cdot\hat{\mathbf{n}}dA}{\int_A (\mathbf{e}_L \wedge \mathbf{h}_L^*)\cdot\hat{\mathbf{z}}dA}dz'\right]\left[\frac{\int_A [n_0^2|_c - n_a^2 + \delta\epsilon(\mathbf{r})](\mathbf{e}_L \wedge \mathbf{h}_L^*)\cdot\hat{\mathbf{z}}dA}{\int_A (\mathbf{e}_L \wedge \mathbf{h}_L^*)\cdot\hat{\mathbf{z}}dA}\right]\epsilon_r(\mathbf{r})\mathbf{e}_j^*\mathbf{e}_L dV}{\int_V n_0^2|_c|\mathbf{e}_j|^2 dV}\right)
\end{aligned}
$$

$$
\begin{aligned}
A_4 = &\\
&- \frac{\omega_p}{\omega_j}\sqrt{\frac{N_j}{N_p}}\frac{\int_V \epsilon_r(\mathbf{r})\mathbf{e}_j^*\mathbf{e}_p dV}{\int_V n_0^2|_c|\mathbf{e}_j|^2 dV} \\
&+ \sum_L \frac{\omega_p}{\omega_j}\sqrt{\frac{N_j}{N_p}}\frac{\int_V \left[\frac{\int_A \epsilon_r(\mathbf{r})(\mathbf{e}_p \wedge \mathbf{h}_L^*)\cdot\hat{\mathbf{z}}dA}{\int_A (\mathbf{e}_L \wedge \mathbf{h}_L^*)\cdot\hat{\mathbf{z}}dA}\right]\epsilon_r(\mathbf{r})\mathbf{e}_j^*\mathbf{e}_L dV}{\int_V n_0^2|_c|\mathbf{e}_j|^2 dV} \\
&- \sum_L i\frac{\omega_L^2\omega_p}{2\omega_j\beta_L c^2}\sqrt{\frac{N_j}{N_p}}\frac{\int_V e^{i\eta(z)}\left[\int_{z_0}^z e^{-i\eta(z')}\frac{\int_A \epsilon_r(\mathbf{r})(\mathbf{e}_p \wedge \mathbf{h}_L^*)\cdot\hat{\mathbf{z}}dA}{\int_A (\mathbf{e}_L \wedge \mathbf{h}_L^*)\cdot\hat{\mathbf{z}}dA}dz'\right][n_0^2|_c - n_a^2 + \delta\epsilon(\mathbf{r})]\mathbf{e}_j^*\mathbf{e}_L dV}{\int_V n_0^2|_c|\mathbf{e}_j|^2 dV} \\
&+ \sum_L i\frac{\omega_L^2\omega_p}{2\omega_j\beta_L c^2}\sqrt{\frac{N_j}{N_p}}\frac{\int_V e^{i\eta(z)}\left[\int_{z_0}^z e^{-i\eta(z')}\frac{\int_A \epsilon_r(\mathbf{r})(\mathbf{e}_p \wedge \mathbf{h}_L^*)\cdot\hat{\mathbf{z}}dA}{\int_A (\mathbf{e}_L \wedge \mathbf{h}_L^*)\cdot\hat{\mathbf{z}}dA}dz'\right]\left[\frac{\int_A [n_0^2|_c - n_a^2 + \delta\epsilon(\mathbf{r})](\mathbf{e}_L \wedge \mathbf{h}_L^*)\cdot\hat{\mathbf{z}}dA}{\int_A (\mathbf{e}_L \wedge \mathbf{h}_L^*)\cdot\hat{\mathbf{z}}dA}\right]\epsilon_r(\mathbf{r})\mathbf{e}_j^*\mathbf{e}_L dV}{\int_V n_0^2|_c|\mathbf{e}_j|^2 dV}
\end{aligned}
$$

$$
\begin{aligned}
A_5 = &\, i\frac{\omega_L^2}{2\omega_j}\sqrt{\frac{N_j}{M_L}}\frac{\int_V e^{i\eta(z)}[n_0^2|_c - n_a^2 + \delta\epsilon(\mathbf{r})]\mathbf{e}_j^*\mathbf{e}_L dV}{\int_V n_0^2|_c|\mathbf{e}_j|^2 dV} \\
&- i\frac{\omega_L^2}{2\omega_j}\sqrt{\frac{N_j}{M_L}}\frac{\int_V e^{i\eta(z)}\left[\frac{\int_A [n_0^2|_c - n_a^2 + \delta\epsilon(\mathbf{r})](\mathbf{e}_L \wedge \mathbf{h}_L^*)\cdot\hat{\mathbf{z}}dA}{\int_A (\mathbf{e}_L \wedge \mathbf{h}_L^*)\cdot\hat{\mathbf{z}}dA}\right]\epsilon_r(\mathbf{r})\mathbf{e}_j^*\mathbf{e}_L dV}{\int_V n_0^2|_c|\mathbf{e}_j|^2 dV}
\end{aligned}
$$

and, with Eq. B.38,

$$
\eta(z) = \frac{\omega_L^2}{2\beta_L c^2}\int_{z_0}^z \frac{\int_A [n_0^2|_c - n_a^2 + \delta\epsilon(\mathbf{r})](\mathbf{e}_L \wedge \mathbf{h}_L^*)\cdot\hat{\mathbf{z}}dA}{\int_A (\mathbf{e}_L \wedge \mathbf{h}_L^*)\cdot\hat{\mathbf{z}}dA}dz'.
$$

Each A_i are constant in regard of time but depends on optical frequencies and the spatial components.

Coupling constants approximations

Relations B.37 and B.40 describe the coupling processes between the waveguide modes and the cavity modes. Nevertheless, in the literature, more approximations are used.

Firstly, in Relation B.37, we neglect the contribution of the partial time derivatives since $a_j(t)$ and $a_p(t)$ do not vary rapidly. Secondly, in Relation B.37 A_1 constant, all the summation terms are considered small compared to unity, leading to $A_1 \approx 1$. Neglecting the time derivatives in Relations B.36 and B.37 would give the same result. Thirdly, we neglect the coupling between modes j and p due to the waveguide, i.e. the last three terms of A_3 are negligible compared to the effect of $\delta\epsilon(\mathbf{r})$. Finally, we consider that the coupling between modes j and p is slow, leading to

$$|A_3 a_p(t)| >> |A_4 \frac{\partial a_p(t)}{\partial t}|.$$

A more familiar form is obtained :

$$\frac{\partial a_j(t)}{\partial t} = (i\Gamma_{jj} - \frac{1}{2\tau_{j,0}} - \frac{1}{2\tau_{j,c}})a_j(t) + \sum_p i\Gamma_{jp} a_p(t) e^{-i(\omega_p-\omega_j)t} + \sum_L i\kappa_{jL} s_L(z_0,t) e^{-i(\omega_L-\omega_j)t} \tag{B.41}$$

$$s_L(z,t) = s_L(z_0,t)e^{i\eta(z)} + i\kappa_{Lj}(z)e^{i\eta(z)}a_j(t)e^{-i(\omega_j-\omega_L)t} + \sum_p i\kappa_{Lp}(z)e^{i\eta(z)}a_p(t)e^{-i(\omega_p-\omega_L)t}.$$

The latter relation is usually evaluated at the waveguide's exit $z = z_1$

$$s_L(z_1,t) = s_L(z_0,t) + i\kappa_{Lj}(z_1)a_j(t)e^{-i(\omega_j-\omega_L)t} + \sum_p i\kappa_{Lp}(z_1)a_p(t)e^{-i(\omega_p-\omega_L)t} \tag{B.42}$$

where the global phase term $e^{i\eta(z_1)}$ is equaled to 1 since it does not influence the measured output power $|s_L(z_1,t)|^2$. It becomes important if, for example, the waveguide-cavity system is part of an interferometer.

The mode j phase difference constant, $j-p$ coupling constant and the intrinsic loss rate of the mode j are respectively

$$\Gamma_{jj} = \frac{\omega_j}{2}\frac{\int_V [n_0^2|_g - n_a^2 + \delta\epsilon(\mathbf{r})]|\mathbf{e}_j|^2 dV}{\int_V n_0^2|_c|\mathbf{e}_j|^2 dV} - \sum_L \frac{\omega_j}{2}\frac{\int_V \left[\frac{\int_A [n_0^2|_g - n_a^2 + \delta\epsilon(\mathbf{r})](\mathbf{e}_j \wedge \mathbf{h}_L^*)\cdot\hat{\mathbf{z}}dA}{\int_A (\mathbf{e}_L \wedge \mathbf{h}_L^*)\cdot\hat{\mathbf{z}}dA}\right]\epsilon_r(\mathbf{r})\mathbf{e}_j^*\mathbf{e}_L dV}{\int_V n_0^2|_c|\mathbf{e}_j|^2 dV} \tag{B.43}$$

$$\Gamma_{jp} = \frac{\omega_p^2}{2\omega_j}\sqrt{\frac{N_j}{N_p}}\frac{\int_V [n_0^2|_g - n_a^2 + \delta\epsilon(\mathbf{r})]\mathbf{e}_j^*\mathbf{e}_p dV}{\int_V n_0^2|_c|\mathbf{e}_j|^2 dV} \approx \frac{\omega_p^2}{2\omega_j}\sqrt{\frac{N_j}{N_p}}\frac{\int_V \delta\epsilon(\mathbf{r})\mathbf{e}_j^*\mathbf{e}_p dV}{\int_V n_0^2|_c|\mathbf{e}_j|^2 dV} \tag{B.44}$$

$$\frac{1}{2\tau_{j,0}} = \frac{\omega_j}{2}\frac{\int_V \mathrm{Im}(\epsilon_r)|\mathbf{e}_j|^2 dV}{\int_V n_0^2|_c|\mathbf{e}_j|^2 dV}. \tag{B.45}$$

$\tau_{j,0}$ is defined as the intrinsic photon's lifetime inside the cavity without external coupling process. In other words, if the waveguide is instantaneously removed at $t = 0$, the power or the energy inside the j mode reaches e^{-1} of its inital value at $t = \tau_{j,0}$. Main loss processes related to $\tau_{j,0}$ are the material absorption, Rayleigh scattering and radiative tunneling.

Up to now, we did not discussed the imaginary part of the perturbations, i.e. $i\delta\epsilon'(\mathbf{r})$. Within Γ_{jj} et Γ_{jp}, this imaginary part describes the coupling process to radiative modes due to a perturbation, for example, a dust particle on the cavity's surface. To do so, we rewrite

$$\begin{aligned}\Gamma_{jj} &\rightarrow \Gamma_{jj} + i\Gamma'_{jj}\\ \Gamma_{jp} &\rightarrow \Gamma_{jp} + i\Gamma'_{jp}\end{aligned}$$

with

$$\Gamma'_{jj} = \frac{\omega_j}{2}\frac{\int_V \delta\epsilon'(\mathbf{r})|\mathbf{e}_j|^2 dV}{\int_V n_0^2|_c|\mathbf{e}_j|^2 dV} - \sum_L \frac{\omega_j}{2}\frac{\int_V \left[\frac{\int_A \delta\epsilon'(\mathbf{r})(\mathbf{e}_j\wedge\mathbf{h}_L^*)\cdot\hat{\mathbf{z}}dA}{\int_A(\mathbf{e}_L\wedge\mathbf{h}_L^*)\cdot\hat{\mathbf{z}}dA}\right]\epsilon_r(\mathbf{r})\mathbf{e}_j^*\mathbf{e}_L dV}{\int_V n_0^2|_c|\mathbf{e}_j|^2 dV} \tag{B.46}$$

$$\approx \frac{\omega_j}{2}\frac{\int_V \delta\epsilon'(\mathbf{r})|\mathbf{e}_j|^2 dV}{\int_V n_0^2|_c|\mathbf{e}_j|^2 dV} \tag{B.47}$$

$$\Gamma'_{jp} \approx \frac{\omega_p^2}{2\omega_j}\sqrt{\frac{N_j}{N_p}}\frac{\int_V \delta\epsilon'(\mathbf{r})\mathbf{e}_j^*\mathbf{e}_p dV}{\int_V n_0^2|_c|\mathbf{e}_j|^2 dV} \tag{B.48}$$

where we neglected the presence of a perturbation in the coupling area as it is small compared to the cavity's area, i.e. $\delta\epsilon'(\mathbf{r})\mathbf{e}_j^*\mathbf{e}_L \rightarrow 0$ and $\delta\epsilon'(\mathbf{r})(\mathbf{e}_j\wedge\mathbf{h}_L^*)\cdot\hat{\mathbf{z}} \rightarrow 0$.

The coupling constants of $j-L$, $L-j$ and $L-p$, and the loss rate due to the $j-L$ coupling are

$$\kappa_{jL} = \frac{\omega_L^2}{2\omega_j}\sqrt{\frac{N_j}{M_L}}\frac{\int_V e^{i\eta(z)}[n_0^2|_c - n_a^2 + \delta\epsilon(\mathbf{r})]\mathbf{e}_j^*\mathbf{e}_L dV}{\int_V n_0^2|_c|\mathbf{e}_j|^2 dV} \tag{B.49}$$

$$- \frac{\omega_L^2}{2\omega_j}\sqrt{\frac{N_j}{M_L}}\frac{\int_V e^{i\eta(z)}\left[\frac{\int_A[n_0^2|_c - n_a^2 + \delta\epsilon(\mathbf{r})](\mathbf{e}_L\wedge\mathbf{h}_L^*)\cdot\hat{\mathbf{z}}dA}{\int_A(\mathbf{e}_L\wedge\mathbf{h}_L^*)\cdot\hat{\mathbf{z}}dA}\right]\epsilon_r(\mathbf{r})\mathbf{e}_j^*\mathbf{e}_L dV}{\int_V n_0^2|_c|\mathbf{e}_j|^2 dV}$$

$$\kappa_{Lj}(z) = \frac{\omega_j^2}{2\beta_L c^2}\sqrt{\frac{M_L}{N_j}}\int_{z_0}^{z} e^{-i\eta(z')}\frac{\int_A[n_0^2|_g - n_a^2 + \delta\epsilon(\mathbf{r})](\mathbf{e}_j\wedge\mathbf{h}_L^*)\cdot\hat{\mathbf{z}}dA}{\int_A(\mathbf{e}_L\wedge\mathbf{h}_L^*)\cdot\hat{\mathbf{z}}dA}dz' \tag{B.50}$$

$$\kappa_{Lp}(z) = \frac{\omega_p^2}{2\beta_L c^2}\sqrt{\frac{M_L}{N_p}}\int_{z_0}^{z} e^{-i\eta(z')}\frac{\int_A[n_0^2|_g - n_a^2 + \delta\epsilon(\mathbf{r})](\mathbf{e}_p\wedge\mathbf{h}_L^*)\cdot\hat{\mathbf{z}}dA}{\int_A(\mathbf{e}_L\wedge\mathbf{h}_L^*)\cdot\hat{\mathbf{z}}dA}dz'$$

$$\frac{1}{2\tau_{j,c}} = \sum_L \frac{\omega_L^2\omega_j}{4\beta_L c^2}\frac{\int_V e^{i\eta(z)}\left[\int_{z_0}^{z} e^{-i\eta(z')}\frac{\int_A[n_0^2|_g - n_a^2 + \delta\epsilon(\mathbf{r})](\mathbf{e}_j\wedge\mathbf{h}_L^*)\cdot\hat{\mathbf{z}}dA}{\int_A(\mathbf{e}_L\wedge\mathbf{h}_L^*)\cdot\hat{\mathbf{z}}dA}dz'\right][n_0^2|_c - n_a^2 + \delta\epsilon(\mathbf{r})]\mathbf{e}_j^*\mathbf{e}_L dV}{\int_V n_0^2|_c|\mathbf{e}_j|^2 dV}$$

$$
\begin{aligned}
&-\sum_L \frac{\omega_L^2 \omega_j}{4\beta_L c^2} \times \\
&\left(\frac{\int_V e^{i\eta(z)} \left[\int_{z_0}^{z} e^{-i\eta(z')} \frac{\int_A [n_0^2|_g - n_a^2 + \delta\epsilon(\mathbf{r})](\mathbf{e}_j \wedge \mathbf{h}_L^*)\cdot\hat{\mathbf{z}} dA}{\int_A (\mathbf{e}_L \wedge \mathbf{h}_L^*)\cdot\hat{\mathbf{z}} dA} dz' \right] \left[\frac{\int_A [n_0^2|_c - n_a^2 + \delta\epsilon(\mathbf{r})](\mathbf{e}_L \wedge \mathbf{h}_L^*)\cdot\hat{\mathbf{z}} dA}{\int_A (\mathbf{e}_L \wedge \mathbf{h}_L^*)\cdot\hat{\mathbf{z}} dA} \right] \epsilon_r(\mathbf{r}) \mathbf{e}_j^* \mathbf{e}_L dV}{\int_V n_0^2|_c |\mathbf{e}_j|^2 dV} \right) \\
&= \sum_L \frac{\omega_L^2}{2\omega_j} \sqrt{\frac{N_j}{M_L}} \frac{\int_V e^{i\eta(z)} \left[\kappa_{Lj}(z)\right] [n_0^2|_c - n_a^2 + \delta\epsilon(\mathbf{r})] \mathbf{e}_j^* \mathbf{e}_L dV}{\int_V n_0^2|_c |\mathbf{e}_j|^2 dV} \\
&\quad - \sum_L \frac{\omega_L^2}{2\omega_j} \sqrt{\frac{N_j}{M_L}} \frac{\int_V e^{i\eta(z)} \left[\kappa_{Lj}(z)\right] \left[\frac{\int_A [n_0^2|_c - n_a^2 + \delta\epsilon(\mathbf{r})](\mathbf{e}_L \wedge \mathbf{h}_L^*)\cdot\hat{\mathbf{z}} dA}{\int_A (\mathbf{e}_L \wedge \mathbf{h}_L^*)\cdot\hat{\mathbf{z}} dA} \right] \epsilon_r(\mathbf{r}) \mathbf{e}_j^* \mathbf{e}_L dV}{\int_V n_0^2|_c |\mathbf{e}_j|^2 dV}
\end{aligned}
\tag{B.51}
$$

where $\eta(z)$ is defined in Eq. B.38.

Similarly to $\tau_{j,0}$, $\tau_{j,c}$ is the extrinsic photon's lifetime due to the waveguide coupling. In other words, if the cavity's losses were instantaneously removed at $t = 0$, the power or the energy inside the j mode reaches e^{-1} of its inital value at $t = \tau_{j,c}$. As we can see, $\tau_{j,c}$ depends on the mode overlap between the modes j and L and their phase conditions.

A closer inspection of these relations reveals a link between κ_{jL}, $\kappa_{Lj}(z)$ and $\tau_{j,c}$. For symmetrical coupling conditions, we have

$$
\frac{1}{2\tau_{j,c}} \approx \sum_L \kappa_{jL} \frac{\kappa_{Lj}(z_1)}{2} \quad \rightarrow \quad \frac{1}{\tau_{j,c}} \approx \sum_L \kappa_{jL} \kappa_{Lj}(z_1) \tag{B.52}
$$

$$
\frac{1}{2\tau_{-j,c}} \approx \sum_L \kappa_{-j-L} \frac{\kappa_{-L-j}(z_0)}{2} \quad \rightarrow \quad \frac{1}{\tau_{-j,c}} \approx \sum_L \kappa_{-j-L} \kappa_{-L-j}(z_0) \tag{B.53}
$$

where $\kappa_{Lj}(z) \approx \frac{\kappa_{Lj}(z_1)}{2}$ goes out of the volume integral of $\frac{1}{2\tau_{j,c}}$ for each dz slice. Furthermore, in the literature, the approximation

$$
\kappa_{jL} \approx \kappa_{Lj}(z_1) \approx \kappa_{-j-L} \approx \kappa_{-L-j}(z_0)
$$

is usually used, giving

$$
\frac{1}{\tau_{j,c}} \approx \frac{1}{\tau_{-j,c}} \approx \kappa_{jL}^2 \quad \Rightarrow \quad \kappa_{jL} \approx \frac{1}{\sqrt{\tau_{j,c}}} \tag{B.54}
$$

with κ_{jL} being real.

All these coefficients are considered constant during measurements and they are proper to each resonance and each coupling conditions. Specifically, they depend on the frequencies, the material properties, the surface roughness, the cavity and waveguide geometries, the waveguide-cavity separation and the angle between them.

B.1.5 Modal coupling : clockwise and counterclockwise modes

In principle, only the mode $p = -j$, propagating in the opposite direction, has a similar eigenfrequency that allows $e^{-i(\omega_j-\omega_p)} \rightarrow 1$. We can then consider that the linear coupling between a clockwise cavity mode is limited to their counterclockwise twin. For example, if surface roughness fulfills the phase-match conditions, energy will be transfered [26]. Those twin modes, j and $-j$ are degenerate and have the same frequency ω_j when the cavity is circular. They can also be described as a superposition of a symmetric and anti-symmetric stationary wave modes with a frequency ω_j. A perturbation spatially fixes these modes and lifts the frequency degeneracy. It can be measured experimentally as double peaks [286]. As whispering gallery modes are very sensitive to perturbation, this is useful to detect a small particle or a biological pathogen [71, 287].

Equations B.41 and B.42 give, for j et L,

$$\frac{\partial a_j(t)}{\partial t} = (i\Gamma_{jj} - \Gamma'_{jj} - \frac{1}{2\tau_{j,0}} - \frac{1}{2\tau_{j,c}})a_j(t) + (i\Gamma_{j-j} - \Gamma'_{j-j})a_{-j}(t) + \sum_L i\kappa_{jL}s_L(z_0,t)e^{-i(\omega_L-\omega_j)t} \tag{B.55}$$

$$s_L(z_1,t) = s_L(z_0,t) + i\kappa_{Lj}(z_1)a_j(t)e^{-i(\omega_j-\omega_L)t} \tag{B.56}$$

and, for $-j$ et $-L$,

$$\begin{aligned}\frac{\partial a_{-j}(t)}{\partial t} = {} & (i\Gamma_{-j-j} - \Gamma'_{-j-j} - \frac{1}{2\tau_{-j,0}} - \frac{1}{2\tau_{-j,c}})a_{-j}(t) \\ & + (i\Gamma_{-jj} - \Gamma'_{-jj})a_j(t) + \sum_L i\kappa_{-j-L}s_{-L}(z_1,t)e^{-i(\omega_L-\omega_j)t}\end{aligned} \tag{B.57}$$

$$s_{-L}(z_0,t) = s_{-L}(z_1,t) + i\kappa_{-L-j}(z_0)a_{-j}(t)e^{-i(\omega_j-\omega_L)t} \tag{B.58}$$

where, for the latter, the mode $-j$ is coupled to $-L$ modes that are propagating from $z = z_1$ to $z = z_0$. For coupling processes in the $-L$ direction, integration interval goes from $z = z_1$ to z in the definitions of $\frac{1}{2\tau_{-j,c}}$, κ_{-j-L} and $\kappa_{-L-j}(z)$.

We often rewrite Relations B.55 to B.58 as solutions proportional to $e^{-i(\omega_L-\omega_j)t}$. Using

$$a_j(t) \;\rightarrow\; a_j(t)e^{-i(\omega_L-\omega_j)t} \;\text{ et }\; a_{-j}(t) \;\rightarrow\; a_{-j}(t)e^{-i(\omega_L-\omega_j)t},$$

we obtain, for j and L,

$$\frac{\partial a_j(t)}{\partial t} = \left(i[\Gamma_{jj} + \omega_L - \omega_j] - \Gamma'_{jj} - \frac{1}{2\tau_{j,0}} - \frac{1}{2\tau_{j,c}}\right) a_j(t)$$

$$
\begin{aligned}
&+ (i\Gamma_{j-j} - \Gamma'_{j-j})a_{-j}(t) + \sum_L i\kappa_{jL}s_L(z_0,t) \\
= &\left(i[\omega_L - (\omega_j - \Gamma_{jj})] - \Gamma'_{jj} - \frac{1}{2\tau_j}\right)a_j(t) \\
&+ (i\Gamma_{j-j} - \Gamma'_{j-j})a_{-j}(t) + \sum_L i\kappa_{jL}s_L(z_0,t)
\end{aligned} \tag{B.59}
$$

$$
s_L(z_1,t) = s_L(z_0,t) + i\kappa_{Lj}(z_1)a_j(t) \tag{B.60}
$$

and, for $-j$ et $-L$,

$$
\begin{aligned}
\frac{\partial a_{-j}(t)}{\partial t} = &\left(i[\Gamma_{-j-j} + \omega_L - \omega_j] - \Gamma'_{-j-j} - \frac{1}{2\tau_{-j,0}} - \frac{1}{2\tau_{-j,c}}\right)a_{-j}(t) \\
&+ (i\Gamma_{-jj} - \Gamma'_{-jj})a_j(t) + \sum_L i\kappa_{-j-L}s_{-L}(z_1,t) \\
= &\left(i[\omega_L - (\omega_j - \Gamma_{-j-j})] - \Gamma'_{-j-j} - \frac{1}{2\tau_{-j}}\right)a_{-j}(t) \\
&+ (i\Gamma_{-jj} - \Gamma'_{-jj})a_j(t) + \sum_L i\kappa_{-j-L}s_{-L}(z_1,t)
\end{aligned} \tag{B.61}
$$

$$
s_{-L}(z_0,t) = s_{-L}(z_1,t) + i\kappa_{-L-j}(z_0)a_{-j}(t) \tag{B.62}
$$

where

$$
\frac{1}{2\tau_j} = \frac{1}{2\tau_{j,0}} + \frac{1}{2\tau_{j,c}} \quad \text{and} \quad \frac{1}{2\tau_{-j}} = \frac{1}{2\tau_{-j,0}} + \frac{1}{2\tau_{-j,c}}. \tag{B.63}
$$

The spectra depend on the frequency or wavelength difference between the laser and the shifted resonance $\omega_L - (\omega_j - \Gamma_{jj})$. Experimentally, the $\omega_j - \Gamma_{jj}$ shift is not important and it is the difference between the laser line and the resonance's center that counts, wherever the resonance was prior to the waveguide perturbation. For this reason, Γ_{jj} and Γ_{-j-j} are often omitted.

Finally, by comparison, we see that

$$
\Gamma_{jj} = \Gamma_{-j-j} = \Gamma_1 \;\text{ and }\; \Gamma_{j-j} = \Gamma_{-jj} = \Gamma_2 \;\Rightarrow\; |\Gamma_{j-j}|^2 = |\Gamma_{-jj}|^2 = |\Gamma_2|^2 = \Gamma_2^2 \tag{B.64}
$$

$$
\Gamma'_{jj} = \Gamma'_{-j-j} = \Gamma'_1 \;\text{ and }\; \Gamma'_{j-j} = \Gamma'_{-jj} = \Gamma'_2 \;\Rightarrow\; |\Gamma'_{j-j}|^2 = |\Gamma'_{-jj}|^2 = |\Gamma'_2|^2 = \Gamma'^2_2 \tag{B.65}
$$

considering that $\delta\epsilon'(\mathbf{r})\mathbf{e}_j^*\mathbf{e}_{-j} = \delta\epsilon'(\mathbf{r})\mathbf{e}_{-j}^*\mathbf{e}_j$, and that $\delta\epsilon(\mathbf{r})$ and $\delta\epsilon'(\mathbf{r})$ are real.

B.1.6 Approximations summary and coupling constants index

The waveguide and cavity coupled-modes equations has been established in the previous chapters by starting from Maxwell equations and using many approximations. For the readers' benefit, we briefly list the approximations used up to now and the various coupling constants with their equation's numbers.

Table B.1 : Linear coupled-modes approximations and outcomes.

Approximation	**Outcome**
Non magnetic materials	Null magnetic susceptibility
Dielectric materials	No free charge and null current
Local field	Susceptibility is spatially local
Fast response	Susceptibility has no memory
Isotropic materials	No slow-fast axis and $\chi^{(2)} = 0$
Bound modes	Radiative part is not considered
No nonlinear effect	$\chi^{(n>1)} = 0$
Slowly varying fields	Time derivatives can be neglected
Transparent materials	$n_0' << n_0$
No mode coupling due to the waveguide	$\delta\epsilon(\mathbf{r})$ has a greater effect
No perturbation in the coupling area	$\delta\epsilon'(\mathbf{r})\mathbf{e}_j^*\mathbf{e}_L \to 0$ and $\delta\epsilon'(\mathbf{r})(\mathbf{e}_j \wedge \mathbf{h}_L^*)\cdot\hat{\mathbf{z}} \to 0$
Symmetrical coupling	$\kappa_{jL} \approx \kappa_{Lj}(z_1)$
Modal coupling	Clockwise and counterclockwise mode coupling only

Table B.2 : Linear rates, coupling constants, and lifetimes.

Coupling constant	**Symbol**	**Definition**
Waveguide phase shift due to the cavity	$\eta(z)$	B.38
Cavity phase shift due to the waveguide and a perturbation	Γ_{jj}	B.43
Cavity losses due to a perturbation	Γ'_{jj}	B.47
Coupling between modes j and p	Γ_{jp}	B.44
Losses during $j-p$ coupling	Γ'_{jp}	B.48
Cavity mode to waveguide mode	κ_{jL}	B.49 and B.54
Waveguide mode to cavity mode	$\kappa_{Lj}(z)$	B.50 and B.54
Intrinsic photon's lifetime	$\tau_{j,0}$	B.45
Extrinsic photon's lifetime	$\tau_{j,c}$	B.51 and B.54
Total photon's lifetime	τ_j	B.63

B.2 Linear steady-state solutions and characteristics

B.2.1 Continuous-wave regime

Relations B.59 to B.62 describe the slowly varying coupling processes between waveguide and cavity modes. To find any transient behavior, one can use numerical simulation techniques such as Runge-Kutta. However, if a continuous-wave (CW) signal is sent into the waveguide, the cavity response will stabilize and enter into steady-state. This is also valid for a quasi-CW signal if it varies with a frequency $\nu << 1/\tau_j$.

In steady-state, we have

$$\frac{\partial a_j(t)}{\partial t} \;\rightarrow\; 0 \;\text{ et }\; \frac{\partial a_{-j}(t)}{\partial t} \;\rightarrow\; 0.$$

We will consider a monochromatic signal ω_L launched from z_0 into a mode L of a single mode waveguide.

Unidirectional source, single mode waveguide, modal coupling and $\delta\epsilon'(\mathbf{r}) \neq 0$

If we consider a signal sent into a single mode L at z_0 ($s_{-L}(z_1,t)=0$),

$$a_j(t) = -\frac{i\kappa_{jL}s_L(z_0,t)+(i\Gamma_{j-j}-\Gamma'_{j-j})a_{-j}(t)}{i[\omega_L-(\omega_j-\Gamma_{jj})]-\Gamma'_{jj}-\frac{1}{2\tau_j}} = -\frac{i\kappa_{jL}s_L(z_0,t)+(i\Gamma_{j-j}-\Gamma'_{j-j})a_{-j}(t)}{i[\omega_L-(\omega_j-\Gamma_{jj})]-\gamma_j}$$

$$a_{-j}(t) = -\frac{(i\Gamma_{-jj}-\Gamma'_{-jj})a_j(t)}{i[\omega_L-(\omega_j-\Gamma_{-j-j})]-\Gamma'_{-j-j}-\frac{1}{2\tau_{-j}}} = -\frac{(i\Gamma_{-jj}-\Gamma'_{-jj})a_j(t)}{i[\omega_L-(\omega_j-\Gamma_{-j-j})]-\Gamma_{-j}}$$

$$s_L(z_1,t) = s_L(z_0,t)+i\kappa_{Lj}(z_1)a_j(t)$$

$$s_{-L}(z_0,t) = i\kappa_{-L-j}(z_0)a_{-j}(t)$$

where $\gamma_j = \Gamma'_{jj}+\frac{1}{2\tau_j}$ and $\gamma_{-j} = \Gamma'_{-j-j}+\frac{1}{2\tau_{-j}}$, giving

$$a_j(t) = \frac{-i\kappa_{jL}s_L(z_0,t)(i[\omega_L-(\omega_j-\Gamma_{-j-j})]-\gamma_{-j})}{(i[\omega_L-(\omega_j-\Gamma_{jj})]-\gamma_j)(i[\omega_L-(\omega_j-\Gamma_{-j-j})]-\gamma_{-j})-(i\Gamma_{j-j}-\Gamma'_{j-j})(i\Gamma_{-jj}-\Gamma'_{-jj})}$$

$$a_{-j}(t) = \frac{(i\Gamma_{-jj}-\Gamma'_{-jj})i\kappa_{jL}s_L(z_0,t)}{(i[\omega_L-(\omega_j-\Gamma_{jj})]-\gamma_j)(i[\omega_L-(\omega_j-\Gamma_{-j-j})]-\gamma_{-j})-(i\Gamma_{j-j}-\Gamma'_{j-j})(i\Gamma_{-jj}-\Gamma'_{-jj})}$$

$$s_L(z_1,t) = s_L(z_0,t)\cdot$$

$$\left[1+\frac{\kappa_{Lj}(z_1)\kappa_{jL}(i[\omega_L-(\omega_j-\Gamma_{-j-j})]-\gamma_{-j})}{(i[\omega_L-(\omega_j-\Gamma_{jj})]-\gamma_j)(i[\omega_L-(\omega_j-\Gamma_{-j-j})]-\gamma_{-j})-(i\Gamma_{j-j}-\Gamma'_{j-j})(i\Gamma_{-jj}-\Gamma'_{-jj})}\right]$$

$$s_{-L}(z_0,t)=$$

$$\frac{\kappa_{-L-j}(z_0)(i\Gamma_{-jj}-\Gamma'_{-jj})\kappa_{jL}s_L(z_0,t)}{(i[\omega_L-(\omega_j-\Gamma_{jj})]-\gamma_j)(i[\omega_L-(\omega_j-\Gamma_{-j-j})]-\gamma_{-j})-(i\Gamma_{j-j}-\Gamma'_{j-j})(i\Gamma_{-jj}-\Gamma'_{-jj})}.$$

We consider that both modes j and $-j$ have the same intrinsic losses and waveguide coupling constants, leading to $\tau_{j,0}\approx\tau_{-j,0}$, $\tau_{j,c}\approx\tau_{-j,c}$, $\tau_j\approx\tau_{-j}$ and $\gamma_j\approx\gamma_{-j}$. Using Relations B.64, B.65, and $\Delta=[\omega_L-(\omega_j-\Gamma_{jj})]$, we get

$$\begin{aligned}a_j(t)=&\kappa_{jL}s_L(z_0,t)\cdot\\&[\frac{\Delta\left(\gamma_j^2-\Delta^2+\Gamma_2^2-\Gamma_2'^2\right)+\gamma_j\left(-2\gamma_j\Delta+2\Gamma_2\Gamma'_2\right)}{\left(\gamma_j^2+\Delta^2\right)^2+2(\Gamma_2^2-\Gamma_2'^2)\left(\gamma_j^2-\Delta^2\right)+(\Gamma_2^2+\Gamma_2'^2)^2-8\gamma_j\Delta\Gamma_2\Gamma'_2}\\&+i\frac{\gamma_j\left(\gamma_j^2-\Delta^2+\Gamma_2^2-\Gamma_2'^2\right)-\Delta\left(-2\gamma_j\Delta+2\Gamma_2\Gamma'_2\right)}{\left(\gamma_j^2+\Delta^2\right)^2+2(\Gamma_2^2-\Gamma_2'^2)\left(\gamma_j^2-\Delta^2\right)+(\Gamma_2^2+\Gamma_2'^2)^2-8\gamma_j\Delta\Gamma_2\Gamma'_2}],\end{aligned}$$

$$\begin{aligned}a_{-j}(t)=&i\kappa_{jL}s_L(z_0,t)\cdot\\&\frac{(i\Gamma_2-\Gamma'_2)\left[\left(\gamma_j^2-\Delta^2+|\Gamma_2|^2-|\Gamma'_2|^2\right)-i\left(-2\gamma_j\Delta+2\Gamma_2\Gamma'_2\right)\right]}{\left(\gamma_j^2+\Delta^2\right)^2+2(\Gamma_2^2-\Gamma_2'^2)\left(\gamma_j^2-\Delta^2\right)+(\Gamma_2^2+\Gamma_2'^2)^2-8\gamma_j\Delta\Gamma_2\Gamma'_2},\end{aligned}$$

$$\begin{aligned}s_L(z_1,t)&=s_L(z_0,t)\cdot\\&\left[1+\frac{\kappa_{Lj}(z_1)\kappa_{jL}(i\Delta-\gamma_{-j})\left[\left(\gamma_j^2-\Delta^2+|\Gamma_2|^2-|\Gamma'_2|^2\right)-i\left(-2\gamma_j\Delta+2\Gamma_2\Gamma'_2\right)\right]}{\left(\gamma_j^2+\Delta^2\right)^2+2(\Gamma_2^2-\Gamma_2'^2)\left(\gamma_j^2-\Delta^2\right)+(\Gamma_2^2+\Gamma_2'^2)^2-8\gamma_j\Delta\Gamma_2\Gamma'_2}\right]\\&=s_L(z_0,t)\cdot\\&[1+\frac{\kappa_{Lj}(z_1)\kappa_{jL}\left[\Delta(-2\gamma_j\Delta+2\Gamma_2\Gamma'_2)-\gamma_j\left(\gamma_j^2-\Delta^2+|\Gamma_2|^2-|\Gamma'_2|^2\right)\right]}{\left(\gamma_j^2+\Delta^2\right)^2+2(\Gamma_2^2-\Gamma_2'^2)\left(\gamma_j^2-\Delta^2\right)+(\Gamma_2^2+\Gamma_2'^2)^2-8\gamma_j\Delta\Gamma_2\Gamma'_2}\\&\quad+i\frac{\kappa_{Lj}(z_1)\kappa_{jL}\left[\Delta\left(\gamma_j^2-\Delta^2+|\Gamma_2|^2-|\Gamma'_2|^2\right)+\gamma_j\left(-2\gamma_j\Delta+2\Gamma_2\Gamma'_2\right)\right]}{\left(\gamma_j^2+\Delta^2\right)^2+2(\Gamma_2^2-\Gamma_2'^2)\left(\gamma_j^2-\Delta^2\right)+(\Gamma_2^2+\Gamma_2'^2)^2-8\gamma_j\Delta\Gamma_2\Gamma'_2}],\end{aligned}$$

and

$$s_{-L}(z_0,t) = i\kappa_{-L-j}(z_0)\kappa_{jL}s_L(z_0,t)\cdot \frac{(i\Gamma_2-\Gamma_2')\left[\left(\gamma_j^2-\Delta^2+|\Gamma_2|^2-|\Gamma_2'|^2\right)-i\left(-2\gamma_j\Delta+2\Gamma_2\Gamma_2'\right)\right]}{\left(\gamma_j^2+\Delta^2\right)^2+2(\Gamma_2^2-\Gamma_2'^2)\left(\gamma_j^2-\Delta^2\right)+(\Gamma_2^2+\Gamma_2'^2)^2-8\gamma_j\Delta\Gamma_2\Gamma_2'}.$$

To link these solutions to experimental values, we need to express the cavity mode energy and the waveguide output power. We find the former, $|a_j(t)|^2$, with

$$|a_j(t)|^2 = |s_L(z_0,t)|^2\frac{|\kappa_{jL}|^2(\gamma_j^2+\Delta^2)}{\left(\gamma_j^2+\Delta^2\right)^2+2(\Gamma_2^2-\Gamma_2'^2)\left(\gamma_j^2-\Delta^2\right)+(\Gamma_2^2+\Gamma_2'^2)^2-8\gamma_j\Delta\Gamma_2\Gamma_2'}$$

The $-j$ mode energy, $|a_{-j}(t)|^2$, is

$$|a_{-j}(t)|^2 = |s_L(z_0,t)|^2\frac{|\kappa_{jL}|^2(\Gamma_2^2+\Gamma_2'^2)}{\left(\gamma_j^2+\Delta^2\right)^2+2(\Gamma_2^2-\Gamma_2'^2)\left(\gamma_j^2-\Delta^2\right)+(\Gamma_2^2+\Gamma_2'^2)^2-8\gamma_j\Delta\Gamma_2\Gamma_2'}.$$

The mode L power at $z=z_1$, $|s_L(z_1,t)|^2$, is

$$\begin{aligned}|s_L(z_1,t)|^2 =& |s_L(z_0,t)|^2\cdot \\ &\left[1+\frac{2\kappa_{Lj}(z_1)\kappa_{jL}\left[\Delta(-2\gamma_j\Delta+2\Gamma_2\Gamma_2')-\gamma_j\left(\gamma_j^2-\Delta^2+|\Gamma_2|^2-|\Gamma_2'|^2\right)\right]}{\left(\gamma_j^2+\Delta^2\right)^2+2(\Gamma_2^2-\Gamma_2'^2)\left(\gamma_j^2-\Delta^2\right)+(\Gamma_2^2+\Gamma_2'^2)^2-8\gamma_j\Delta\Gamma_2\Gamma_2'}\right. \\ &\left.+\frac{\kappa_{Lj}^2(z_1)\kappa_{jL}^2(\gamma_j^2+\Delta^2)}{\left(\gamma_j^2+\Delta^2\right)^2+2(\Gamma_2^2-\Gamma_2'^2)\left(\gamma_j^2-\Delta^2\right)+(\Gamma_2^2+\Gamma_2'^2)^2-8\gamma_j\Delta\Gamma_2\Gamma_2'}\right] \\ =& |s_L(z_0,t)|^2\cdot \\ &\left[\frac{\left(\gamma_j^2+\Delta^2\right)\left[(\gamma_j-\kappa_{Lj}(z_1)\kappa_{jL})^2+\Delta^2\right]}{\left(\gamma_j^2+\Delta^2\right)^2+2(\Gamma_2^2-\Gamma_2'^2)\left(\gamma_j^2-\Delta^2\right)+(\Gamma_2^2+\Gamma_2'^2)^2-8\gamma_j\Delta\Gamma_2\Gamma_2'}\right. \\ &\left.+\frac{(\Gamma_2^2+\Gamma_2'^2)^2+2(\Gamma_2^2-\Gamma_2'^2)\left[\gamma_j(\gamma_j-\kappa_{Lj}(z_1)\kappa_{jL})-\Delta^2\right]-4\Delta\Gamma_2\Gamma_2'(2\gamma_j-\kappa_{Lj}(z_1)\kappa_{jL})}{\left(\gamma_j^2+\Delta^2\right)^2+2(\Gamma_2^2-\Gamma_2'^2)\left(\gamma_j^2-\Delta^2\right)+(\Gamma_2^2+\Gamma_2'^2)^2-8\gamma_j\Delta\Gamma_2\Gamma_2'}\right]\end{aligned}$$

Finally, we find the mode $-L$ power at $z=z_0$, $|s_{-L}(z_0,t)|^2$, with

$$|s_{-L}(z_0,t)|^2 = |s_L(z_0,t)|^2\frac{|\kappa_{-L-j}(z_0)|^2|\kappa_{jL}|^2(\Gamma_2^2+\Gamma_2'^2)}{\left(\gamma_j^2+\Delta^2\right)^2+2(\Gamma_2^2-\Gamma_2'^2)\left(\gamma_j^2-\Delta^2\right)+(\Gamma_2^2+\Gamma_2'^2)^2-8\gamma_j\Delta\Gamma_2\Gamma_2'}$$

Using B.52 to B.54, we obtain

$$|a_j(t)|^2 \approx \frac{|s_L(z_0,t)|^2}{\tau_{j,c}} \frac{(\gamma_j^2+\Delta^2)}{\left(\gamma_j^2+\Delta^2\right)^2 + 2(\Gamma_2^2-\Gamma_2'^2)\left(\gamma_j^2-\Delta^2\right) + (\Gamma_2^2+\Gamma_2'^2)^2 - 8\gamma_j\Delta\Gamma_2\Gamma_2'} \tag{B.66}$$

$$|a_{-j}(t)|^2 \approx \frac{|s_L(z_0,t)|^2}{\tau_{j,c}} \frac{(\Gamma_2^2+\Gamma_2'^2)}{\left(\gamma_j^2+\Delta^2\right)^2 + 2(\Gamma_2^2-\Gamma_2'^2)\left(\gamma_j^2-\Delta^2\right) + (\Gamma_2^2+\Gamma_2'^2)^2 - 8\gamma_j\Delta\Gamma_2\Gamma_2'} \tag{B.67}$$

$$\begin{aligned} |s_L(z_1,t)|^2 \approx & |s_L(z_0,t)|^2 \cdot \\ & \Big[\frac{\left(\gamma_j^2+\Delta^2\right)\left[(\gamma_j-\frac{1}{\tau_{j,c}})^2+\Delta^2\right]}{\left(\gamma_j^2+\Delta^2\right)^2 + 2(\Gamma_2^2-\Gamma_2'^2)\left(\gamma_j^2-\Delta^2\right) + (\Gamma_2^2+\Gamma_2'^2)^2 - 8\gamma_j\Delta\Gamma_2\Gamma_2'} \\ & + \frac{(\Gamma_2^2+\Gamma_2'^2)^2 + 2(\Gamma_2^2-\Gamma_2'^2)\left[\gamma_j(\gamma_j-\frac{1}{\tau_{j,c}})-\Delta^2\right] - 4\Delta\Gamma_2\Gamma_2'(2\gamma_j-\frac{1}{\tau_{j,c}})}{\left(\gamma_j^2+\Delta^2\right)^2 + 2(\Gamma_2^2-\Gamma_2'^2)\left(\gamma_j^2-\Delta^2\right) + (\Gamma_2^2+\Gamma_2'^2)^2 - 8\gamma_j\Delta\Gamma_2\Gamma_2'}\Big] \end{aligned} \tag{B.68}$$

$$|s_{-L}(z_0,t)|^2 \approx \frac{|s_L(z_0,t)|^2}{\tau_{j,c}^2} \frac{(\Gamma_2^2+\Gamma_2'^2)}{\left(\gamma_j^2+\Delta^2\right)^2 + 2(\Gamma_2^2-\Gamma_2'^2)\left(\gamma_j^2-\Delta^2\right) + (\Gamma_2^2+\Gamma_2'^2)^2 - 8\gamma_j\Delta\Gamma_2\Gamma_2'} \tag{B.69}$$

In CW regime, the system's output power equals the system's input power at any time, leading to

$$\underbrace{|s_L(z_0,t)|^2}_{Input\ power} = \underbrace{|s_L(z_1,t)|^2 + |s_{-L}(z_0,t)|^2}_{Output\ powers} + \underbrace{(2\Gamma_{jj}' + \frac{1}{\tau_{j,0}})(|a_j(t)|^2 + |a_{-j}(t)|^2)}_{Lost\ cavity\ power} + \underbrace{2\Gamma_2'(a_j a_{-j}^* + a_j^* a_{-j})}_{Lost\ mode\ coupling\ power} \tag{B.70}$$

The first two terms on the right side define the output power through the signal's transmission and reflection. The third term is the lost cavity mode power through intrinsic and perturbation losses. The last term is also the lost cavity mode power through perturbation, but between clockwise and counterclockwise modes.

Unidirectional source, single mode waveguide, modal coupling and $\delta\epsilon'(\mathbf{r}) = 0$

Solutions are similar to previous Sections B.66 to B.69, but we set $\gamma_j \rightarrow \frac{1}{2\tau_j}$ and $\Gamma_{j-j}' \rightarrow 0$ (or $\Gamma_2' \rightarrow 0$) :

$$|a_j(t)|^2 \approx \frac{|s_L(z_0,t)|^2}{\tau_{j,c}} \frac{(\frac{1}{4\tau_j^2}+\Delta^2)}{\left(\frac{1}{4\tau_j^2}+\Delta^2\right)^2 + 2\Gamma_2^2\left(\frac{1}{4\tau_j^2}-\Delta^2\right) + \Gamma_2^4} \tag{B.71}$$

$$|a_{-j}(t)|^2 \approx \frac{|s_L(z_0,t)|^2}{\tau_{j,c}} \frac{\Gamma_2^2}{\left(\frac{1}{4\tau_j^2}+\Delta^2\right)^2 + 2\Gamma_2^2\left(\frac{1}{4\tau_j^2}-\Delta^2\right)+\Gamma_2^4} \tag{B.72}$$

$$|s_L(z_1,t)|^2 \approx |s_L(z_0,t)|^2 \cdot \frac{\left(\frac{1}{4\tau_j^2}+\Delta^2\right)\left[(\frac{1}{2\tau_j}-\frac{1}{\tau_{j,c}})^2+\Delta^2\right]+\Gamma_2^2\left(\Gamma_2^2+2\left[\frac{1}{2\tau_j}(\frac{1}{2\tau_j}-\frac{1}{\tau_{j,c}})-\Delta^2\right]\right)}{\left(\frac{1}{4\tau_j^2}+\Delta^2\right)^2 + 2\Gamma_2^2\left(\frac{1}{4\tau_j^2}-\Delta^2\right)+\Gamma_2^4} \tag{B.73}$$

$$|s_{-L}(z_0,t)|^2 \approx \frac{|s_L(z_0,t)|^2}{\tau_{j,c}^2} \frac{\Gamma_2^2}{\left(\frac{1}{4\tau_j^2}+\Delta^2\right)^2 + 2\Gamma_2^2\left(\frac{1}{4\tau_j^2}-\Delta^2\right)+\Gamma_2^4} \tag{B.74}$$

In CW regime, the power conservation is written as

$$|s_L(z_0,t)|^2 = |s_L(z_1,t)|^2 + |s_{-L}(z_0,t)|^2 + \frac{1}{\tau_{j,0}}(|a_j(t)|^2 + |a_{-j}(t)|^2) \tag{B.75}$$

Unidirectional source, single mode waveguide and no modal coupling

Solutions are similar to previous Sections B.71 to B.74, but we set $\Gamma_{j-j} \rightarrow 0$ (or $\Gamma_2 \rightarrow 0$) :

$$|a_j(t)|^2 \approx \frac{|s_L(z_0,t)|^2}{\tau_{j,c}} \frac{1}{\frac{1}{4\tau_j^2}+[\omega_L-(\omega_j-\Gamma_{jj})]^2} \quad \text{et} \quad |a_{-j}(t)|^2 \approx 0, \tag{B.76}$$

$$|s_L(z_1,t)|^2 \approx |s_L(z_0,t)|^2 \frac{[\frac{1}{2\tau_j}-\frac{1}{\tau_{j,c}}]^2+[\omega_L-(\omega_j-\Gamma_{jj})]^2}{\frac{1}{4\tau_j^2}+[\omega_L-(\omega_j-\Gamma_{jj})]^2} \quad \text{et} \quad |s_{-L}(z_0,t)|^2 \approx 0. \tag{B.77}$$

In CW regime, the power conservation is written as

$$|s_L(z_0,t)|^2 = |s_L(z_1,t)|^2 + \frac{|a_j(t)|^2}{\tau_{j,0}} \tag{B.78}$$

B.2.2 Q-factors, transmission coefficient and intracavity power

Q-factor and Finesse

To compare different types of optical resonators, we often use two figures of merit that characterize their mode's resonances : the Q-factor $Q_{j,T}$ and the Finesse $\mathcal{F}$.

The Q-factor of an optical mode is proportional to the stored energy over the lost energy during one optical cycle $T_{\omega_j} = 2\pi/\omega_j$. It represents the number of optical cycles N_{ω_j} until the energy of its initial value falls off to e^{-1}.

The Finesse $\mathcal{F}$ is proportional to the stored energy over the lost energy during one resonator round-trip $T_{rt} = 2\pi m_j/\omega_j$. It represents the number of round-trips N_{rt} until the energy of its initial value falls off to e^{-1}.

For a mode with ω_j and m_j, we express both as

$$Q_{j,T} = 2\pi \frac{|a_j(t)|^2}{-\frac{\partial |a_j(t)|^2}{\partial t} T_{\omega_j}} = \omega_j \frac{|a_j(t)|^2}{-\frac{\partial |a_j(t)|^2}{\partial t}} \tag{B.79}$$

$$\mathcal{F} = 2\pi \frac{|a_j(t)|^2}{-\frac{\partial |a_j(t)|^2}{\partial t} T_{rt}} = \frac{\omega_j}{m_j} \frac{|a_j(t)|^2}{-\frac{\partial |a_j(t)|^2}{\partial t}} = \frac{Q_{j,T}}{m_j}. \tag{B.80}$$

Using $\frac{d|a_j|^2}{dt} = a_j \frac{da_j^*}{dt} + a_j^* \frac{da_j}{dt}$, Eq. B.59, and Eq. B.61, we have

$$Q_{j,T} = \omega_j \left(2\gamma_j + i\Gamma_2 \frac{[a_j a_{-j}^* - a_j^* a_{-j}]}{|a_j|^2} + \Gamma_2' \frac{[a_j a_{-j}^* + a_j^* a_{-j}]}{|a_j|^2} \right)^{-1} \tag{B.81}$$

$$= \omega_j \left(2\gamma_j + \frac{2[\gamma_j(\Gamma_2^2 - \Gamma_2'^2) - 2\Delta\Gamma_2\Gamma_2']}{\gamma_j^2 + \Delta^2} \right)^{-1} \tag{B.82}$$

$$Q_{j,T} \overset{\Delta=0}{\rightarrow} \frac{\omega_j}{2\gamma_j + \frac{2(\Gamma_2^2 - \Gamma_2'^2)}{\gamma_j}} = \frac{\omega_j}{2\Gamma_{jj}' + \frac{1}{\tau_j} + \frac{2(\Gamma_2^2 - \Gamma_2'^2)}{\gamma_j}} \tag{B.83}$$

In the literature, we often see a simpler case where $\Gamma_{jj}' = \Gamma_2 = \Gamma_2' = 0$ (i.e. no loss due to a perturbation) :

$$Q_{j,T} = \omega_j \frac{|a_j(t)|^2}{\left(\frac{1}{\tau_{j,0}} + \frac{1}{\tau_{j,c}}\right)|a_j(t)|^2} \qquad \Rightarrow \boxed{\frac{1}{Q_{j,T}} = \left(\frac{1}{\omega_j \tau_{j,0}} + \frac{1}{\omega_j \tau_{j,c}}\right) = \frac{1}{\omega_j \tau_j}} \tag{B.84}$$

$$\mathcal{F} = \frac{Q_{j,T}}{m_j} = \frac{\omega_j \tau_j}{m_j} \qquad \Rightarrow \boxed{F = \frac{N_\omega}{m_j} = N_{rt}} \tag{B.85}$$

If the input signal is blocked $|s_L(z_0, t)|^2 = 0$, the mode energy decreases as $|a_j(t)|^2 e^{-t/\tau_j}$.

We can also rewrite the intrinsic photon's lifetime $\tau_{j,0}$ as different loss processes :

$$\frac{1}{\tau_j} = \frac{1}{\tau_{\mathrm{j,c}}} + \frac{1}{\tau_{\mathrm{j,0}}} \tag{B.86}$$

$$= \frac{1}{\tau_{\mathrm{j,c}}} + \frac{1}{\tau_{\mathrm{j,abs}}} + \frac{1}{\tau_{\mathrm{j,diff}}} + \frac{1}{\tau_{\mathrm{j,rad}}} + \dots \tag{B.87}$$

$$\frac{1}{Q_{j,T}} = \frac{1}{Q_{\mathrm{j,c}}} + \frac{1}{Q_{\mathrm{j,0}}} \tag{B.88}$$

$$= \frac{1}{Q_{\mathrm{j,c}}} + \frac{1}{Q_{\mathrm{j,abs}}} + \frac{1}{Q_{\mathrm{j,diff}}} + \frac{1}{Q_{\mathrm{j,rad}}} + \dots \tag{B.89}$$

where $Q_{j,c}$ is the *coupling (or extrinsic) Q-factor* of the mode j and $Q_{j,0}$ is the *intrinsic Q-factor*. $Q_{j,T}$ is the *total Q-factor*. It can also be written as the *loaded Q-factor* Q_L, that implies a "loading" from an external coupling like a waveguide. When the mode j is implicit, these Q-factors are usually rewritten as Q_T, Q_c, Q_0, etc.

As radiative tunneling is usually negligible, the intrinsic Q-factor upper limit is set by the material absorption and Rayleigh scattering. Using B.45 and $\mathrm{Im}(\epsilon_r) \approx 2n_c n_c' = \frac{n_0 \alpha_{lin}}{k_j}$, we get

$$\frac{1}{2\tau_{j,0}} = \frac{\omega_j}{2Q_{j,0}} \approx \frac{\omega_j}{2k_j} \frac{\int_V n_c \alpha_{lin} |\mathbf{e}_j|^2 dV}{\int_V n_0^2|_c |\mathbf{e}_j|^2 dV} \approx \frac{\omega_j \alpha_{lin}}{2n_c k_j} \quad \Rightarrow \quad Q_{j,0} = \frac{k_j n_c}{\alpha_{lin}} = \frac{2\pi n_c}{\lambda_j \alpha_{lin}}$$

where n_c is the cavity's material refractive index, and considering that $\mathbf{e}_j$ is much larger inside the cavity. This last $Q_{j,0}$ definition is often seen in literature [1, 24].

Normalized transmission coefficient

To obtain $Q_{j,0}$ and $Q_{j,c}$, we need to measure the normalized transmission coefficient T_j at $\Delta = \omega_L - (\omega_j - \Gamma_{jj}) = 0$ and the total Q-factor $Q_{j,T}$. The former is written using Relations B.73, B.87 and B.89 :

$$T_j = \frac{|s_L(z_1,t)|^2}{|s_L(z_0,t)|^2} = \frac{\left(\frac{1}{4\tau_j^2} + \Delta^2\right)\left[(\frac{1}{2\tau_j} - \frac{1}{\tau_{j,c}})^2 + \Delta^2\right] + \Gamma_2^2\left(\Gamma_2^2 + 2\left[\frac{1}{2\tau_j}(\frac{1}{2\tau_j} - \frac{1}{\tau_{j,c}}) - \Delta^2\right]\right)}{\left(\frac{1}{4\tau_j^2} + \Delta^2\right)^2 + 2\Gamma_2^2\left(\frac{1}{4\tau_j^2} - \Delta^2\right) + \Gamma_2^4} \tag{B.90}$$

leading to, for $|\Gamma_2|^2 \to 0$,

$$T_j = \frac{|s_L(z_1,t)|^2}{|s_L(z_0,t)|^2} = \frac{(\frac{1}{2\tau_j} - \frac{1}{\tau_{j,c}})^2 + \Delta^2}{\frac{1}{4\tau_j^2} + \Delta^2}$$

$$\Rightarrow \; T_{j,0} = \frac{|s_L(z_1,t)|^2}{|s_L(z_0,t)|^2}|_{\omega_L=\omega_j-\Gamma_{jj}} = 4\tau_j^2\left(\frac{1}{2\tau_j}-\frac{1}{\tau_{j,c}}\right)^2$$
$$\Rightarrow \; T_{j,0} = \left(\frac{\tau_{j,c}-\tau_{j,0}}{\tau_{j,c}+\tau_{j,0}}\right)^2 = \left(\frac{Q_c-Q_0}{Q_c+Q_0}\right)^2 = \left(\frac{1-K}{1+K}\right)^2 \quad \text{for} \quad K=\frac{Q_0}{Q_c} \tag{B.91}$$

where K is defined as the normalized coupling constant [36]. It indicates which loss process is larger. The normalized transmission coefficient, T_j, is bounded between 0 and 1.

The total Q-factor can be measured using the resonance's spectral full width at half maximum (FWHM), $\Delta\omega_j$, where $|s_L(z_1,t)|^2/|s_L(z_0,t)|^2 = (1+T_{j,0})/2$:

$$\frac{1+T_{j,0}}{2} = \frac{(\omega_{\text{FWHM}}-\omega_j)^2+(\frac{1}{\tau_{j,c}}-\frac{1}{2\tau_j})^2}{(\omega_{\text{FWHM}}-\omega_j)^2+(\frac{1}{2\tau_j})^2} \Rightarrow (\omega_{\text{FWHM}}-\omega_j)^2 = \frac{-2}{1-T_{j,0}}\left(\frac{1}{\tau_{j,c}^2}-\frac{1}{\tau_j\tau_{j,c}}\right)-\left(\frac{1}{2\tau_j}\right)^2$$
$$\Rightarrow (\omega_{\text{FWHM}}-\omega_j) = \frac{1}{4\tau_j^2} = \frac{1}{2\tau_j}$$
$$\Rightarrow \Delta\omega_j = \frac{1}{\tau_j}$$
$$\Rightarrow Q_{j,T} = \frac{\omega_j}{\Delta\omega_j} = \frac{-\lambda_j}{\Delta\lambda_j}. \tag{B.92}$$

This is not surprising since the resonance is a Lorentzian curve, i.e. the frequency Fourier transform of a decaying exponential curve in time. It is important to note that only a Lorentzian curve can be characterized using its FWHM value. When there is mode coupling or any resonance's asymmetry, numerical fits are preferred.

Once $T_{j,0}$ and $Q_{j,T}$ are known, it is possible to retrieve $Q_{j,0}$ and $Q_{j,c}$ except for one detail : since B.91 is symmetric, we do not know which is larger. We get

$$Q_{j,c} = \frac{2Q_{j,T}}{1\pm\sqrt{T_{j,0}}} \quad \text{et} \quad Q_{j,0} = \frac{2Q_{j,T}}{1\mp\sqrt{T_{j,0}}} \tag{B.93}$$

where the upper and lower signs correspond to the *overcoupled regime* and *undercoupled regime*. It is possible to change the coupling conditions to solve this issue. It is also possible to use a technique developed during the master's thesis based on a Stokes parameters measurement [241].

Intracavity power and accumulation factor

The energy stored in a high Q-factor cavity can be very large and it leads to large intracavity circulating power. Using Relation B.23 for a first radial order mode of a microsphere, we have

$$P_j(t) = \frac{\frac{n_{eff}^2}{n_c^2}|a_j(t)|^2}{T_t} = \frac{n_{eff}^2}{n_c^2}\frac{\omega_j}{2\pi m_j}|a_j(t)|^2.$$

An explicit expression is found, for a simple case where $\Gamma_1' = \Gamma_2' = 0$, using Relation B.71 :

$$P_j(t) = \frac{n_{eff}^2}{n_c^2}\frac{\omega_j}{2\pi m_j}\frac{|s_L(z_0,t)|^2}{\tau_{j,c}}\frac{(\frac{1}{4\tau_j^2}+\Delta^2)}{\left(\frac{1}{4\tau_j^2}+\Delta^2\right)^2 + 2\Gamma_2^2\left(\frac{1}{4\tau_j^2}-\Delta^2\right)+\Gamma_2^4}$$

$$P_j(t)_{\omega_L=\omega_j-\Gamma_{jj}} = \frac{n_{eff}^2}{n_c^2}\frac{\omega_j}{2\pi m_j}\frac{|s_L(z_0,t)|^2}{\tau_{j,c}}\frac{1}{4\tau_j^2}\frac{1}{\left[\frac{1}{4\tau_j^2}+\Gamma_2^2\right]^2}$$

decreased by the counterclockwise mode coupling rate. In a case where it is negligible ($\Gamma_2 \to 0$), we get the accumulation factor

$$\Upsilon_j = \frac{P_j(t)}{|s_L(z_0,t)|^2} = \frac{n_{eff}^2}{n_c^2}\frac{2\omega_j}{\pi m_j}\frac{\tau_j^2}{\tau_{j,c}} = \frac{n_{eff}^2}{n_c^2}\frac{2}{\pi m_j}\frac{Q_{j,T}^2}{Q_{j,c}}. \tag{B.94}$$

Using $m_j = \omega_j n_{\text{eff}} R_c/c = 2\pi n_{\text{eff}} R_c/\lambda_j$ and Relation B.88, we get

$$\Upsilon_j = \frac{\lambda_j^2 m_j}{2\pi^3 n_c^2 R_c^2}\frac{Q_{j,T}^2}{Q_{j,c}} = \frac{\lambda_j n_{\text{eff}}}{\pi^2 n_c^2 R_c}Q_{j,c}\left(1+\frac{Q_{j,c}}{Q_{j,0}}\right)^{-2},$$

similar to what is seen in literature [285]. For a typical high Q-factor cavity, $Q_{j,T} \sim Q_{j,c}/2 = 10^6$, $\lambda_j = 1550$ nm, $R_c = 20$ μm and $m_j = 100$, we have $\Upsilon_j > 2300$. This means that a 1 mW signal leads to an intracavity power of 2.3 W and an intensity > 11 MW/cm^2 considering a mode area of 20 μm^2. This shows why WGM microcavities are often used as low pump power nonlinear sources.

B.3 Eigenmodes of a microsphere

The previous sections show the coupled-modes theory for linear and nonlinear interactions. These descriptions rely on coupling constants based on overlap integrals of the different optical fields involed. These optical fields are solutions of the homogeneous vectorial wave equation for the cavity B.33 and the waveguide B.34. The solutions are called the eigenmodes. It is easier to deal with coupling constants instead of fields because the vectorial solutions are usually not known analytically for many types of WGM structure such as disks or rings.

In the case of microspheres, the vectorial solutions are known and are described in many references with different approximations and different notations [7, 15, 20, 21, 49] [2]. The solutions are written for the spherical coordinates (ρ, θ, ϕ) shown in Fig. B.3 and have the following form [7]

$$\mathbf{E}_j(\mathbf{r}, t) = \frac{a_j(t) e^{-i\omega_j t} \mathbf{e}_j(\mathbf{r})}{2\sqrt{N_j}} + \text{c.c.}$$

$$\mathbf{e}_j(\mathbf{r}) = \left[e_\rho(\rho, \theta, \phi)\hat{\rho} + e_\theta(\rho, \theta, \phi)\hat{\theta} + e_\phi(\rho, \theta, \phi)\hat{\phi} \right]$$

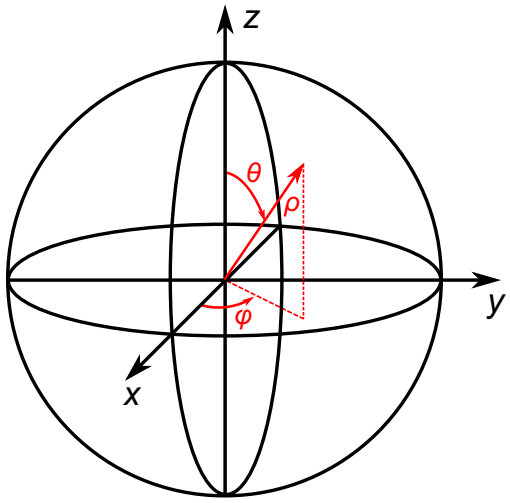

Figure B.3 : Spherical coordinates.

2. The solutions found in these references are not consistent even if they are referencing each other. The solutions presented here are based only on [7] and really satisfy Eq. B.33

B.3.1 TE solutions

For the transverse-electric solutions (TE modes), we have :

Inside TE $(0 < \rho < R_c, n_0 = n_c)$

$$e_\rho^{IN}(\rho,\theta,\phi) = 0$$

$$e_\theta^{IN}(\rho,\theta,\phi) = i\sqrt{\frac{\pi}{2}} m_j e^{im_j\phi} \left[\frac{J_{l_j+1/2}(n_c k_j \rho)}{\sqrt{n_c k_j \rho}}\right] \left[\frac{P_{l_j}^{m_j}(\cos(\theta))}{\sin(\theta)}\right]$$

$$e_\phi^{IN}(\rho,\theta,\phi) = \sqrt{\frac{\pi}{2}} e^{im_j\phi} \left[\frac{J_{l_j+1/2}(n_c k_j \rho)}{\sqrt{n_c k_j \rho}}\right] \left[\frac{[l_j+1]\cos(\theta) P_{l_j}^{m_j}(\cos(\theta)) - [l_j - m_j + 1] P_{l_j+1}^{m_j}(\cos(\theta))}{\sin(\theta)}\right]$$

$$h_\rho^{IN}(\rho,\theta,\phi) = -i\sqrt{\frac{\pi}{2}} \frac{e^{im_j\phi}}{\mu_0 \omega_j} \left[\frac{l_j(l_j+1)}{\rho\sqrt{n_c k_j \rho}} J_{l_j+1/2}(n_c k_j \rho)\right] P_{l_j}^{m_j}(\cos(\theta))$$

$$h_\theta^{IN}(\rho,\theta,\phi) = i\sqrt{\frac{\pi}{2}} \frac{e^{im_j\phi}}{\mu_0 \omega_j} \left[\sqrt{\frac{n_c k_j}{\rho}} J_{l_j-1+1/2}(n_c k_j \rho) - \frac{l_j}{\rho} \frac{J_{l_j+1/2}(n_c k_j \rho)}{\sqrt{n_c k_j \rho}}\right] \times \left[\frac{[l_j - m_j + 1] P_{l_j+1}^{m_j}(\cos(\theta)) - [l_j+1]\cos(\theta) P_{l_j}^{m_j}(\cos(\theta))}{\sin(\theta)}\right]$$

$$h_\phi^{IN}(\rho,\theta,\phi) = i\sqrt{\frac{\pi}{2}} \frac{m_j e^{im_j\phi}}{\mu_0 \omega_j} \left[\sqrt{\frac{n_c k_j}{\rho}} J_{l_j-1+1/2}(n_c k_j \rho) - \frac{l_j}{\rho} \frac{J_{l_j+1/2}(n_c k_j \rho)}{\sqrt{n_c k_j \rho}}\right] \left[\frac{P_{l_j}^{m_j}(\cos(\theta))}{\sin(\theta)}\right]$$

Outside TE $(0 < \rho < R_c, n_0 = n_c)$

$$e_\rho^{OUT}(\rho,\theta,\phi) = 0$$

$$e_\theta^{OUT}(\rho,\theta,\phi) = i\sqrt{\frac{\pi}{2}} m_j e^{im_j\phi} C_j^{TE} \left[\frac{H_{l_j+1/2}^{(1)}(n_a k_j \rho)}{\sqrt{n_a k_j \rho}}\right] \left[\frac{P_{l_j}^{m_j}(\cos(\theta))}{\sin(\theta)}\right]$$

$$e_\phi^{OUT}(\rho,\theta,\phi) = \sqrt{\frac{\pi}{2}} e^{im_j\phi} C_j^{TE} \left[\frac{H_{l_j+1/2}^{(1)}(n_a k_j \rho)}{\sqrt{n_a k_j \rho}}\right] \times \left[\frac{[l_j+1]\cos(\theta) P_{l_j}^{m_j}(\cos(\theta)) - [l_j - m_j + 1] P_{l_j+1}^{m_j}(\cos(\theta))}{\sin(\theta)}\right]$$

$$h_\rho^{OUT}(\rho,\theta,\phi) = -i\sqrt{\frac{\pi}{2}} \frac{e^{im_j\phi}}{\mu_0 \omega_j} C_j^{TE} \left[\frac{l_j(l_j+1)}{\rho\sqrt{n_c k_j \rho}} J_{l_j+1/2}(n_c k_j \rho)\right] P_{l_j}^{m_j}(\cos(\theta))$$

$$h_\theta^{OUT}(\rho,\theta,\phi) = i\sqrt{\frac{\pi}{2}} \frac{e^{im_j\phi}}{\mu_0 \omega_j} C_j^{TE} \left[\sqrt{\frac{n_c k_j}{\rho}} H_{l_j-1+1/2}^{(1)}(n_a k_j \rho) - \frac{l_j}{\rho} \frac{H_{l_j+1/2}^{(1)}(n_a k_j \rho)}{\sqrt{n_c k_j \rho}}\right] \times$$

$$\left[\frac{[l_j - m_j + 1]P_{l_j+1}^{m_j}(\cos(\theta)) - [l_j + 1]\cos(\theta)P_{l_j}^{m_j}(\cos(\theta))}{\sin(\theta)}\right]$$

$$h_\phi^{OUT}(\rho,\theta,\phi) = i\sqrt{\frac{\pi}{2}}\frac{m_j e^{im_j\phi}}{\mu_0\omega_j}C_j^{TE}\left[\sqrt{\frac{n_c k_j}{\rho}}H_{l_j-1+1/2}^{(1)}(n_a k_j\rho) - \frac{l_j}{\rho}\frac{H_{l_j+1/2}^{(1)}(n_a k_j\rho)}{\sqrt{n_c k_j\rho}}\right]\left[\frac{P_{l_j}^{m_j}(\cos(\theta))}{\sin(\theta)}\right]$$

Inside-Outside continuity

$$C_j^{TE} = \sqrt{\frac{n_a}{n_c}}\frac{J_{l_j+1/2}(n_c k_j R_c)}{H_{l_j+1/2}^{(1)}(n_a k_j R_c)}$$

TE Characteristic equation

$$\frac{n_c}{n_a}\frac{J_{l_j-1+1/2}(n_c k_j R_c)}{J_{l_j+1/2}(n_c k_j R_c)} = \frac{H_{l_j-1+1/2}^{(1)}(n_a k_j R_c)}{H_{l_j+1/2}^{(1)}(n_a k_j R_c)}$$

where $P_l^m(x)$ are the associated Legendre polynomials, $J_{l_j+1/2}(x)$ is the Bessel function of the first kind and $H_{l_j+1/2}^{(1)}(x)$ is the Hankel function of the first kind [242]. The solutions explicitly show the coordinate separation in ρ, θ and ϕ functions. l_j and m_j are the polar and azimuthal integers numbers of the jth mode, in reference to the hydrogen atom solutions of the Schrödinger equation in quantum mechanics.

B.3.2 TM solutions

For the transverse-magnetic solutions (TM modes), we have :

Inside TM $(0 < \rho < R_c, n_0 = n_c)$

$$e_\rho^{IN}(\rho,\theta,\phi) = \sqrt{\frac{\pi}{2}}e^{im_j\phi}\left[\frac{l_j(l_j+1)}{(n_c k_j\rho)^{3/2}}J_{l_j+1/2}(n_c k_j\rho)\right]P_{l_j}^{m_j}(\cos(\theta))$$

$$e_\theta^{IN}(\rho,\theta,\phi) = \sqrt{\frac{\pi}{2}}e^{im_j\phi}\left[\frac{J_{l_j-1+1/2}(n_c k_j\rho)}{\sqrt{n_c k_j\rho}} - \frac{l_j}{(n_c k_j\rho)^{3/2}}J_{l_j+1/2}(n_c k_j\rho)\right]\times$$
$$\left[\frac{[l_j - m_j + 1]P_{l_j+1}^{m_j}(\cos(\theta)) - [l_j + 1]\cos(\theta)P_{l_j}^{m_j}(\cos(\theta))}{\sin(\theta)}\right]$$

$$e_\phi^{IN}(\rho,\theta,\phi) = i\sqrt{\frac{\pi}{2}}m_j e^{im_j\phi}\left[\frac{J_{l_j-1+1/2}(n_c k_j\rho)}{\sqrt{n_c k_j\rho}} - \frac{l_j}{(n_c k_j\rho)^{3/2}}J_{l_j+1/2}(n_c k_j\rho)\right]\left[\frac{P_{l_j}^{m_j}(\cos(\theta))}{\sin(\theta)}\right]$$

$$h_\rho^{IN}(\rho,\theta,\phi) = 0$$

$$h_\theta^{IN}(\rho,\theta,\phi) = \sqrt{\frac{\pi}{2}}\frac{m_j e^{im_j\phi}}{\mu_0\omega_j}\left[\sqrt{\frac{n_c k_j}{\rho}}J_{l_j+1/2}(n_c k_j\rho)\right]\left[\frac{P_{l_j}^{m_j}(\cos(\theta))}{\sin(\theta)}\right]$$

$$h_\phi^{IN}(\rho,\theta,\phi) = i\sqrt{\frac{\pi}{2}}\frac{e^{im_j\phi}}{\mu_0\omega_j}\left[\sqrt{\frac{n_c k_j}{\rho}}J_{l_j+1/2}(n_c k_j\rho)\right]\times$$

$$\left[\frac{[l_j - m_j + 1]P_{l_j+1}^{m_j}(\cos(\theta)) - [l_j + 1]\cos(\theta)P_{l_j}^{m_j}(\cos(\theta))}{\sin(\theta)}\right]$$

Outside TM $(0 < \rho < R_c, n_0 = n_c)$

$$e_\rho^{OUT}(\rho,\theta,\phi) = \sqrt{\frac{\pi}{2}}e^{im_j\phi}C_j^{TM}\left[\frac{l_j(l_j+1)}{(n_ak_j\rho)^{3/2}}H_{l_j+1/2}^{(1)}(n_ak_j\rho)\right]P_{l_j}^{m_j}(\cos(\theta))$$

$$e_\theta^{OUT}(\rho,\theta,\phi) = \sqrt{\frac{\pi}{2}}e^{im_j\phi}C_j^{TM}\left[\frac{H_{l_j-1+1/2}^{(1)}(n_ak_j\rho)}{\sqrt{n_ak_j\rho}} - \frac{l_j}{(n_ak_j\rho)^{3/2}}H_{l_j+1/2}^{(1)}(n_ak_j\rho)\right]\times$$
$$\left[\frac{[l_j - m_j + 1]P_{l_j+1}^{m_j}(\cos(\theta)) - [l_j + 1]\cos(\theta)P_{l_j}^{m_j}(\cos(\theta))}{\sin(\theta)}\right]$$

$$e_\phi^{OUT}(\rho,\theta,\phi) = i\sqrt{\frac{\pi}{2}}m_je^{im_j\phi}C_j^{TM}\left[\frac{H_{l_j-1+1/2}^{(1)}(n_ak_j\rho)}{\sqrt{n_ak_j\rho}} - \frac{l_j}{(n_ak_j\rho)^{3/2}}H_{l_j+1/2}^{(1)}(n_ak_j\rho)\right]\left[\frac{P_{l_j}^{m_j}(\cos(\theta))}{\sin(\theta)}\right]$$

$$h_\rho^{OUT}(\rho,\theta,\phi) = 0$$

$$h_\theta^{OUT}(\rho,\theta,\phi) = \sqrt{\frac{\pi}{2}}\frac{m_je^{im_j\phi}}{\mu_0\omega_j}C_j^{TM}\left[\sqrt{\frac{n_ak_j}{\rho}}H_{l_j+1/2}^{(1)}(n_ak_j\rho)\right]\left[\frac{P_{l_j}^{m_j}(\cos(\theta))}{\sin(\theta)}\right]$$

$$h_\phi^{OUT}(\rho,\theta,\phi) = i\sqrt{\frac{\pi}{2}}\frac{e^{im_j\phi}}{\mu_0\omega_j}C_j^{TM}\left[\sqrt{\frac{n_ak_j}{\rho}}H_{l_j+1/2}^{(1)}(n_ak_j\rho)\right]\times$$
$$\left[\frac{[l_j - m_j + 1]P_{l_j+1}^{m_j}(\cos(\theta)) - [l_j + 1]\cos(\theta)P_{l_j}^{m_j}(\cos(\theta))}{\sin(\theta)}\right]$$

Inside-Outside continuity

$$C_j^{TM} = \left(\frac{n_a}{n_c}\right)^{3/2}\frac{n_ck_jR_cJ_{l_j-1+1/2}(n_ck_jR_c) - l_jJ_{l_j+1/2}(n_ck_jR_c)}{n_ak_jR_cH_{l_j-1+1/2}^{(1)}(n_ak_jR_c) - l_jH_{l_j+1/2}^{(1)}(n_ak_jR_c)}$$

TM Characteristic equation

$$\frac{1}{n_c}\frac{J_{l_j-1+1/2}(n_ck_jR_c)}{J_{l_j+1/2}(n_ck_jR_c)} - \frac{1}{n_a}\frac{H_{l_j-1+1/2}^{(1)}(n_ak_jR_c)}{H_{l_j+1/2}^{(1)}(n_ak_jR_c)} = \frac{l_j}{k_jR_c}\left(\frac{1}{n_c^2} - \frac{1}{n_a^2}\right)$$

The characteristic equations solutions $k_j = 2\pi/\lambda_j$ are found by matching the field components at the sphere surface :

$$\hat{n}\cdot(n_c^2\mathbf{E_c}) = \hat{n}\cdot(n_a^2\mathbf{E_a}) \text{ and } \hat{n}\cdot\mathbf{H_c} = \hat{n}\cdot\mathbf{H_a} \qquad \text{parallel fields}$$
$$\hat{n}\wedge\mathbf{E_c} = \hat{n}\wedge\mathbf{E_a} \text{ and } \hat{n}\wedge\mathbf{H_c} = \hat{n}\wedge\mathbf{H_a} \qquad \text{perpendicular fields}$$

with $\hat{n}$ an unitary vector on the sphere surface pointing outside.

B.4 Explicit Raman scattering coupled-modes theory in WGM microcavities

B.4.1 Raman scattering

Raman scattering comes from the inelastic scattering of an optical signal's photon and a material's phonon. Figure B.4 shows the energy transfer of two processes. The incoming photon with an energy $\hbar\omega_p$ loses an energy quanta $\hbar\Omega_v$ to the material's lattice. The outgoing Stokes photon has residual energy $\hbar\omega_s < \hbar\omega_p$. When the incoming photon gains an energy quanta from the lattice, the outgoing photon (anti-Stokes) goes out with an energy $\hbar\omega_a > \hbar\omega_p$. It is possible to describe these processes classically and integrate them inside the previous coupled-modes equations. This section is based on [243, 244].

The material is viewed as diatomic molecules that vibrate with a frequency Ω_v. The distance between atoms, from their equilibrium positions, is described by the vector $\mathbf{Q}_v(\mathbf{r}, t)$ following the definition in [243]. The material's polarizability α - not to be confused with the linear absorption - quantifies its reaction to an external optical field. In linear optics, the sole contribution from the electron α_{el}, linked to $\chi^{(1)}$, is usually considered. Here, we will also consider the nucleus contribution when it moves out of his equilibrium position. Its contribution is added using a linear expansion :

$$\alpha = \alpha_{el} + \sum_i \left(\frac{\partial \alpha}{\partial Q_{v,i}}\right)_0 Q_{v,i}(\mathbf{r}, t) \;\rightarrow\; \alpha_{el} + \left(\frac{\partial \alpha}{\partial Q_v}\right)_0 Q_v(\mathbf{r}, t)$$

where we summed the ith vector component. To simplify, we can consider that the molecule oscillates along one direction, parallel with the external electric field. The polarizability is now scalar.

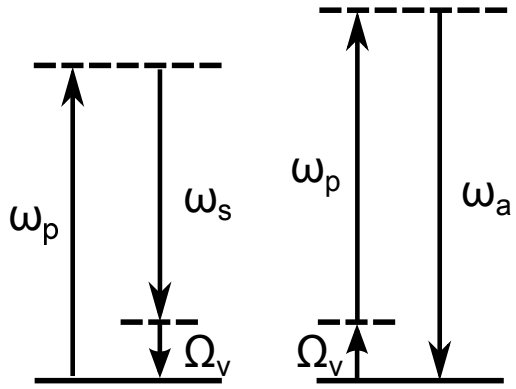

Figure B.4 : Stokes photon $\hbar\omega_s$ and anti-Stokes photon $\hbar\omega_a$ creation through Raman scattering of a pump signal photon $\hbar\omega_p$.

A vibration wave of frequency ω_v generated by an electric field $\mathbf{E}(\mathbf{r},t)$ follows [243, 244]

$$\beta_v \nabla^2 Q_v(\mathbf{r},t) + \frac{\mathrm{d}^2}{\mathrm{d}t^2} Q_v(\mathbf{r},t) + 2\Gamma_v \frac{\mathrm{d}}{\mathrm{d}t} Q_v(\mathbf{r},t) + \Omega_v^2 Q_v(\mathbf{r},t) = N \left(\frac{\partial \alpha}{\partial Q_v} \right)_0 \mathbf{E}^2(\mathbf{r},t) \tag{B.95}$$

where β_v quantifies the wave dispersion, Γ_v quantifies the wave attenuation and Ω_v is the natural vibration frequency of the material. This equation's solution is written as Eq. B.1

$$Q_v(\mathbf{r},t) = \frac{q_v(\mathbf{r},t) e^{i\mathbf{k}_v \cdot \mathbf{r} - i\omega_v t}}{2} + \text{c.c.}$$

where $q_v(\mathbf{r},t)$ represents slow variations. It depends on the source term $\propto \mathbf{E}^2$. Any normalization factor is set to unity as it does not affect further developments. The solution of Eq. B.95 is approximated by

$$-\beta_v k_v^2 - \omega_v^2 Q_v(\mathbf{r},t) - i2\omega_v \Gamma_v Q_v(\mathbf{r},t) + \Omega_v^2 Q_v(\mathbf{r},t) = N \left(\frac{\partial \alpha}{\partial Q_v} \right)_0 \mathbf{E}^2(\mathbf{r},t) \tag{B.96}$$

leading to

$$Q_v(\mathbf{r},t) = \frac{q_v(\mathbf{r},t) e^{i\mathbf{k}_v \cdot \mathbf{r} - i\omega_v t}}{2} + \text{c.c.} = \frac{N \left(\frac{\partial \alpha}{\partial Q_v} \right)_0 \mathbf{E}^2(\mathbf{r},t)}{\Omega_v^2 - \beta_v k_v^2 - \omega_v^2 - i2\omega_v \Gamma_v} = N \left(\frac{\partial \alpha}{\partial Q_v} \right)_0 f_v(\omega_v) \mathbf{E}^2(\mathbf{r},t) \tag{B.97}$$

With modal coupling, the pump p, the Stokes s and the anti-Stokes a optical waves are represented by $\mathbf{E}_p$, $\mathbf{E}_{-p}$, $\mathbf{E}_s$, $\mathbf{E}_{-s}$, $\mathbf{E}_a$ and $\mathbf{E}_{-a}$. Using the solution form B.1, we have

$$\mathbf{E}^2 \propto (\mathbf{e}_p + \mathbf{e}_{-p} + \mathbf{e}_s + \mathbf{e}_{-s} + \mathbf{e}_a + \mathbf{e}_{-a} + \text{c.c.})^2.$$

Following energy conservation and phase matching conditions, we have $\omega_v = \omega_p - \omega_s = \omega_a - \omega_p = \sqrt{\Omega_v^2 - \beta_v k_v^2}$ and $\mathbf{k}_v = \mathbf{k}_p - \mathbf{k}_s = \mathbf{k}_a - \mathbf{k}_p$ where $\mathbf{k}_{p,s,a}$ are the optical modes wave vectors. Raman scattering implies the optical phonons. Their dispersion is usually considered constant for any k_v, leading to $\Omega_v >> \beta_v k_v^2$ and $\sqrt{\Omega_v^2 - \beta_v k_v^2} \approx \Omega_v$. This reveals the existence of waves with frequency Ω_v and $\mathbf{k}_v = \mathbf{k}_p \mp \mathbf{k}_s = \mathbf{k}_a \mp \mathbf{k}_p$ [243]. For a pump signal propagating in a clockwise direction $\mathbf{k}_p$, there are two Stokes and anti-Stokes signals propagating in the clockwise and counterclockwise direction.

The explicit formulation of B.97 is

$$Q_v(\mathbf{r},t) = N \left(\frac{\partial \alpha}{\partial Q_v} \right)_0 \times \tag{B.98}$$

$$\Bigg(\frac{f_v(\omega_p-\omega_s)e^{-i(\omega_p-\omega_s)t}}{2\sqrt{N_pN_s}}\times$$
$$\Big[a_p(t)a_s^*(t)\mathbf{e}_p\mathbf{e}_s^* + a_p(t)a_{-s}^*(t)\mathbf{e}_p\mathbf{e}_{-s}^* + a_{-p}(t)a_s^*(t)\mathbf{e}_{-p}\mathbf{e}_s^* + a_{-p}(t)a_{-s}^*(t)\mathbf{e}_{-p}\mathbf{e}_{-s}^*\Big]$$
$$+\frac{f_v(-\omega_p+\omega_s)e^{+i(\omega_p-\omega_s)t}}{2\sqrt{N_pN_s}}\times$$
$$\Big[a_p^*(t)a_s(t)\mathbf{e}_p^*\mathbf{e}_s + a_p^*(t)a_{-s}(t)\mathbf{e}_p^*\mathbf{e}_{-s} + a_{-p}^*(t)a_s(t)\mathbf{e}_{-p}^*\mathbf{e}_s + a_{-p}^*(t)a_{-s}(t)\mathbf{e}_{-p}^*\mathbf{e}_{-s}\Big]$$
$$+\frac{f_v(\omega_a-\omega_p)e^{-i(\omega_a-\omega_p)t}}{2\sqrt{N_aN_p}}\times$$
$$\Big[a_a(t)a_p^*(t)\mathbf{e}_a\mathbf{e}_p^* + a_a(t)a_{-p}^*(t)\mathbf{e}_a\mathbf{e}_{-p}^* + a_{-a}(t)a_p^*(t)\mathbf{e}_{-a}\mathbf{e}_p^* + a_{-a}(t)a_{-p}^*(t)\mathbf{e}_{-a}\mathbf{e}_{-p}^*\Big]$$
$$+\frac{f_v(-\omega_a+\omega_p)e^{+i(\omega_a-\omega_p)t}}{2\sqrt{N_aN_p}}\times$$
$$\Big[a_a^*(t)a_p(t)\mathbf{e}_a^*\mathbf{e}_p + a_a^*(t)a_{-p}(t)\mathbf{e}_a^*\mathbf{e}_{-p} + a_{-a}^*(t)a_p(t)\mathbf{e}_{-a}^*\mathbf{e}_p + a_{-a}^*(t)a_{-p}(t)\mathbf{e}_{-a}^*\mathbf{e}_{-p}\Big]\Bigg)$$

The vibration $Q_v(\mathbf{r},t)$ influences the optical field through the polarizability and the electric polarization vector

$$\mathbf{P}(\mathbf{r},t) = N\alpha\mathbf{E} = N\left[\alpha_0 + \left(\frac{\partial\alpha}{\partial Q_v}\right)_0 Q_v(\mathbf{r},t)\right]\mathbf{E}(\mathbf{r},t) = \underbrace{\epsilon_0\chi^{(1)}\mathbf{E}(\mathbf{r},t)}_{\mathbf{P}^{(1)}(\mathbf{r},t)} + \underbrace{N\left(\frac{\partial\alpha}{\partial Q_v}\right)_0 Q_v(\mathbf{r},t)\mathbf{E}(\mathbf{r},t)}_{\mathbf{P}_{Raman}(\mathbf{r},t)}.$$

It splits into a linear part $\mathbf{P}^{(1)}(\mathbf{r},t)$ and the nonlinear part of Raman scattering $\mathbf{P}_{Raman}(\mathbf{r},t)$. Following the energy conservation and the phase matching conditions, we get

$$\mathbf{P}_{Raman}(\mathbf{r},t) = \tag{B.99}$$
$$\Bigg(e^{-i\omega_pt}a_p(t)\mathbf{e}_p\times$$
$$\left[\frac{F_{p-s}|a_s(t)|^2|\mathbf{e}_s|^2}{4N_s\sqrt{N_p}} + \frac{F_{p-s}|a_{-s}(t)|^2|\mathbf{e}_{-s}|^2}{4N_s\sqrt{N_p}} + \frac{F_{p-a}|a_a(t)|^2|\mathbf{e}_a|^2}{4N_a\sqrt{N_p}} + \frac{F_{p-a}|a_{-a}(t)|^2|\mathbf{e}_{-a}|^2}{4N_a\sqrt{N_p}}\right]$$
$$+e^{-i\omega_pt}a_{-p}(t)\mathbf{e}_{-p}\times$$
$$\left[\frac{F_{p-s}|a_s(t)|^2|\mathbf{e}_s|^2}{4N_s\sqrt{N_p}} + \frac{F_{p-s}|a_{-s}(t)|^2|\mathbf{e}_{-s}|^2}{4N_s\sqrt{N_p}} + \frac{F_{p-a}|a_a(t)|^2|\mathbf{e}_a|^2}{4N_a\sqrt{N_p}} + \frac{F_{p-a}|a_{-a}(t)|^2|\mathbf{e}_{-a}|^2}{4N_a\sqrt{N_p}}\right]$$
$$+e^{-i(\omega_s+\omega_a-\omega_p)t}\times$$

$$
\left[(F_{s-p}+F_{a-p})\frac{a_p^*(t)a_a(t)a_s(t)\mathbf{e}_p^*\mathbf{e}_a\mathbf{e}_s}{4\sqrt{N_pN_sN_a}}+(F_{s-p}+F_{a-p})\frac{a_{-p}^*(t)a_{-a}(t)a_{-s}(t)\mathbf{e}_{-p}^*\mathbf{e}_{-a}\mathbf{e}_{-s}}{4\sqrt{N_pN_sN_a}}\right]
$$
$$
+e^{-i\omega_s t}a_s(t)\mathbf{e}_s\left[\frac{F_{s-p}|a_p(t)|^2|\mathbf{e}_p|^2}{4N_p\sqrt{N_s}}+\frac{F_{s-p}|a_{-p}(t)|^2|\mathbf{e}_{-p}|^2}{4N_p\sqrt{N_s}}\right]
$$
$$
+e^{-i\omega_s t}a_{-s}(t)\mathbf{e}_{-s}\left[\frac{F_{s-p}|a_p(t)|^2|\mathbf{e}_p|^2}{4N_p\sqrt{N_s}}+\frac{F_{s-p}|a_{-p}(t)|^2|\mathbf{e}_{-p}|^2}{4N_p\sqrt{N_s}}\right]
$$
$$
+e^{-i(2\omega_p-\omega_a)t}\left[\frac{F_{p-a}a_p^2(t)a_a^*(t)\mathbf{e}_p^2\mathbf{e}_a^*}{4N_p\sqrt{N_a}}+\frac{F_{p-a}a_{-p}^2(t)a_{-a}^*(t)\mathbf{e}_{-p}^2\mathbf{e}_{-a}^*}{4N_p\sqrt{N_a}}\right]
$$
$$
+e^{-i\omega_a t}a_a(t)\mathbf{e}_a\left[\frac{F_{a-p}|a_p(t)|^2|\mathbf{e}_p|^2}{4N_p\sqrt{N_a}}+\frac{F_{a-p}|a_{-p}(t)|^2|\mathbf{e}_{-p}|^2}{4N_p\sqrt{N_a}}\right]
$$
$$
+e^{-i\omega_a t}a_{-a}(t)\mathbf{e}_{-a}\left[\frac{F_{a-p}|a_p(t)|^2|\mathbf{e}_p|^2}{4N_p\sqrt{N_a}}+\frac{F_{a-p}|a_{-p}(t)|^2|\mathbf{e}_{-p}|^2}{4N_p\sqrt{N_a}}\right]
$$
$$
+e^{-i(2\omega_p-\omega_s)t}\left[\frac{F_{p-s}a_p^2(t)a_s^*(t)\mathbf{e}_p^2\mathbf{e}_s^*}{4N_p\sqrt{N_s}}+\frac{F_{p-s}a_{-p}^2(t)a_{-s}^*(t)\mathbf{e}_{-p}^2\mathbf{e}_{-s}^*}{4N_p\sqrt{N_s}}\right]\Bigg)
$$

where only the contributing terms are retained and where

$$
F_{i-j}=N^2\left(\frac{\partial\alpha}{\partial Q_v}\right)_0^2 f_{i-j}=N^2\left(\frac{\partial\alpha}{\partial Q_v}\right)_0^2\frac{1}{\Omega_v^2-(\omega_i-\omega_j)^2-i2(\omega_i-\omega_j)\Gamma_v}
$$
$$
=N^2\left(\frac{\partial\alpha}{\partial Q_v}\right)_0^2\frac{\Omega_v^2-(\omega_i-\omega_j)^2+i2(\omega_i-\omega_j)\Gamma_v}{[\Omega_v^2-(\omega_i-\omega_j)^2]^2+4(\omega_i-\omega_j)^2\Gamma_v^2}.
$$

F_{i-j} is important since it indicates whether there is attenuation or amplification. When $\pm\omega_p\mp\omega_s=\pm\Omega_v$ or $\pm\omega_a\mp\omega_p=\pm\Omega_v$, the real part of F_{i-j} is small compared to the imaginary part. We have attenuation for $\mathrm{Im}(F_{p-s}))>0$ or $\mathrm{Im}(F_{a-p}))>0$ and amplification for $\mathrm{Im}(F_{s-p}))<0$ or $\mathrm{Im}(F_{p-a}))<0$.

B.4.2 Coupled mode equations for stimulated Raman scattering emission

With the explicit form of $\mathbf{P}_{Raman}(\mathbf{r},t)$, we can rewrite Eq. B.35

$$
\sum_{l=p,s,a,-p,-s,-a}\frac{i\omega_l e^{-i\omega_l t}}{c^2\sqrt{N_l}}\frac{\partial a_l(t)}{\partial t}\epsilon_r(\mathbf{r})\mathbf{e}_l(\mathbf{r})+\frac{a_l(t)e^{-i\omega_l t}}{2c^2\sqrt{N_l}}[n_0^2|_g-n_a^2]\omega_l^2\mathbf{e}_l(\mathbf{r})
$$
$$
+\frac{a_l(t)e^{-i\omega_l t}}{2c^2\sqrt{N_l}}[\delta\epsilon(\mathbf{r})+i\mathrm{Im}(\epsilon_r)]\omega_l^2\mathbf{e}_l(\mathbf{r})
$$
$$
+\sum_L\frac{i\beta_L e^{-i\omega_L t}}{\sqrt{M_L}}\frac{\partial s_L(z,t)}{\partial z}\epsilon_r(\mathbf{r})\mathbf{e}_L(\mathbf{r})+\frac{s_L(z,t)e^{-i\omega_L t}}{2c^2\sqrt{M_L}}[n_0^2|_c-n_a^2]\omega_L^2\mathbf{e}_L(\mathbf{r})
$$
$$
+\frac{s_L(z,t)e^{-i\omega_L t}}{2c^2\sqrt{M_L}}[\delta\epsilon(\mathbf{r})+i\mathrm{Im}(\epsilon_r)]\omega_L^2\mathbf{e}_L(\mathbf{r})
\tag{B.100}
$$

$$= \mu_0 \frac{\partial^2}{\partial t^2} \left[\mathbf{P}_{Raman}(\mathbf{r}, t) \right]$$

Similarly to section B.1.4, we multiply by $\mathbf{e}^*_{(p,s,a)}(\mathbf{r})$ from the left and we integrate over a volume V. We then consider that nonlinear terms are slowly varying as

$$\frac{\partial^2}{\partial t^2} \left(a_s(t) a_a(t) a_p^*(t) e^{-i(\omega_s + \omega_a - \omega_p)t} \right) \sim -(\omega_s + \omega_a - \omega_p)^2 a_s(t) a_a(t) a_p^*(t) e^{-i(\omega_s + \omega_a - \omega_p)t}. \quad \text{(B.101)}$$

Using the coupling constants listed in Table B.2, coupled-modes equations for Stokes modes $a_{\pm s}(t)$ are

$$\begin{aligned}
\frac{\partial a_{\pm s}(t)}{\partial t} = & \left(i\Gamma_{\pm s \pm s} - \Gamma'_{\pm s \pm s} - \frac{1}{2\tau_{s,0}} - \frac{1}{2\tau_{s,c}} \right) a_{\pm s}(t) + \left(i\Gamma_{\pm s \mp s} - \Gamma'_{\pm s \mp s} \right) a_{\mp s}(t) \\
& + i\frac{1}{4} \omega_s \mu_0 c^2 |a_p(t)|^2 a_{\pm s}(t) \frac{\int_V F_{s-p} |\mathbf{e}_p|^2 |\mathbf{e}_{\pm s}|^2 dV}{N_p \int_V n_0^2|_c |\mathbf{e}_{\pm s}|^2 dV} \\
& + i\frac{1}{4} \omega_s \mu_0 c^2 |a_{-p}(t)|^2 a_{\pm s}(t) \frac{\int_V F_{s-p} |\mathbf{e}_{-p}|^2 |\mathbf{e}_{\pm s}|^2 dV}{N_s \int_V n_0^2|_c |\mathbf{e}_{\pm s}|^2 dV} \\
& + i\frac{1}{4} \frac{(2\omega_p - \omega_a)^2}{\omega_s} \mu_0 c^2 a_{\pm p}^2(t) a_{\pm a}^*(t) \frac{\sqrt{N_s}}{N_p \sqrt{N_a}} e^{-i(2\omega_p - \omega_a - \omega_s)t} \frac{\int_V F_{p-a} \mathbf{e}_{\pm p}^2 \mathbf{e}_{\pm a}^* \mathbf{e}_{\pm s}^* dV}{\int_V n_0^2|_c |\mathbf{e}_{\pm s}|^2 dV}.
\end{aligned}$$

For anti-Stokes modes $a_{\pm a}(t)$, we get

$$\begin{aligned}
\frac{\partial a_{\pm a}(t)}{\partial t} = & \left(i\Gamma_{\pm a \pm a} - \Gamma'_{\pm a \pm a} - \frac{1}{2\tau_{a,0}} - \frac{1}{2\tau_{a,c}} \right) a_{\pm a}(t) + \left(i\Gamma_{\pm a \mp a} - \Gamma'_{\pm a \mp a} \right) a_{\mp a}(t) \\
& + i\frac{1}{4} \omega_a \mu_0 c^2 |a_p(t)|^2 a_{\pm a}(t) \frac{\int_V F_{a-p} |\mathbf{e}_p|^2 |\mathbf{e}_{\pm a}|^2 dV}{N_p \int_V n_0^2|_c |\mathbf{e}_{\pm a}|^2 dV} \\
& + i\frac{1}{4} \omega_a \mu_0 c^2 |a_{-p}(t)|^2 a_{\pm a}(t) \frac{\int_V F_{a-p} |\mathbf{e}_{-p}|^2 |\mathbf{e}_{\pm a}|^2 dV}{N_s \int_V n_0^2|_c |\mathbf{e}_{\pm a}|^2 dV} \\
& + i\frac{1}{4} \frac{(2\omega_p - \omega_s)^2}{\omega_a} \mu_0 c^2 a_{\pm p}^2(t) a_{\pm s}^*(t) \frac{\sqrt{N_a}}{N_p \sqrt{N_s}} e^{-i(2\omega_p - \omega_a - \omega_s)t} \frac{\int_V F_{p-s} \mathbf{e}_{\pm p}^2 \mathbf{e}_{\pm s}^* \mathbf{e}_{\pm a}^* dV}{\int_V n_0^2|_c |\mathbf{e}_{\pm a}|^2 dV}.
\end{aligned}$$

Finally, for the pump modes $a_{\pm p}(t)$, we have

$$\begin{aligned}
\frac{\partial a_{\pm p}(t)}{\partial t} = & \left(i\Gamma_{\pm p \pm p} - \Gamma'_{\pm p \pm p} - \frac{1}{2\tau_{p,0}} - \frac{1}{2\tau_{p,c}} \right) a_{\pm p}(t) + \left(i\Gamma_{\pm p \mp p} - \Gamma'_{\pm p \mp p} \right) a_{\mp p}(t) \\
& + \sum_L i\kappa_{pL} s_L(z_0, t) e^{-i(\omega_L - \omega_p)t} \\
& + i\frac{1}{4} \omega_p \mu_0 c^2 |a_s(t)|^2 a_{\pm p}(t) \frac{\int_V F_{p-s} |\mathbf{e}_s|^2 |\mathbf{e}_{\pm p}|^2 dV}{N_s \int_V n_0^2|_c |\mathbf{e}_{\pm p}|^2 dV}
\end{aligned}$$

$$
\begin{aligned}
&+ i\frac{1}{4}\omega_p\mu_0 c^2|a_{-s}(t)|^2 a_{\pm p}(t)\frac{\int_V F_{p-s}|\mathbf{e}_{-s}|^2|\mathbf{e}_{\pm p}|^2 dV}{N_s\int_V n_0^2|_c|\mathbf{e}_{\pm p}|^2 dV}\\
&+ i\frac{1}{4}\omega_p\mu_0 c^2|a_a(t)|^2 a_{\pm p}(t)\frac{\int_V F_{p-a}|\mathbf{e}_a|^2|\mathbf{e}_{\pm p}|^2 dV}{N_a\int_V n_0^2|_c|\mathbf{e}_{\pm p}|^2 dV}\\
&+ i\frac{1}{4}\omega_p\mu_0 c^2|a_{-a}(t)|^2 a_{\pm p}(t)\frac{\int_V F_{p-a}|\mathbf{e}_{-a}|^2|\mathbf{e}_{\pm p}|^2 dV}{N_a\int_V n_0^2|_c|\mathbf{e}_{\pm p}|^2 dV}\\
&+ i\frac{1}{4}\frac{(\omega_s+\omega_a-\omega_p)^2}{\omega_p}\mu_0 c^2 a_{\pm s}(t)a_{\pm a}(t)a^*_{\pm p}(t)\frac{e^{-i(\omega_s+\omega_a-2\omega_p)t}}{\sqrt{N_s N_a}}\times\\
&\quad\frac{\int_V (F_{s-p}+F_{a-p})(\mathbf{e}^*_{\pm p})^2\mathbf{e}_{\pm s}\mathbf{e}_{\pm a}dV}{\int_V n_0^2|_c|\mathbf{e}_{\pm p}|^2 dV}.
\end{aligned}
$$

From these equations, we can see that Raman scattering is a four-wave mixing process, thus a 3rd order nonlinear effect. Some terms directly fulfill conservation of energy and phase matching conditions. However, the anti-Stokes signal growth depends on the last term and the phase matching conditions as the two other terms express attenuation. The phase matching conditions depend on the cavity and material dispersion and are difficult to realize in practice. For this reason, we can often neglect the mode equations for $a_{\pm a}(t)$.

We define the Raman gain g_R ($\mathrm{J}^{-1}\mathrm{s}^{-1}$) in the cavity as

$$
g_R = i\frac{1}{4}\omega_s\mu_0 c^2\frac{\int_V F_{s-p}|\mathbf{e}_p|^2|\mathbf{e}_s|^2 dV}{N_p\int_V n_0^2|_c|\mathbf{e}_s|^2 dV} = i\frac{1}{2}\omega_s c^2\frac{\mu_0}{\epsilon_0}\frac{\int_V F_{s-p}|\mathbf{e}_p|^2|\mathbf{e}_s|^2 dV}{\int_V n_0^2|_c|\mathbf{e}_p|^2 dV\int_V n_0^2|_c|\mathbf{e}_s|^2 dV} \tag{B.102}
$$

To link it to the material Ramain gain or *bulk* Raman gain $g_R^{(b)}$ (m/W), we consider that $\Omega_v = \omega_p - \omega_s = \omega_a - \omega_p$ and that the modes propagate mostly in the cavity as $\int_V n_0^2|_c|\mathbf{e}_s|^2 dV \approx n_s^2\int_V |\mathbf{e}_s|^2 dV$. This leads to

$$
F_{s-p} = -iN^2\left(\frac{\partial\alpha}{\partial Q_v}\right)_0^2\frac{1}{2\Omega_v\Gamma_v} = -F_{p-s} = -F_{a-p} = F_{p-a}
$$

and

$$
g_R \approx \frac{\omega_s\mu_0 c^2}{4\epsilon_0 n_p^2 n_s^2\Omega_v\Gamma_v V_{ppss}}N^2\left(\frac{\partial\alpha}{\partial Q_v}\right)_0^2
$$

where $V_{ppss} = \frac{\int_V |\mathbf{e}_p|^2 dV\int_V |\mathbf{e}_s|^2 dV}{\int_V |\mathbf{e}_p|^2|\mathbf{e}_s|^2 dV}$ is the effective volume that quantify the modes overlap. We find the notation of [123–125] for

$$
\begin{aligned}
g_R &\approx \frac{c^2 g_R^{(b)}}{2n_p n_s V_{ppss}}\\
g_R^{(b)} &= \frac{\omega_s}{2\epsilon_0^2 c^2 n_p n_s\Omega_v\Gamma_v}N^2\left(\frac{\partial\alpha}{\partial Q_v}\right)_0^2
\end{aligned} \tag{B.103}
$$

This results in 4 coupled equations :

$$\begin{aligned}
\frac{\partial a_p(t)}{\partial t} &= \left(i\Gamma_{pp} - \Gamma'_{pp} - \frac{1}{2\tau_{p,0}} - \frac{1}{2\tau_{p,c}}\right) a_p(t) + \left(i\Gamma_{p-p} - \Gamma'_{p-p}\right) a_{-p}(t) \\
&\quad - g_R \frac{\omega_p}{\omega_s} \left(|a_s(t)|^2 + |a_{-s}(t)|^2\right) a_p(t) + \sum_L i\kappa_{pL} s_L(z_0, t) e^{-i(\omega_L - \omega_p)t} \\
\frac{\partial a_{-p}(t)}{\partial t} &= \left(i\Gamma_{-p-p} - \Gamma'_{-p-p} - \frac{1}{2\tau_{p,0}} - \frac{1}{2\tau_{p,c}}\right) a_{-p}(t) + \left(i\Gamma_{-pp} - \Gamma'_{-pp}\right) a_p(t) \\
&\quad - g_R \frac{\omega_p}{\omega_s} \left(|a_s(t)|^2 + |a_{-s}(t)|^2\right) a_{-p}(t) \\
\frac{\partial a_s(t)}{\partial t} &= \left(i\Gamma_{ss} - \Gamma'_{ss} - \frac{1}{2\tau_{s,0}} - \frac{1}{2\tau_{s,c}}\right) a_s(t) + \left(i\Gamma_{s-s} - \Gamma'_{s-s}\right) a_{-s}(t) \\
&\quad + g_R \left(|a_p(t)|^2 + |a_{-p}(t)|^2\right) a_s(t) \\
\frac{\partial a_{-s}(t)}{\partial t} &= \left(i\Gamma_{-s-s} - \Gamma'_{-s-s} - \frac{1}{2\tau_{s,0}} - \frac{1}{2\tau_{s,c}}\right) a_{-s}(t) + \left(i\Gamma_{-ss} - \Gamma'_{-ss}\right) a_s(t) \\
&\quad + g_R \left(|a_p(t)|^2 + |a_{-p}(t)|^2\right) a_{-s}(t)
\end{aligned}$$

B.5 Laser system in WGM microcavities

The simplest two-level rate equations for optical fibers are expressed as [247]

$$\frac{dN_2(\mathbf{r},t)}{dt} = \frac{I_p}{\hbar\omega_p}\left(\sigma_{ap}N_1(\mathbf{r},t) - \sigma_{ep}N_2(\mathbf{r},t)\right) + \frac{I_s}{\hbar\omega_s}\left(\sigma_{as}N_1(\mathbf{r},t) - \sigma_{es}N_2(\mathbf{r},t)\right) - \frac{N_2(\mathbf{r})}{\tau_{Tm}} \tag{B.104}$$

$$\text{with } N_T(\mathbf{r}) = N_1(\mathbf{r}) + N_2(\mathbf{r}), \tag{B.105}$$

$$\frac{dP_p(z,t)}{dz} = \sigma_{ep}\int_A I_p(\rho,\theta,t)N_2(\mathbf{r},t)dA - \sigma_{ap}\int_A I_p(\rho,\theta,t)N_1(\mathbf{r},t)dA, \tag{B.106}$$

$$\frac{dP_s(z,t)}{dz} = \sigma_{es}\int_A I_s(\rho,\theta,t)N_2(\mathbf{r},t)dA - \sigma_{as}\int_A I_s(\rho,\theta,t)N_1(\mathbf{r},t)dA. \tag{B.107}$$

N_1 and N_2 are the ions density (ions/m^3) in the ground and upper levels respectively at a position $\mathbf{r}$. The total ions density N_T is fixed and is considered to be constant in the cavity, $N_T(\mathbf{r}) \to N_T$. The amplified spontaneous emission noise is set to zero for simplicity, as spontaneously emitted photons with frequencies $\omega \neq \omega_s$ do not propagate for long in the cavity. τ_{Tm} is the decay time of the spontaneous emission of the thulium $^3F_4 \to {}^3H_6$ transition and is related to the ions concentration [248].

The rate equations that rule over the laser dynamics in fibers are not optimized for WGM microcavities [249] and need to be modified to take into account mode overlap, which is not always the case for WGM laser models [40].

The (ρ,θ,z) coordinates of the fiber geometry is replaced by the spherical coordinates (ρ,θ,ϕ). The optical path increment dz is then replaced by $\rho d\phi$. $d\phi$ can then be replaced by its time increment $d\phi = \omega_j/m_j dt$. The ions densities $N_1(\mathbf{r})$ and $N_2(\mathbf{r})$ are considered to be constant along the ϕ coordinate, so $N_{1/2}(\mathbf{r}) \to N_{1/2}(\rho,\theta)$.

The last two relations B.106 and B.107 are rewritten to take into account the curvature

$$\begin{aligned} dI_{p/s} &= \left(\sigma_{ep/s}I_{p/s}(\rho,\theta,t)N_2(\rho,\theta,t) - \sigma_{ap/s}I_{p/s}(\rho,\theta,t)N_1(\rho,\theta,t)\right)dz \\ &= \left(\sigma_{ep}I_{p/s}(\rho,\theta,t)N_2(\rho,\theta,t) - \sigma_{ap/s}I_{p/s}(\rho,\theta,t)N_1(\rho,\theta,t)\right)\rho\frac{\omega_{p/s}}{m_{p/s}}dt \\ \Rightarrow \frac{d\int_A I_{p/s}dA}{dt} &= \frac{\omega_{p/s}}{m_{p/s}}\left(\sigma_{ep/s}\int_A I_{p/s}(\rho,\theta,t)N_2(\rho,\theta,t)\rho dA - \sigma_{ap/s}\int_A I_{p/s}(\rho,\theta,t)N_1(\rho,\theta,t)\rho dA\right) \end{aligned}$$

where $dA = \rho\sin(\theta)d\rho d\theta$.

Using Relations B.15 and B.16 for sphere's modes, we find for TE modes

$$\frac{d|a_p(t)|^2}{dt} = \frac{\omega_p}{m_p}\frac{|a_p(t)|^2}{\int_A \frac{|e_{p,\theta}(\rho,\theta,t)|^2}{\rho\sin\theta}dA}\left[(\sigma_{ep}+\sigma_{ap})\int_A \frac{N_2(\rho,\theta,t)|e_{p,\theta}(\rho,\theta,t)|^2}{\rho\sin\theta}\rho dA - \sigma_{ap}N_T\int_A \frac{|e_{p,\theta}|^2}{\rho\sin\theta}\rho dA\right]$$

$$\frac{d|a_s(t)|^2}{dt} = \frac{\omega_s}{m_s}\frac{|a_s(t)|^2}{\int_A \frac{|e_{s,\theta}(\rho,\theta,t)|^2}{\rho\sin\theta}dA}\left[(\sigma_{es}+\sigma_{as})\int_A \frac{N_2(\rho,\theta,t)|e_{s,\theta}(\rho,\theta,t)|^2}{\rho\sin\theta}\rho dA - \sigma_{as}N_T\int_A \frac{|e_{s,\theta}|^2}{\rho\sin\theta}\rho dA\right]$$

where $e_{p/s,\theta}$ are the e_θ components of the pump and signal field respectively. $|e_{p/s,\rho}|^2$ are used for TM modes.

Together with the rate equation B.105, these last two equations can not be solved easily as $N_2(\rho,\theta,t)$ distribution is unknown and depends on the mode field distributions, the pump power and the signal power. Considering a low signal power regime, for example near lasing threshold, we can approximate N_2 as

$$N_2(\rho,\theta,t) \to N_2^{max}\frac{I_p(\rho,\theta,t)}{I_p^{max}}$$

where N_2^{max} is the N_2 value at the spatial position where the pump intensity I_p is maximum. Therefore, $N_2(\rho,\theta,t)$ follows the pump field distribution.

Everything can now be rewritten in a form similar to section B.1. With no modal coupling, we have the simplest form

$$\begin{aligned}
&\frac{dN_2^{max}}{dt}A_p|a_p(t)|^2\frac{B_p}{C^{max}} = \qquad\qquad (B.108)\\
&N_T\left[\frac{\sigma_{ap}}{\hbar\omega_p}A_p|a_p|^2B_p + \frac{\sigma_{as}}{\hbar\omega_s}A_s|a_s|^2B_s\right] - \frac{N_2^{max}}{\tau_{Tm}}\frac{B_p}{C^{max}} - \frac{(\sigma_{ep}+\sigma_{ap})}{\hbar\omega_p}A_p|a_p|^2N_2^{max}\frac{B_{pp}}{C^{max}}\\
&- \frac{(\sigma_{es}+\sigma_{as})}{\hbar\omega_s}A_s|a_s|^2N_2^{max}\frac{B_{ps}}{C^{max}}\\
&\frac{da_p}{dt} = \frac{\omega_p}{2m_p}a_p(t)\left[(\sigma_{ep}+\sigma_{ap})N_2^{max}\frac{B_{pp}}{B_p'C^{max}} - \sigma_{ap}N_T\frac{B_p}{B_p'}\right] - \frac{1}{2\tau_p}a_p(t)\\
&\qquad + i(\omega_L-\omega_p)a_p(t) + i\kappa_{pL}s_L(z_0,t)\\
&\qquad = g_{Tm}^{(p)}a_p(t) - \frac{1}{2\tau_p}a_p(t) + i(\omega_L-\omega_p)a_p(t) + i\kappa_{pL}s_L(z_0,t) \qquad (B.109)\\
&\frac{da_s}{dt} = \frac{\omega_s}{2m_s}a_s(t)\left[(\sigma_{es}+\sigma_{as})N_2^{max}\frac{B_{ps}}{B_s'C^{max}} - \sigma_{as}N_T\frac{B_s}{B_s'}\right] - \frac{1}{2\tau_s}a_s(t)\\
&\qquad = g_{Tm}^{(s)}a_s(t) - \frac{1}{2\tau_s}a_s(t) \qquad (B.110)
\end{aligned}$$

where

$$A_{p/s} = \frac{m_{p/s}}{2\omega_{p/s}\mu_0 N_{p/s}},\ C^{max} = \frac{|e^{max}_{p/s,\theta}(t)|^2}{(\rho\sin\theta)|_{max}},$$
$$B_{p/s} = \int_A \frac{|e_{p/s,\theta}(\rho,\theta,t)|^2}{\rho\sin\theta}\rho dA,\ B'_{p/s} = \int_A \frac{|e_{p/s,\theta}(\rho,\theta,t)|^2}{\rho\sin\theta}dA$$
$$B_{pp} = \int_A \frac{|e_{p,\theta}(\rho,\theta,t)|^4}{\rho^2\sin^2\theta}\rho dA \text{ and } B_{ps} = \int_A \frac{|e_{p,\theta}(\rho,\theta,t)|^2|e_{s,\theta}(\rho,\theta,t)|^2}{\rho^2\sin^2\theta}\rho dA.$$